2014

IMPROVEMENTS AND APPLICATIONS OF STATE-OF-THE-ART NUMERICAL MODELS FOR SIMULATING TSUNAMI HAZARD

Tayebeh Sadat Tajalli Bakhsh
University of Rhode Island, ttajalli@my.uri.edu

IMPROVEMENTS AND APPLICATIONS OF STATE_OF_THE_ART NUMERICAL MODELS FOR SIMULATING TSUNAMI HAZARD

BY

TAYEBEH SADAT TAJALLI BAKHSH

A DISSERTATION SUBMITTED IN PARTIAL FULFILLMENT OF THE REQUIREMENTS FOR THE DEGREE OF DOCTOR OF PHILOSOPHY IN OCEAN ENGINEERING

UNIVERSITY OF RHODE ISLAND

2014

DOCTOR OF PHILOSOPHY DISSERTATION

OF

TAYEBEH SADAT TAJALLI BAKHSH

APPROVED:

Dissertation Committee:

Major Professor Stephan T. Grilli

Jason Dahl

John King

Nasser H. Zawia

DEAN OF THE GRADUATE SCHOOL

UNIVERSITY OF RHODE ISLAND
2014

ABSTRACT

The large recent catastrophic events of Indian Ocean with over 300,000 fatalities in 9 different countries and the 2011 Tohoku tsunami in Japan with about 20,000 fatalities and over $100B damage to the Japanese economy, have shown the limitations of some of the modeling approaches used in the past and have stimulated the development of both new models and novel modeling methodologies. In this thesis, some improvements in tsunami modeling is contributed, in part to better simulate tsunami generation by the co-seismic seafloor displacement caused by megathrust earthquakes like the one in **Manuscript 1** (*Pure and Applied Geophysics, 170, 1333-1359, 2013*), and also model tsunamis generated by Submarine Mass Failures (SMFs) on or near the continental shelf break **Manuscript 2** (published online on *Natural Hazards,* 42pps. Nov. 15th,2014). Besides, when assessing coastal tsunami hazard along simple coastlines, one usually sets the static reference level in tsunami models to the largest astronomic tide, typically with 10% exceedence; one also accounts for a potential sea level rise. However, in complex estuaries such as Chesapeake Bay or New York/Hudson River harbor, the dynamic effects of tidal currents on the incoming tsunami waves could, in some situations, enhance tsunami impact. In the **Manuscript 3** (to be submitted) of this thesis, a new approach is implemented to simulate dynamic tide-tsunami interactions and is applied to the full case study of tsunami hazard assessment for the Chesapeake Bay mouth and the James River, which are very vulnerable, low lying, coastal environments equipped with major ports (e.g., Norfolk, Virginia Port authority) and resort areas (e.g., Virginia Beach). In the **Manuscript 4** (To be submitted), by applying the new modeling tools

together with the most recent bathymetric and geophysical data, we revisit the simulation of perhaps the most significant and damaging SMF tsunami case study in modern history: the 1998 Papua New Guinea (PNG) tsunami, to make a valid benchmark for landslide generated tsunami waves.

Accurate tsunami hazard assessment for a specific coastal area requires modeling tsunami impact and inundation from all the possible extreme near- and far-field tsunami sources in a given ocean basin. Tsunami generation from each of these sources must first be performed, which usually requires applying a separate model representing the considered geophysical phenomenon (e.g., subaerial landslide, earthquake, volcanic eruption, submarine mass failure,…). Tsunami propagation to the study site must be conducted. Because of the many spatial and temporal scales involved, this requires using a variety of numerical grids. In this thesis, to perform tsunami propagation and coastal impact simulations with a one-way coupling modeling approach, in a series of nested grids of increasingly fine resolution (with commensurately accurate bathymetric data) is implemented. The tsunami propagation model used here, FUNWAVE-TVD (Shi eta l., 2012; Kirby et al., 2013), is a fully nonlinear and dispersive Boussinesq long wave model that features accurate dissipation by breaking and bottom friction processes. The model has Cartesian and spherical implementations, which are used for simulating nearshore and deep water ocean nested grids, respectively. The model is used to simulate both Submarine Mass Failure tsunami sources and complex co-seismic sources such as for is NHWAVE (Ma et al., 2012), which is a three-dimensional non-hydrostatic sigma-layer model. Coupling between NHWAVE and FUNWAVE will also be applied in the work.

ACKNOWLEDGEMENTS

The completion of this doctoral dissertation was not possible without the assistance of many people. I would like to express my gratitude to my adviser, Dr Stephan Grilli, for his support, guidance and providing me the chance to work with him as a graduate student. Without his supervision these publications would not have been possible.

I would like also to thank my committee members, Dr. Dahl, Dr. King, Dr. Wu, Dr. Annette Grilli and Dr Shen for their time and scientific inputs. I would like to express my appreciation to Gail Paolino, for her kindness, support and help in all situations and conditions; her presence in the department made my life in grad school much easier.

I would love to express my deepest gratitude to my family, who are so far away but always with me; each of them is my precious world. No world could convey my feelings and appreciation to you.

Also I would like to thank my best friends, here in the USA and all around the globe. They are the most valuable achievement of my life. There are a few of them but they mean a lot to me: Alesandra, Amin, Gelareh, Hyewon, Jeannie, Kevin, Maedeh, Mahboubeh, Marzieh, Maryam, Mona, Reza, Tahereh.

Finally, I would like to thank my previous professors who helped me in finding my path through school.

PREFACE

This dissertation is written based on the University of Rhode Island "Guidelines for the Format of Theses and Dissertations" standards for Manuscript format. This dissertation is composed of four manuscripts that have been combined to satisfy the requirements of the department of Ocean Engineering, College of Engineering, University of Rhode Island.

MANUSCRIPT 1: Numerical simulation of the 2011 Tohoku tsunami based on a new transient FEM co-seismic source

This manuscript was published in "Pure and Applied Geophysics, 170, 1333-1359, 2013".

MANUSCRIPT 2: Modeling of SMF tsunami hazard along the upper US East Coast: Detailed impact around Ocean City, MD.

This manuscript is accepted in "Natural Hazards" (NHAZ-D-14-00194R1), and is available online.

MANUSCRIPT 3: Dynamic tidal effects on tsunami coastal hazard in large estuaries: Case of the Chesapeake Bay/James River, USA

This manuscript is ready to be submitted.

MANUSCRIPT 4: Novel Parameterization and Modeling of the 1998 Papua New Guinea SMF Tsunami

This manuscript is ready to be submitted.

TABLE OF CONTENTS

LIST OF FIGURES

LIST OF TABLES

MANUSCRIPT 1

Published in ***Pure Appl. Geophys***. 170 (2013), 1333–1359 **.**

Numerical simulation of the 2011 Tohoku tsunami based on a new transient FEM co-seismic source: Comparison to far- and near-field observations

STEPHAN T. GRILLI[1], JEFFREY C. HARRIS[1], TAYEBEH S. TAJALLI BAKHSH[1], TIMOTHY L. MASTERLARK[2], CHRISTODOULOS KYRIAKOPOULOS [3], JAMES T. KIRBY[4], and FENGYAN SHI[4]

[1] Department of Ocean Engineering, University of Rhode Island, Narragansett, Rhode Island, USA.

[2]Department of Geological Sciences, The University of Alabama (UoA), Tuscaloosa, Alabama, USA.

[3]Instituto Nazionale di Geofisica e Vulcanologia, Rome, Italy.

[4]Center for Applied Coastal Research, University of Delaware, Newark, Delaware, USA.

Abstract

Abstract In this work, we simulate the 2011 M9 Tohoku-Oki tsunami using new co-seismic tsunami sources based on inverting onshore and offshore geodetic data, using 3D Finite Element Models (FEM). Such FEMs simulate elastic dislocations along the plate boundary interface separating the stiff subducting Pacific Plate, and relatively weak forearc and volcanic arc of the overriding Eurasian plate. Due in part to the simulated weak forearc materials, such sources produce significant shallow slip along the updip portion of the rupture near the trench (several tens of meters). To assess the accuracy of the new approach, we compare observations and numerical simulations of the tsunami far- and near-field coastal impact for: (i) one of the standard seismic inversion sources (UCSB; Shao et al (2011)); and (ii) the new FEM sources. Specifically, results of numerical simulations for both sources, performed using the fully nonlinear and dispersive Boussinesq wave model FUNWAVETVD, are compared to DART buoy, GPS tide gage, and inundation/runup measurements. We use a series of nested model grids with varying resolution (down to 250 m nearshore) and size, and assess effects on model results of the latter and of model physics (such as when including dispersion or not). We also assess the effects of triggering the tsunami sources in the propagation model: (i) either at once as a hot start, or with the spatio-temporal sequence derived from seismic inversion; and (ii) as a specified surface elevation or as a more realistic time and space-varying bottom boundary condition (in the latter case, we compute the initial tsunami generation up to 300 s using the non-hydrostatic model NHWAVE).

Although additional refinements are expected in the near future, results based on the current FEM sources better explain long wave near field observations at DART and GPS buoys near Japan, and measured tsunami inundation, while they simulate observations at distant DART buoys as well or better than the UCSB source. None of the sources, however, are able to explain the largest runup and inundation measured between 39.5° and 40.25° N, which could be due to insufficient model resolution in this region (Sanriku/Ria) of complex bathymetry/topography, and/or to additional tsunami generation mechanisms not represented in the co-seismic sources (e.g., splay faults, submarine mass failure). This will be the object of future work.

Keywords: The Tohoku 2011 tsunami. Tsunami source modeling by FEM with geodetic data assimilation. Tsunami propagation modeling (near- and far-field) in a Boussinesq model. Comparison of model results with surface elevation, runup, and inundation observations. Wave dispersion effects. Sensitivity analyses to boundary conditions, model physics, and grid parameters.

1 Introduction

On March 11th, 2011, at 2:46 pm JST (05:46 UTC) a massive earthquake of magnitude Mw = 9.0 struck near the northeastern coast of Japan (37°49' N, 143° 03' E; Figure 1.1), with substantial slip at fairly shallow depths (about 10-20 km), causing large seafloor motions that triggered very high tsunami waves. The main earthquake shocks lasted for 3-4 minutes and, owing to the proximity of the epicenter to shore, the first significant waves reached Japan only 10 minutes after the event started, thus allowing for very little warning time. The tsunami caused extensive and often near total destruction along the coast of the Tohoku region, between 35° - 43° N. Post-tsunami surveys of runups and inundation depths showed maximum values in the 20-40 m range mostly between 37.7° - 40.2° N, where the Miyagi and Iwate Prefectures are located (The 2011 Tohoku Earthquake Tsunami Joint Sur vey Group 2011; Mori et al 2012). [The largest measured runup of 40.1 m occurred in a narrow valley of Ofunato (Iwate; 39.1° N).] The largest runups occurred in the north, along the Sanriku/Ria coast (located north of 37° N), which has a very complicated bathymetry and topography that tends to amplify tsunami impact. By contrast, the area located directly south, which mostly consists of plains, was less impacted by the tsunami. As a result of the tsunami, thousands of people in Japan lost their lives or were reported missing (nearly 16,000 and 4,000, respectively, with 99.6% of those occurring in the Iwate Prefecture; only a very small percentage of casualties was directly caused by the earthquake) a large number of people were injured, and millions more were affected

by the lack of water and food, electricity, and transportation (IOC/UNESCO 2011). This dramatic outcome occurred despite the widespread coastal protections against tsunamis (e.g., seawalls and breakwaters), advanced early warning systems, and evacuation procedures that have been installed, perfected, and rehearsed in Japan over the past few decades. Without these multiple measures, however, in view of the extreme size of this event, it is likely that the human toll in Japan would have been far worse.

Within one hour of the event, when the tsunami reached the nearest DART buoys (Deep-water Assessment and Reporting of Tsunami network; Gonzalez et al (1998); Figure 1.1), propagation models of the anticipated far-field impact of the tsunami caused sufficient concern (particularly with the US Pacific Tsunami Warning Center; PTWC) to trigger evacuations and warnings in many distant areas across the Pacific Ocean. Large impact was predicted as far as South America (e.g., Chile), where waves were expected to arrive after more than 20 h of propagation. In the meantime, through a chain of failures of coastal protections and back-up power systems caused by the earthquake and the tsunami inundation, the core of one of the reactors at the Fukushima Dai-Ichi nuclear power plant (near 37° 25' N) started melting, eventually causing explosions that released large doses of radiation, forcing a complete evacuation in the days following the event of all people living within tens of kilometers of the power plant that will likely last for many decades.

At least three historical events had been identified in paleo-tsunami and other records to have caused large coastal impact and runup in the Tohoku region, i.e., the 869 Jogan (with book records showing coastal inundations perhaps even greater than

for the 2011 event), the 1611 Keicho Sanriku (tsunami height 6–8 m), the 1896 Meiji (maximum runup 38.2 m), and the 1933 Showa (maximum runup 29.2 m) tsunamis (Hatori 1975; Abe et al 1990; Minoura et al 2001; Sawai et al 2008). These and other

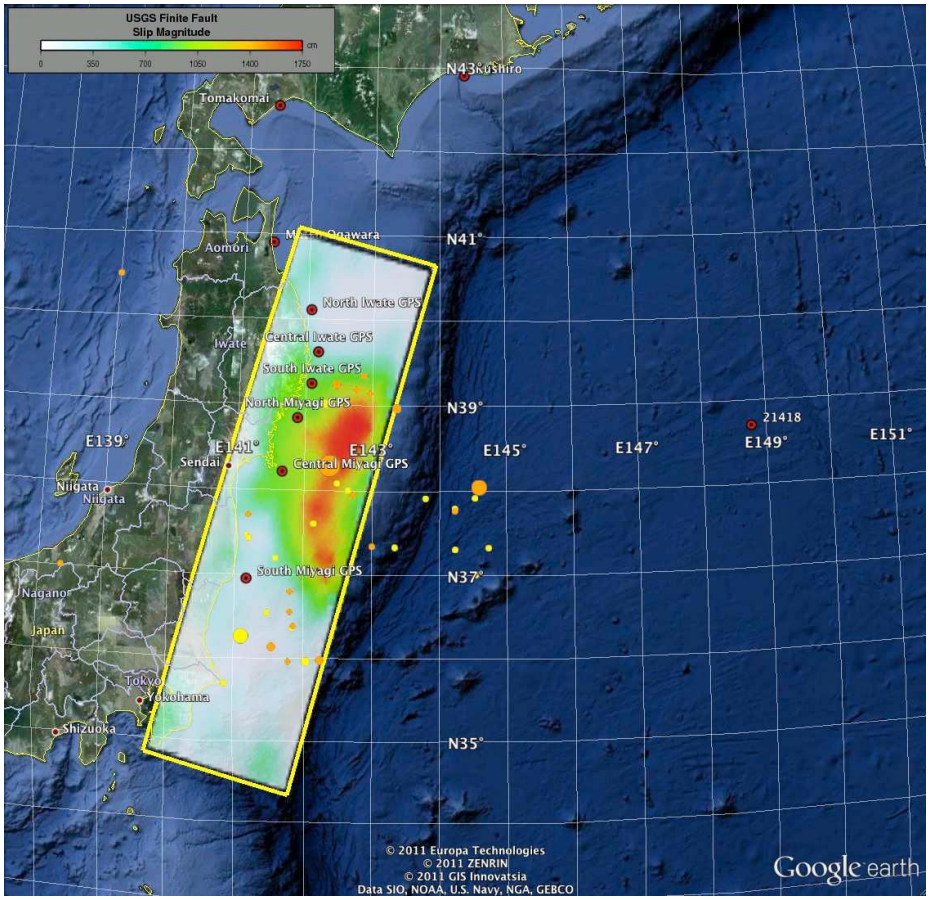

Figure 1.1 Location and maximum slip magnitude (color scale) of USGS finite fault model source for the M9 Tohoku-Oki earthquake of March 11th, 2011, at 2:46 pm JST (05:46 UTC). Plain yellow and orange circles indicate the location of the main aftershocks (of varying depth (color) and magnitude (size)), during the first 10 hrs following the event (the largest symbol within the maximum slip area marks the epicenter). Red dots mark the location of nearshore GPS buoys (labeled) and the one DART buoys nearest Japan (unlabeled to the right). [The Tohoku region occupies the northeastern portion of Honshu, the largest island of Japan, approximately north of 36° N, and consists of six prefectures: Akita, Aomori, Fukushima, Iwate, Miyagi and Yamagata. The darkest blue area east of Tohoku denotes the expression of the Japan trench on the seafloor.]

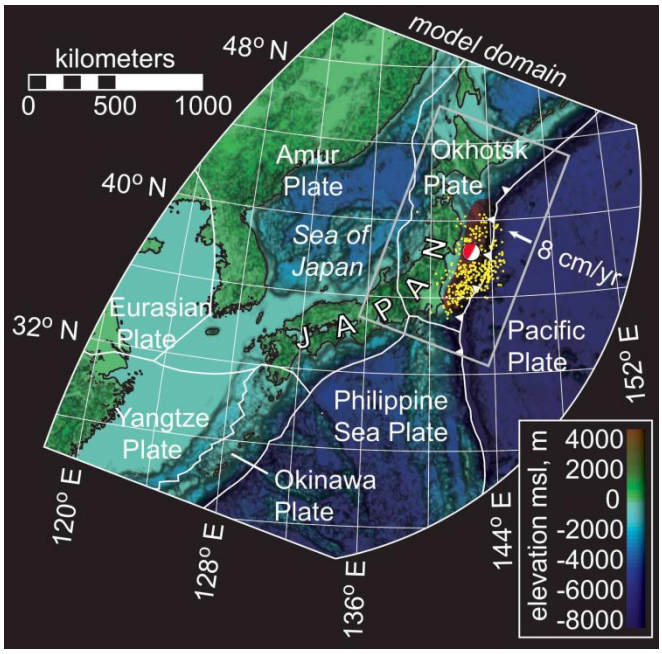

Figure 1.2 Seismotectonics of the M9 2011 Tohoku Earthquake. The surface projection of the rupture zone is marked by the red polygon. The epicenter is shown with the USGS CMT focal mechanism (see Figure 1.1). Yellow dots are epicenters for M > 4 aftershocks, spanning 11 March through 06 May 2011. The Pacific-Okhotsk plate convergence is about 8 cm/yr. Plate boundaries are modified from Bird (2003).

significant events were assembled into a compounded historical record of runup and inundation in the area, which closely resembles post-tsunami survey observations of the Tohoku tsunami impact (The 2011 Tohoku Earthquake Tsunami Joint Survey Group 2011; Mori et al 2012). Based in part on such historical records and on knowledge of local tectonics, large earthquakes with magnitude as high as $M_w \simeq 8.2$ had been expected for this area of Japan in the near future (although further south). However, the large magnitude of the Tohoku-Oki earthquake and especially of the generated tsunami were largely unexpected, at least by those in charge of tsunami hazard assessment and mapping in Japan.

This tsunami is indeed believed to have been the largest in Japan's recorded history (Hayashi et al 2011). The earthquake ruptured the boundary separating the subducting Pacific Plate from the overriding Okhotsk Plate (a small and narrow plate that is distinct from the North American Plate; Seno et al (1996)). This segment of the plate boundary intersects the seafloor at the Japan Trench (Figure 1.2), where it dips about 10◦ to a down-dip distance of about 100 km from the trench. The dip of the subducting plate then increases along the seismogenic zone to the west (Hasegawa et al 2007). The rupture area, 150 km east of Sendai, Japan, extends a few hundred km in the along strike direction, offshore of the Prefectures of Aomori, Miyagi, and Fukushima. At the latitude of the earthquake, the Pacific Plate moves approximately westwards with respect to the Okhotsk Plate at a rate of 8 cm/yr (DeMets et al 1994) (Figure 1.2). The focal mechanisms reported by Harvard CMT, the U.S. Geological Survey (USGS), and the Earthquake Research Institute at the University of Tokyo, all indicated that the earthquake was predominantly thrust with a moment more than $M_o \simeq 4.0 \times 10^{22}$ N.m and a variety of seismic, geodetic, and tsunami genesis studies concluded that the magnitude was indeed Mw = 9.0 (e.g., Ide et al (2011); Simons et al (2011)). Some geodetic inversion models (e.g., Ozawa et al (2011); Pollitz et al (2011)) suggest that the peak slip may have exceeded 30-35 m in some areas, while some seismic inversion models suggest over 50-60 m of maximum slip (e.g., Ammon et al (2011); Shao et al (2011); Lay et al (2011a)). Owing to the small dip angle, such large slip values caused very large uplift of the seafloor, likely reaching well over 10 m in a large central area of the tsunami source (Figure 1.1).

1.1 Modeling of the Tohoku-Oki tsunami

Early forecasts of the Tohoku tsunami far-field impact, such as those issued by NOAA's PTWC, were not based on realtime tsunami modeling, but instead on the SIFT (Short-term Inundation Forecast for Tsunamis) database; i.e., these were developed through a tsunami data inversion technique and site-specific inundation forecasts (Gica et al 2008). The SIFT database is a library of tsunami events (referred to as "unit sources"), which were pre-computed using a propagation model, for a series of design earthquakes distributed along all the active faults (Gica et al 2007), each 100 by 50 km in size and with a moment magnitude of Mw = 7.5. For a specific event, the inversion uses the SIFT unit sources whose locations and pre-defined parameters (i.e., dip and rake-angles, slip, depth of source) are closest to the earthquake epicenter and characteristics, adjusted for the observed moment magnitude (Gica et al 2008). Realtime tsunami elevation data measured by the deep water DART buoys network are used in the inversion to weigh these approximate sources, by constraining the predicted combined elevations to closely agree with DART measurements. These calibrated tsunami events are then used to provide rapid predictions of far-field impact.

Real-time tsunami forecasting in the near-field is more site specific and, hence, is much more difficult to perform and thus less developed. After the event, Tsushima et al (2011) inverted the offshore wave data from various tsunami wave buoys, recorded 5–10 min before the tsunami reached the coastal tide gages nearest to the earthquake source, and estimated the distribution of the initial offshore sea-surface elevation. They then combined tsunami waveforms from this estimated source to

forecast the waves' arrival times and amplitudes at coastal tide gauges. Results agreed sufficiently well with observations to indicate that such a forecasting method could contribute to reliable near-field tsunami warnings. Somewhat more detailed and comprehensive is the approach of Fujii et al (2011), who estimated a tsunami source for the event by inverting tsunami waveforms recorded at tide and wave gages, GPS wave gauges, and deep water DART buoys. The initial seismic parameters were determined from the USGS W-phase moment tensor solution (e.g., strike, dip, slip angle), but the initial wave elevation was based on models of individual subfaults, which were then used to estimate the slip over the total fault, using a least-squares method.

Detailed modeling of the event, both earthquake and tsunami generation, and of tsunami propagation and near- and far-field impacts, which is the object of the present work, is a more involved and lengthy process that was tackled by several groups in the months following the event. Such modeling can help better understand and explain the processes that led to the triggering of such large waves and caused widespread coastal destruction; and hopefully allow to be better prepared for future similar events, in terms of mitigation and forecast. Such work first involves developing a relevant tsunami source, that accounts for local geological and tectonic processes (i.e., the Japan trench and subduction zone structures) as well as observed seismic (i.e., inverted seismic waves from seismograph measurements) and geodetic (i.e, directly measured seafloor and land deformation) data. Using such a source together with sufficiently accurate and resolved bathymetric and topographic data, numerical models of tsunami generation, propagation, and coastal impact can then be

run, whose results are compared to available field data (e.g., tide gage and deep water DART buoys, runup and inundation measurements). Modeling refinements follow and, once a reasonable agreement between simulations and observations is achieved, numerical results can be used to better understand tsunami processes that unfolded during the event, such as explaining the failures of coastal protection structures. Improved design and construction methods for tsunami mitigation techniques can finally be suggested. Along this line, for instance, Yamazaki et al (2011b,2012) studied the effects of the Tohoku tsunami on Hawaii, using two of the early proposed finite-source models obtained from seismic and geodetic inversions (Lay et al 2011b), and applying their "Non hydrostatic Evolution of Ocean Wave" (NEOWAVE) tsunami propagation model (Yamazaki et al 2009). They used forward modeling of tsunami records at the 4 DART buoys located nearest Japan to refine the location of the main fault slip. They then modeled far-field tsunami propagation and compared model results to DART buoy measurements made throughout the Pacific, GPS buoy and wave gage data near the Japanese coast, and tide gage and runup measurements in Hawaii. They reported a reasonable agreement at most locations between simulations and observations, although they needed to introduce a time shift in the computed time series at the farthest distant locations.

1.2 Modeling of the Tohoku-Oki earthquake source

Since the occurrence of the Tohoku event, a large variety of seismic models of the earthquake have been proposed. These were usually based on inverting seismic and/or gedetic data, using the Okada (1985) model, which assumes a superposition of

planar dislocations (i.e., finite faults) embedded in homogeneous elastic half-spaces (HEHS), or a similarly idealized source model of the subduction zone (e.g., Dziewonski's 1981 spherical layered PREM seismological model; see, e.g., Ammon et al (2011); Geospatial Information Authority of Japan (2011); Koper et al (2011); Pararas-Carayannis (2011); Pollitz et al (2011); Ozawa et al (2011); Shao et al (2011)). One of these seismic inversion sources, referred to as UCSB (Shao et al 2011), will be used in this study.

In the present work, to better account for the actual geometry of the Japan trench and its forearc, as well as inhomogeneities in material properties in the subduction zone (e.g., weaker forearc and stiffer subducting plate materials), we developed and used our own source, based on a more comprehensive and detailed Finite Element Modeling (FEM) (Masterlark 2003) of the subduction zone near Japan. An earlier implementation of this approach was successfully applied to the 2004 M9 Sumatra-Andaman earthquake (Masterlark and Hughes 2008). This new tsunami source (referred to as University of Alabama; UA), which is detailed later, was developed by inverting onshore and offshore geodetic data (similar to other sources listed above) but, rather than using Okada's idealized HEHS solution, we used 3D FEMs that simulate elastic dislocations along the plate boundary interface separating the stiff subducting Pacific Plate, and relatively weak forearc and volcanic arc of the overriding Eurasian plate.

Another aspect of tsunami sources that may significantly affect the accuracy of simulations in a propagation model is whether one assumes that the maximum seafloor deformation is triggered at once in the model for the entire source area, or that sub-

areas of the source are triggered as a time sequences that mimics the actual earthquake event. Such a time sequence can be obtained as a result of seismic inversion methods. For tsunamis that are only triggered over a relatively small source area (such as for Tohoku 2011), it has been customary to assume that the source can be triggered at once. However, it appears from seismic inversion results of this event (e.g., Harvard CMT) that the main event lasted for 3-4 minutes, during which tsunami waves may have propagated a large distance onshore. Hence, in the present case, it may be important to consider this timing effect and resolve the wave interferences (constructive or destructive) that may have resulted. The sensitivity of tsunami simulations to this timing aspect will be presented later in the present work. Additionally, we will study the sensitivity of results to the way the tsunami is initially specified in the propagation model: (i) either as a free surface elevation with no initial velocity (as it is customary to do in most studies owing to the near incompressibility of water and small rise times); (ii) or as a more realistic time dependent bottom boundary condition (in this case a different type of model, NHWAVE, that allows for such a boundary condition to be specified on the seafloor as a function of space and time, will first be used during 300 s, before moving results into a long wave propagation model; this is detailed later).

1.3 Tsunami generation and propagation models

Large co-seismic tsunamis have usually been simulated using numerical models based on the non-dispersive (i.e., hydrostatic) Nonlinear Shallow Water (NSW) wave equations (e.g., Kowalik and Murty (1993); Satake (1995)). By contrast,

since the late 1990s, our research group has pioneered the use of fully nonlinear and dispersive (i.e., non-hydrostatic) Boussinesq models (BM), with extended dispersion properties. These were initially applied to the simulation of landslide tsunamis, in which dispersive effects are important owing to the shorter wavelengths (Watts et al 2003; Day et al 2005; Tappin et al 2008; Abadie, Harris, and Grilli 2012), but more recently also to the simulation of co-seismic tsunamis (Grilli et al 2007, 2010; Ioualalen et al 2007; Karlsson et al 2009). Although dispersive effects may not always be significant in long tsunami wave trains, when they are called for, BM equations feature the more extended physics required to simulating such effects. Ioualalen et al (2007), for instance, showed differences in the computed elevation of leading waves, for the 2004 Indian Ocean tsunami event near Thailand, of up to 30% when simulating the tsunami using a BM with or without the dispersive terms (i.e., in NSW mode in the latter case). The BM model used in this work, FUNWAVE, was initially developed and validated for coastal wave dynamics problems (Wei et al 1995; Chen et al 2000, 2003; Kennedy et al 2000); later, however, FUNWAVE was used to perform many successful tsunami case studies, as discussed above. In its most recent implementation, FUNWAVE-TVD, in Cartesian (Shi et al 2012) or spherical coordinates with Coriolis effects (Kirby et al 2009, 2012) (note, the latter implementation is currently only weakly nonlinear), the code uses a Total Variation Diminishing (TVD) shock-capturing algorithm to more accurately simulate wave breaking and inundation. The code is fully parallelized using the Message Passing Interface (MPI) protocol. Because of their more complex equations, BMs are typically more computationally demanding than NSW models. However, the optimized MPI implementation of FUNWAVE-TVD

has highly scalable algorithms, with a typical acceleration of computations of more than 90% the number of cores in a computer cluster (Shi et al 2012). Hence, running such models over large ocean basin-scale grids with sufficiently fine resolution, is no longer problematic.

In the present study, FUNWAVE-TVD is used in its Cartesian implementation to simulate the near-field tsunami propagation from the source to the Japan coast and in its spherical implementation to simulate the far-field tsunami propagation from the source to distant locations in the Pacific Ocean. Results will show that dispersive effects do not appear to be very significant in the near-field for the type of tsunami sources used to date for Tohoku 2011 (i.e., purely coseismic). However, as these sources are refined (both in space and time) to include more complex geological and seafloor processes (e.g., sub-faults, splay faults, submarine mass failure), one will increasingly have to model the superposition and interactions of shorter and hence more dispersive waves, which requires using models that simulate this type of physics (such as BMs). Additionally, although in the present work we will not use a fine enough coastal grid resolution for such phenomena to appear in simulation results, recent work showed that, even very long waves may transform into undular bores over a wide shelf, as they approach the shore (Madsen et al 2008; Kim and Lynett 2011). Such bores are made of a large number of short waves (with periods more akin to very long swells), which are thus highly dispersive, overlying a longer surge, that may enhance tsunami coastal impact. Non-dispersive NSW models cannot simulate such processes (Kim and Lynett 2011).

In the following, we first present in Section 2 the field data used in the comparisons with model results. We then present in Section 3 the definition and development of the tsunami sources used as initial conditions in the propagation models. In Section 4, we briefly summarize the propagation model equations and features and discuss model setup. Results are finally presented and discussed in Section 5. Specifically, we report on simulations of the far- and near-field coastal impact of the Tohoku tsunami, using FUNWAVE-TVD. The model is initialized with either the USCB or the new UA source. Results are compared with measurements of surface elevations at DART and tide gage buoys, and runup and inundation heights on the shore. Computations are performed in a series of nested model grids, with varying resolution (down to 250 m nearshore) and sizes. Some cases are run with or without dispersion terms in the BM equations, to assess effects on results of the latter. Additionally, as indicated before, we also study the sensitivity of model results to the type of initialization.

2 Field Data

Many field measurements of the tsunami were made both during and after the event, which primarily consisted of: (i) deep water DART buoy measurements of surface elevation (Lay et al 2011b); (ii) nearshore GPS buoy or tide gauge measurements of surface elevation (Yamazaki et al 2011a); and (iii) onshore field surveys of runup and inundation height (The 2011 Tohoku Earthquake Tsunami Joint Survey Group 2011; Mori et al 2011, 2012). These recorded data and post-event surveys, which were conducted by a large international team of scientists along a

2,000 km stretch of the Japanese coast at more than 5,300 individual locations, generated the largest tsunami survey dataset ever (Mori et al 2011, 2012).

2.1 DART buoys

Offshore, tsunami measurements from the DART network are critical elements in (near) realtime tsunami forecasting and modeling (Titov et al 2005). There are 39 operational DART buoys installed and operational throughout the Pacific and Atlantic oceans, whose measurements can be obtained on the internet as soon as they are available (http://www.ndbc.noaa.gov/dart.html). At each buoy, data is routinely collected in 15 s to 15 minute intervals, depending on the level of alert. When the passage of a tsunami has been identified at a particular buoy (after the DART network has been put on alert), average surface elevation data is transmitted every 15 s during the initial few minutes, followed by 60 s intervals (Gonzalez et al 1998). To obtain the tsunami signal, this data first needs to be filtered to remove the tidal signal. In this study, we analyzed data from the 18 DART buoys, which were located in the path of the tsunami (Lay et al 2011b), and used it for comparison with model results obtained at the same locations (Figure 1. 3). Here, DART data was detided using a Butterworth filter and then interpolated to get equal intervals of 15 s.

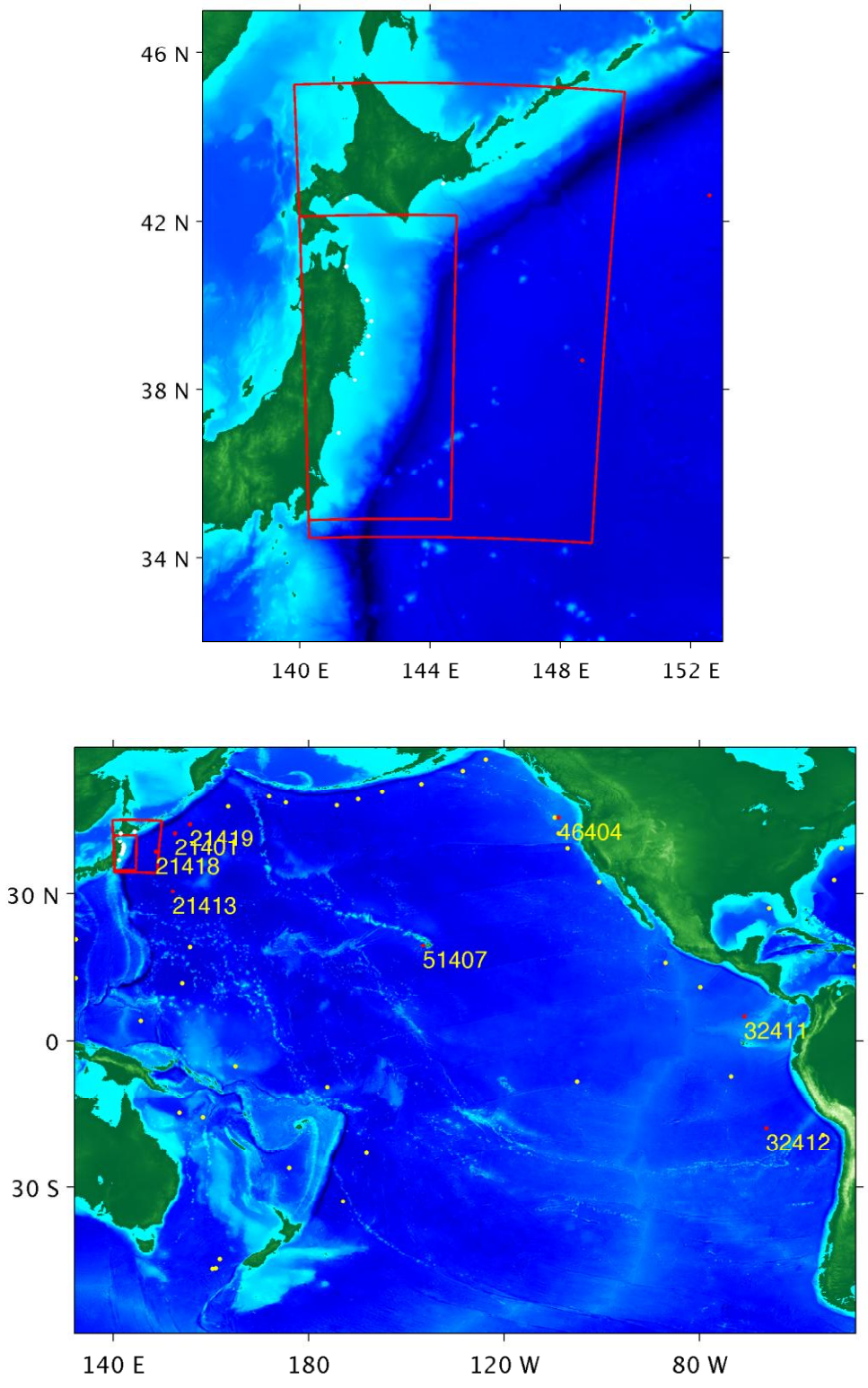

Figure 1.3 Computational domains for : (a) near-field (regional) simulations with FUNWAVE-TVD (Cartesian grid) and NHWAVE; and (b) far-field (Pacific basin scale) simulations with FUNWAVE-TVD (4' spherical grid), with the marked location of 18 DART buoys (yellow dots not used; labeled red dots used in comparisons). The smaller and larger red boxes mark the boundaries of the coastal 250 m, and regional 1000 m, resolution grids, respectively (Table 1.1). The white dots in panel (a) indicate the location of the GPS buoys of Figure 1.11

2.2 GPS buoys

Near the Japanese coastline, a series of moored GPS-mounted buoys from the NOWPHAS (Nationwide Ocean Wave information network for Ports and HArbourS; http://nowphas.mlit. go.jp/infoeng.html) are moored in water depth of 100 to 300 m and at a distance of 10 to 20 km from the coastline (Figure 1.2). These sturdy buoys resisted the large tsunami waves during the Tohoku 2011 event and provided time series of surface elevation, through the measurement of their 3D position every one second (using RTK-GPS technology to position the GPS mounted on top of each buoy). Tsunami elevation was obtained by a low-pass filtering, with a moving average technique (Kato et al 2005).

2.3 Runup and inundation field measurements

Field surveys started two days after the tsunami and were conducted by several research groups totaling 299 scientists from 64 different universities/institutes (The 2011 Tohoku Earthquake Tsunami Joint Survey Group 2011; Mori et al 2011, 2012). Inundation (local tsunami height above sea level) and runup heights (elevation at maximum inundation) were measured at a total of 5,247 points (see Figure 1. 17 central panel). Inundation heights were obtained from watermarks on trees, walls, and buildings, and detided for the time of tsunami impact. Runup heights were derived from the maximum extent of debris deposits and water marks.

2.4 Bathymetric and topographic data

Bathymetric and topographic data was obtained and compounded from several sources. These include: the 1 arc-minute resolution ETOPO1 database (Amante and Eakins 2009); the 500 m resolution J-EGG500 bathymetry (JODC-Expert Grid data for Geography) along the Japanese coastline and the 1 arc-second ASTER topographic data (Advanced Space Borne Thermal Emission and Reflection Radiometer; Yamaguchi et al (1998)). Although Digital Elevation Models (DEMs) have already been developed for this area (e.g., the GMRT of Ryan et al (2009)), which already compile available topography datasets into grids useful for computational models, early tests showed that these DEMs do not provide a smooth topography along the Japanese coastline, which is problematic for simulating coastal impact of tsunamis in propagation models.

For the coarser computational grids, which are used to model the tsunami distant propagation across the Pacific Ocean, or for our initial 1 km resolution simulations near the tsunami source, the grid bathymetry was only generated based on ETOPO1 data. For higher resolution grids, such as used nearshore (e.g., 250 m), we interpolated both the ASTER topography and the JODC bathymetry to our computational grid (using a linear interpolation method). For points, which are in the ocean (i.e., where the ASTER topographic height is zero), the depth was found by interpolating between all other points (i.e., the final result is a linear interpolation of ASTER and JODC data onto the computational grid). The most substantial problem with this approach is that, in narrow bays where no bathymetric measurements are available from the JODC data, depth is set to zero in the entire area, most likely

causing an underprediction of tsunami runup in such cases (such as along the Sanriku/Ria coast; see result section below).

3 Source model and initial conditions

As discussed in the introduction, the traditional approach to initializing a long wave propagation model for co-seismic tsunami simulations is based on the Okada (1985) solution, which provides the seafloor deformation due to the motion (slip) of a fault in an elastic homogeneous half-space. In the latter, the dip angle is defined as the angle between the fault and a horizontal plane (between 0^o and 90^o); the strike angle is the fault direction relative to north (0^o to 360^o ; defined such that the fault dips to the right of this angle); and the rake is the direction the hanging wall moves, measured relative to the fault strike (-180^o to 180^o). In finite fault source models, such as USGS's (Figure 1.1), which are obtained by seismic inversion (i.e., using seismic waves measured at many seismographs around the earth, together with a model of the earth crust), Okada's solution is applied to many subfaults, on the basis of the inverted slip distribution (and other parameters). Many inverted slip distributions have been published since the event, which were discussed in the introduction. Among those, we found that the source referred to as UCSB (Shao et al 2011) provided the best agreement with tsunami measurements. [To reach this conclusion, we simulated two preliminary UCSB sources as well as both a preliminary and a final USGS source.]

As discussed in the introduction, to better account for the actual geometry of the Japan trench and its forearc, as well as inhomogeneities in material properties in the subduction zone, we also developed and used our own source, referred to as

University of Alabama (UA) source. The UA source is based on a detailed Finite Element Modeling (FEM) of the subduction zone near Japan, in which onshore and offshore geodetic data measured during the event are assimilated as part of the solution. While still not perfect, as we shall see, this source produces significant shallow slip, several tens of meters along the updip portion of the rupture near the trench (likely due to the simulated weak forearc material), which allows better simulating some of the tsunami observed features and impact. In the following, we present and compare results of tsunami generation, propagation, and impact for the UCSB and UA sources.

3.1 UCSB source

The source we denote as UCSB is based on the slip history derived by Shao et al (2011) using tele-seismic body and surface seismic waves. The UCSB source assumes the earthquake epicenter was located at 38.10° N and 142.86° E, and the seismic moment was $M_o = 5.84 \times 10^{22}$ N.m, for a dip angle of 10° and a strike angle of 198°. Figure 1.4 shows the maximum slip distribution obtained for this source, as well as the corresponding maximum seafloor uplift (note, for comparison with uplift predicted by the UA source, the UCSB uplift is replotted in Figure 1.7d at the same scale and compared to field measurements). For the time-dependent triggering of this source, the rise-time computations are based on an asymmetric cosine parameterization, described by Ji et al (2002). As we shall see, the time-dependent triggering of this source in FUNWAVE results in somewhat different wave elevations

at the end of the earthquake main shock, as compared to the instantaneous triggering of the entire source.

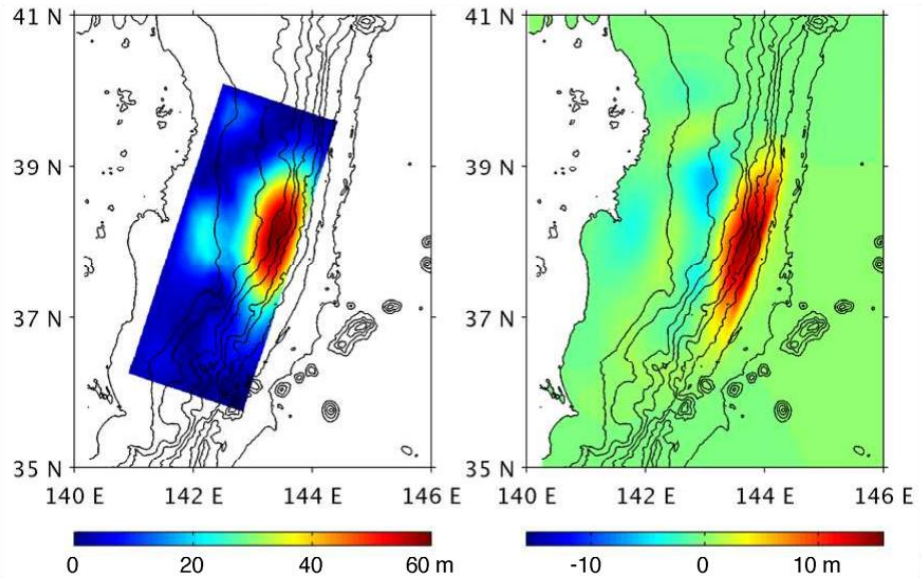

Figure 1.4 UCSB source (Shao et al 2011): (a) Source area and maximum slip distribution; and (b) vertical seafloor displacement.

3.2 UA source

As discussed above, this source (referred to as UA; Figures 1.5 to 1.7) is developed by simulating the deformation of the M9 2011 Tohoku earthquake using FEMs of the subduction zone, rather than idealized semi-analytical solutions (e.g., Okada). These FEMs, which simulate an assembly of dislocation surfaces embedded in a 3D elastic domain, are constructed with Abaqus (2009) and share the general geometry, mesh, and distribution of material properties of FEMs presented by Masterlark and Hughes (2008) and Hughes et al (2010). The domain is partitioned into six regions representing the different elastic properties of the forearc, volcanic arc, shallow and deep backarc, oceanic crust, and mantle (Figure 1.5). An innovational

aspect of this model is its ability to simulate dislocation along a dipping fault having relatively weak materials of the overriding plate juxtaposed across the fault from relatively stiff oceanic crust of the downgoing slab (Masterlark and Hughes 2008).

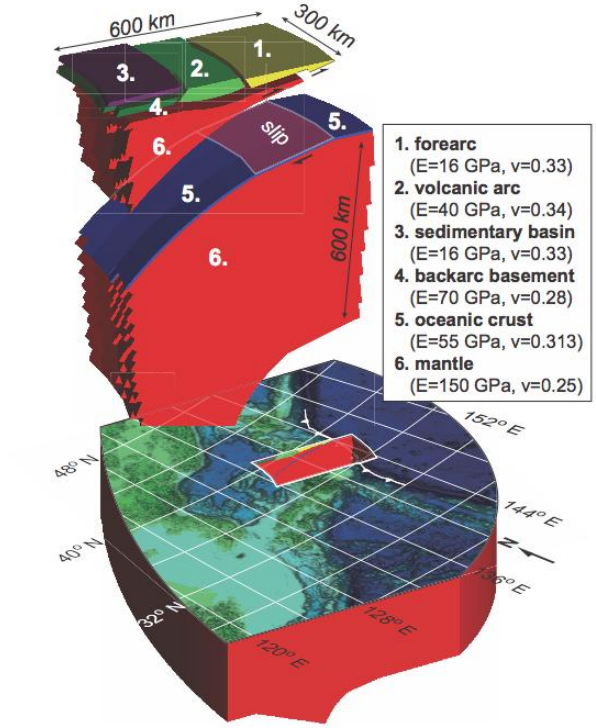

Figure 1.5 FEM domain and FEM Configuration. The domain is partitioned to include a characteristic distribution of elastic properties for the subduction zone according to Hughes et al (2010). A portion of the near-field region is shown in exploded view to reveal the structure and configuration of materials. Material properties of the mantle and crust are drained and undrained, respectively. The juxtaposition of weak and strong materials across the dipping fault is fundamental to the subduction zone structure and strongly influences deformation predictions. The rupture is simulated with elastic dislocations along the dipping surface separating the stiff subducting slab and weak overriding plate. This downdip interface between the two plates is welded. The top of the domain is a stress-free surface and the lateral and basal boundaries are zero displacement. The initial conditions are equilibrium. The coseismic slip is calibrated to onshore and offshore geodetic data, using least-squares inverse methods and FEM-generated Greens functions.

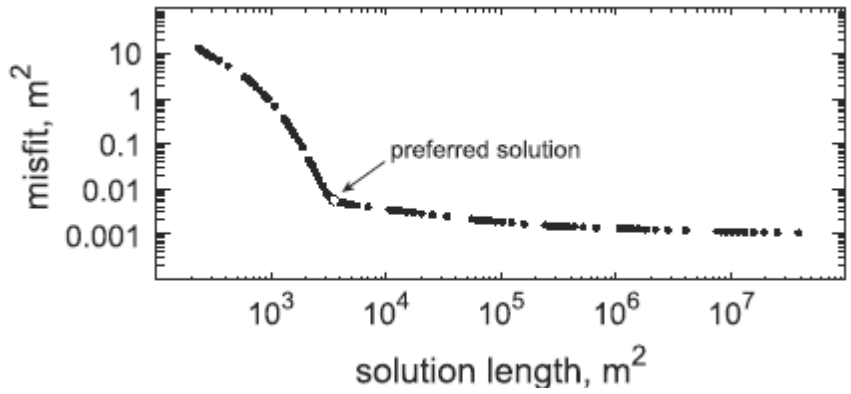

Figure 1.6 L-curve. Each black circle represents the solution length versus misfit associated with a given damping coefficient. The knee of the L-curve is the preferred solution, which is a compromise between fitting the data versus satisfying the smoothing constraints (Aster et al 2005).

The FEM domain is configured to simulate net deformation along a rupture surface having the along-strike curvature of the Japan Trench and a dip of about 12°. The dimensions of the curved rupture are about 750 km×200 km along-strike and downdip, respectively. This rupture surface is partitioned into 98 dislocation patches. The distribution of slip along the rupture is calibrated via least-squares inverse methods, by assimilating three- component geodetic data from 521 onshore GPS stations (GEONET of Japan, processed by the ARIA team at JPL/Caltech; ftp://sideshow.jpl.nasa.gov/pub/usrs/ARIA) and 5 offshore stations (Sato et al 2011) that characterize the nearfield coseismic deformation of the M9 Tohoku earthquake.

The forward model for deformation caused by a distribution of dislocation patches, scaled to account for the relative data uncertainties and regularized with Laplacian smoothing is:

$$[G_W + \beta L]m = d_W \quad (1)$$

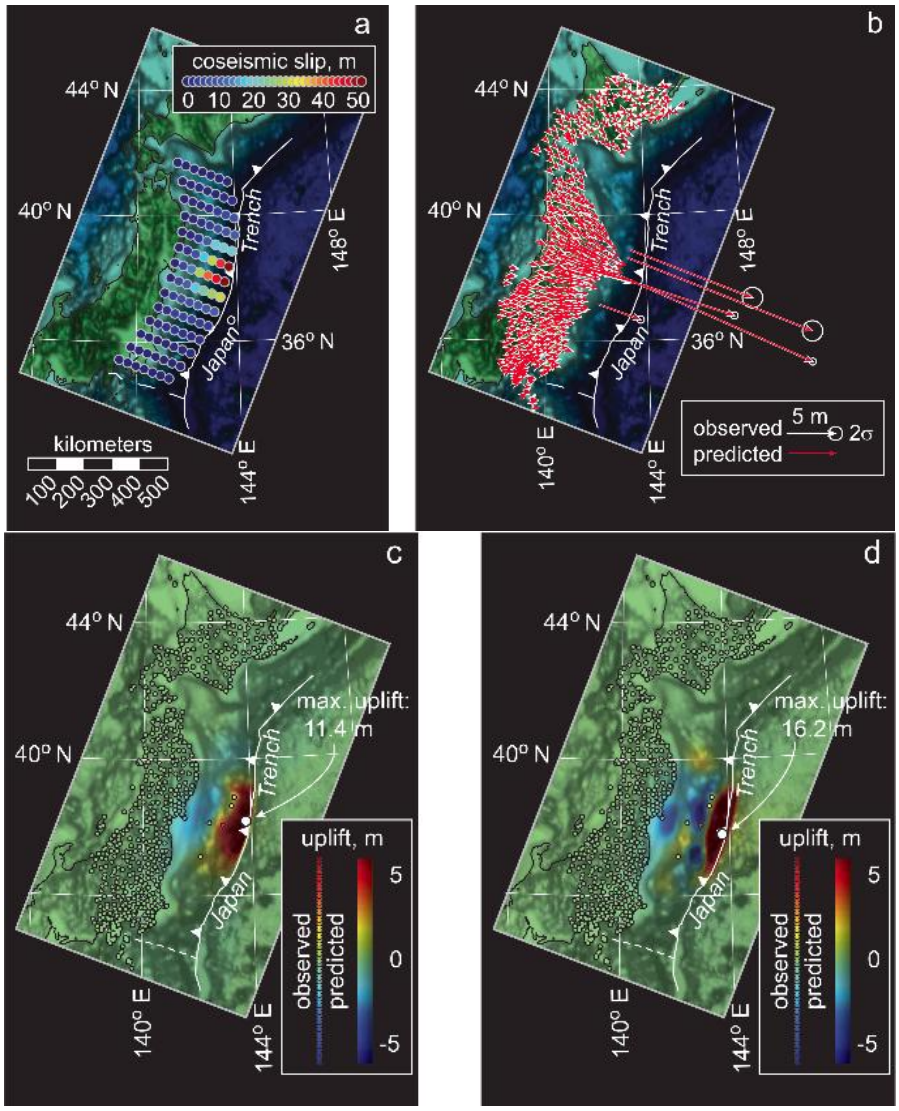

Figure 1.7 FEM-based coseismic slip and deformation. (a) Coseismic slip distribution. The position of each circle represents the surface projection of the centroid for a slip patch, each of which comprises four note pairs that simulate elastic dislocation with kinematic constraint equations (Masterlark and Hughes 2008). The coseismic slip is concentrated near the trench, with a maximum magnitude of 51 m. Both horizontal (b) and vertical (c) deformation are well predicted by the FEM. Vertical predictions for UCSB source (d) poorly predict seafloor geodetic data (Sato et al 2011) and, in particular, predict that the main transition from subsidence to uplift is several tens of kilometers closer to the trench than is indicated by the offshore geodetic data.

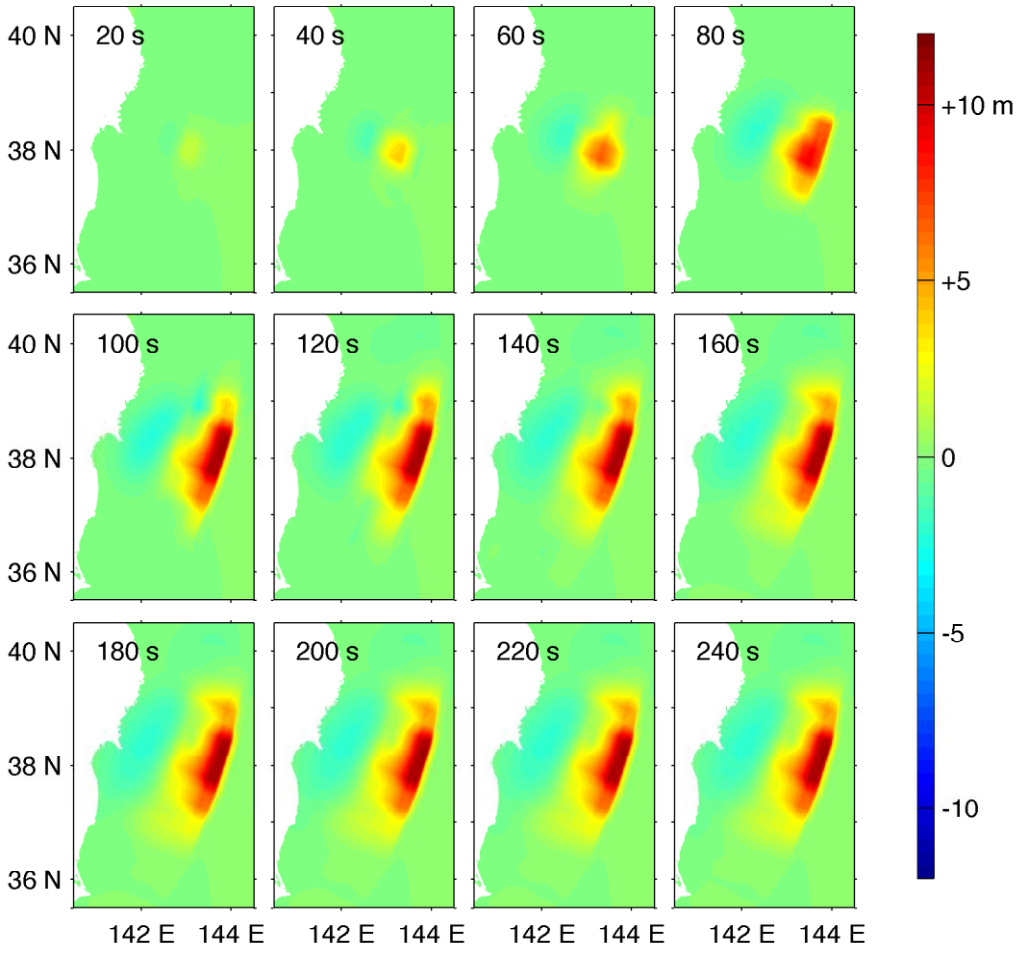

Figure 1.8 Snapshots of cumulative seafloor uplift caused by the UA source, as a function of time, in 20 s intervals. The timing sequence is obtained from Yue and Lay (2011).

where G_w = WG and d_w = Wd, G is a matrix of Green's functions for displacement due to dislocation for both thrust and strike-slip components, m is a column vector of dislocation parameters, d is a column vector of displacement observations, and W is a diagonal matrix, where diagonal elements correspond to the relative data uncertainties, L is a matrix of coefficients that satisfies $\nabla^2 m = 0$ for a given set of boundary conditions. The boundary conditions for the Laplacian smoothing are zero slip along

the northern, southern, and downdip edges of the rupture. The trench-normal slip gradient is zero along the updip boundary, which follows the trace of the Japan Trench (Figure 1.7). The Green's functions are calculated with the FEMs using the method of kinematic constraint equations (Masterlark 2003) and undrained elastic parameters (Wang 2000).

We sweep through damping coefficients, β, and determine a suite of corresponding least-squares solutions for m by inverting the forward model. The damping coefficient controls the trade-off between fitting the data and having a smooth solution. We then calculate the weighted least-squares misfit (e^T e), where e is the prediction error $e=d_w - G_w m$ and T is the transpose operator, as a function of regularized solution length $(Lm)^T$ (Lm). The solution that corresponds to the knee of the curve plotted as the logarithm of e^T e versus the logarithm of $(Lm)^T$ (Lm) provides a good compromise between fitting the data and smoothing (Aster et al 2005) (Figure 1.6). This is our preferred solution. The maximum magnitude of slip for this solution is about 51 m, and the solution corresponds to a moment magnitude of M_w = 8.8, which is perhaps slightly on the lower side. For this reason, we also investigated an alternative solution that corresponds to a moment magnitude of M_w = 9.0 (in better agreement with seismogenic studies of the event) by reducing the damping coefficient, which relaxes the smoothing constraints and consequently improves the fit to the data. The maximum slip magnitude for this alternative solution is 85 m. Predictions of geodetic data are excellent for both models. The slip distributions and predictions are illustrated in Figure 1.7. Finally, the time sequence information necessary to perform the time triggering of this source in the tsunami propagation models is obtained from

the GPS inversion performed by Yue and Lay (2011), and Figure 1.8 shows the resulting combination of the UA source uplift shown in Figure 1.7c and this time sequence.

4 Hydrodynamic models

This study makes use of three closely related numerical models; spherical- and Cartesian- coordinate versions of the Boussinesq-type model FUNWAVE-TVD (Shi et al 2012; Kirby et al 2012), and the non-hydrostatic model NHWAVE (Ma et al 2012). NHWAVE is used here to specify a time-dependent source for tsunami generation triggered by the transient motion of the seafloor, which is not a feature of FUNWAVE-TVD. FUNWAVE-TVD is used in its spherical coordinate form to model tsunami propagation over ocean-scale distances, while the Cartesian version is used to model local response and inundation in Japan's coastal regions. A brief overview of each model is provided here; readers are referred to the primary citations for further details.

Results of FUNWAVE-TVD simulations of the Tohoku 2011 tsunami are presented in the next section, based on different initial conditions and model setups. We compute the tsunami far-field propagation in the domain shown in Figure 1. 3 and compare results with measurements at some of the DART buoys also shown on the figure. Near-field tsunami impact is computed in a smaller, but more finely resolved, regional domain encompassing both the earthquake source and the Japan coastline (see also Figure 1.3) and results are compared with measurements made at coastal GPS buoys and runup/inundation data obtained from field surveys. For both domains,

sponge layers are specified along open boundaries, which are sufficiently wide to absorb outgoing waves and hence nearly eliminate wave reflection from the domain boundaries.

4.1 Horizontal model structure

Both FUNWAVE-TVD and NHWAVE make use of a finite-volume TVD scheme, using a well-balanced scheme for the pressure gradient following Liang and Marche (2009). This scheme is used to represent basic local and advective accelerations and pressure gradient effects. The scheme is mass conserving and handles shock tracking and moving boundary effects accurately and efficiently. Both models are parallelized using a horizontal domain decomposition, and the parallelization is implemented using the MPI protocol. Both models utilize a third-order Strong Stability Preserving (SSP) Runge-Kutta scheme (Gottlieb et al 2001) for forward marching in time, and adaptive time-stepping based on flow conditions is implemented in both models.

4.2 Cartesian FUNWAVE-TVD

The Cartesian-coordinate version of FUNWAVE-TVD, described by Shi et al (2012), solves the fully nonlinear and weakly dispersive Boussinesq equations of Wei and Kirby (1995), extended to include provisions for a time-dependent reference elevation (Kennedy et al (2001)) and correct potential vorticity conservation to the order of approximation in the velocity field structure (Chen (2006)). Following earlier work by Erduran et al (2005) and Tonelli and Petti (2009), the code employs a hybrid

numerical scheme, which uses a MUSCL-TVD finite volume formulation for the underlying NSW equations (Yamamoto et al 1998; Erduran et al 2005), together with a finite difference treatment of higher-order dispersive terms representing the effects due to deviation from hydrostatic pressure conditions. During simulations, when the local surface elevation to depth ratio exceeds 0.8, wave breaking is assumed to occur and the model Boussinesq equations are switched to the NSW equations by turning off dispersive terms. Earlier work shows that, with this method, the TVD front tracking algorithm in the model and related numerical diffusion yield accurate representations of wave height decay in the surfzone (Shi et al 2012). FUNWAVE-TVD has been validated against a large set of analytical, laboratory, and field tsunami benchmarks (Tehranirad et al 2011) as part of the development of tsunami hazard maps for the US East Coast (see also Abadie, Harris, and Grilli (2012) for a recent application).

4.3 Spherical FUNWAVE-TVD

The spherical-coordinate version of FUNWAVE-TVD, described by Kirby et al (2009, 2012), solves weakly nonlinear and dispersive Boussinesq equations on a rotating sphere. The governing equations are put in conservative, well-balanced form and implemented using the same numerical approach as used for the Cartesian version of the code (Shi et al 2012). Kirby et al (2012) describe the parallelization of the resulting model and perform a parametric test of the importance to tsunami evolution of both dispersive and Coriolis effects resulting from a range of relative tsunami source width in the main propagation direction.

4.4 NHWAVE

The non-hydrostatic wave model NHWAVE, developed by Ma et al (2012), provides a numerical solution of the three-dimensional Navier Stokes equations for incompressible flow, but with the simplifying assumption of a single-valued water surface displacement. The model uses a second-order Godunov-type TVD method (Zhou et al 2001; Liang and Marche 2009) for horizontal gridding, applied on multiple vertical levels defined by a standard bottom- and surface-following σ coordinate formulation. The effect of a time-dependent moving bottom is implemented in the model, which may thus be used to simulate the transient nature of tsunami sources due to both co-seismic and submarine mass failure (SMF) events. Ma et al (2012) have validated the SMF aspect of the model performance in comparison to laboratory data for highly dispersive conditions presented by Enet and Grilli (2007). The model uses the package HYPRE (2006) to solve the resulting Poisson pressure equation. The present model application assumes perfect fluid conditions. Solutions of the resulting numerical implementation of the Euler equations are usually accurately obtained using only three to five vertical σ levels, as shown in Ma et al (2012).

Table 1-1 Grid sizes and resolutions, and sources of bathymetry, for the Tohoku 2011 simulations with NHWAVE or FUNWAVE-TVD (Cartesian or spherical).

Grid/model	Size	Resolution	Bathymetry
Regional/NHWAVE	(-250, 250) km; (-400, 400) km	1 km	ETOPO1 (1’ arc)
Regional/FUNWAVE	(-250, 550) km; (-500, 700) km	1 km	ETOPO1 (1’ arc)
Pacific/FUNWAVE	(132° E, 68° W); (60° S, 60° N)	4’ arc	ETOPO1 (1’ arc)
Coastal/FUNWAVE	(-250, 150) km; (-450, 350) km	250 m	JODC (500 m) / ASTER (3” arc)

5 Results

We simulate the propagation of the Tohoku 2011 tsunami across the Pacific Ocean, as well as its coastal transformations, runup, and inundation along the Japanese coastline, in a series of computational domains (Table 1-1). To correct for Earth's sphericity in models that use Cartesian coordinates, a transverse secant Mercator projection is used (similar to the UTM system), with its origin located at (39° N, 143° E). This transformation leads to small grid distortions, which are deemed negligible

In all simulations, free-slip (wall) boundary conditions are applied on the lateral boundaries of the computational domains. To prevent non-physical reflection from these boundaries, sponge layers are specified over a number of grid cells (inside of the outer domain boundary marked in Figure 1.3), for which damping terms are activated in the model equations. Specifically, in simulations of tsunami propagation with FUNWAVE over the Pacific grid, sponge layers are 100 km thick along all lateral boundaries. For the NHWAVE and FUNWAVE simulations in the 1000 m regional grid, sponge layers are 50 km thick in the north and south ends of the domain, and 200 km thick in the east. Finally, for the FUNWAVE simulations in the 250 m coastal grids, sponge layers are 50 km thick along the north, east and south boundaries. Note, in order to avoid the triggering of instabilities due to sharply varying bathymetry during wetting-drying in NHWAVE simulations in the regional grids, the critical depth for wetting-drying is set to 1 m, and the bottom drag coefficient to 0.001. Since NHWAVE is only used to compute the initial tsunami waveform, one does not have to resolve wetting-drying at the coast anyway. In all FUNWAVE-TVD simulations, the minimum depth for the wetting-drying algorithm is set to 1 cm and

the bottom drag coefficient to 0.01. Work done while validating the hydrodynamic models for NOAA's National Tsunami Hazard Mitigation Program (NTHMP) mandatory benchmarks (Tehranirad et al 2011) has shown that, for the type of grid resolution used here, nearshore and inundation results are relatively insensitive to the value of the bottom drag coefficient. Higher-resolution inundation mapping, however, where buildings and vegetation can be resolved, would naturally require a more complex parameterization of friction.

All numerical simulations begin with 300 s of computations of the initial tsunami wave- form in the 500 by 800 km, 1000 m resolution, regional grid (Table 1-1). As discussed before, we first study the sensitivity of results to whether the co-seismic tsunami sources are triggered at once or in a time sequence in the propagation model. In the latter case, we also verify whether it is relevant to linearly superimpose non-moving free surface elevations, when triggering large tsunami waves in a time sequence. To assess this effect, we directly specify the seafloor deformation as a time-dependent bottom boundary condition, rather than as a "hot start" initial condition on the free surface, with no velocity; since one can only specify the initial condition on the free surface in FUNWAVE-TVD, we use NHWAVE to do so. Thus, three types of initializations are tested and compared in the regional grid: either (a) a hot start of FUNWAVE-TVD, by specifying the maximum seafloor vertical displacement of each co-seismic source (e.g., such as in Figure 1.4, b) over the entire domain at once, as a

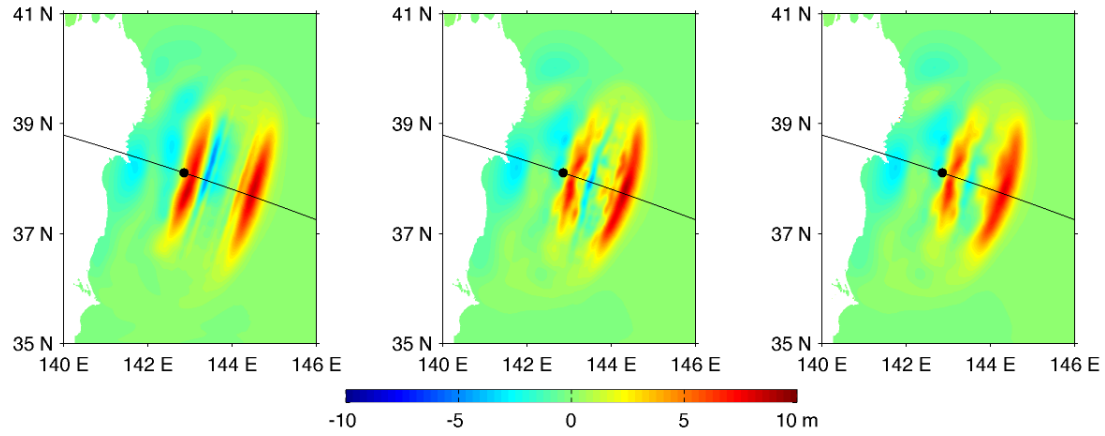

Figure 1.9 Sensitivity of initial tsunami elevation computed at t = 300 s, to the initialization method used, for the UCSB co-seismic source : (a) instantaneous triggering on the free surface in FUNWAVE-TVD, using the maximum seafloor uplift; (b) time-varying triggering on the free surface in FUNWAVE-TVD, using the instantaneous seafloor uplift; and (c) time-varying seafloor uplift specified as a boundary condition in NHWAVE (with 3 vertical σ -levels). Black lines indicate locations of transect used in Figure 1.10, and the black dot is the origin of the axis in the latter figure.

free surface elevation without initial velocity; or the time-dependent triggering of each co-seismic source, (b) as a bottom boundary condition in NHWAVE, or (c) directly on the free surface in FUNWAVE without initial velocity. Results at 300 s (or 5 mins.) are then interpolated, through a one-way coupling, from the regional grid onto one of two FUNWAVE-TVD grids (Table 1-1): either (i) directly on the 4' arc spherical grid for far-field transpacific simulations; or (ii) following an additional 10 min. of propagation in the 1000 m FUNWAVE grid, onto the 250 m resolution coastal Cartesian grid (in order to both get the westward propagating waves to fully enter the 250 m grid and separate these from the eastward propagating wave), to perform all near-field simulations. The latter include computations of time series at GPS tide buoys as well as computations of runup and inundation along the coast.

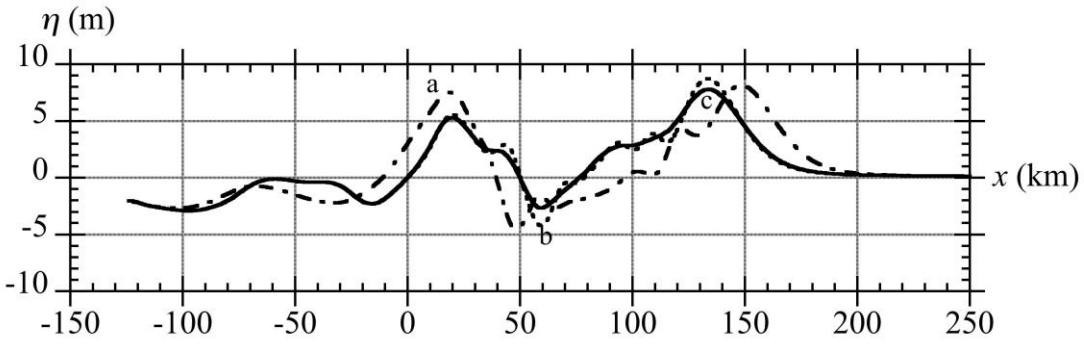

Figure 1.10 Transects in results of Figure 1.9, perpendicular to the fault (at 198°), relative to the JMA hypocenter (38.10 N 142.860 E), method : (—) (a); (– – –) (b); (– - –) (c). Positive distances refer to distance east, towards the Pacific, and negative distances to distance west, towards the Japanese coastline.

5.1 Result sensitivity to initialization method

The sensitivity of results to the three source triggering methods was assessed for the UCSB co-seismic source shown in Figure 1.4. Figures 1.9 and 1.10 show the initial free surface elevations at t = 300 s and a transect in those, respectively, simulated using the three different initialization methods discussed above. Significant differences can be seen, in both surface elevation and wavelength, between the instantaneous method (a) and the two time-dependent methods (b,c). Smaller differences can then be observed between the latter two methods, with the time-triggering in NHWAVE resulting in slightly reduced maximum (positive or negative) elevations and in waveforms with less higher-frequency oscillations than for the time-triggering in FUNWAVE-TVD. This might be due to the adjustment of the solution kinematics to the non-physical superposition of free surface increments with no initial velocity. Overall, these results justify using the 3rd more accurate and realistic method to compute the initial tsunami waveform, which will be done in all the following computations for both the UCSB and UA sources. Note, for the latter source, as

indicated before, the timing information for the time triggering of seafloor uplift patches is obtained from Yue and Lay (2011).

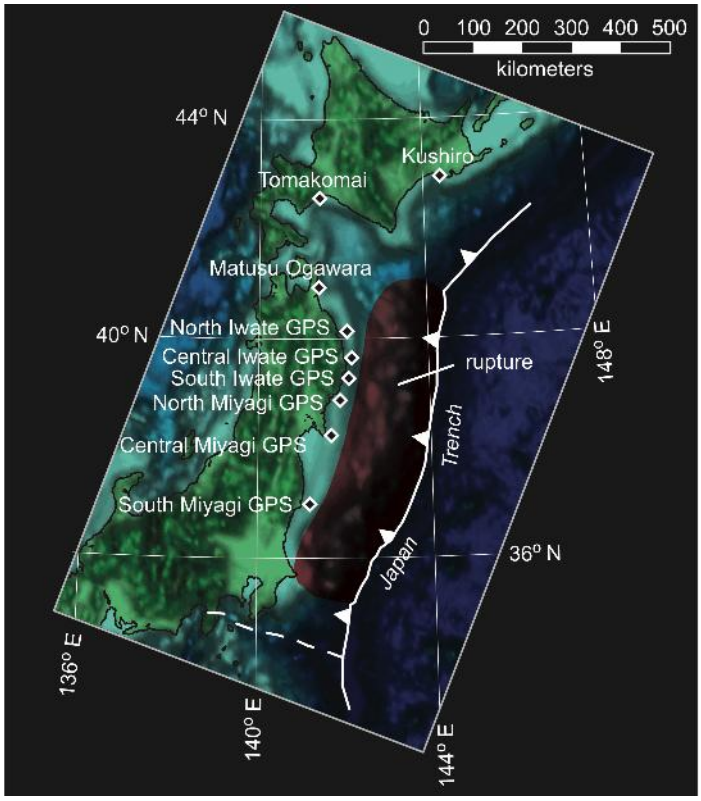

Figure 1.11 Locations of GPS buoy stations (Yamazaki et al 2011a)

5.2 Surface elevation at coastal GPS buoys

The accuracy of tsunami generation using the UCSB and UA sources is assessed by comparing simulated surface elevations in the regional grid computations against observations made at nine coastal stations equipped with GPS buoys (Figure 1.11). After initialization at t = 300 s with NHWAVE results (with time-dependent triggering on the seafloor), the Cartesian FUNWAVE-TVD code is run on the 800 by 1200 km regional grid, with a 1000 m resolution (Table 1-1). [Note, results for the M9 UA source are not detailed here as they were found to agree less well with

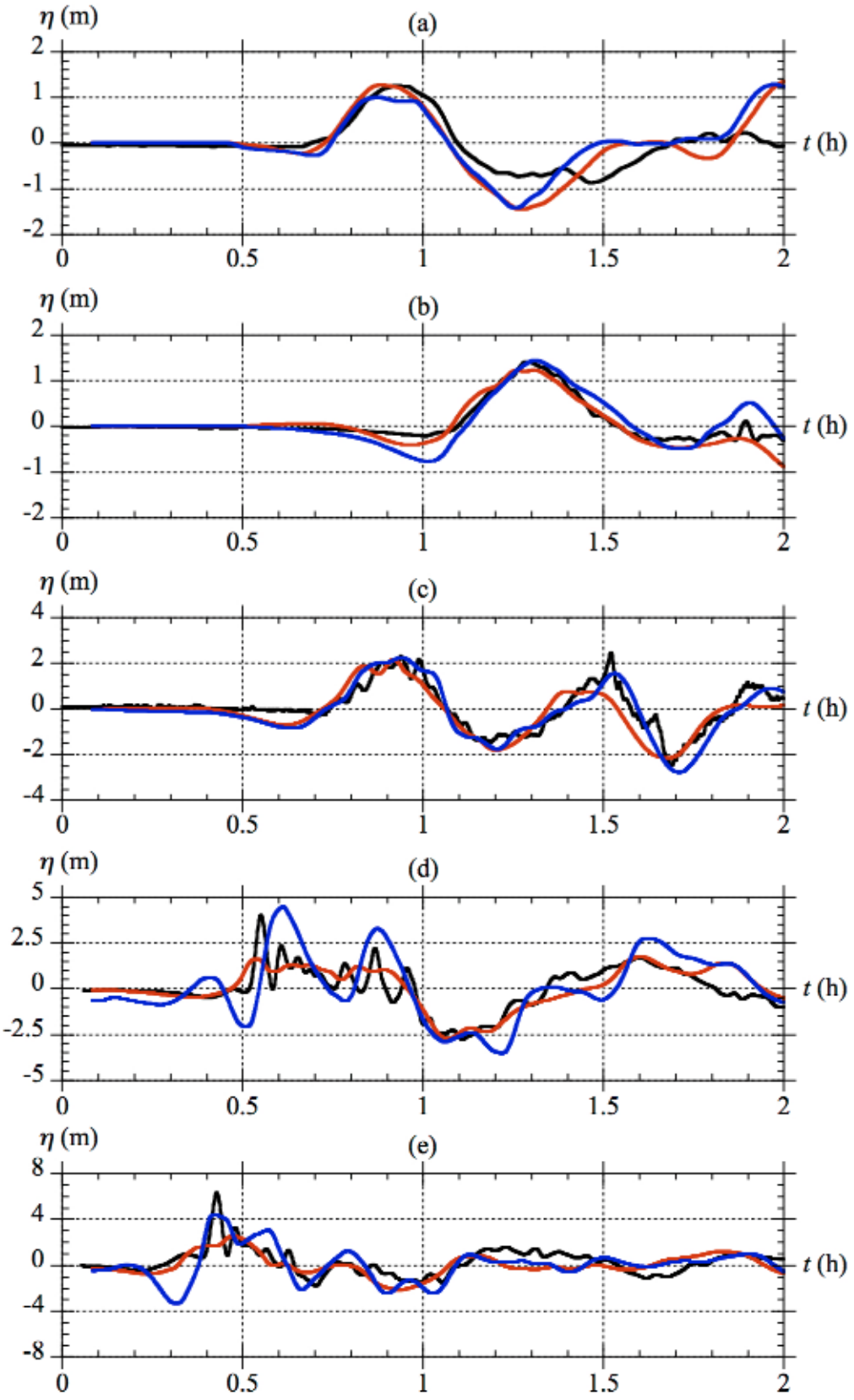
η (m)
(a)
2
1
0
-1
-2
0
0.5
1
1.5
2
t (h)
η (m)
(b)
2
1
0
-1
-2
0
0.5
1
1.5
2
t (h)
η (m)
(c)
4
2
0
-2
-4
0
0.5
1
1.5
2
t (h)
η (m)
(d)
5
2.5
0
-2.5
-5
0
0.5
1
1.5
2
t (h)
η (m)
(e)
8
4
0
-4
-8
0
0.5
1
1.5
2
t (h)

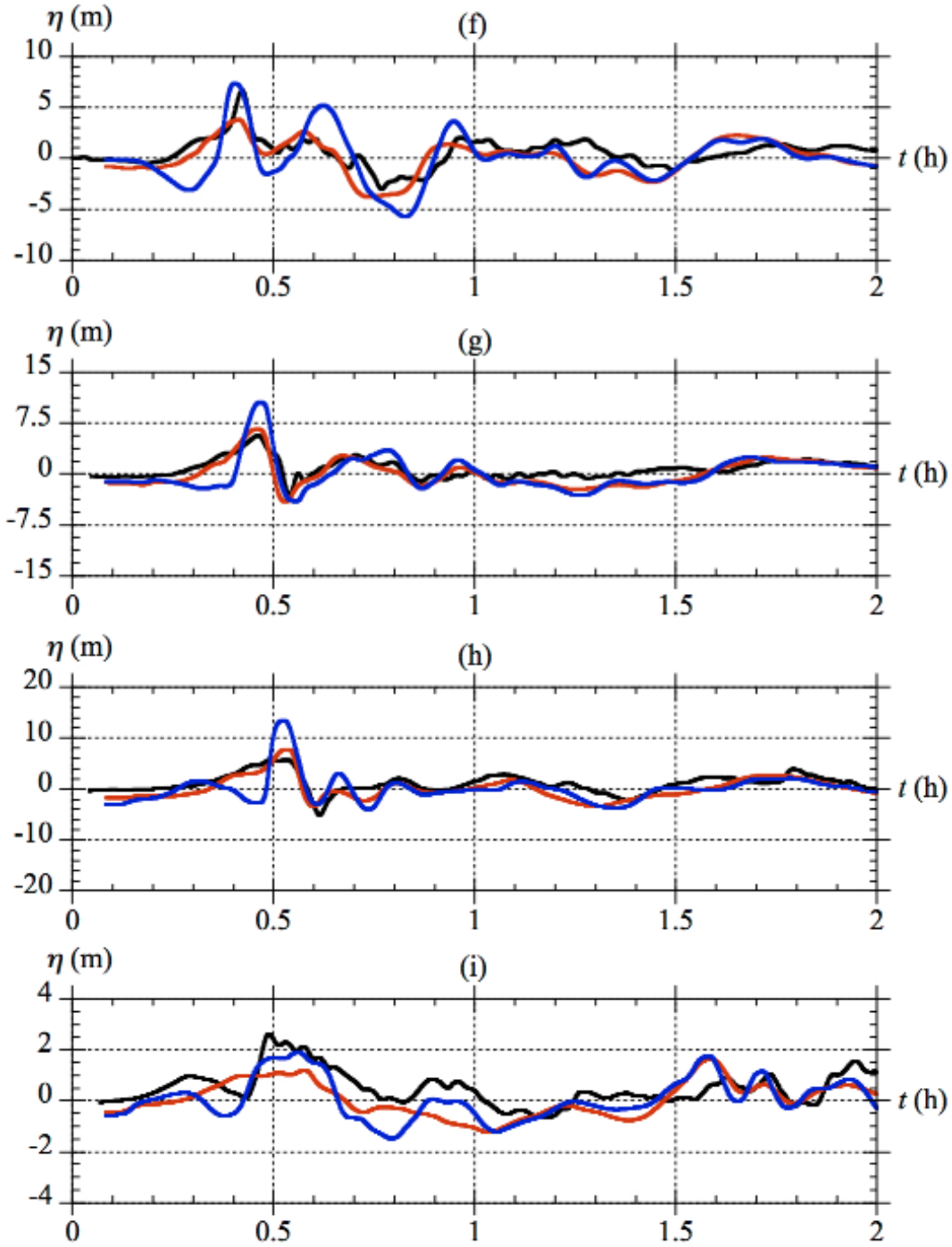

Figure 1.12 Surface elevations at GPS buoys near Japan as a function of time. Panels (a) to (i) are for stations located, from N to S (Figures 1.4, 1.11), at: (a) Kushiro; (b) Tomakomai; (c) Matsu Ogawara; (d) North Iwate; (e) Central Iwate; (f) South Iwate; (g) North Miyagi; (h) Central Miyagi; (i) South Miyagi. Each panel compares observations (black) to computations for the: UCSB (M9) source (blue) and UA (M8.8) source (red). [Note, source triggering in NHWAVE is time-dependent and specified on the seafloor.]

observations than those of the M8.8 UA source; hence, hereafter, the latter source is used and referred to as simply the UA source.] Overall, results of the UA source are found in better agreement with observations than those of the UCSB source (Figure 1.12). While both sources are in good agreement with observations for the 3 northern buoys (a-c), the UA source is in much better agreement than the UCSB source for two of the 3 southern buoys (g and h), and the difference between both sources is not very significant in absolute terms at the most southern buoy, i (which is near the area of the Fukushima nuclear power plant). For the middle 3 buoys (d-f), neither source matches the data as well as for the other buoys. However, except for the first crest that it underpredicts, the UA source predicts the long waveform more accurately than the UCSB source. Neither source is able to reproduce the shorter wave oscillations that were measured at the three middle buoys.

Note that our findings for the UCSB source results are somewhat similar to those of Yamazaki et al (2011b), which show generally good agreement with the buoy data, but for some stations (i.e., North and Central Miyagi) their simulations underpredict the observed amplitude, and for others (i.e., South Miyagi, which they refer to as the Fukushima GPS station) they overpredict the initial amplitude.

5.3 Transpacific propagation and dispersive effects

The far-field propagation in the Pacific Ocean basin is simulated using the spherical FUNWAVE-TVD code in the 4’ arc resolution ocean basin grid (Table 1-1; spanning 132° E to 68° W and 60° S to 60° N; Figure 1.3), initialized by NHWAVE results at t = 300 s (obtained with time-dependent triggering specified on the seafloor).

The simulation is run for 24 hours of tsunami propagation, in order for waves to reach the most distant DART buoys and the South American coastline.

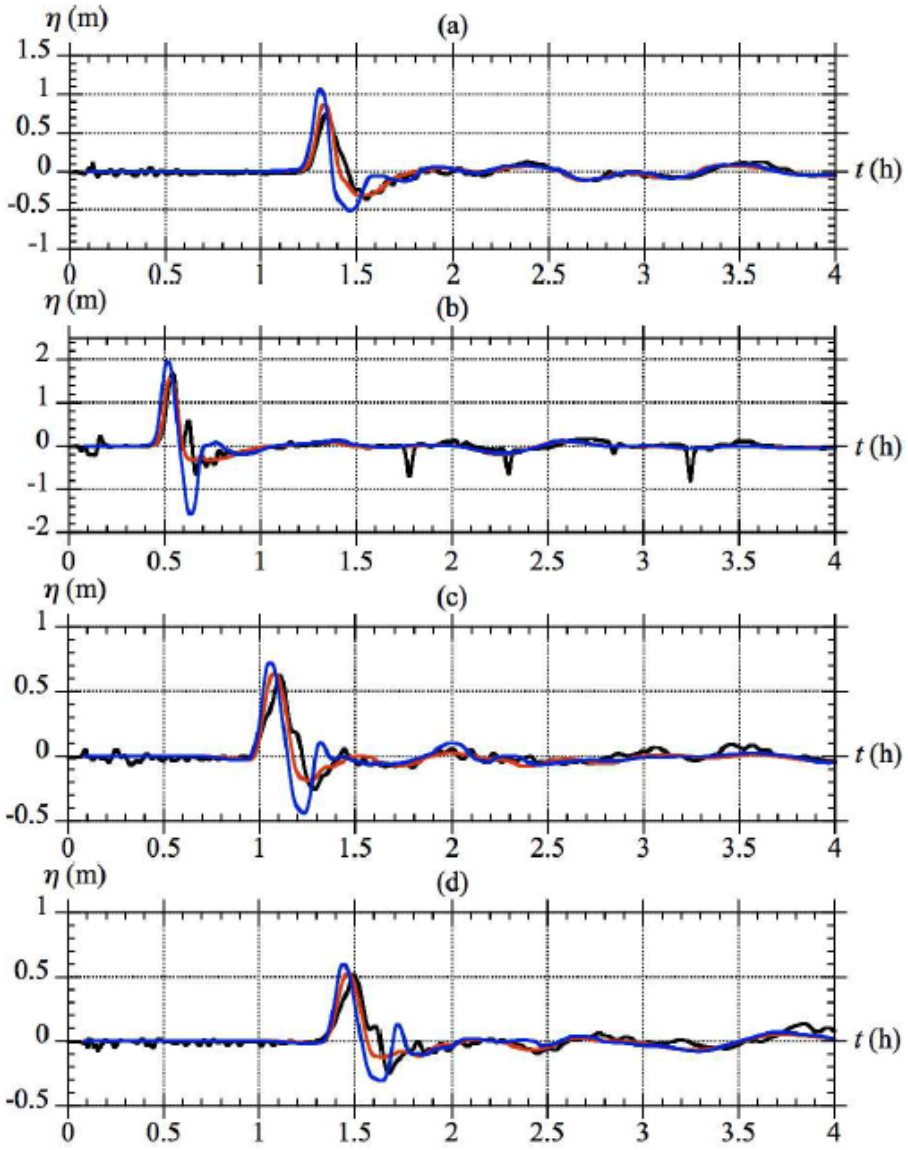

Figure 1.13 Surface elevation at DART buoys near Japan (Figure 1.3) #: (a) 21413; (b) 21418; (c) 21401; and (d) 21419. Comparison between observations (black) and computations with FUNWAVE-TVD using the: UCSB source (blue); and the UA source (red). [Note, source triggering in NHWAVE is time-dependent and specified on the seafloor.]

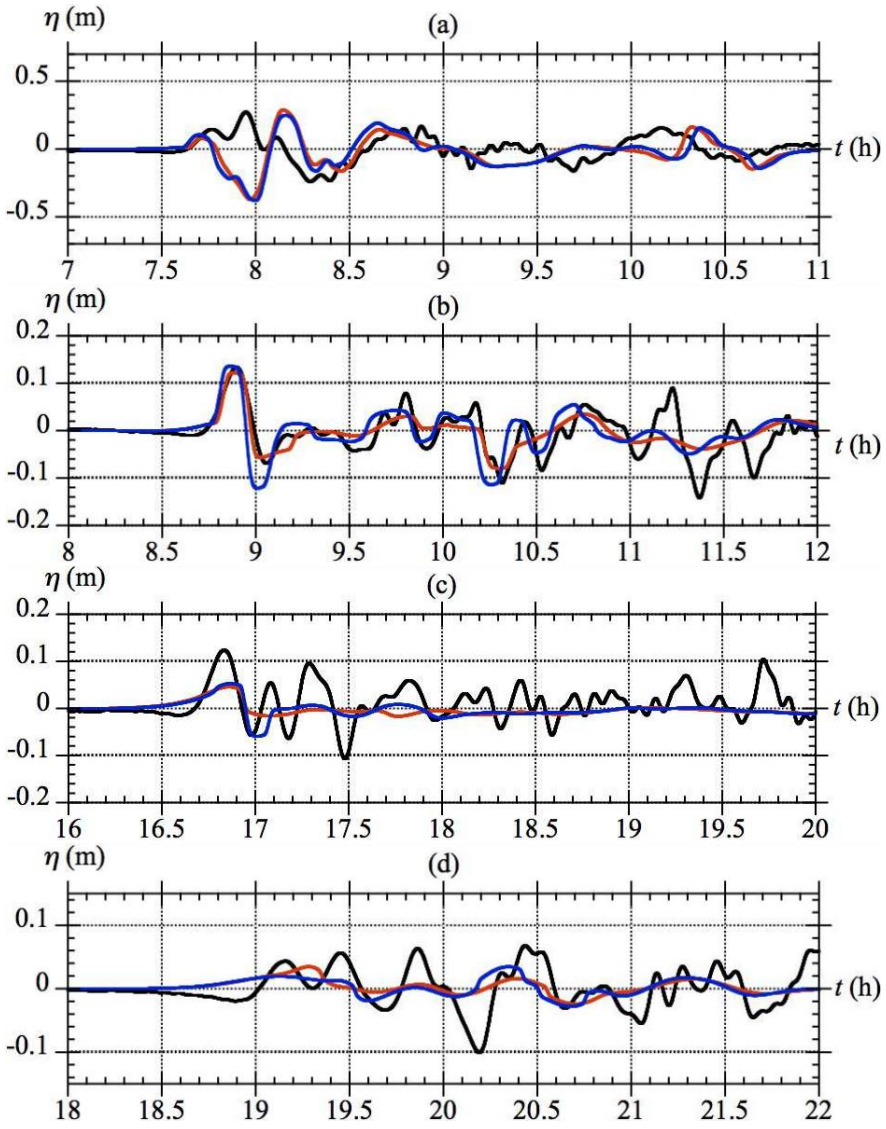

Figure 1.14 Surface elevation at DART buoys far from the source (Figure 1.3) # (Δ t =): (a) 51407 (+6.6 min); (b) 46404 (+7.2 min); (c) 32411 (+15.8 min); and (d) 32412 (+15.2 min). Comparison between observations (black) and computations with FUNWAVE-TVD using the: UCSB source (red), and UA source (blue). Times listed in parentheses indicate the time shift (Δt) added to simulation results in order to synchronize these with observations. [Note, source triggering in NHWAVE is time-dependent and specified on the seafloor.]

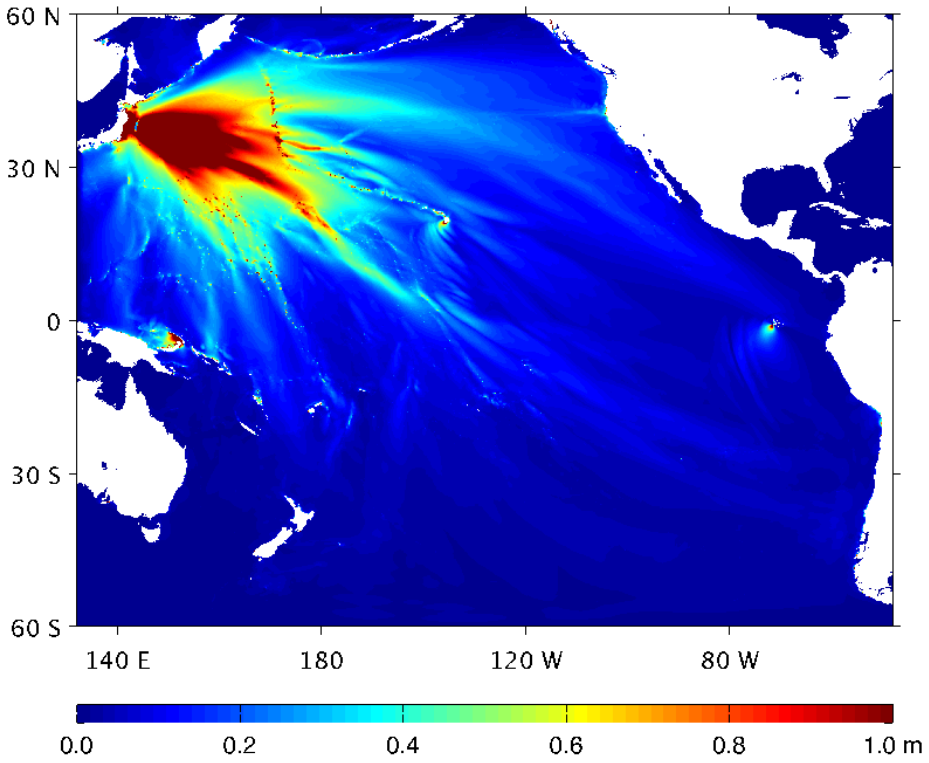

Figure 1.15 Envelope of maximum computed wave elevation with FUNWAVE-TVD in the spherical (4') Pacific grid using the UCSB source.

Figure 1.13 shows a comparison of computed and measured surface elevations at the four DART buoys closest to Japan (i.e., No. 21413, 21418, 21401, and 21419; Figure 1.3). Overall, results for both the UCSB and UA sources agree quite well with observations. The UCSB source, however, consistently overpredicts the leading wave crest elevation at each location and, more notably, overpredicts the amplitude of the leading wave troughs. Both the UA and UCSB sources predict that the wave arrives slightly sooner than seen in observations, but this is more pronounced for the UCSB source. Figure 1.14 similarly shows a comparison of computed and measured surface elevations at four distant DART buoys (i.e., No. 51407, 46404, 32411, and 32412; Figure 1.3). Similar to Yamazaki et al (2011b, 2012), we find that at distant DART

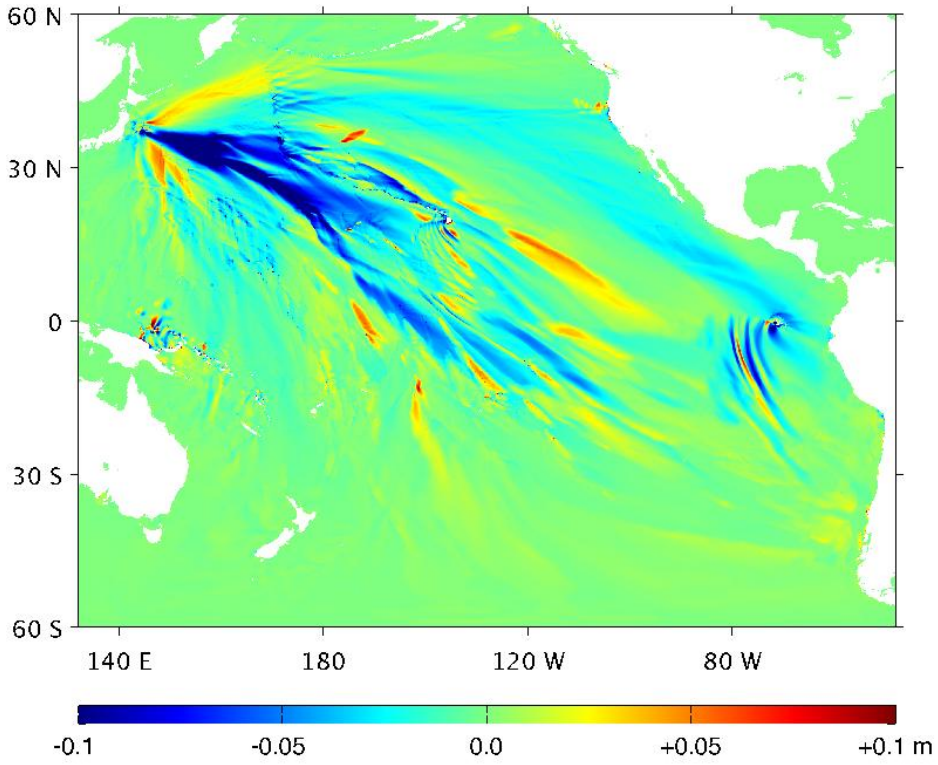

Figure 1.16 Difference between the envelope of maximum wave elevation computed with FUNWAVE-TVD in the spherical (4') Pacific grid using the UCSB source, with (as in Figure 1.15) and without dispersion.

buoys the tsunami arrives earlier than observed (about 7 to 15 mins). Hence, to allow for an easier comparison, slight time shifts have been added to simulations in the figure, in order to synchronize the first elevation wave with that observed. These only represent about 1.5% of the tsunami propagation time to each buoy. Results from Watada et al (2011) suggest that this discrepancy is common with many tsunami models and may be attributed largely to the elasticity and self-gravity of the Earth. The predicted surface elevations at distant DART buoys generally agree reasonably well with observations (particularly in view of their smaller magnitude than for the DART buoys closest to Japan), and neither source appears to yield significantly different

results, indicating that differences that appear may be determined by the model setup. The best agreement is found in Hawaii and in Oregon (e.g., No. 51407 and 46404); at the latter buoy the UA source matches the leading wave much better than the UCSB source. Both the UCSB and UA sources underpredict the wave elevation similarly at DART stations near the South American shorelines (e.g., No. 32411 and 32412). Our results seem to agree better with measurements closest to Japan than those of Yamazaki et al (2011b, 2012) who, for instance, underpredict the amplitude of the tsunami at DART buoy No. 21418 by about 50%, whereas both the UA and UCSB sources used in our model reproduce the observations better. Alternatively, Yamazaki et al (2011b, 2012) reproduce the waves measured at distant DART buoys perhaps slightly better. This may be related to the resolution of the respective models; our present simulations used a fairly coarse 4' arc basin scale grid, as opposed to their 2' arc resolution grid.

Figure 1.15 shows the envelope of computed maximum wave elevation (for the UCSB source). The tsunami energy is seen to propagate across the ocean in some preferential directions associated with both the source characteristics and the ocean bathymetry, in which ridges may cause wave-guiding effects. This is particularly clear for the eastward propagation towards Northern California, around 40° N; large wave oscillations (nearly 4 m trough to crest) and damage were indeed observed at this latitude in Crescent City, CA.

The effect of dispersion on the tsunami transpacific propagation is finally assessed by re-running these simulations without dispersion terms in FUNWAVE-TVD's equations, i.e., in NSW mode. Figure 1.16 shows a difference plot between the

envelope of maximum surface elevation computed with (i.e., as in Figure 1.15) and without dispersion. As could be expected from the short propagation distances and the coarse grid resolution, little dispersive effects can be seen in the near field close to Japan. In the far-field, however, non-negligible differences with NSW results, of more than ±10 cm, can be seen in deep water, which may amount to 20-40% of the tsunami amplitude at some locations. This is on the same order of magnitude as that of dispersive effects reported by Ioualalen et al (2007) for the 2004 Indian Ocean tsunami and justifies using a BM in the present case. A more detailed discussion and analysis of dispersive effects and their comparison to Coriolis force effects for the Tohoku 2011 event can be found in Kirby et al (2012).

Note, as we only consider here changes in maximum wave height due to dispersion, results do not show effects of dispersion on trailing waves such as noted by Saito et al (2011) at DART No. 21418. The dispersive tail, which is coarsely resolved in the DART buoy No. 21418 observations, does not appear in our simulations, whether using the UA or UCSB source (Figure 1.13b), or any other finite-fault based sources that we attempted previously. We note, however, that the tsunami source used by Saito et al. was based on an inversion of observed tsunami wave elevations only, while our modeling efforts have been solely from geophysical and seismic data, and have not been adjusted to fit wave observations. It is possible that seismic and geodetic inversions do not have sufficient resolution to produce these secondary waves, or more likely that a non-seismic contribution to the tsunami may be significant, such as from splay faulting or submarine mass failures. This will be the

object of future work and will require field data to better constrain the potential seafloor mechanisms.

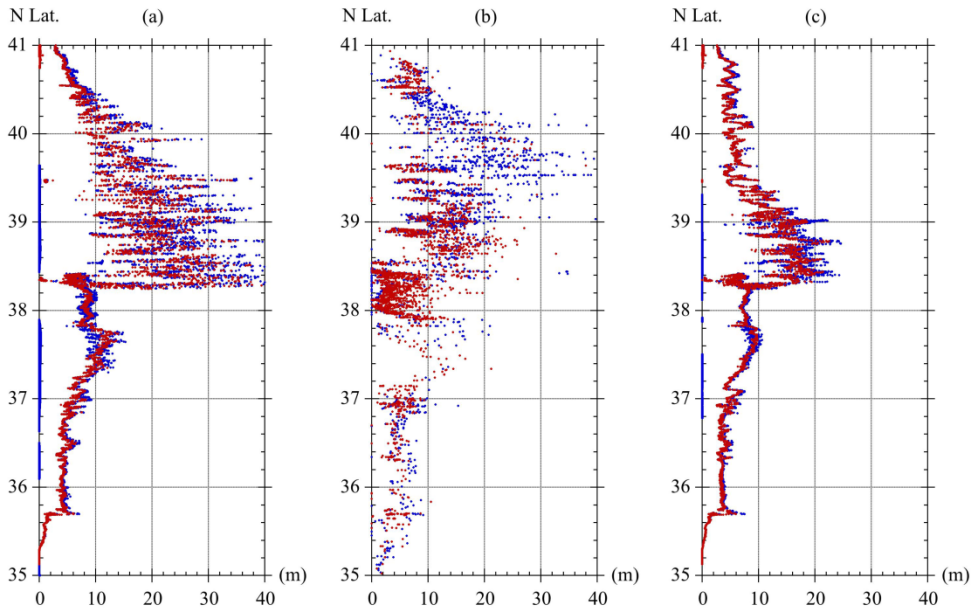

Figure 1.17 Runup (blue circles) and inundation height (red dots) along the Japanese coastline based on: (a) simulation with the M9 UCSB source; (b) field survey; and (c) simulations with the M8.8 UA source.

5.4 Runup and inundation

We study the tsunami coastal impact on Japan, in terms of runup and inundation, using results of simulations in the 250 m resolution coastal Grid (Table 1-1). Following the transition from the NHWAVE to the FUNWAVE-TVD 1000 m regional grid at t = 300 s, we interpolate results from the latter grid onto the 250 m resolution coastal grid after 15 min. of tsunami propagation (i.e., 5 min. simulated with NHWAVE and 10 min. simulated with FUNWAVE-TVD). The resulting initial condition is simulated for another 2 hours in the coastal grid, which has 50 km wide sponge layers on the north, south, and east sides of the domain to prevent unwanted reflection. The bathymetry specified in the coastal grid is defined from the best

publicly available data; thus, using linear interpolation, we combine the 500 m resolution JODC bathymetry along the Japanese coastline with 1" arc ASTER topographic data.

Figure 1.17 shows runup (i.e., maximum elevation of wetted land) and inundation height (i.e., maximum wave elevation at shoreline) computed with FUNWAVE-TVD in the coastal grid, for the UA and UCSB sources. We see that the observed runup and inundation values are well predicted in the region between 35° and 38.25° N, for both sources. Between 38.25° and 39° N, the UA source results agree quite well with the maximum observed values of runup and inundation height in the region, while the UCSB results overpredict both of these by almost a factor of 2. Between 39° and 39.5° N, this finding is reversed and the UA source results underpredict observations by almost a factor of 2, while the UCSB source results are in better agreement with observations (although still overpredicting these). Between 39.5° and 40.25° N, the runup is underpredicted for both sources. As indicated in the introduction, in view of the still insufficient resolution of the coastal grid, this could be due in part to effects of the complex bathymetry and topography in this part of the Japanese coastline, the Sanriku/Ria coast, which could greatly enhance tsunami runup. Even at a 250 m resolution, the tsunami in most locations only inundated a few grid points onshore in the model. By contrast, in the south, the coastline is made of plains and, accordingly, runup and inundation values are well predicted by the model using either sure (and almost identical).

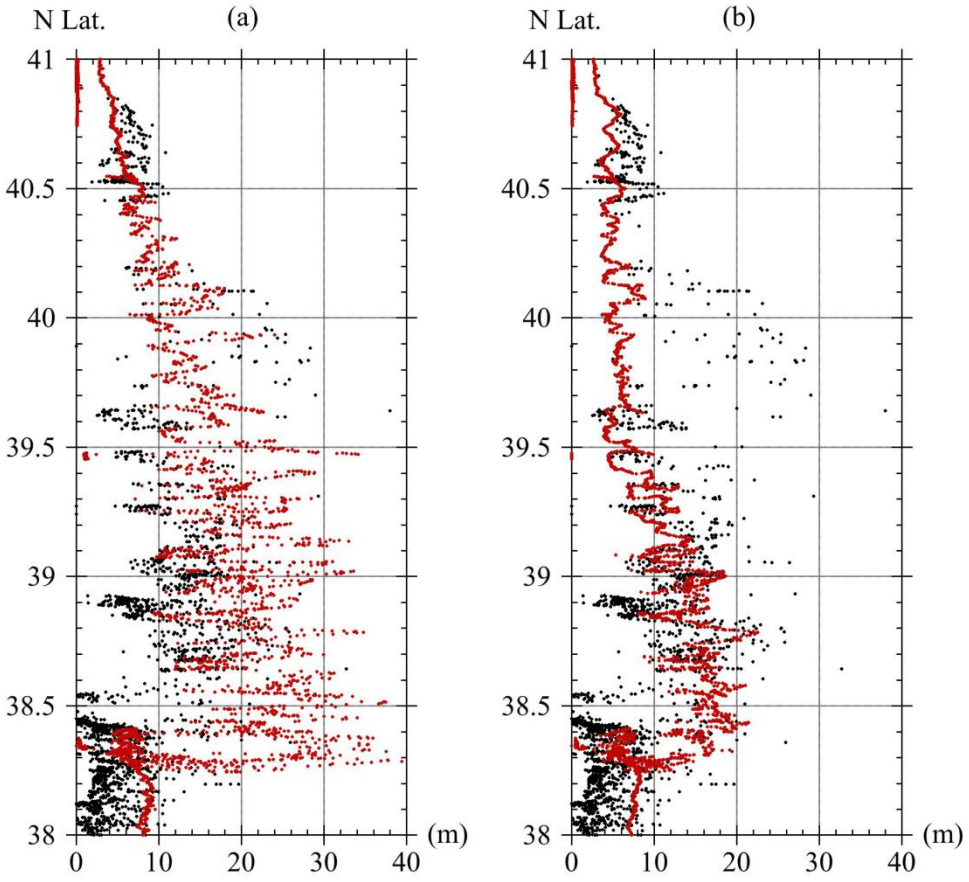

Figure 1.18 Zoom in Figure 1.17 results north of 38 deg. N. Inundation measured (black dots) and computed (red) with: (a) M9 UCSB source; and (b) M8.8 UA source.

In order to better predict runup in the north, one needs to represent the complex topography of the coastline in the model, by using a much finer grid (perhaps down to 30-50 m resolution). This would also require using a better resolved bathymetry than the 500 m data set currently used and will be the object of future work. For this reason, we believe that, with the current bathymetric data and 250 m coastal grid resolution, inundation results should be more reliable than runup, as they are predicted at the shoreline, which warrants a further analysis. This is done in Figure 1.18, where computed inundations for both sources are directly compared to observed inundation

values, north of 38° N. In this region, results for the UA source are in good agreement with observations, except between 39.7° and 40.2° N, where these are significantly underpredicted in the model. This is an area where the UA source may lack in tsunami generation, perhaps due to underpredicted seafloor deformations, but this could also be due to other phenomena not included in the co-seismic sources (e.g., splay faults, submarine mass failures,...). By contrast, as before, the UCSB source significantly overpredicts the observed inundation up to 39.7° N and, like the UA source, underpredicts the inundation between 39.7° and 40.2° N, albeit by a smaller factor. The UCSB source thus overpredicts seafloor deformation between 38.25° and 39.7° and underpredicts it between 39.7° and 40.2° N, similar to the UA source. Overall, however, based on the inundation metrics, the UA source is seen to agree better with tsunami observations.

6 Summary

We simulated tsunami generation propagation, near-field (coastal), and far-field impact of the Tohuku 2011 tsunami, using the nonlinear and dispersive Boussinesq wave model FUNWAVE-TVD (in Cartesian or spherical coordinates), and compared results to field observations of surface elevation at DART buoys, GPS gage buoys, and runup and inundation along the most impacted coastal area of Japan (from 35°-41° N). FUNWAVE was initialized based on co-seismic tsunami sources developed from seismic (UCSB; Shao et al (2011)) or GPS data (UA) inversion. We used a series of nested model grids, with varying resolution (from 4’ in deep water

down to 250 m nearshore) and size, and assessed effects on results of the inclusion of dispersive effects and model initialization method; namely, the triggering of tsunami sources in the propagation model: (i) either at once as a hot start, or with the spatiotemporal sequence derived from seismic inversion; and (ii) as a specified surface elevation or as a more realistic time and space-varying bottom boundary condition (in the latter case, we computed the initial tsunami generation up to 300 s using the non-hydrostatic model NHWAVE).

Present results showed that dispersive effects are negligible in the near-field, owing to the short propagation distances and coarse grid resolution, but may account for 20-40% of tsunami amplitude in deep water, hence justifying the use of a Boussinesq model. When using finer coastal grids, however, incoming tsunami waves may propagate nearshore in the form of strongly dispersive undular bores (as was observed during the 2004 Indian Ocean tsunami; Madsen et al (2008)), that will also require a model such as FUNWAVE for accurate modeling. The sensitivity of results to the three source triggering methods was assessed for the UCSB co-seismic source. Comparing results at t = 300 s, significant differences were found in both surface elevation and wavelength, between the instantaneous method (i) and the two time-dependent methods (ii). Smaller differences were observed between the latter methods, with the time-triggering in NHWAVE resulting in slightly reduced maximum (positive or negative) elevations and in waveforms with less higher-frequency oscillations than for the time-triggering in FUNWAVE-TVD. These results justify using the 3rd more accurate and realistic method to compute the initial tsunami

waveform (i.e., the time dependent bottom boundary condition in NHWAVE), which was done in all the applications.

The UA source is a new co-seismic tsunami source developed here, based on inverting onshore and offshore geodetic data using 3D Finite Element Models (FEM) that simulate elastic dislocations along the plate boundary interface separating the stiff subducting Pacific Plate, and relatively weak forearc and volcanic arc of the overriding Eurasian plate.Standard sources based on seismic inversion often have very simple underlying fault models (such as Okada, 1985; UCSB), yielding deeper slip in homogeneous half-spaces, which may underpredict the amplitude of the tsunami in some areas and lag the wave in time. By contrast, in part due to the simulated weak forearc materials, the UA source produces significant shallow slip along the updip portion of the rupture near the trench that may enhance tsunami generation. Salient features of the observed tsunami far-field and coastal impact were well reproduced for both the UCSB and UA sources, but coastal impact was over- or under-estimated at some locations. Overall, however, results obtained for the UA source were found in better agreement with observations at nearshore GPS gages and DART buoys, and at some distant DART buoys, than those for the UCSB source. Regarding the simulation of runup and inundation, it was concluded that the current finer resolution FUNWAVE grid was still too coarse at 250 m (as well as the underlying bathymetry at 500 m), to accurately simulate runup, particularly in the Sanriku/Ria area (39.5° and 40.25° N) where maximum impact (up to 40 m runup) occurred, which has complex bathymetry and topography that may require grids as small as 30-50 m for proper modeling. Inundation, however, was deemed less sensitive to grid resolution and used as a metric

to assess the accuracy of simulation results along the Japan coast. Hence, it was found that both sources accurately predicted inundation observations south of 38° N. To the north, results for the UA source were found in good agreement with observations, except between 39.7° and 40.2° N, where these were underpredicted. In addition to the complex coastline mentioned above, this is an area where the UA source may lack in tsunami generation, perhaps due to underpredicted seafloor deformations, but this could also be due to other phenomena not included in the co-seismic sources (e.g., splay faults, submarine mass failures,...). By contrast, the UCSB source significantly overpredicted observed inundations up to 39.7° N and, like the UA source, underpredicted the inundation between 39.7° and 40.2° N, albeit by a smaller factor.

Overall, based on the inundation metric along the coast and the agreement with GPS and DART buoy data, results using the newly proposed FEM UA source were found to agree better with tsunami observations, in both the near- and far-field, than those using the UCSB source. As indicated, the UA source may need additional refinements to better explain observations between 39.7° and 40.2° N; these are currently in development and expected to be available in the near future. However, the current UA source already accounts for geologic inhomogeneities (both material and geometrical), which are neglected in Okada- based approaches (which it in fact generalizes) and thus, when combined with accurate tsunami generation and propagation models, as reported here, it has the potential to better explain the large runup and inundation observed to the north of the impacted area, as a result of coseimsic processes.

Finally, there were early indications that Submarine Mass Failures (SMFs) may have been triggered in the Japan trench by the Tohoku-Oki M9 earthquake. The inclusion in tsunami generation models of such SMF sources (as was done, e.g., in Watts et al (2003); Day et al (2005); Tappin et al (2008)) may help further explain some of the large runups not accounted for in the present work. The most likely candidate SMF tsunami source would be a large failure or deformation near the trench axis (Fujiwara et al 2011; Ito et al. 2011).

Acknowledgement: The first five authors wish to acknowledge support from grant EAR-09-11499/11466 of the US National Sciences Foundation (NSF) Geophysics Program. The last two authors acknowledge the Coastal Geosciences Program, Office of Naval Research for support for development of the FUNWAVE-TVD and NHWAVE models. Academic licensing and technical support for Abaqus software is provided by Dassault Syste`mes Simulia Corp.

References

Abadi S , Harris JC, Grilli ST, Fabre R (2012) Numerical modeling of tsunami waves generated by the flank collapse of the Cumbre Vieja Volcano (La Palma, Canary Islands): tsunami source and near field effects. Journal of Geophysical Research 117(C05030).

Abaqus (2009) Abaqus. Dassault Systemes Simulia Corp., Providence, RI, 6.9-EF edn, URL http://www.simulia.com

Abe H, Sugeno Y, Chigama A (1990) Estimation of the height of the Sanriku Jogan 11 earthquake-tsunami (A.D. 869) in the Sendai Plain. Zisin [Earthquakes] 43:513–525

Amante C, Eakins BW (2009) ETOPO1 one arc-minute global relief model: Procedures, data sources and analysis. NOAA Technical Memorandum NESDIS NGDC-24:19 pp

Ammon CJ, Lay T, Kanamori H, Cleveland M (2011) A rupture model of the great 2011 Tohoku earthquake. Earth Planets Space (accepted):4 pp.

Aster R, Borchers B, Thurber C (2005) Parameter estimation and inverse problems. Elsevier Academic Press

Bird P (2003) An updated digital model of plate boundaries. Geochemistry Geophysics Geosystems 4(3):55 pp., DOI 10.1029/2001GC000252.

Chen Q (2006) Fully nonlinear Boussinesq-type equations for waves and currents over porous beds. Journal of Engineering Mechanics 132:220–230

Chen Q, Kirby JT, Dalrymple RA, Kennedy AB, Chawla A (2000) Boussinesq modeling of wave transformation, breaking and runup. II: Two horizontal dimensions. J Waterway, Port, Coastal and Ocean Engrng 126:48–56

Chen Q, Kirby JT, Dalrymple RA, Shi F, Thornton EB (2003) Boussinesq modeling of longshore currents. Journal of Geophysical Research 108(C11):3362, DOI 10.1029/2002JC001308

Day SJ, Watts P, Grilli ST, Kirby J (2005) Mechanical models of the 1975 kalapana, hawaii earthquake and tsunami. Marine Geology 215(1-2):59–92, DOI 10.1016/j.margeo.2004.11.008

DeMets C, Gordon R, Argus D (1994) Effect of recent revisions to the geomagnetic reversal time scale on estimates of current plate motions. Geophysical Research Letters 21:2191–2194

Enet F, Grilli ST (2007) Experimental study of tsunami generation by three-dimensional rigid underwater landslides. Int J Num Meth Fluids 133:442–454

Erduran KS, Ilic S, Kutija V (2005) Hybrid finite-volume finite-difference scheme for solution of Boussinesq equations. Int J Num Meth Fluids 49:1213–1232

Fujii Y, Satake K, Sakai S, Shinohara M, Kanazawa T (2011) Tsunami source of the 2011 off the Pacific coast of Tohoku Earthquake. Earth Planets Space 63:815–820

Fujiwara T, Kodaira S, No T, Kaiho Y, Takahashi N, Kaneda Y (2011) Tohoku-Oki earthquake: Displacement reaching the trench axis. Science 334:1240

Geospatial Information Authority of Japan (2011) The 2011 off the Pacific coast of Tohoku Earthquake: Crustal Deformation and Fault Model (Preliminary), http://www.gsi.go.jp/cais/topic110313- index-e.html,2011

Gica E, Spillane M, Titov V (2007) Tsunami hazard assessment using Short-term Inundation Forecasting for Tsunamis (SIFT) tool. In: EASTEC International Symposium 2007 - Dynamic Earth: its Origin and Future, Sendai, Japan

Gica E, Spillane M, Titov V, Chamberlin C, Newman J (2008) Development of the forecast propagation database for NOAA's Short-term Inundation Forecast for Tsunamis (SIFT). Tech. rep., NOAA Tech. Memo. OAR PMEL-139,89 pp

Gonzalez FI, Milburn HM, Bernard EN, Newman JC (1998) Deep-ocean Assessment and Reporting of Tsunamis (DART): brief overview and status report. In: Proceedings of the International Workshop on Tsunami Disaster Mitigation, Tokyo, Japan, URL http://www.ndbc.noaa.gov/dart/brief.shtml

Gottlieb S, Shu CW, Tadmor E (2001) Strong stability-preserving high-order time discretization methods. SIAM Review 43:89–112

Grilli S, Ioualalen M, Asavanant J, Shi F, Kirby J, Watts P (2007) Source constraints and model simulation of the December 26, 2004 Indian Ocean tsunami. Journal of Waterway Port Coastal and Ocean Engineering 133(6):414–428, DOI 10.1061/(ASCE)0733-950X(2007)133:6(414)

Grilli S, Dubosq S, Pophet N, Prignon Y, Kirby J, Shi F (2010) Numerical simulation and first-order hazard analysis of large co-seismic tsunamis generated in the Puerto Rico trench: near-field impact on the north shore of puerto rico and far-field impact on the us east coast. Natural Hazards and Earth System Sciences 10:2109–2125, DOI 10.5194/nhess-2109-2010

Hasegawa A, Uchida N, Igarashi T, Matsuzawa T, Okada T, Miura S, Suwa Y (2007) Asperities and quasistatic slips on the subducting plate boundary east of Tohoku, Northeast Japan. In: TH Dixon and JC Moore (ed) The seismogenic zone of subduction thrust faults, Columbia University Press, New York, pp 451–475

Hatori T (1975) Tsunami magnitude and wave source regions of historical Sanriku tsunamis in Northeast Japan. Bulletin of Earthquake Research Institute 50:397–414

Hayashi Y, Tsushima H, Hirata K, Kimura K, Maeda K (2011) Tsunami source area of the 2011 off the Pacific coast of Tohoku Earthquake determined from tsunami arrival times at offshore observation stations. Earth Planets Space 63:809–813

Hughes K, Masterlark T, Mooney W (2010) Poroelastic stress-coupling between the M9.2 2004 Sumatra- Andaman and M8.7 2005 Nias earthquakes. Earth and Planetary Science Letters 293:289–299, DOI 10.1016/j.epsl.2010.02.043

HYPRE (2006) High Performance Preconditioners. User's Manual, software version 2.0.0. UCRL-CODE- 222953. Center for Applied Scientific Computing, Lawrence Livermore National Laboratory

Ide S, Baltay A, Beroza G (2011) Shallow dynamic overshoot and energetic deep rupture in the 2011 Mw 9.0 Tohoki-Oki earthquake. Science DOI 10.1126/science.1207020

IOC/UNESCO (2011) Casualties by the earthquake and tsunami of March 11, 2011. Bulletin No 29 (9/30/2011), Intergovernmental Oceanographic Commission URL http://www.ngdc.noaa.gov/hazard/tsunami/pdf/

Ioualalen M, Asavanant J, Kaewbanjak N, Grilli S, Kirby J,Watts P (2007)Modeling the 26th December 2004 Indian Ocean tsunami: Case study of impact in Thailand. Journal of Geophysical Research 112(C07024), DOI 10.1029/2006JC003850

Ito Y, et al. (2011) Frontal wedge deformation near the source region of the 2011 Tohoku-Oki earthquake. Geophysical Research Letters 38:L000G05, DOI 10.1029/2011GL048355

Ji C, Wald DJ, Helmberger DV (2002) Source description of the 1999 Hector Mine, California, earthquake, part I:Wavelet domain inversion theory and resolution analysis. Bulletin of the Seismological Society of America 92:1192–1207

Karlsson J, Skelton A, Sanden M, Ioualalen M, Kaewbanjak N, andJ Asavanant NP, von Matern A (2009) Reconstructions of the coastal impact of the 2004 Indian Ocean tsunami in the Khao Lak area, Thailand. Journal of Geophysical Research 114(C10023), DOI 10.1029/2009JC005516

Kato T, Terada Y, Ito K, Hattori R, Abe T, Miyake T, Koshimura S, Nagai T (2005) Tsunami due to the 2004 September 5th off the Kii peninsula earthquake, Japan, recorded by a new GPS buoy. Earth Planets Space 57:297–301

Kennedy AB, Chen Q, Kirby JT, Dalrymple RA (2000) Boussinesq modeling of wave transformation, breaking, and runup. I: 1D. J Waterway, Port, Coastal and Ocean Engrng 126(1):39–47

Kennedy AB, Kirby JT, Chen Q, Dalrymple RA (2001) Determination of inverse depths using direct Boussinesq modelling. Wave Motion 33:225–243

Kim DH, Lynett PJ (2011) Dispersive and nonhydrostatic pressure effects at the front of surges. Journal of Hydraulic Engineering 137(7):754–765, DOI 10.1061/(ASCE)HY.1943-7900.0000345

Kirby JT, Pophet N, Shi F, Grilli ST (2009) Basin scale tsunami propagation modeling using boussinesq models: Parallel implementation in spherical coordinates. In Proc WCCE-ECCE-TCCE Joint Conf on Earthquake and Tsunami (Istanbul, Turkey, June 22-24) paper 100:(published on CD)

Kirby JT, Shi F, Harris JC, Grilli ST (2012) Sensitivity analysis of trans-oceanic tsunami propagation to dispersive and Coriolis effects. Ocean Modeling (in revision):42 pp.

Koper KD, Hutko AR, Lay T, Ammon CJ, Kanamori H (2011) Frequency-dependent rupture process of the 11 March 2011 Mw 9.0 Tohoku earthquake: Comparison of short-period P wave backprojection images and broadband seismic rupture models. Earth Planets Space 58:1–4

Kowalik Z, Murty TS (1993) Numerical modeling of ocean dynamics. World Scientific Pub.

Lay T, Ammon C, Kanamori H, Xue L, Kim M (2011a) Possible large near-trench slip during the 2011 Mw 9.0 off the Pacific coast of Tohoku Earthquake. Earth Planets Space 63:687–692

Lay T, Yamazaki Y, Ammon CJ, Cheung KF, Kanamori H (2011b) The great 2011 Earthquake off the Pacific coast of Tohoku (Mw 9.0): Comparison of deep-water tsunami signals with finite-fault rupture model predictions. Earth Planets Space 63:797–801

Liang Q, Marche F (2009) Numerical resolution of well-balanced shallow water equations with complex source terms. Advances in Water Resources 32:873–884

Ma G, Shi F, Kirby JT (2012) Shock-capturing non-hydrostatic model for fully dispersive surface wave processes. Ocean Modeling 43-44:22–35

Madsen PA, Fuhrman DR, Schäffer HA (2008) On the solitary wave paradigm for tsunamis. J Geophys Res 113(C12012), DOI 10.1029/2008JC004932

Masterlark T (2003) Finite element model predictions of static deformation from dislocation sources in a subduction zone: Sensitivities to homogeneous, isotropic, poisson-solid, and half-space assumptions. J Geophys Res 108(B11):17pp, DOI 10.1029/2002JB002296

Masterlark T, Hughes K (2008) The next generation of deformation models for the 2004 M9 Sumatra-Andaman Earthquake. Geophysical Research Letters 35:5 pp, DOI 10.1029/2008GL035198

Minoura K, Imamura F, Sugawara D, Kono Y, Iwashita T (2001) The 869 Jogan tsunami deposit and recurrence interval of large-scale tsunami on the Pacific coast of northeast Japan. Journal of Natural Disaster Science 23(2):83–88

Mori N, Takahashi T, The 2011 Tohoku Earthquake Tsunami Joint Survey Group (2012) Nationwide Post Event Survey and Analysis of the 2011 Tohoku Earthquake Tsunami. Coastal Engineering Journal 54(1):1250001.

Mori N, Takahashi T, Yasuda T, Yanagisawa H (2011) Survey of 2011 Tohoku earthquake tsunami inundation and runup. Geophysical Research Letters 38(L00G14):6 pp., DOI 10.1029/2011GL049210

Okada Y (1985) Surface deformation due to shear and tensile faults in a half space. Bulletin of the Seismological Society of America 75(4):1135–1154

Ozawa S, Nishimura T, Suito H, Kobayashi T, Tobita M, Imakiire T (2011) Coseismic and postseismic slip of the 2011 magnitude-9 Tohoku-Oki earthquake. Nature 475(7356):373–376, DOI 10.1038/nature10227

Pararas-Carayannis G (2011) Tsunamigenic source mechanism and efficiency of the March 11, 2011 Sanriku earthquake in Japan. Science of Tsunami Hazards 30(2):126–152

Pollitz F, B¨urgmann R, Banerjee P (2011) Geodetic slip model of the 2011 M9.0 Tohoku earthquake. Geophysical Research Letters 38:L00G08

Ryan W, Carbotte S, Coplan J, O'Hara S, Melkonian A, Arko R,Weissel R, Ferrini V, Goodwillie A, Nitsche F, Bonczkowski J, Zemsky R (2009) Global multi-resolution topography synthesis. Geochem Geophys Geosyst 10(Q03014), DOI 10.1029/2008GC002332

Saito T, Ito Y, Inazu D, Hino R (2011) Tsunami source of the 2011 Tohoku-oki earthquake, Japan: Inversion analysis based on dispersive tsunami simulations. Geophysical Research Letters 38:L00G19, DOI 10.1029/2011GL049089

Satake K (1995) Linear and nonlinear computations of the 1992 Nicaragua earthquake tsunami. Pure Appl Geophys 144:455–470

Sato M, Ishikawa T, Ujirara N, Yoshida S, Fujita M, Mochizuki M, Asada A (2011) Displacement above the hypocenter of the 2011 Tohoku-Oki Earthquake. Science 332:1395, DOI 10.1126/science.1207401

Sawai Y, Shishikura M, Komatsubara J (2008) A study of paleotsunami using hard corer in Sendai plain (Sendai City, Natori City, Iwanuma City, Watari Town, Yamamoto Town), Miyagi, Japan. Geological Survey of Japan, National Institute of Advanced Industrial Science and Technology Tsukuba, Japan URL http://unit.aist.go.jp/actfault-eq/english/reports/h19seika/index.html

Seno T, Sakurai T, Stein S (1996) Can the Okhotsk plate be discriminated from the North American plate ? Journal of Geophysical Research 101:11,305–11,316

Shao G, Li X, Ji C, Maeda T (2011) Focal mechanism and slip history of 2011 Mw 9.1 off the Pacific coast of Tohoku earthquake, constrained with teleseismic body and surface waves. Earth Planets Space 63:559–564

Shi F, Kirby JT, Harris JC, Geiman JD, Grilli ST (2012) A high-order adaptive time-stepping TVD solver for Boussinesq modeling of breaking waves and coastal inundation. Ocean Modeling 43-44:36–51

Simons M, Minson S, Sladen A, Ortega F, Jiang J, Owen S, L Meng JPA, Wei S, Chu R, Helmberger D, Kanamori H, Hetland E, Moore A, Webb F (2011) The 2011

Magnitude 9.0 Tohoku-Oki Earthquake: Mosaicking the Megathrust from Seconds to Centuries. Science DOI 10.1126/science.1206731

Tappin D, Watts P, Grilli S (2008) The Papua New Guinea tsunami of 1998: anatomy of a catastrophic event. Natural Hazards and Earth System Sciences 8:243–266, URL http://www.nat-hazards-earth-systsci. net/8/243/2008/

Tehranirad B, Shi F, Kirby JT, Harris JC, Grilli ST (2011) Tsunami benchmark results for fully nonlinear Boussinesq wave model FUNWAVE-TVD,Version 1.0. Tech. rep., No. CACR-11-02, Center for Applied Coastal Research, University of Delaware

The 2011 Tohoku Earthquake Tsunami Joint Survey Group (2011) Nationwide field survey of the 2011 off the Pacific coast of Tohoku earthquake tsunami. Journal of Japan Society of Civil Engineers 67(1):63–66

Titov VV, Gonzalez FI, Bernard EN, Eble MC, Mojfeld HO, Newman JC, Venturato AJ (2005) Real-time tsunami forecasting: Challenges and solutions. Nat Hazards 35:3541, DOI 10.1007/s11069- 004-2403-3

Tonelli M, Petti M (2009) Hybrid finite volume - finite difference scheme for 2DH improved Boussinesq equations. Coast Engrng 56:609–620

Tsushima H, Hirata K, Hayashi Y, Kimura YTK, Sakai S, Shinohara M, Kanazawa T, Hino R, Maeda K (2011) Near-field tsunami forecasting using offshore tsunami data from the 2011 off the Pacific coast of Tohoku Earthquake Hiroaki Tsushima. Earth Planets Space 63:821–826

Wang H (2000) Theory of linear poroelasticity: With applications to geomechanics. Princeton University Press

Watada S, Satake K, Fujii Y (2011) Origin of travel time anomalies of distant tsunami. In: AGU Fall Meeting 2011 poster NH11A

Watts P, Grilli ST, Kirby JT, Fryer GJ, Tappin DR (2003) Landslide tsunami case studies using a Boussinesq model and a fully nonlinear tsunami generation model. Natural Hazards and Earth System Sciences 3:391–402

Wei G, Kirby JT (1995) A time-dependent numerical code for extended Boussinesq equations. Journal of Waterway, Port, Coastal and Ocean Engineering 120:251–261

Wei G, Kirby JT, Grilli ST, Subramanya R (1995) A fully nonlinear Boussinesq model for surface waves. I. Highly nonlinear, unsteady waves. Journal of Fluid Mechanics 294:71–92

Yamaguchi Y, Kahle A, Tsu H, Kawakami T, Pniel M (1998) Overview of advanced space borne thermal emission and reflection radiometer (ASTER). IEEE Trans Geosci Remote Sensing 36:1062–1071

Yamamoto S, Kano S, Daiguchi H (1998) An efficient CFD approach for simulating unsteady hypersonic shock-shock interference floes. Comput Fluids 27:571–580

Yamazaki Y, Kowalik Z, Cheung KF (2009) Depth-integrated, nonhydrostatic model for wave breaking and runup. International Journal of Numerical Methods in Fluids 61(5):473–497

Yamazaki Y, Lay T, Cheung K, Yue H, Kanamori H (2011a) Modeling near-field tsunami observations to improve finite fault slip models for the 11March 2011 Tohoku earthquake. Geophysical Research Letters 38:L049130, DOI 10.1029/2011GL049130

Yamazaki Y, Volker R, Cheung KF, Lay T (2011b) Modeling the 2011 Tohoku-oki Tsunami and its Impacts on Hawaii. In: Proceedings of OCEANS 2011. Waikoloa, HI, USA. 9 pp.

Yamazaki Y, Cheung K, Pawlak G, Lay T (2012) Surges along the Honolulu coast from the 2011 Tohoku tsunami. Geophysical Research Letters 39:L09604, DOI 10.1029/2012GL051624

Yue H, Lay T (2011) Inversion of high-rate (1 sps) GPS data for rupture process of the 11March 2011 Tohoku earthquake (Mw 9.1). Geophysical Research Letters 38:L00G09, DOI 10.1029/2011GL048700

Zhou JG, Gauson DM, Mingham CG, Ingraml DM (2001) The surface gradient method for the treatment of source terms in the shallow water equations. J Comp Phys 168:1–25

MANUSCRIPT 2

Published online on ***Natural Hazard;*** Nov.15th.2014

Modeling of SMF tsunami hazard along the upper US East Coast: Detailed impact around Ocean City, MD

Stephan T. Grilli[1,+], Christopher O'Reilly[1,*], Jeffrey C. Harris[1,**], Tayebeh Tajalli Bakhsh[1], Babak Tehranirad[2], Saeideh Banihashemi[2], James T. Kirby[2], Christopher D.P. Baxter1, Tamara Eggeling[1,***], Gangfeng Ma[3] and Fengyan Shi[2]

[1]Dept. of Ocean Engineering, University of Rhode Island, Narragansett, RI 02882

[2]Center for Applied Coastal Research, Dept. of Civil and Environmental Eng., University of Delaware, Newark, DE 19716

[3]Dept. of Civil and Environmental Engng., Old Dominion University, Norfolk, VA 2352

[*] Now at: Navatek Ltd., North Kingstown, RI 02852

[**] Now at: Saint-Venant Laboratory for Hydraulics, Université Paris-Est, Chatou F-78400

[***] Now at Delta Marine Consultants, P.O. Box 268, 2800 AG, Gouda, The Netherlands

[+] Corresponding author

Abstract

With support from the United States (US) National Tsunami Hazard Mitigation Program (NTHMP), the authors have been developing tsunami inundation maps for the upper US East Coast (USEC), using high-resolution numerical modeling. These maps are envelopes of maximum elevations, velocity or momentum flux, caused by the probable maximum tsunamis (PMTs) identified in the Atlantic oceanic basin, including from far-field coseismic or volcanic sources, and near-field Submarine Mass Failures (SMFs); the latter are the object of this work. Despite clear field evidence of past large scale SMFs within our area of interest, such as the Currituck slide complex (CSC), their magnitude, pre-failed geometry, volume and mode of rupture are poorly known. A screening analysis based on Monte Carlo Simulations (MCS) identified areas for possible tsunamigenic SMF sources along the USEC, indicating an increased level of tsunami hazard north of Virginia, potentially surpassing the inundation generated by a typical 100 year hurricane storm surge in the region, as well as that from the most extreme far-field coseismic sources in the Atlantic; to the south, the MCS indicated that SMF tsunami hazard significantly decreased. Subsequent geotechnical and geological analyses delimited 4 high-risk areas along the upper USEC where the potential for large tsunamigenic SMFs, identified in the MCS, was realistic on the basis of field data (i.e., sediment nature and volume/availability). In the absence of accurate site-specific field data, following NTHMP's recommendation, for the purpose of simulating tsunami hazard from SMF PMTs, we parameterized an extreme SMF source in each of the 4 areas as a so-called "Currituck proxy", i.e., a SMF having the same volume, dimensions, and geometry as the historical SMF.

In this paper, after briefly describing our state-of-the-art SMF tsunami modeling methodology, in a second part, we parameterize and model the historical Currituck event, including: (i) a new reconstruction of the SMF geometry and kinematics; (ii) the simulation of the resulting tsunami source generation; and (iii) the propagation of the tsunami source over the shelf to the coastline, in a series of nested grids. A sensitivity analysis to model and grid parameters is performed on this case, to ensure convergence and accuracy of tsunami simulation results. Then, we model in greater detail and discuss the impact of the historical Currituck tsunami event along the nearest coastline where its energy was focused, off of Virginia Beach and Norfolk, as well as near the mouth of the Chesapeake Bay; our results are in qualitative agreement with an earlier modeling study. In a third part, following the same methodology, we model tsunami generation and propagation for SMF Currituck proxy sources sited in the 4 identified areas of the USEC. Finally, as an illustration of our SMF tsunami hazard assessment work, we present detailed tsunami inundation maps, as well as some other products, for one of the most impacted and vulnerable areas, near and around Ocean City, MD. We find that coastal inundation from near-field SMF tsunamis may be comparable to that caused by the largest far-field sources. Because of their short propagation time and, hence, warning times, SMF tsunamis may pose one of the highest coastal hazards for many highly populated and vulnerable communities along the upper USEC, certainly comparable to that from extreme hurricanes.

Keywords: Tsunami hazard assessment; coastal hazard; submarine mass failure; numerical modeling of long wave propagation; seismic hazard.

Introduction

Since 1995, the United States (US) National Tsunami Hazard Mitigation Program (NTHMP; http://nthmp.tsunami.gov/index.html) has supported the development of tsunami inundations maps for selected areas of the US coastline, based on high resolution numerical modeling, to allow for a better assessment and mitigation of extreme tsunami risks. Since 2009, in the wake of the devastating Indian Ocean Tsunami (e.g., Grilli et al., 2007; Ioualalen et al., 2007), this effort has been extended to include all US coastal regions. As part of this activity, the authors were tasked to develop tsunami hazard maps for the US East Coast (USEC). While a probabilistic tsunami hazard analysis (PTHA) is being planned for future phases of this NTHMP project, at present, inundation maps are being developed as the envelope of coastal inundation caused by all the probable maximum tsunamis (PMTs) in the considered oceanic basin. For the USEC, this is the Atlantic Ocean basin, in which PMTs can be due to a variety of geological processes (or sources), including (Grilli et al., 2011): (i) far-field coseismic sources, such as caused by a M9 earthquake affecting the entire Puerto Rico Trench (PRT; e.g., Grilli et al., 2010b), or a repeat of the M8.7-8.9 1755 Lisbon earthquake in the Açores Convergence Zone (e.g., Barkan et al., 2009); (ii) a far-field subarerial landslide source due to a large volcanic collapse in the Canary Islands (e.g., Abadie et al., 2012; Harris et al., 2012); and (iii) near-field Submarine Mass Failures (SMFs), on or near the continental shelf break (e.g., Grilli et al., 2009; Schnyder et al., 2013). The latter SMF sources, particularly those occurring on the mainly silicate shelf of the US North East, and their potential impact on the USEC are the object of the present paper.

Although only a few historical SMF tsunamis have been clearly identified to have impacted the USEC region (e.g., Fine et al., 2005; Piper et al., 1999), ten Brink et al. (2008, 2009a,b), Chaytor et al. (2009) and Twichell et al. (2009) report that underwater landslide scars cover a significant portion of the continental slope and rise off of the USEC; many of these landslides are old and of a large volume (greater than 100 km^3). Although seismicity is moderate along the upper USEC continental slope and upper rise of the western Atlantic Ocean (up to M7.2 earthquakes have been reported), it is sufficient to trigger large SMFs (ten Brink et al., 2008, 2009a,b; Grilli et al., 2009). While SMF tsunamis are overall less energetic than large coseismic tsunamis, they may occur in fairly shallow water at a short distance from shore, and generate much more directional and focused waves, which may cause significant inundation along a narrow section of the coast (e.g., Watts et al., 2003; Grilli and Watts, 2005; Watts et al., 2005; Tappin et al., 2008; Grilli et al., 2009). This warrants their analysis and modeling, together with other far-field sources, as part of the comprehensive tsunami hazard assessment we are conducting for the USEC.

Despite the clear field evidence of past large scale SMFs within our area of interest, their magnitude, pre-failed geometry, volume and mode of rupture are poorly known. Because of this lack of data and the uncertainty in identifying locations and parameters of future potential SMFs, Grilli et al. (2009) performed a screening analysis based on Monte Carlo Simulations (MCS), within an area initially spanning from New Jersey to Cape Cod. In the MCS, distributions of relevant parameters (seismicity, sediment properties, and SMF type, location, geometry, excess pore pressure) were used to perform a large number of stochastic stability analyses of actual

slope transects within the study area. This allowed computing statistical distributions of potential tsunamigenic SMFs and, from simplified propagation and runup computations, their expected 100 and 500 year runup. This work was later extended further south, all the way to Florida (Krauss, 2011), thus identifying potential tsunamigenic SMF sources along the entire USEC area. Results of the MCS indicated an increased level of SMF tsunami hazard for return periods of 500 years north of Virginia (Figure 2.1), with predictions of 5-6 m runup in some areas (e.g., off of Atlantic City), surpassing the inundation generated by a typical 100 year hurricane storm surge in the region. To the south, overall, SMF tsunami hazard significantly decreased.

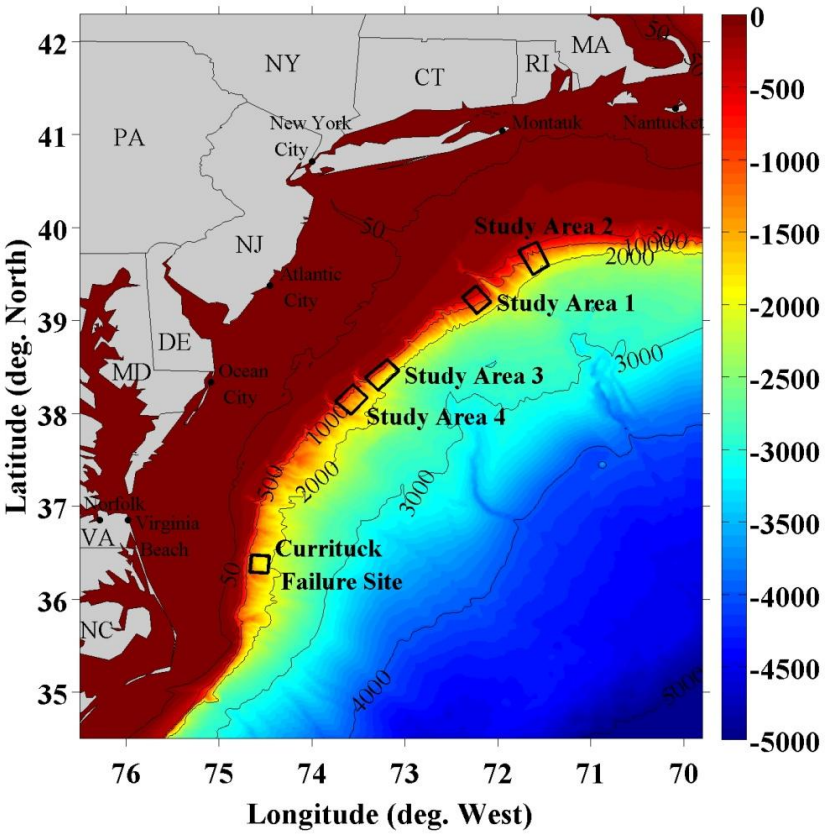

Figure 2.1 Map of the region of interest in simulations of SMF tsunami hazard along the upper USEC (from Virginia to Cape Cod), with four areas (1-4) identified for potentially large tsunamigenic SMF sources (Grilli et al., 2009; Eggeling, 2012). Depth is in meters, in the color scale and bathymetric contours. The historical Currituck SMF site is also marked.

Following this screening work, additional geophysical and geotechnical analyses were performed in areas deemed at higher risk in the MCS analysis (Eggeling, 2012), to better understand the sub-bottom data, assess sediment availability, and the potential for large SMFs. This led to the identification of 4 areas along the upper USEC, from Virginia to Cape Cod, where the potential for large tsunamigenic SMFs identified in the MCS analysis was found to be realistic on the basis of field data (i.e., sediment nature and volume/availability) (Figure 2.1). The historical Currituck slide complex, which is the largest paleo-slide identified along the western Atlantic Ocean continental slope and rise, is located about 150 km south of area 4 (see also Figure 2.2). This SMF, which occurred between 24 and 50 ka ago, when sea level was much lower, has been extensively studied from geological and slide triggering points of view (Bunn and McGregor, 1980; Prior et al., 1986; Locat et al., 2009). Tsunami generation by a reconstituted Currituck SMF was also studied by Geist et al. (2009).

Because the NTHMP inundation mapping work done at this stage only considers the PMTs for each type of source, and in the absence of more accurate or detailed geological and geophysical field data to perform more refined slope stability analyses, it was collegially decided within NTHMP to use the parameters and geometry of the Currituck slide as a proxy for the maximum SMF tsunami that could occur along the upper USEC region, in each of the 4 identified areas of Figure 2.1. This approach was later approved by the NTHMP Mapping and Modeling sub-committee, for the development of the first generation of tsunami inundation maps along the upper USEC, from Maryland to Cape Cod.

Accordingly, in this paper, after briefly describing in a first part our SMF tsunami modeling methodology, in a second part, we present the parameterization and modeling of the historical Currituck event, including: (i) a new reconstruction of the SMF geometry and kinematics; (ii) the simulation of the resulting tsunami source generation; and (iii) the propagation of the tsunami source over the shelf to the coastline, in a series of nested grids. A sensitivity analysis to model and grid parameters is performed to ensure convergence and accuracy of SMF tsunami simulation results; we also qualitatively compare our results to earlier published work for the Currituck tsunami event. Then, we model in greater detail and discuss the impact of the historical Currituck tsunami event along the nearest coastline where its energy is focused, off of Virginia Beach and Norfolk, as well as near the mouth of the Chesapeake Bay. In a third part, following the same methodology, we parameterize and model tsunami generation and propagation for four SMF Currituck proxy sources sited in the 4 identified high-risk SMF areas. Finally, as an illustration of our SMF tsunami hazard assessment work, we present detailed tsunami inundation maps, as well as some other products (e.g., maps of velocity, momentum flux, vorticity), for one of the most impacted and vulnerable areas, near and around Ocean City, MD.

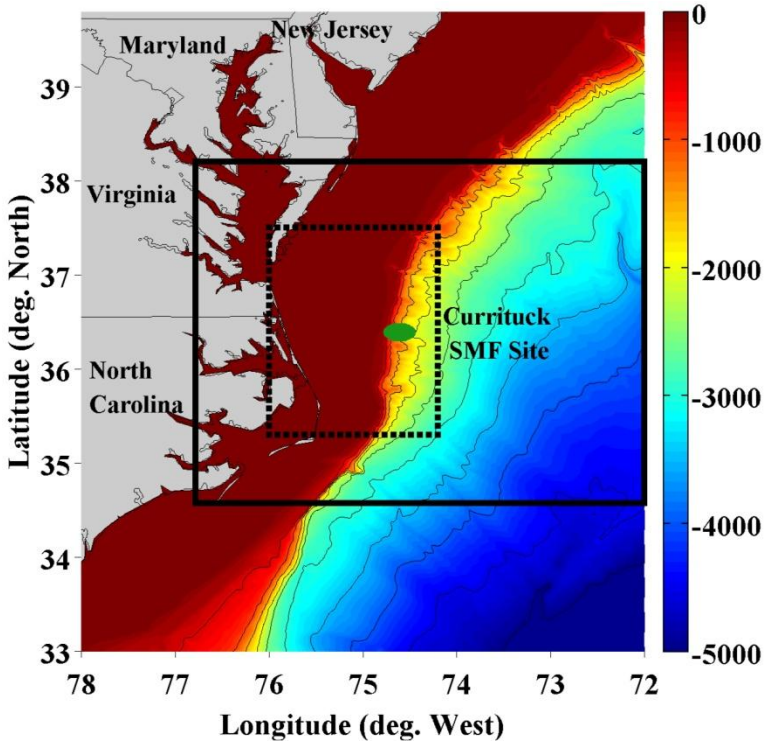

Figure 2.2 Map of the area surrounding the historical Currituck SMF, with depth indicated in meters in the color scale and bathymetric contours. The green ellipse is the footprint of the assumed initial SMF failure (center located at 74.61W and 36.39N, where 1 deg in longitude is 89 km). The solid black box marks the boundary of the 500 m resolution grid used in NHW and FNW SMF tsunami simulations (with 800 x 900 cells and lower left corner coordinates of 76.8W and 34.6N). The dashed black box is a zoomed-in area used to visualize some of the simulation results (lower left corner coordinates, 76.0W and 35.3N).

2 SMF tsunami modeling methodology

2.1 SMF tsunami generation and propagation models

SMF tsunami sources are modeled in the three-dimensional (3D) non-hydrostatic model NHWAVE (Ma et al., 2012) (NHW), which has a boundary fitting σ-coordinate grid in the vertical direction and a Cartesian horizontal grid. After the SMF has stopped moving (for time $t > t_f$), surface elevation and horizontal velocity are interpolated into the nonlinear and dispersive long-wave Boussinesq model FUNWAVE-TVD (FNW), in which tsunami propagation from the source region to the

various coastlines is simulated. Both Cartesian fully nonlinear (Shi et al., 2012) and spherical weakly nonlinear (Kirby et al., 2013) grid implementations are available for FNW, and simulations are performed in a series of one-way coupled nested grids, with increasingly fine resolution and commensurately accurate bathymetric and topographic data towards the coast. The rationale for this coupled modeling approach is that: (i) FNW cannot currently simulate waves generated by a moving bottom; (ii) NHW can simulate a moving bottom and is 3D, hence, more accurate to simulate SMF tsunami generation during which velocities are less uniform over depth than for the subsequent tsunami propagation (see, e.g., Grilli et al., 2002); (iii) FNW is more accurate than NHW for simulating coastal wave transformations, in particular, detecting wave breaking and modeling the related dissipation, and moving shoreline algorithm; (iv) FNW is more computationally efficient as it only has a 2D grid, which hence is at least 3 times smaller than the minimum required NHW grid to provide a similar accuracy of horizontal velocity in the vertical direction (i.e., 3 σ-layers), for an identical horizontal resolution; and finally (v) FNW also has a spherical implementation, which allows accurately simulating far-field tsunami propagation, whereas NHW only has a Cartesian horizontal grid, which limits its use to small latitudinal and longitudinal ranges.

The latter feature, however, is not used in the present paper, although combinations of spherical and Cartesian nested grids were used in earlier work (see, e.g., Grilli et al., 2013b; Kirby et al., 2013). Indeed, in the present work, because all simulations are performed in regional or nearshore grids with small latitudinal and longitudinal ranges, we only used Cartesian nested grids in FNW, with distances

corrected according to a UTM type projection; this allows having undistorted grid cells nearshore, which lead to more accurate numerical results in areas with strongly nonlinear waves and many breaking zones. Additionally, because only the Cartesian implementation of FNW is fully nonlinear, it must be used anyway for the finer levels of nested grids, nearshore and on the coast, where tsunami waves become strongly nonlinear.

For each source, SMF geometry and kinematics are parameterized based on local bathymetry and geology, and used as bottom boundary conditions to force NHW simulations. NHW, solves the inviscid Euler equations (viscous and turbulent effects can be included, but are neglected in the present study) with fully nonlinear free surface boundary conditions. The model has been fully validated for both coseismic and, more importantly, rigid SMF tsunami generation and propagation, according to NTHMP and NOAA guidelines (Tehranirad et al., 2012). For long wave generation, NHW grids typically only require 3 vertical σ-layers, owing to the fairly uniform horizontal velocity over depth (this aspect will be verified in this paper for SMF tsunamis). FNW was also fully validated against a series of tsunami benchmarks, as part of a NTHMP Model Validation Workshop (http://nthmp.tsunami.gov/documents/nthmpWorkshop ProcMerged.pdf; Tehranirad et al., 2011). In both models, open boundary conditions are represented by absorbing (sponge) layers. The one-way coupling method used in FNW works as follows: time series of surface elevation and horizontal velocity are calculated in a coarser grid level, along the boundary of the next finer grid level. Computations are then restarted in the finer grid on the basis of these time series used as boundary conditions. Because

reflected waves are included in the time series, the open boundary conditions are automatically satisfied between nested grids. A similar coupled modeling approach was already applied to the simulation of the coastal impact of transoceanic tsunamis along the USEC, such as from the collapse of the Cumbre Vieja Volcano in the Canary Islands (Abadie et al. 2012; Harris et al., 2012), for which the subaerial landslide tsunami source was computed using the multi-fluid 3D Navier-Stokes solver THETIS (Abadie et al., 2010). The same NHW/FNW coupling methodology was applied to simulating the coastal impact of the Tohoku 2011 tsunami, where the seismic source was specified as a time and space varying bottom boundary condition, to simulate tsunami generation in NHW (Grilli et al., 2013b).

In each model grid, the deep water bathymetry is obtained from the 1 arc-min resolution ETOPO-1 data (Amante and Eakins, 2009), available at NOAA's National Geophysical Data Center (NGDC) (http://www.ngdc.noaa.gov/mgg/global/), while nearshore bathymetry and topography is obtained from the 3 arc-sec (about 90 m) resolution NGDC Coastal Relief Models (CRMs) (http://www.ngdc.noaa.gov/mgg/coastal/coastal.html) and the 1/3 arc-sec (about 10 m) NOAA-NGDC tsunami DEMs, wherever available (http://www.ngdc.noaa.gov/mgg/inundation/ tsunami/inundation.html). All of these data sources, which have been reconciled with each other by NGDC, are seamlessly interpolated to construct model grids. Additional high resolution DEMs for a portion of the Maryland to Cape Cod region have been obtained from ongoing FEMA hurricane and storm surge modeling efforts, but these are not utilized in the results presented here.

Both NHW and FNW have been implemented in parallel MPI FORTRAN, for an efficient solution on computer clusters with shared memory. FNW, in particular was shown to be highly scalable, with a reduction of CPU time by about 90% the number of processors used, as compared to a single-CPU implementation (Shi et al., 2012). In these conditions, all the simulations presented in the paper were performed on a 12 CPU (two 2.93 GHz 6-Core Intel® XeonTM processors) Apple Desktop computer with 64GB RAM memory, in total computational times varying between a few hours and about 22 hrs for the largest grids used. Clearly, on larger clusters, these CPU times could be significantly reduced.

2.2 SMF kinematics

Earlier modeling work on SMF tsunamis (Grilli and Watts 1999, 2005; Grilli et al. 2002; Lynett and Liu, 2002, 2005; Watts et al., 2005) indicates that, besides volume and mean submergence depth, the initial SMF acceleration is the dominant factor for tsunami generation; hence, worst case scenario tsunamis are typically obtained for rigid slumps (i.e., rotational landslides), in which initial acceleration is larger than for rigid translational slides, or deforming SMFs, of similar parameters. Moreover, in many cases, SMF deformation only plays a secondary role in tsunami generation, since it takes time before it significantly affects the fluid flow, and large deformations, when they occur, take place in deeper water where the SMF is no longer tsunamigenic. Hence, in the absence of more accurate field data and to be on the conservative side, for the SMF tsunami generation simulations in NHW, we assumed that both the actual Currituck slide and its 4 proxies failed as rigid slumps.

For rigid slumps, kinematics is specified based on the analytical laws developed by Grilli and Watts (1999, 2005), Grilli et al. (2002) and Watts et al. (2005). Additionally, as in Enet and Grilli (2007), we idealize SMF geometry as a "Quasi-Gaussian" mound of elevation ζ (whose steepness is controlled by a shape parameter ε; here ε = 0.717, and elliptical footprint of length b, width w, and maximum thickness T defined as (Figure 2.3),

$$\zeta(\xi,\chi)=\frac{T}{1-\varepsilon}\max[0,\operatorname{sech}(k_b\xi)\operatorname{sech}(k_w\chi)-\varepsilon]$$
$$k_b=\frac{2}{b}acosh\frac{1}{\varepsilon}$$
$$k_w=\frac{2}{w}acosh\frac{1}{\varepsilon} \qquad (1)$$

where (ξ,χ) are the local down-slope and span-wise horizontal coordinates, rotated in the direction of SMF motion θ. With this geometry and parameters, the SMF volume is given by,

$$V_b=bwT\left(\frac{f^2-\varepsilon}{1-\varepsilon}\right) \quad with \quad f=\frac{2}{C}atanh\sqrt{\frac{1-\varepsilon}{1+\varepsilon}} \quad and \quad C=\operatorname{acosh}\left(\frac{1}{\varepsilon}\right) \qquad (2)$$

Earlier modeling work (Locat et al., 2009) indicates that, during its tsunamigenic period of motion, the Currituck SMF achieved a relatively small maximum displacement (runout) $s_f < b$ in its main direction of motion down the slope, over an unknown time of motion t_f. The combination of rigid block SMF and small displacement parallel to the slope supports modeling the SMF kinematics as a rigid slump, with constant basal friction and negligible hydrodynamic drag (Grilli and Watts, 2005). This type of kinematics was considered in earlier work (see above-listed

references), leading to a pendulum-like center of mass motion *s(t)* parallel to the local mean slope of angle α. In the absence of more detailed information on SMF kinematics, we will use this simple law of motion, which reads,

$$S(t)=\begin{cases} 0 & t < t_i \\ S_0\left(1-\cos\left\{\frac{t-t_i}{t_0}\right\}\right) & t_i \le t \le t_i + \pi t_0 \\ 2s_0 & t_i + \pi t_0 \le t \end{cases} \quad (3)$$

with $s_0=s_f/2$ and $t_0=t_f/\pi$ the characteristic time and distance of motion, respectively, and $t_i=0$ the initial triggering time.

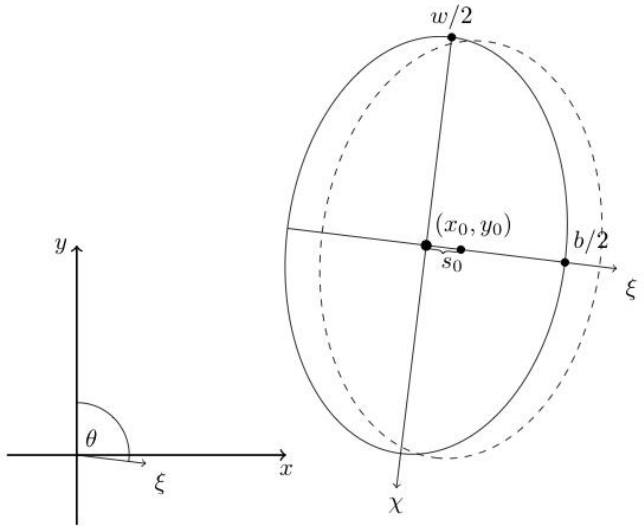

Figure 2.3 Geometric parameterization of a SMF initially centered at (x_0, y_0) moving in direction ξ, with an azimuth angle θ from North and center of mass motion *s(t)* measured parallel to the mean local slope of angle α; *(x,y)* denote the longitudinal and latitudinal horizontal directions, respectively.

Unlike the simple planar slopes modeled in earlier numerical work (Grilli et al., 2002, 2010a) and in laboratory experiments (Enet and Grilli, 2007), here we specify the SMF elevation over or below the actual seafloor bathymetry $h_0(x,y)$, depending on

whether we reconstruct a historical failure such as the Currituck SMF (Figure 2.4), or we consider a future failure (this will be detailed later for both cases). Given the initial SMF center of mass location (x_0, y_0) in global axes (x,y) (i.e., coordinates of the center of the elliptical footprint) and azimuth angle of SMF motion θ, we define the coordinate transformation to the local SMF slope-parallel coordinate system (ξ,χ) (Figure 2.3) as,

$$\xi = \{(x - x_0)cos\theta - (y - y_0)sin\theta\} - s(t)cos\alpha$$
$$\chi = (x - x_0)sin\theta - (y - y_0)cos\theta \quad (4)$$

with $s(t)$ given by Eq. (3). [Note that, since Currituck is a historical event, in the modeling, $h_0(x,y)$ must be the pre-failed bathymetry and not the current one. This requires first reconstructing pre-failed conditions, which is detailed in the next section.] Then, the instantaneous seafloor depth above the SMF is given by,

$$h(x,y,t) = h_0(x,y) + \zeta\{\xi(x,y,t),\chi(x,y)\} - \zeta\{\xi(x,y,t_i),\chi(x,y)\} \quad (5)$$

with $\Delta h = h - h_0$. The seafloor motion described by Eq. (5) is similar to a horizontal translation downslope of part of the seabed, while accounting for actual bathymetry. The vertical seafloor velocity (also used in NHW as a bottom boundary condition) is then computed as,

$$\frac{dh}{dt}(x,y,t) = \frac{d}{dt}\{\zeta\{\xi(x,y,s(t)),\chi(x,y)\}\} \quad (6)$$

which can be easily derived from Eqs. (1-5).

For rigid slumps, hydrodynamic drag can be neglected due to low velocity and small amplitude of motion, and inertia includes both the SMF mass $M_b = \rho_b V_b$, with ρ_b denoting the bulk density and the specific density being defined as $\gamma = \rho_b/\rho_w$, with ρ_w the water density, and an added mass $\Delta M_b = C_m \rho_w V_b$, defined by way of an added mass coefficient C_m. Assuming a constant basal friction, a nearly circular rupture surface of radius R, and a small angular displacement $\Delta\phi$, Grilli and Watts (2005) derived the characteristic distance and time of motion for rigid slumps as,

$$s_0 = \frac{R\Delta\phi}{2} \quad \text{and} \quad t_0 = \sqrt{\frac{R}{g}\frac{\gamma+C_m}{\gamma-1}} \quad R \cong \frac{b^2}{8T} \tag{7}$$

with g denoting the gravitational acceleration. The last equation (7), proposed by Watts et al. (2005), is a semi-empirical relationship to estimate the radius of slump motion as a function of slump downslope length and maximum thickness.

3 Simulation of the Currituck SMF Tsunami generation, propagation and coastal impact

Tsunami generation and propagation for the historical Currituck SMF event was modeled by a few authors, including Geist et al. (2009) who used the dispersive weakly nonlinear Boussinesq model COULWAVE. They extracted the SMF geometry from the bathymetry and specified its motion as a bottom boundary condition (Lynett and Liu, 2002, 2005), based on a rigid slide kinematics similar to that proposed by Grilli et al. (1999, 2002, 2005), although details are lacking. They simulated the Currituck tsunami (2D) wave field using a range of potential SMF movements (i.e.,

vertical displacement and duration of motion), bounded by the mobility analysis of Locat et al. (2009), and studied the effects of slide duration (from t_f = 7.2 to 20 min, with the most realistic duration being 10 min) and bottom friction coefficient (C_d = 0.001 to 0.01, with the most realistic value being 0.0025; note, C_d is a non-dimensional coefficient used in a standard quadratic bottom shear stress formulation) on tsunami generation and propagation. Additionally, a high resolution (5 m grid) fully nonlinear simulation was performed along a one-dimensional E-W transect, highlighting the importance of wave breaking, dispersion, and nonlinearity on near shore propagation; however, no detailed nearshore tsunami impact was computed. Geist et al.'s results indicate that, for a given bottom friction coefficient, nearshore runup is primarily affected by SMF volume, and then by failure duration (i.e., slide acceleration), which is consistent with earlier findings (e.g., Grilli et al., 2005).

3.1 Modeling of the Currituck SMF geometry

Detailed descriptions of the stratigraphy and morphology of the Currituck SMF have been reported on the basis of seismic surveys by Bunn and McGregor (1980), Prior et al. (1986), and Locat et al. (2009). The latter work in particular presents a morpho-stratigraphic model of the failed mass and a depositional model of the runout zone, based on which the salient tsunamigenic characteristics of the Currituck SMF can be inferred (see, Locat et al.'s Figures 2.3 and 2.4). Thus, we find that the Currituck event consisted of two separate failed masses: Slide 1, which had a ~100 km^3 volume of sediment and Slide 2, which had a ~60 km^3 volume, and that the

failure occurred fairly rapidly. This justifies that, for the purpose of tsunami generation, the Currituck SMF be modeled as a single failed mass.

Based on these geological analyses, we located the center of mass of the pre-failed Currituck SMF at x_0 = 74.7W and y_0 = 36.5N (Figure 2.2), in a 1800 m depth, and assumed it had a maximum down-slope length b = 30 km and width w = 20 km (Figure 2.3), with a maximum thickness of roughly T = 750 m close to the center of the failed area. With these dimensions Eq. (2) yields a volume of failed sediment, V_b = 134 km^3, which is in reasonable agreement with past geological work, in which slide volume was estimated to V_b = 128-165 km^3 (Prior et al., 1986). The headwall of Slide 2 begins at an approximate 500m depth and is about 200 m thick; we assumed that this headwall roughly marks the shallower boundary of the failed area, which constraints

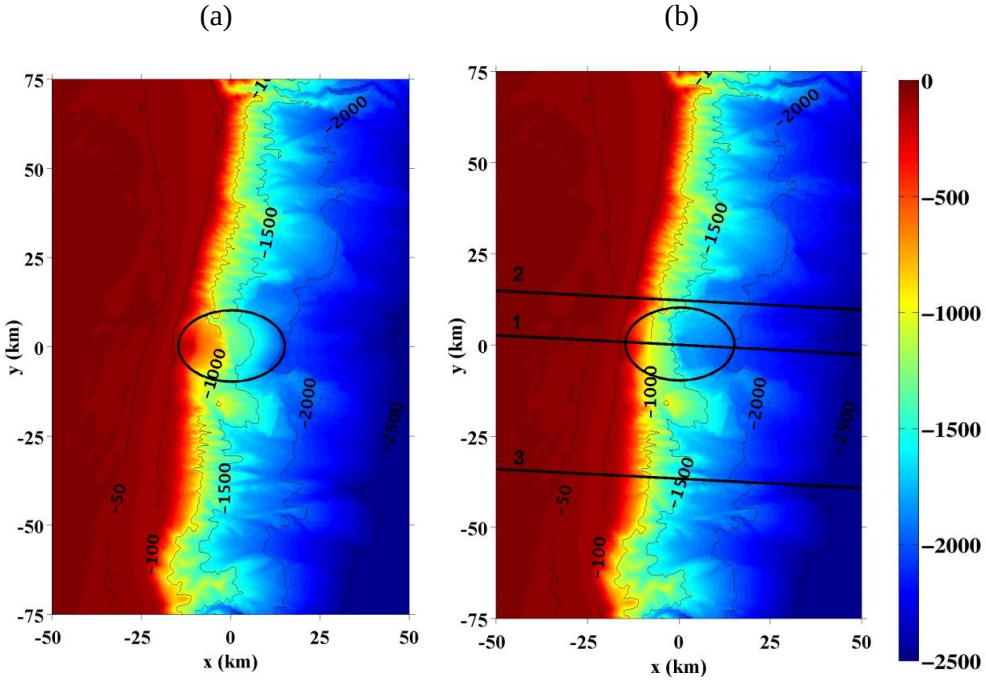

Figure 2.4 Bathymetry around the Currituck SMF site. Color scale and bathymetric contours give depth in meters. The ellipse is the SMF footprint, similar to that shown in Figure 2.2, and axes mark the distance measured from the SMF center (at 74.61W and 36.39N): (a) reconstructed pre-failed bathymetry; (b) current (post-failed) bathymetry with black lines marking bathymetric transects shown in Figure 2.5 The Currituck SMF central axis corresponds to transect 1.

the pre-failed SMF horizontal footprint (Figure 2.4a). Although parts of the SMF traveled for large distances on the seafloor, to establish the SMF kinematics relevant to tsunami generation, we will only consider and parameterized the runout distance (and related time of motion) corresponding to the so-called tsunamigenic part of SMF motion; this is detailed later. Finally, based on the literature and on the seafloor morphology, we assumed that the SMF traveled due East, i.e., in azimuthal direction $\theta = 90$ deg., which is nearly perpendicular to the isobaths.

3.2 Currituck SMF geometry/bathymetry reconstruction

The pre-failed bathymetry of the Currituck SMF is reconstructed by adding the sediment volume V_b to the post-failed area. However, a direct addition of the SMF geometry described by Eq. (1) to the current bathymetry would not accurately reconstruct the failed slope as it was determined that, during its motion, the failed sediment from Slide 2 moved (flowed) into and partially filled the back of the cavity left by Slide 1 (Prior et al., 1986). Therefore, part of the sediment within the reconstructed Currituck SMF should consist of sediment currently found at the site (i.e., sediment having flowed from Slide 2 into the back of Slide 1 after the main tsunamigenic period of motion). To account for this, after some trials and error, we first removed a T = 250 m thick SMF from the post-event site (also described by Eq. (1) and with the same width and length as the full SMF; (— - —) transect in dashed red). The pre-failed bathymetry used in NHW simulations was finally obtained by adding the full SMF volume and geometry, with maximum thickness T = 750 m to this

modified transect (solid black transect in (— - —)); at its center, the pre-failed SMF is now in a d = 1300 m depth.

(— - —) illustrates the SMF pre-failed bathymetry reconstruction and compares it to the surrounding area. Although the Currituck pre-failed bathymetry and geometry (assumed Quasi-Gaussian here) are unknown, the bathymetry of the surrounding continental slope can be used as a first approximation to validate our reconstruction. Thus, (— - —) compares the current bathymetric transects 2 and 3 (marked in Figure 2.4b), which pass through areas north and south of the failure site, to transect 1, which passes through the center of the reconstructed Currituck SMF bathymetry, before and after reconstruction. We see that transects 2 and 3 are consistent with each other, and that the reconstructed pre-failed transect 1 is consistent with both of these, confirming that reconstruction is relevant. Further improvements could be achieved by adding a few small canyons, but these would likely be inconsequential for tsunami generation (Locat et al., 2009). Finally, it should be pointed out that transect 1, shown in (— - —), only predicts the bathymetry at the end of the tsunamigenic part of SMF motion (estimated in the next section to last for about 12 minutes). Beyond this time, based on earlier work (Locat et al., 2009), the mound of failed sediment (shown between 0 and 30 km in the Figure 2.5) is expected to keep spreading out in all directions, mostly down-slope but also up-slope in the back of the SMF to fill part of the initial small cavity that was removed prior to adding the SMF volume. However, based on earlier work (e.g., Grilli and Watts, 2005; Abadie et al., 2012), wave generation due to this spreading motion in very deep water is expected to be small. Grilli and Watts (2005) (and others such as Geist et al., 2009), indeed showed that initial acceleration and

short term motion of fairly rigid SMFs are responsible for most of the tsunami generation. Abadie et al. (2012), who modeled a strongly deforming partly submerged and partly subaerial slide, by performing a detailed analysis of energy exchanges between the SMF debris flow and fluid motion, showed that the tsunamigenic part of SMF motion only lasted for a short time. A thick near-bottom debris flow propagated for a long time after the initial tsunamigenic motion, but it essentially induced a recirculation of failed material onto itself, with very little additional energy conveyed to the water motion, and hence negligible wave generation; in any case, additional wave generation if any, as a result of this debris flow, would only add to the offshore propagating waves and not to the tsunami directed onshore, which is the object of the present work.

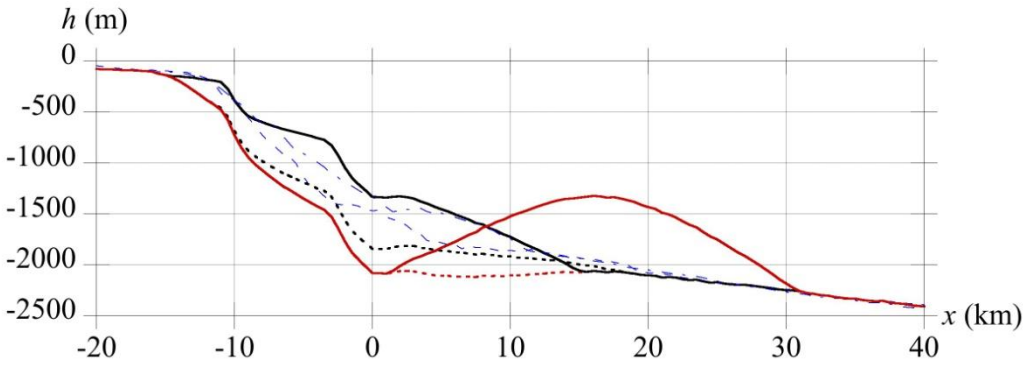

Figure 2.5 Bathymetric transects through and adjacent to the center of the Currituck slide, marked in Figure 2.4: (- - -) current post-failed bathymetry along the SMF direction of motion (transect 1); current post-failed bathymetry along transects 2 (— —) and 3 (— - —); (—) reconstructed pre-failed bathymetry along transect 1; (- - -) transect 1 bathymetry with a Currituck SMF of 250 m maximum thickness removed; and (—) transect 1 bathymetry at the end of the SMF tsunamigenic motion duration (at time $t = t_f$), computed with Eqs. (3-5).

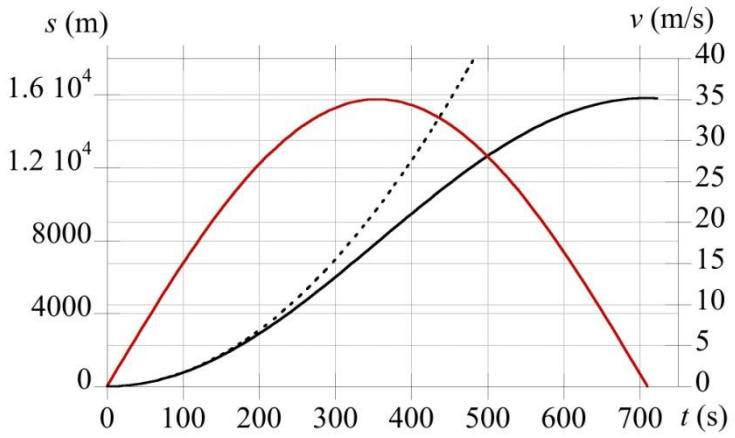

Figure 2.6 Currituck SMF (slump) motion *s(t)* (—) (and velocity v(t) (—) as a function of time t (Eqs. (3-6)), used to specify the bottom boundary condition in NHW simulations; (- - -) simple accelerating law of motion: $s(t) \approx 0.5\, a_0\, t^2$.

3.3 Detailed Currituck SMF kinematics

The Currituck SMF is modeled as a rigid slump, with geometry described by Eqs. (1-2) and kinematics by Eqs. (3-6), both of which are specified as bottom boundary conditions in NHW simulations. Assuming γ = 1.85 and C_m =1, as in Grilli and Watts (2005), Eq. (7) yields R = 150 km and a characteristic time of motion t_0 = 226 s, resulting in a failure duration t_f = 11.9 minutes, which is consistent with the likeliest duration of 10 min proposed by Geist et al. (2009) (although their law of motion and slide displacement were quite different). This duration is also consistent with that of the tsunamigenic slide motion inferred from the slide velocity profiles calculated by Locat et al. (2009) (shown in their Figure 2.14a). They used two types of deforming slide models (Bingham and Bilinear) to calculate the velocity of the Currituck SMF frontal element. On this basis, they concluded that the peak slide velocity during the event was likely between 30 and 40 m/s. Since the distance traveled by the Currituck SMF during the tsunamigenic part of its motion is unknown, we selected the slide runout s_f and characteristic distance traveled s_0 such that, with the

above t_0 value, the maximum slump velocity predicted by Eq. (3) would match that of Locat et al. (2009), i.e., $v_{max} = s_0/t_0 \approx 35$ m/s. This yields $s_0 = 7{,}910$ m, $s_f = 15.8$ km (Figure 2.6), and $\Delta\phi = 0.11$ rad or 6.0 deg, which is consistent with the assumed small angular displacement of the rigid slump theory; finally, the SMF initial acceleration is $a_0 = s_0/t_0 = 0.155$ m/s^2. The bathymetry, computed using Eqs. (3-5) at the end of tsunami generation at $t = t_f$, is shown in (—·—) (solid red transect). Beyond this point the SMF would have reached the lower velocity and acceleration region described by Locat et al. (2009), and assumed to be zero (i.e., negligible for tsunami generation) here (Figure 2.6), and would disperse over the seafloor without additional tsunamigenic effects.

It should be noted that this simplified pendulum-like slump kinematics $s(t)$ represents the SMF displacement parallel to the average slope α, which for a small angular displacement $\Delta\phi$ is identical to a small circular arc, or chord, along a circle of radius R. Grilli and Watts (2005) and Watts et al. (2005) showed that, for rigid SMFs, during the initial accelerating part of the motion, when the SMF is most tsunamigenic, whether assuming a slide or a slump motion, the kinematics can be approximated by, $s(t) \approx 0.5\, a_0\, t^2$. This simplified accelerating law of motion is marked in Figure 2.6, and we see that up to $t = t_0$, differences are quite small with Eq. (3) (8% difference at this time). For later times, the slump is gradually decelerated by gravity and basal friction, until it stops for $t = t_f$; a slide, by contrast, would reach a terminal velocity on the slope, when hydrodynamic drag and basal friction will balance inertia and gravity forcing and further decelerate when reaching the abyssal plain.

3.4 Simulation of the Currituck tsunami source generation and early propagation

3.4.1 Simulation of SMF tsunami source generation with NHW

Generation of the Currituck SMF tsunami source is simulated with NHW up to at least t_f = 710 s (11.9 min.), during which time bottom boundary conditions are specified based on the geometry, bathymetry, and slump-like kinematics discussed in the previous sections (Figure 2.6; Table 1). We first use a 3D NHW grid with 3 σ-layers, and a 500 m resolution Cartesian horizontal mesh; the grid as a horizontal footprint of 450 by 400 km (900 x 800 cells), which is shown in Figure 2.2. The figure also shows a smaller area of 165.5 by 244 km, over which we zoom in to better visualize results in some of the following figures. A sensitivity analyses detailed later will confirm that a 500 m resolution with 3 σ-layers is adequate to ensure convergence of the present simulations with NHW. Finally, to maximize tsunami generation, we assumed that there is no bottom friction in NHW at this initial stage of simulations (i.e., $C_d = 0$).

Figure 2.7 shows shows instantaneous surface elevations computed in NHW at 4 different times, up to 800 s (13.3 min.), i.e., slightly after the slump has stopped moving (at t_f = 710 s). In Figure 2.7d, after the tsunamigenic duration of motion, surface elevations are large and range between approximately -20 and +20 m. Figure 2.8 shows surface elevations computed along an E-W transect through the SMF center, for these and other results obtained at later times, up to 2000 s (33.3 min.). More specifically, Figure 2.7 and Figure 2.8 show that, at 125 s after initiation of slide motion, the SMF source surface elevation takes the form of two inverted quasi-Gaussian humps located symmetrically above the initial slide location ($x = 0$). This is

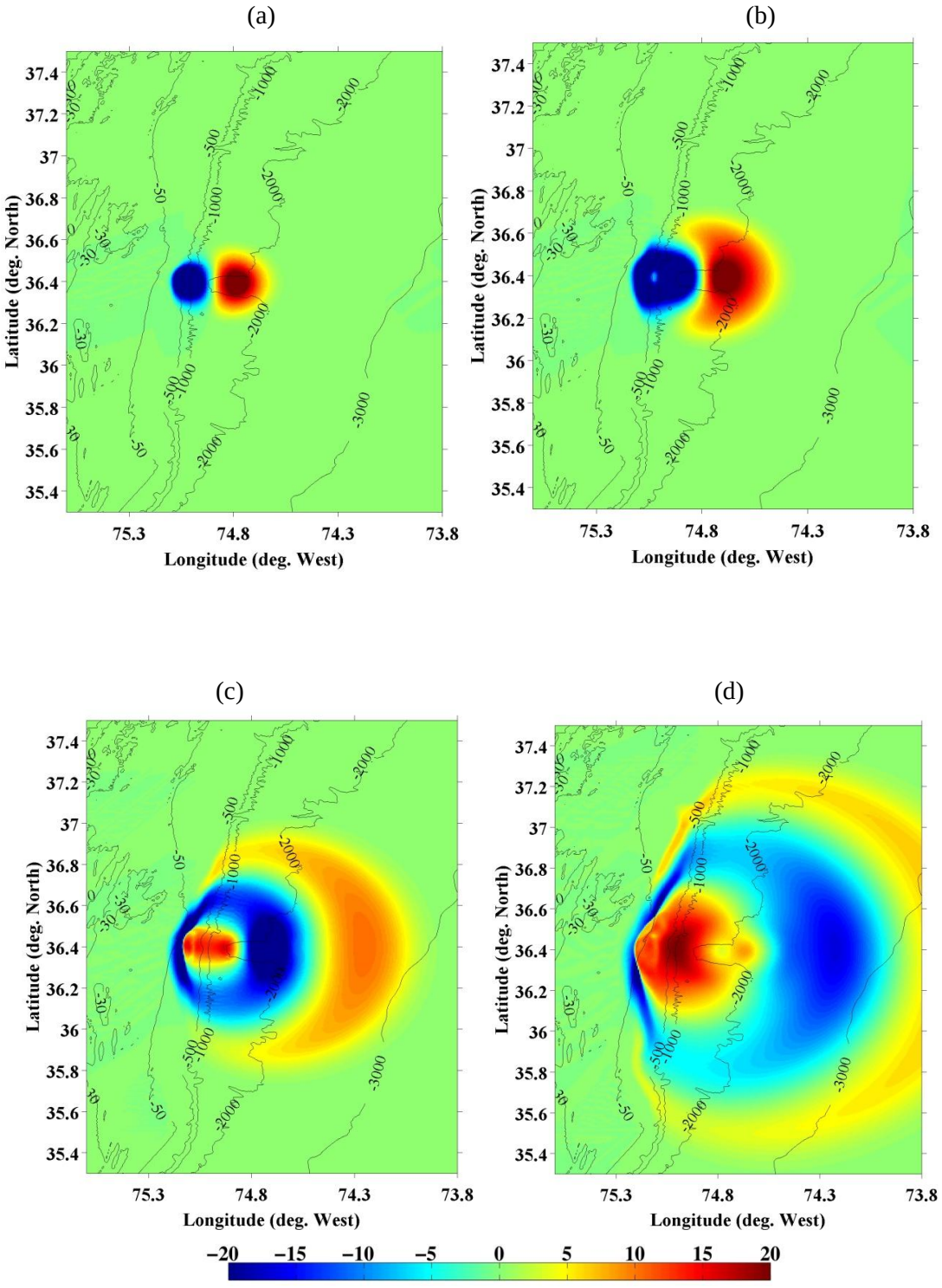

Figure 2.7 Currituck SMF tsunami source generation in NHW (C_d = 0; 500 m resolution grid, 3 σ-layers). Instantaneous surface elevation (color scale is in meter) at: (a) 125 s; (b) 250 s; (c) 500 s; and (d) 800 s (13.3 min.) after SMF triggering (see Figure 2.8 for E-W transects through these results). Bathymetric contours are marked in meter.

qualitatively consistent with earlier results of fully nonlinear potential flow computations for rigid SMFs of idealized shape moving down a plane slope, reported by Grilli et al. (1999, 2002, 2005, 2010a) and Watts et al. (2005). Between 250 and 800 s, the same figures show that the initial negative elevation wave propagates onshore, together with a new "rebound" wave crest that appears within its trough. Both of these waves later shoal-up and transform through interactions with the continental shelf slope and cause onshore tsunami impact; this incoming wave train thus initially looks like a so-called N-wave (Figure 2.8 , curves b and c).

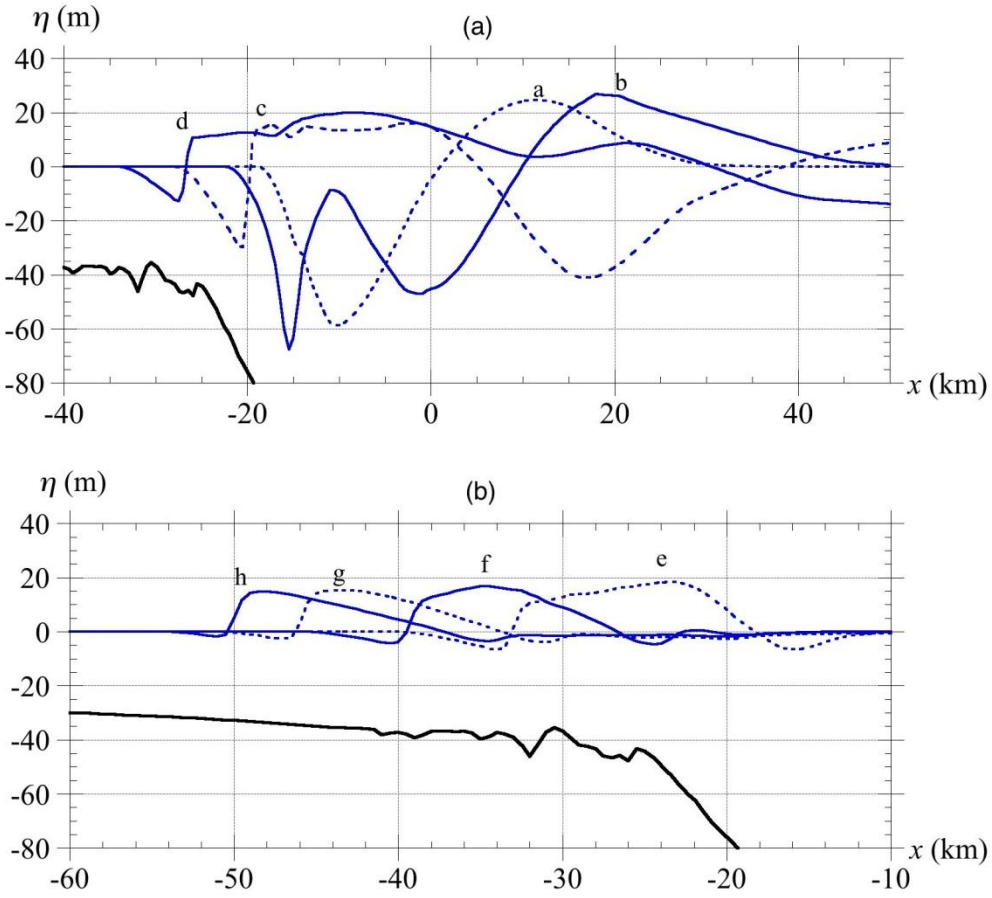

Figure 2.8 Instantaneous surface elevations (—, - - -) in NHW simulations of the Currituck SMF tsunami (C_d = 0; 500 m resolution grid, 3 σ-layers), at: (a) 125 s; (b) 250 s; (c) 500 s; (d) 800 s (13.3 min); (e) 1100 s; (f) 1400 s; (g) 1700 s; and (h) 2000 s (33.3 min) after SMF triggering. Results are shown along an E-W transect through the SMF center (36.39 N lat.), as a function of the distance to the center of the SMF; (—) denotes the ocean depth.

During the same time period, the positive (Quasi-Gaussian) elevation wave, initially generated in deeper offshore waters, propagates further offshore as a cylindrical wave crest of decreasing elevation. Among those waves, the larger elevation (10-15 m) waves near the SMF main eastern direction of motion keep propagating offshore towards the far-field. The smaller elevation (5-7 m) waves to the north, however, start refracting over the shelf slope and propagating towards the Delaware Bay (Figure 2.7d); this was also observed in Geist et al.'s (2009) qualitatively similar simulations and will be further detailed later when performing a computation in a larger domain. This overall pattern of wave generation is fully consistent with earlier modeling work by Grilli et al. (2002, 2010a) for idealized SMF geometry and bathymetry, and confirms that the main onshore propagating tsunami is mainly a result of the initial surface depression, which is fully generated around $t = t_0$ (see Figure 2.7b and curve b in Figure 2.8a), hence, during the accelerating phase of the SMF motion (Figure 2.6); this also confirms that any subsequent wave generation due to near-bottom debris flows occurring for $t > t_f$, if any, would not contribute to the onshore propagating tsunami waves.

During its interactions with the continental shelf slope, both shoaling and reflection of the onshore propagating tsunami N-wave occur, as well as directional spreading (see results at 500 and 800 s in Figure 2.7 and Figure 2.8). At 800 s (13.3 min.), the maximum wave elevation reaches about 20 m offshore. For later times (Figure 2.8, curves e to h), as waves propagate further onshore and over the shelf edge, the maximum height (trough to crest) of the incoming N-wave first stays near the same value (with shoaling compensating the decay due to directional spreading),

reaching 19 m over the shelf at t = 1100 s, in a depth of 40 m, before it starts decreasing as the wave more strongly spreads out laterally (see results up to t = 2000 s here and in Figure 2.9). This decay in elevation will be enhanced by dissipation, first due to bottom friction and later to breaking, both of which will be modeled in FNW increasingly finer nested grids, when simulating tsunami propagation over the shelf (see results in a following section).

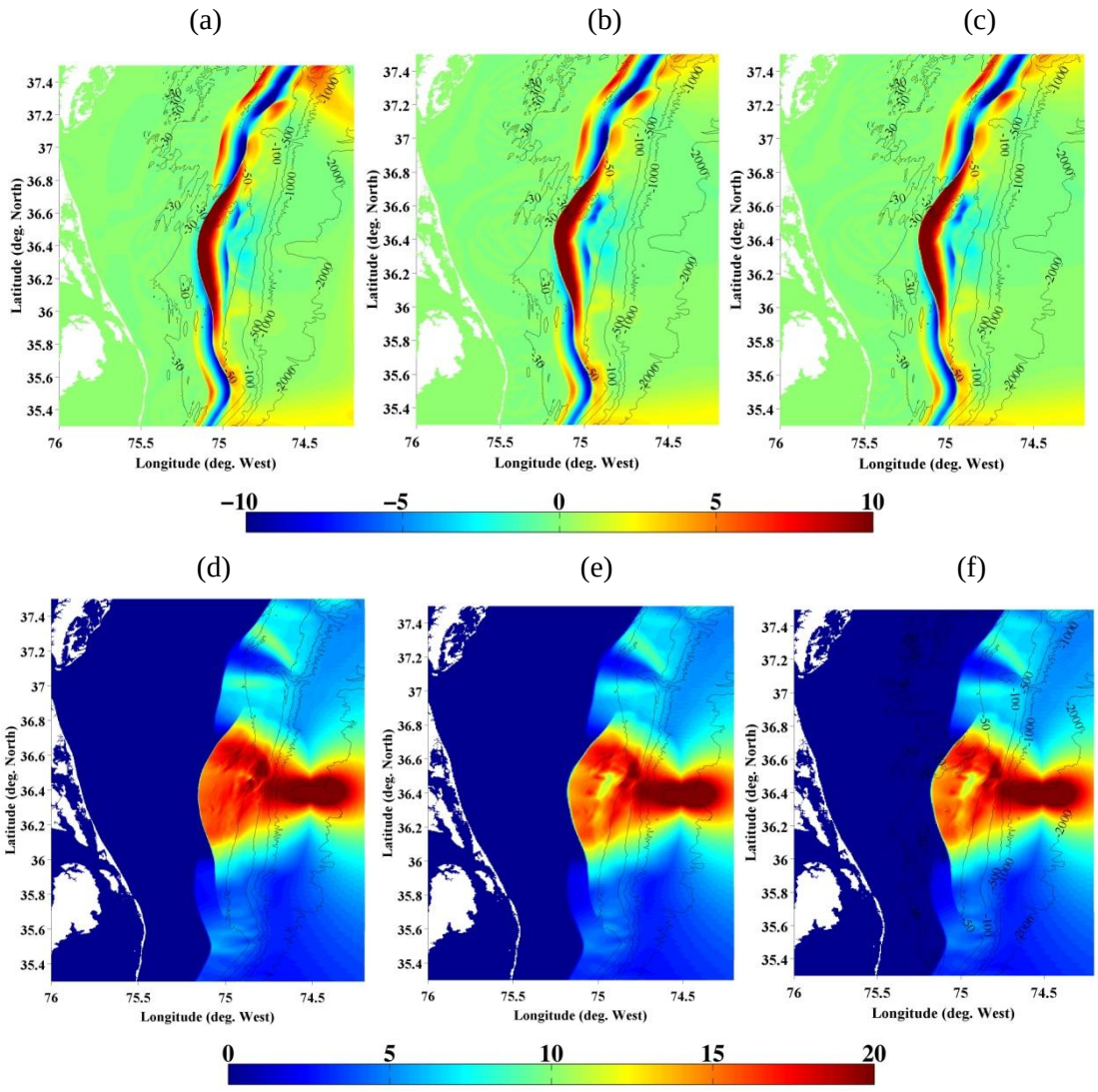

Figure 2.9 Instantaneous (a,b,c) and maximum (d,e,f) surface elevation (color scales are in meters) at t = 2000 s (33.3 min.) after SMF triggering in NHW simulations of the Currituck SMF tsunami (C_d = 0; same case as in Figure 2.7 and Figure 2.8), using: (a,d) a 250 m resolution grid with 3 σ-layers; (b,e) a 500 m resolution grid with 3 σ-layers; or (c,f) a 500 m resolution grid with 5 σ-layers. Results are shown in the zoomed in area of Figure 2.2; bathymetric contours are marked in meters.

3.4.2 Convergence of NHW results

Here, we verify that the generation of the Currituck SMF tsunami source in NHW is sufficiently accurate (i.e., converged) in a 500 m resolution grid with 3 σ-layers in the vertical direction. To do so, we compare these results to those obtained in a 500 m resolution grid with 5 σ-layers and in a 250 m resolution grid with 3 σ-layers, thus assessing changes due to a finer vertical or horizontal discretization. Once NHW convergence is assessed in a 500 m resolution grid with 3 σ-layers, these model parameters will be used in simulations of tsunami generation for Currituck SMF proxies specified in each of the 4 selected areas along the USEC (Figure 2.1).

Results of NHW's convergence study are first shown in Figure 2.9, in the form of both instantaneous and maximum surface elevations computed at t = 33 min, in the three tested grids configurations. The agreement between all results is very good, as can be more easily assessed in Figure 2.10, in an E-W transects through the center of the SMF of surface elevations computed at t = 33 min in the three grids. Figure 2.10a shows that refining the horizontal grid resolution by a factor of 2 yields very similar surface elevations, but introduces a slight time shift in results (i.e., waves appear to be slightly slower in the finer grid likely because of the better resolved bathymetry). Figure 2.10b shows that increasing the number of σ-layers from 3 to 5, thereby doubling the vertical grid resolution, yields slightly faster waves of similar surface elevation nearshore (although there appears to be slightly larger differences in elevation offshore). Finally, Figure 2.11 shows envelopes of maximum surface elevations computed along the same transect, for the various cases discussed before. Although there are larger differences over the continental shelf slope, as a function of

discretization resolution and number of σ-layers, nearshore, all the computed maximum elevations are in good agreement, which supports our choice of model parameters for NHW.

3.4.3 Coupling of NHW and FNW to simulate the tsunami coastal propagation

We verify the relevance and accuracy of the one-way coupling of NHW's 3D results, obtained in a 500 m resolution grid with 3 σ-layers, to FNW's 2D results in a horizontal grid with identical 500 m resolution and surface area, to pursue simulations of nearshore propagation and coastal impact. Based on the tsunamigenic duration of slide motion (Figure 2.6), FNW is initialized with NHW results soon after the end of slump motion, i.e., at t = 800 s (13.3 m; Figure 2.7d). Because the horizontal grids have identical cells in both models, surface elevation and horizontal velocity (interpolated at the required level of 0.513 times the local depth, from σ-layer results in NHW) is easily used to initialize FNW and pursue computations in this model for later times. To prevent reflection at open boundaries, sponge layers are specified in FNW's grid over a width of 60 km or 120 grid cells inward from the northern and southern boundaries, and 100 km or 200 grid cells inward from the eastern boundary (see details in Shi et al., 2012). These sponge layers do not fall within the zoomed in area used to visualize results.

In Figure 2.12, we compare both instantaneous and maximum surface elevations computed in NHW at t = 33 min to FNW's results computed at the same

(a)

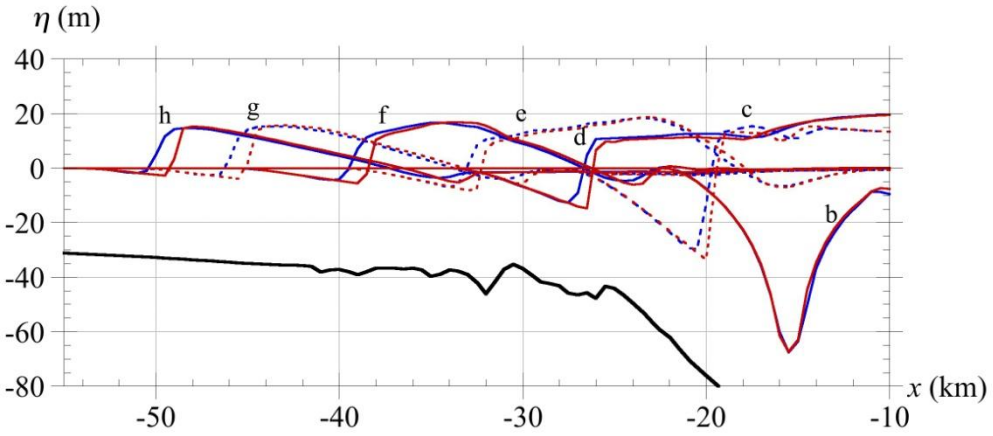

(b)

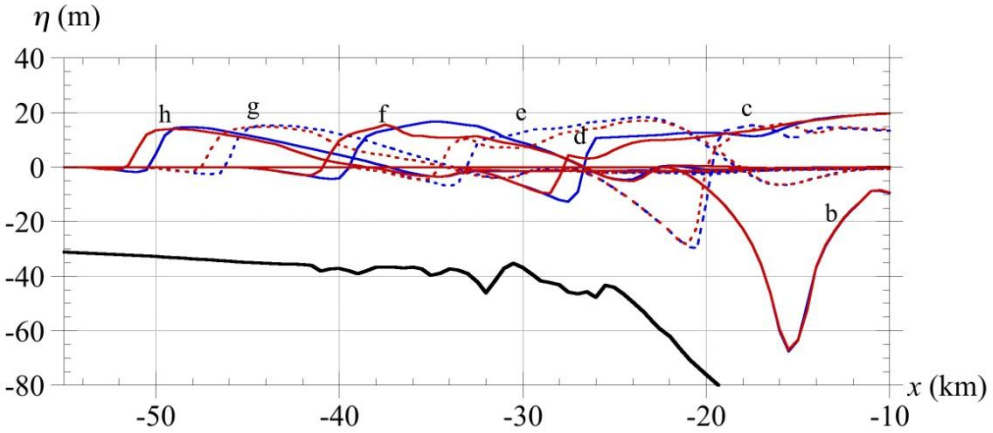

(c)

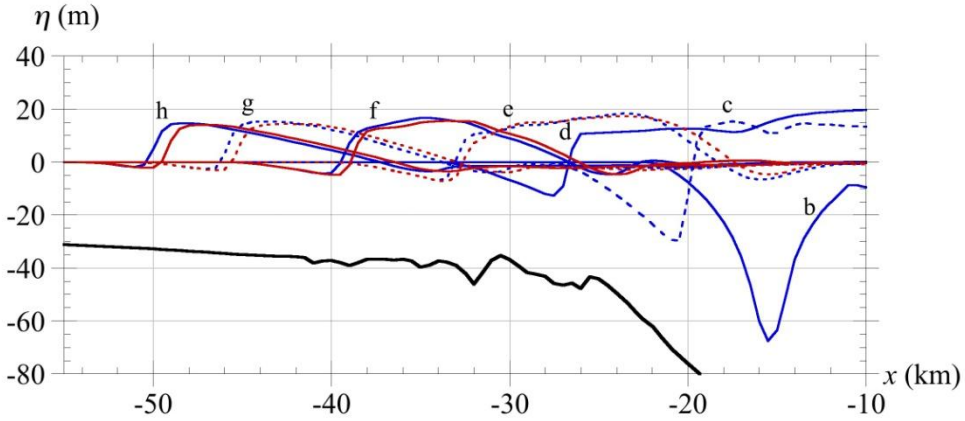

Figure 2.10 Comparison of NHW (500 m, 3 σ-layers) surface elevations of Figure 2.8 (—, - - -) with those of (—, - - -): (a) NHW in a 250 m resolution grid with 3 σ-layers; (b) NHW in a 500 m resolution grid with 5 σ-layers; (c) FNW in a 500 m resolution grid initialized with NHW 500 m resolution grid results at 800 s (13.3 min.). We use C_d = 0 and results are shown along an E-W transect through the SMF center (36.39 N lat.), as a function of the distance to the center of the SMF.

time, after being initialized with NHW results at 13.3 min. [Note, because no bottom friction was specified in NHW during these simulations, for the purpose of comparison, these FNW simulations also assume a bottom friction coefficient $C_d = 0$. Because the tsunami is still in fairly deep water, however, this should not matter for results computed at this stage of propagation.] We see that results of both models are in good agreement at this stage. The same surface elevation are compared Figure 2.10c, at various times, and in Figure 2.11 for the maximum envelope along an E-W transect passing through the SMF center. Again, FNW and NHW results obtained on the same horizontal grid are in good agreement nearshore, over the continental shelf. In the transects of Figure 2.10c, surface elevations computed over the shelf in both models appear to be nearly identical, with FNW's results only slightly lagging in time as compared to NHW's results. Such a time lag, however, does not affect maximum inundation and runup.

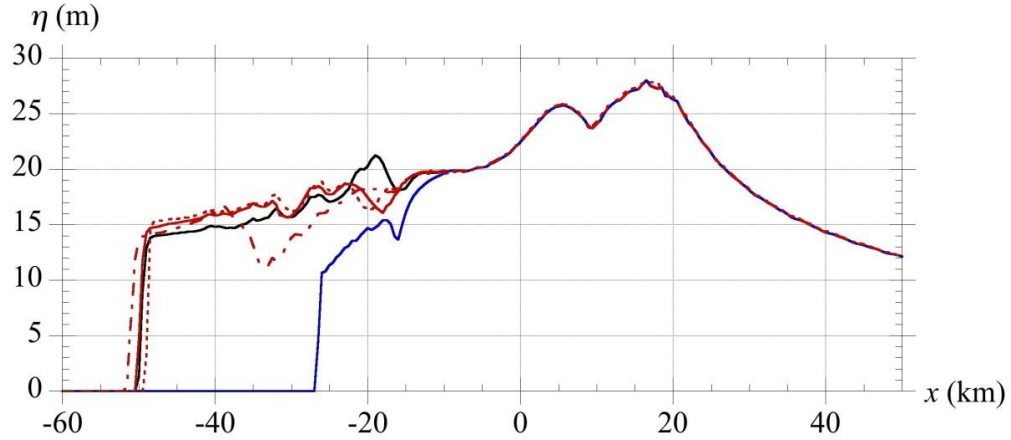

Figure 2.11 Maximum surface elevation in simulations of the Currituck SMF tsunami (C_d = 0), along an E-W transect through the SMF center (36.39 N lat), as a function of the distance to the center of the SMF, at: (—) 800 s (13.3 min) in NHW 500 m resolution grid with 3 σ-layers (Figure 2.7); and 2000 s (33 min) in FNW 500 m resolution grid (—) (Figure 2.12c), NHW 500 m resolution grid with 3 σ-layers (—) (Figure 2.12d), NHW 250 m resolution grid with 3 σ-layers (- - -) (Figure 2.9c), and NHW 500 m resolution grid with 5 σ-layers (— - —) (Figure 2.9d).

Figure 2.11 confirms these observations. In shallow water, for x ≤ -25 km (or depth less than 45 m), the maximum envelopes of surface elevation computed at 33 min. with FNW and NHW (using 3 σ-layers) are in good agreement. From x = -15 to -25 km, discrepancies are larger, but this is likely due to small "numerical adjustements" of NHW's initial solution to the parameters and grid used in FNW. Finally, for x = -25 to -35 km, differences of NHW's solution using 5 σ-layers with other solutions are larger, likely due to the more complex velocity profile over depth in this larger depths area, which is better represented with 5 layers. In shallower water, however, the 5-layer solution is in good agreement with the 3-layer solution.

The good agreement between FNW and NHW results for maximum surface elevation and wave profiles in shallow water thus supports using the two model coupling approach that will be used in all the following simulations in this work.

3.5 Simulation of the Currituck SMF tsunami propagation to shore

3.5.1 Coarse grid regional and nearshore simulations

We compute the Currituck tsunami propagation to shore with FNW, by one-way coupling in a series of nested Cartesian grids. Simulations start in the 500 m resolution regional grid used so far for the convergence and accuracy study, still initialized at 800 s with NHW results, but computaitons are run for a longer time than before. We use the standard value of the bottom friction coefficient, C_d = 0.0025, corresponding to coarse to fine sand. In their simulations along a one-dimensional cross-shore transect, Geist et al. (2009) studied the sensitivity of SMF tsunami

elevation to bottom friction and showed that using larger friction coefficient values significantly reduced tsunami coastal impact. We tested this as well in our simulations (results not shown) and observed that for C_d = 0.01 the inundation depth along the

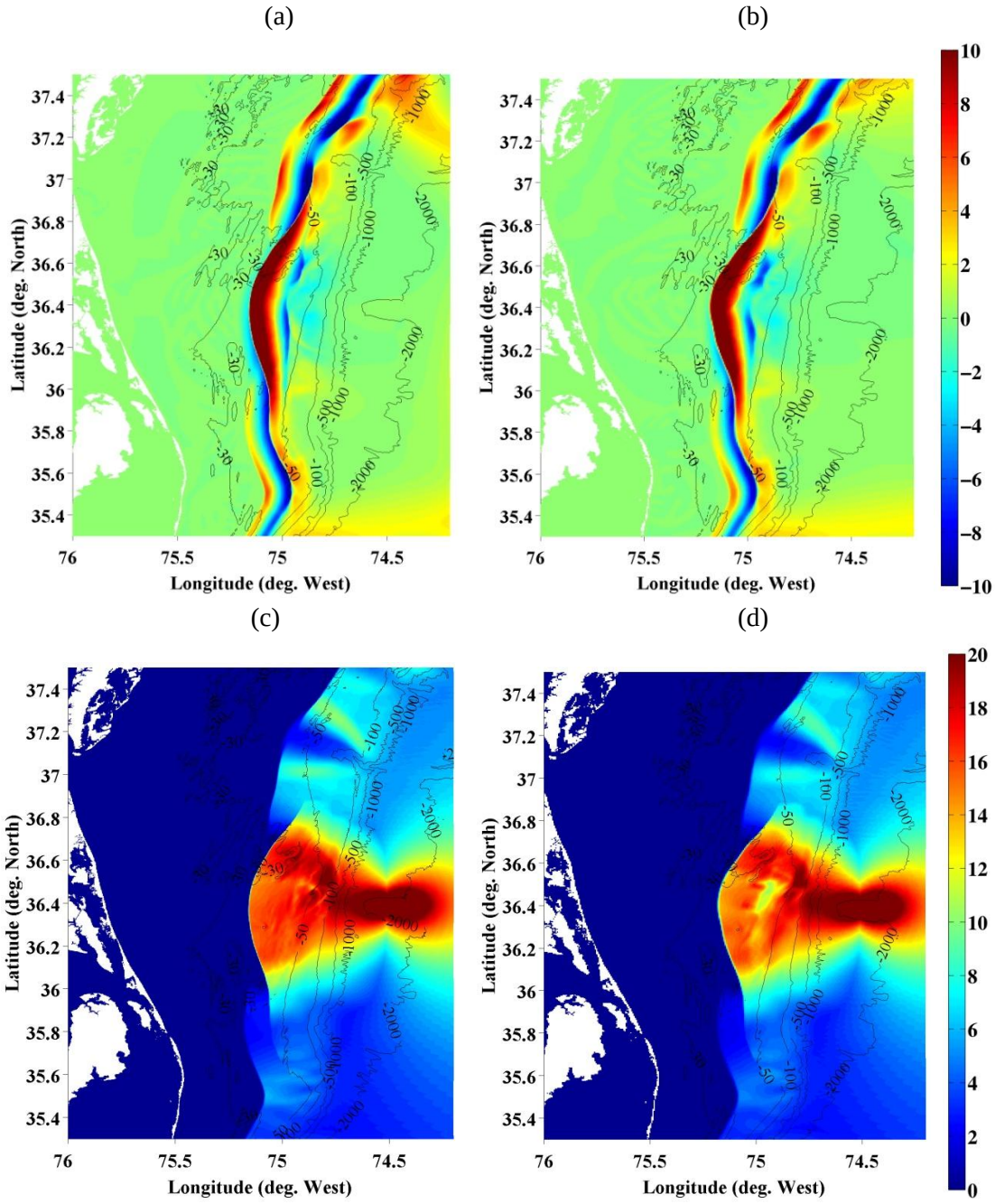

Figure 2.12 Instantaneous (a,b) and maximum (c,d) surface elevations (color scale is in meter) in simulations of the Currituck SMF tsunami, at t = 2000 s (33.3 min) after SMF triggering, computed using (C_d = 0; 500 m horizontal grid): (a,c) FNW; (b,d): NHW (with 3 σ-layers). FNW is initialized from NHW results computed at 800 s (13.3 min;Figure 2.7). Results are shown in zoomed in area of Figure 2.2; bathymetric contours are marked in meter.

shore near Virginia Beach is reduced by a factor of 2 or more, as compared to simulations using C_d = 0.0025. Hence, such large values should not be used for tsunami hazard assessment, unless they can be clearly justified by land use and/or the anticipated amount and size of coastal debris transported by the tsunami flow. This important aspect of modeling tsunami coastal impact will be left out for future work.

Figure 2.13 shows a sequence of instantaneous surface elevations computed with FNW in the 500 m resolution grid, up to t = 99 min, at which time tsunami waves are impacting the entire coastline from North Carolina to Virginia Beach (Figure 2.1). As a result of frequency dispersion, the tsunami wavetrain that propagates towards shore is made up of a series of elevation and depression waves. Specifically, between 82 and 99 min, the leading tsunami waves reach the entire shoreline of the barrier islands south of Virginia Beach, down to the outer banks of North Carolina, causing 5-6 m maximum surface elevations that overtop the barrier island at many locations (Figure 2.13c and d). At 99 min., 2-3 m elevation waves also reach the south of the Delmarva Peninsula eastern shore and the mouth of the Chesapeake Bay (Figure 2.13d). Clearly, however, the 500 m resolution grid used here is insufficient to accurately compute nearshore propagation and coastal tsunami impact (inundation and runup). This is done below in smaller nested grids, with 125 and 32 m resolution.

Figure 2.14a shows the envelope of maximum surface elevation computed in the 500 m FNW grid up to 99 min (same results as in Figure 2.13). As expected for a SMF tsunami (e.g., Tappin et al., 2008), we observe a fairly narrow directional spreading of the largest waves, both onshore and offshore. We also see a fairly large decrease in maximum surface elevation westward, towards shore. This decay is further

illustrated in Figure 2.14b, along an E-W transect, and is due in part to directional spreading of wave energy and in part to dissipation from bottom friction over the wide

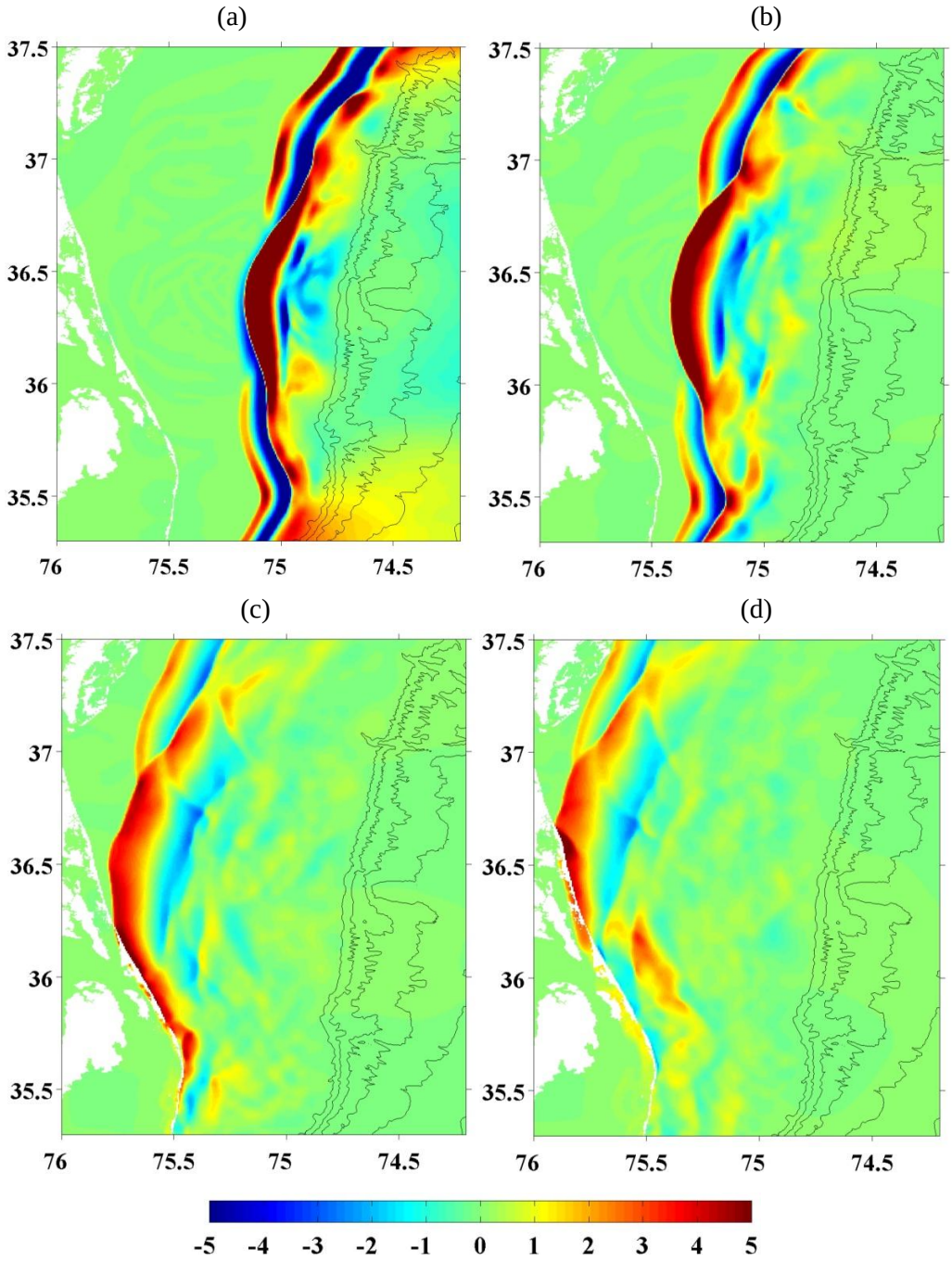

Figure 2.13 Instantaneous surface elevation (color scale is in meters) in FNW simulations of the Currituck SMF tsunami (C_d = 0.0025; 500 m resolution grid), initialized from NHW results at 800 s (C_d = 0; 500 m resolution grid; 3 σ-layers; Figure 2.7), at t = (a) 33; (b) 49; (c) 82; and (d) 99 min. Results are shown in zoomed in area of Figure 2.2; axes are lat (deg. N) and lon (deg. W).

and shallow shelf and, in shallower water, wave breaking closer to shore. Although Geist et al.'s (2009) Currituck source parameters, method of tsunami generation, and grid resolution differ from ours in a number of important aspects, numerical results in their Figure 2.4 can be compared to those in Figure 2.13, which show surface elevations computed at similar times; Figure 2.14 can also be similarly compared to Geist et al.'s (2009) Figures 2.5a,b. Overall, we find a good qualitative agreement between both studies, but our results show more complex wavetrains that also seem to be more influenced by the bottom bathymetry, perhaps in part because of the higher resolution of our simulations (better seen in the next section). We also predict a longer characteristic wavelength of incoming waves than in Geist et al., and a slightly larger leading wave, relative to the rest of the incoming wave field. This longer wavelength and other differences in the generated incoming wave train result from differences in pre-failed SMF reconstruction, wave generation modeling (ours being 3D while theirs is 2D), and model type and resolution, between the present work and Geist et al.'s. While maximum predicted surface elevations are in reasonable agreement nearshore, we also note that the spread of the surface envelope is wider in the present FNW results than in Geist et al.'s study.

Finally, Geist et al. (2009) also pointed out that outgoing (i.e., offshore propagating) waves generated by the Currituck SMF, although initially propagating towards a dominant estward direction, ended up refracting on the northern part of the shelf, causing a large impact along the coast of New Jersey (see their Figure 2.11). We verified that this also occurred in our simulations, by using a larger 800 by 800 km, 1600 by 1600 mesh FNW grid, with identical 500 m resolution (C_d = 0.0025; SW

corner at 32.72 N 79.18 W; 100 km thick sponge layers on the Eastern boundary and 60 km on the southern and northern boundaries). Simulations are again initialized

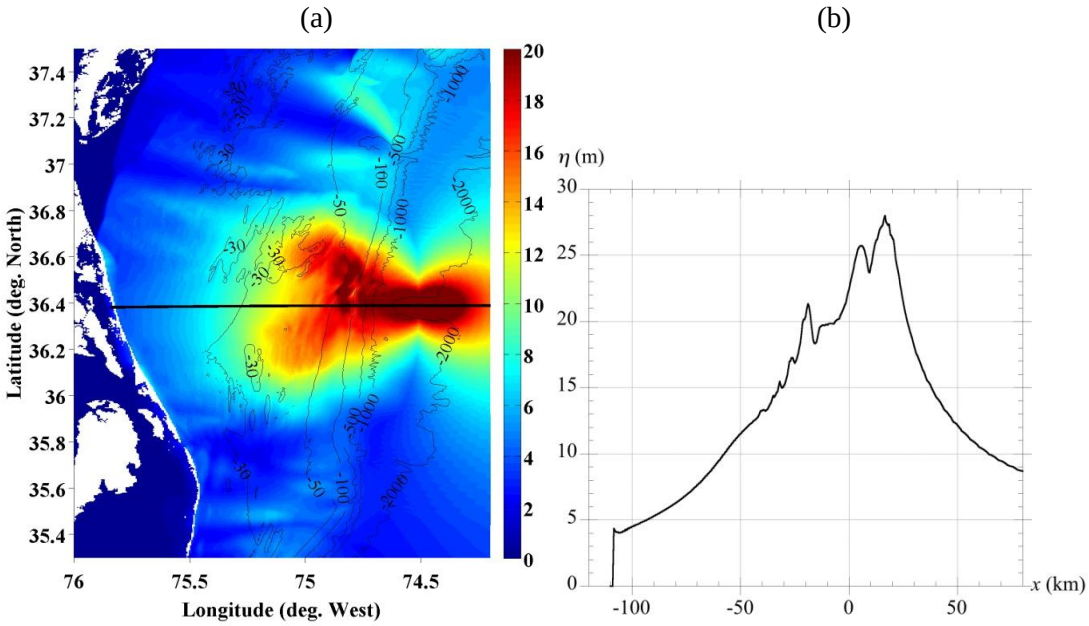

Figure 2.14 Maximum surface elevation in FNW simulations of the Currituck SMF tsunami, up to t = 99 min (C_d = 0.0025; 500 m resolution grid): (a) over the entire 500 m resolution grid (elevation color scale in meter and bathymetric contours in meter); (b) along an E-W transect (marked by the black solid line in (a)) through the SMF center, in the direction of the Curritck Banks, as a function of the distance to the SMF center.

from NHW results at t = 13.3 min (with 3 σ layers; C_d = 0. Figure 2.15 shows the instantaneous surface elevations computed at 55 min, at which time some of the smaller waves that were initially propagating offshore in the smaller domain (e.g., Figure 2.7d; northern part of the outgoing cylindrical wave) have been bent to the north by refraction into propagating onshore, over the continental shelf slope and shelf. For the NTHMP tsunami inundation mapping work, this indicates that simulations in nested grids of the 4 SMF sources (Figure 2.1) should be initiated in a large enough domain (even larger than used in Figure 2.15), to accurately capture such wave refraction effects.

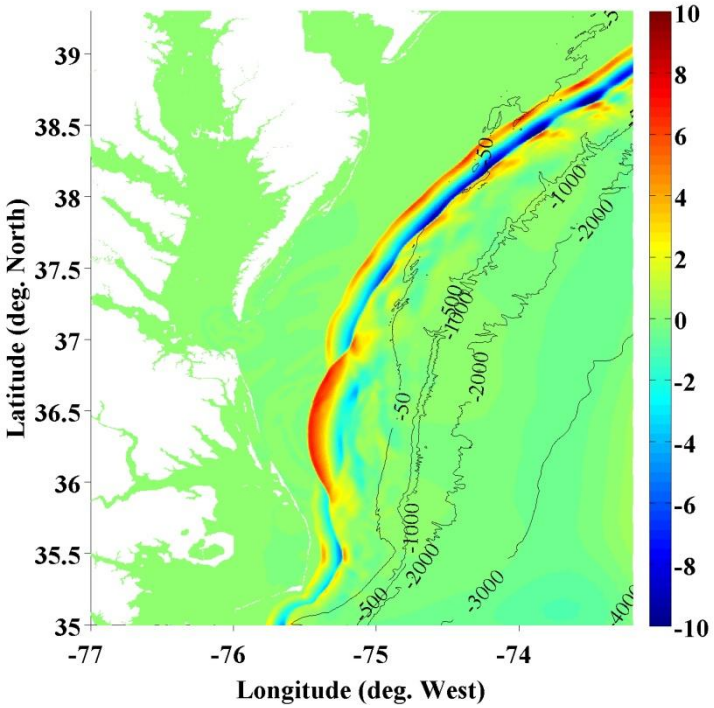

Figure 2.15 Same FNW computations as in Figure 2.13, but over a larger 500 m resolution grid (800 by 800 km; 1600 by 1600 grid; C_d = 0.0025; SW corner at 32.72 N 79.18 W), in order to better simulate wave refraction over the northern continental slope off of New Jersey.

3.5.2 Fine grid nearshore simulations off of Virginia Beach and in the Chesapeake Bay

Using FNW in finer resolution nested grids, we compute in greater detail the impact caused by the Currituck SMF tsunami on the nearest most affected coastal areas around Virginia Beach (36.8 N) and the mouth of the Chesapeake Bay (37 N). Besides the interest of better assessing coastal tsunami impact than in the coarser regional grid, these simulations will validate the one-way coupled computations in nested grids, which will also be used for tsunami hazard assessment along the entire USEC. The reference level in these simulations is the so-called "sea level", defined by NOAA-NGDC as approximately the Mean Low Low tide (MLLT) level. By contrast, in the SMF tsunami hazard assessment, we will perform for the USEC, using the 4

SMF proxies, the reference level in the finer coastal grids will be increased to mean high water (MHW) level.

Simulations are performed with FNW in 125 m and 32 m resolution nested grids, located on the shelf, west of the source area (Figure 2.16). Due to the fairly narrow incident wave train at this stage, simulations in the 125 m resolution grid are initialized (for this case only) by interpolating FNW 500 m resolution grid results (surface elevation and current), once salient waves have completely entered the finer grid; simulations in the next level of nesting (32 m resolution grid) will then be pursued by one-way coupling. Initialization was deemed acceptable at t = 26.6 min, which is the time of the instantaneous surface elevation shown in Figure 2.16 (as computed in the 500 m resolution grid). Simulations in the 32 m resolution grid will be forced along the boundary, from time series computed in the 125 m resolution grid results, also starting at t = 26.6 min.

More specifically, Figure 2.16 shows the footprint of the 500 m FNW regional grid (900 x 800 mesh; 450 by 400 km; see also Figure 2.2). The 125 m resolution grid is defined on the west side of this grid (marked by a vertical solid line in the figure (1997 x 3197 mesh; 160 by 400 km; SW corner located at 76.8 W and 34.6 N, as for the 500 m resolution grid). The footprint of the 32 m resolution grid is marked by the smaller dashed box located within the 125 m resolution grid (3565 x 2913 mesh; 111.4 by 91 km; SW corner located at 76.57 W and 36.75 N). Sponge layers in the 125 m resolution grid are 60 km thick on the eastern boundary and 50 km thick on the northern and southern boundaries. Results will show that the northern and southern tsunami wave tails are properly damped in the sponge layers, while the main westward

propagating tsunami waves, which dominate hazard for Virginia Beach and the Chesapeake Bay, are not affected. No sponge layers are needed in the 32 m resolution grid since both incident and reflected waves are included in the time series used as boundary conditions, which hence satisfies the offshore open boundary conditions. Computations in the 125 and 32 m resolution grids are run from t = 26.6-250 min, to make sure that wave reflection off the various coastal boundaries is accounted for in time series used in the 32 m resolution grid, thus fully satisfying the open boundary conditions. This approach was successfully used to simulate the Tohoku 2011 tsunami with 3 levels of nesting (Grilli et al., 2013b).

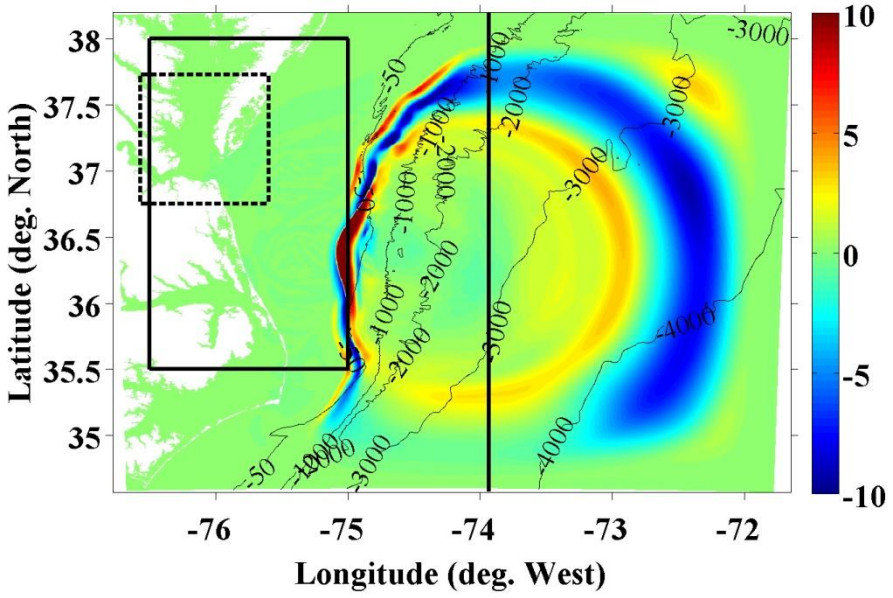

Figure 2.16 Free surface elevation (color scale is in meters) at t = 26.6 min in FNW simulations of the Currituck SMF tsunami (in 450x400 km area, 500 m resolution grid; C_d = 0.0025; initialized at 13.3 min from NHW 500 m resolution grid results). At this time, simulations are initialized in the 125 m (to the left of the black line at 73.9 W) and restarted in the 32 m (dashed black box), resolution grids. The black box is the zoomed in area used to show results in Figure 2.17 and Figure 2.19. Bathymetric contours are marked in meter.

Results of simulations in the 125 m and 32 m resolution grids are shown in Figure 2.17 to Figure 2.20. The black box in Figure 2.16 (76.5-75 W and 35.5-38 N)

marks the zoomed in area used in Figure 2.17 and Figure 2.19 to show 125 m resolution grid results, centered around Virginia Beach and the mouth of the Chesapeake Bay. Figure 2.17 shows a time sequence of instantaneous free surface elevation, computed from t = 26.6 to 200.6 min in the 125 m resolution grid. Over this time, the tsunami propagates both westward towards the North Carolina and Virginia Beach coastlines as well as northwestward into the Chesapeake Bay. We note that Figure 2.17b approximately corresponds to the surface elevation computed in the 500 m resolution grid shown in Figure 2.13c. Clearly, wave patterns and surface elevations appear to be very similar, although, as expected, more details can be seen in the 125 m resolution grid results. The good agreement between 125 and 500 m resolution grid results is further confirmed in Figure 2.18, which compares surface elevation computed along an E-W transect through the SMF center (marked in Figure 2.17a).

Differences between 125 m and 500 m resolution grid results, as could be expected (Grilli et al., 2013a), are mostly: (i) a steeper front of the leading wave; and (ii) higher-frequency oscillations in the trailing oscillatory tail of the tsunami wave train. Note that profiles (b,d,f) shown along the transect correspond to the times of Figure 2.17a,b,c, respectively.

Regarding coastal tsunami impact, towards the end of simulations in Figure 2.17 and Figure 2.18, the entire barrier island from Virginia Beach to the south of it, is overtopped by waves of over 5 m elevation; maximum tsunami impact occurs in Virginia Beach at t = 116 min (Figure 2.17c). For later times, the tsunami floods inland areas around Virginia Beach and further south, while large waves also propagate into the Chesapeake Bay. In particular, refraction north of Virginia Beach

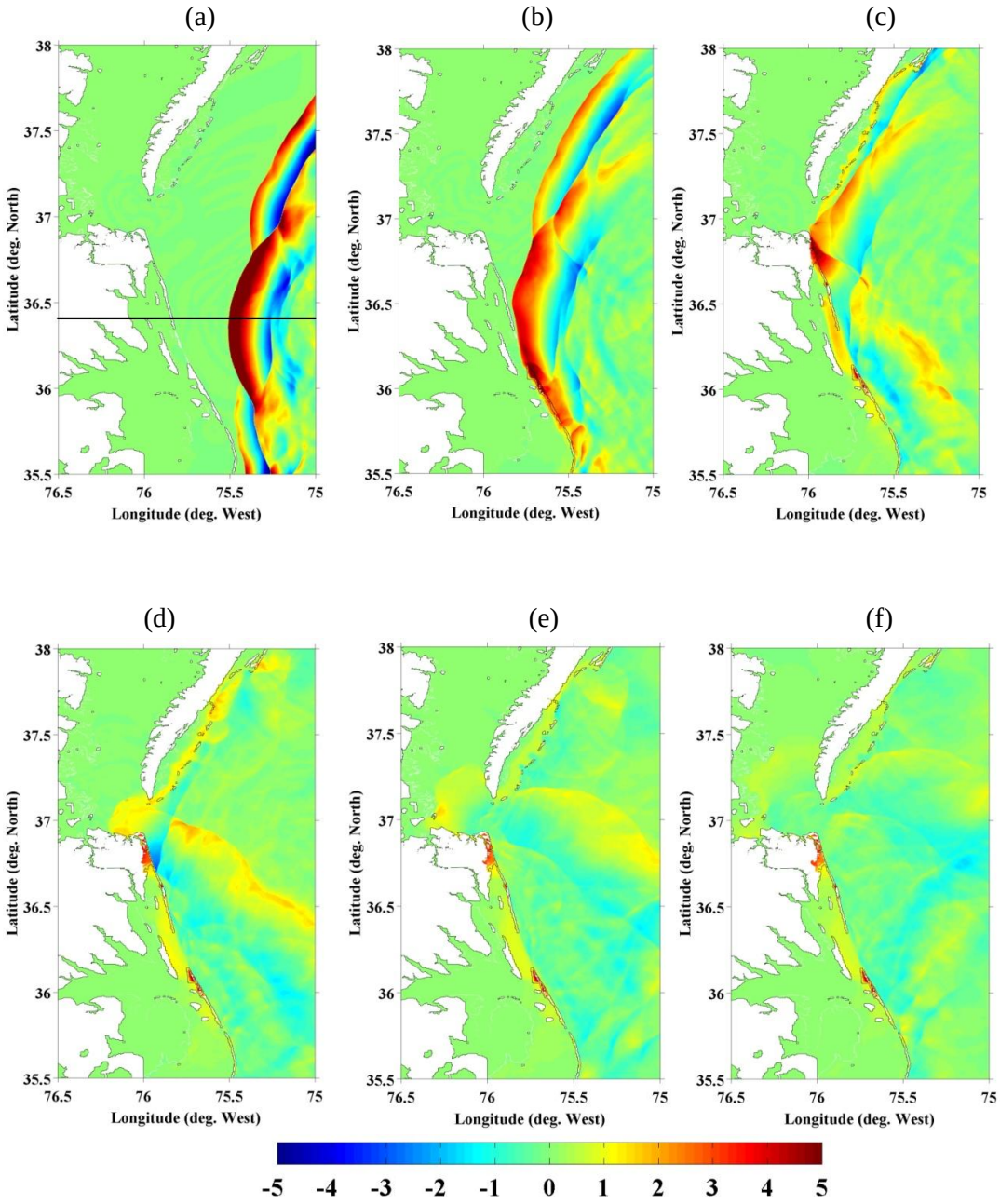

Figure 2.17 Instantaneous surface elevation (color scale in meters) in FNW simulations of the Currituck SMF tsunami in the 125 m resolution grid (C_d = 0.0025) (Figure 2.16), initialized at 26.6 min from FNW 500 m resolution grid results. Results are shown over the zoomed in area marked in Figure 2.16, at t = (a) 56.6; (b) 86.6; (c) 116.6; (d) 146.6; (e) 176.6; and (f) 200.6 min. The black solid line in panel (a) marks the E-W transect in the direction of Currituck Banks, where results are shown in Figure 2.18.

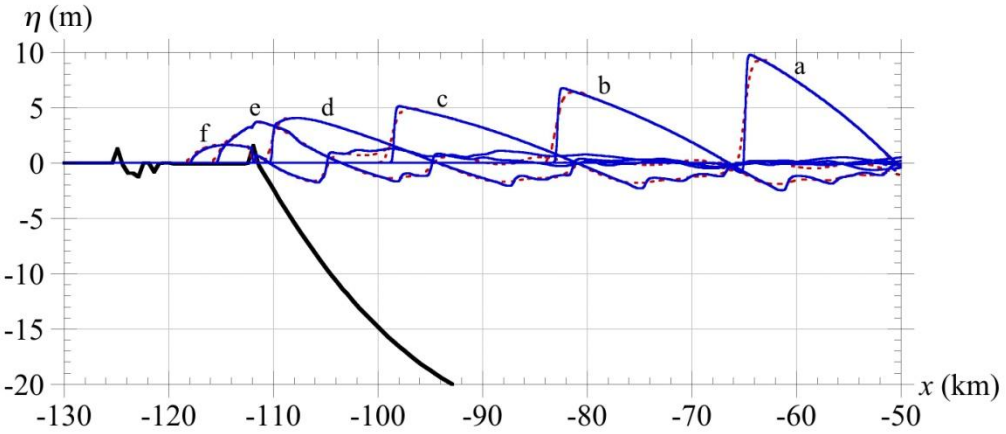

Figure 2.18 Comparison of instantaneous surface elevations in FNW simulations of the Currituck SMF tsunami (C_d = 0.0025) along an E-W transect through the SMF center (36.39 N lat.; Figure 2.17a), as a function of the distance to the center of the SMF, in 125 m (—) and500 m (- - -) grids. Computations are initialized in the 500 m resolution grid from NHW 500 m resolution grid results at 13.3 min, and in the 125 m resolution grid from 500 m FNW resolution grid results at 26.6 min. Surface profiles are shown at t = (a) 41.6; (b) 56.6; (c) 71.6; (d) 86.6; (e) 101.6; and (f) 116.6 min; (—) denotes the ocean depth.

causes waves to be diverted around the headland and impact the Norfolk area with 2-3 m surface elevations (Figure 2.17d). This can also be seen in the maximum surface elevations shown in Figure 2.19, where the Virginia Beach-Norfolk area is flooded with 3-6 m inundation. Maximum surface elevations at the mouth of the Chesapeake Bay are about 3 m. The 125 m resolution grid resolution, however, is not sufficient to properly resolve both small scale coastal morphology features and shorter higher-frequency waves that would be generated near the front of leading tsunami wave crests (i.e., dispersive shock waves; see Geist et al., 2009, Figure 2.12 and Grilli et al., 2013a, Figure 2.10). This would require grid resolutions of 10 m or less and will be the object of future work, planned in the Virginia Beach-Norfolk area as part of NTHMP.

Tsunami propagation into the Chesapeake Bay is nevertheless further analyzed here in the finer 32 m resolution grid. Figure 2.19 compares maximum surface

elevations computed in the 125 and 32 m resolution grids and, in particular for the latter, shows the significant extent of inundated areas, both along the ocean exposed shores and inside the Bay (compare maximum penetration of the inundation to the zero-level shoreline shown as a black contour), although surface elevations appear to rapidly decrease as the tsunami propagates into the Bay. In this respect, Figure 2.20 compares surface elevations computed in both 125 and 32 m grids along a transect into the Bay (marked in Figure 2.19), for the same time sequence as in Figure 2.17. While the tsunami elevations reach nearly 7 m over the shelf, they reduce to 3 m at the mouth of the Bay (x = 0 here) and then to 1 m further inside the fairly shallow Bay. Figure 2.20b compares results computed in the 125 and 32 m resolution grids for 5 times; while there are shorter wavelength waves resolved in the 32 m resolution grid

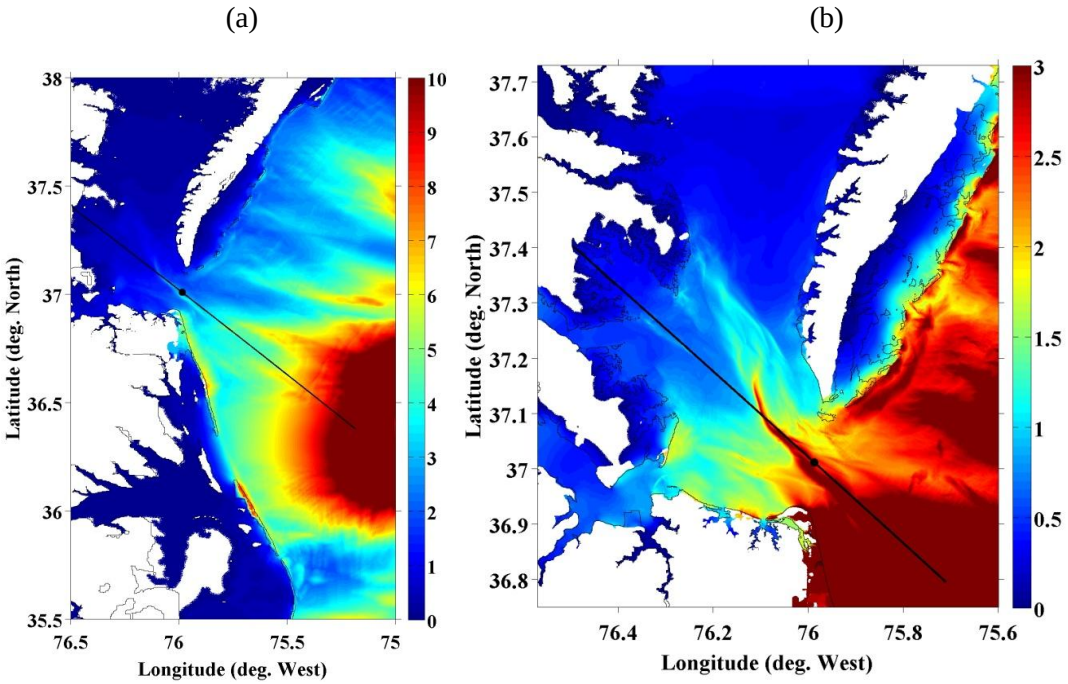

Figure 2.19 Maximum surface elevation (color scale is in meters) up to t = 250 min, in FNW simulations of the Currituck SMF tsunami (C_d = 0.0025): (a) in the 125 m resolution grid (Figure 2.16, Figure 2.17; results are shown over the zoomed in area marked in Figure 2.16); (b) in the 32 m resolution grid (Figure 2.16). The black lines mark the location of a transect used for showing surface elevation in Figure 2.20 (x = 0 is marked by a black dot). The zero-elevation shoreline is marked as a black contour level in both figures, showing the extent of flooding.

results, surface elevations are essentially identical, although there is a space/time lag between both grid results. Because of the shallowness and complex bathymetry of the Bay, results in the 32 m resolution grid are expected to be more accurate, particularly, for predicting details of maximum inundation along the complex shoreline, as also seen in Figure 2.19b.

4 Simulation of SMF tsunami hazard along upper USEC for NTHMP

4.1 SMF source selection and sediment availability in study area

As discussed in the introduction, as part of tsunami inundation mapping work done for NTHMP, SMF tsunami hazard is assessed along the upper USEC using SMF proxies similar to the historical Currituck slide (Figure 2.2). These tsunamis represent worst-case scenarios equivalent to the probable maximum SMF tsunami in the region from Virginia to Cape Cod. These SMFs were sited on the basis of: (i) earlier geotechnical work and slope stability analyses based on Monte Carlo simulations (MCS; Grilli et al., 2009; Krause, 2011); and (ii) actual field data on sediment and sub-bottom profiles (Eggeling, 2012). This led to selecting four areas, marked in Figure 2.1 as Study Areas 1 to 4, which have a clear potential for large tsunamigenic SMF sources, both in terms of low slope stability safety factors and sufficient sediment availability for causing large SMFs. Among those, Grilli et al.'s (2009) MCS results (their Figure 2.18) indicated that Areas 3 and 4, which are located off of Atlantic City, NJ, have the highest potential for tsunamigenic SMFs. In addition to this area, MCS results also identified an increased tsunami risk off of the Hudson River

estuary and the Long Island southern coastline, which correspond to SMFs occurring approximately within Study Areas 1 and 2.

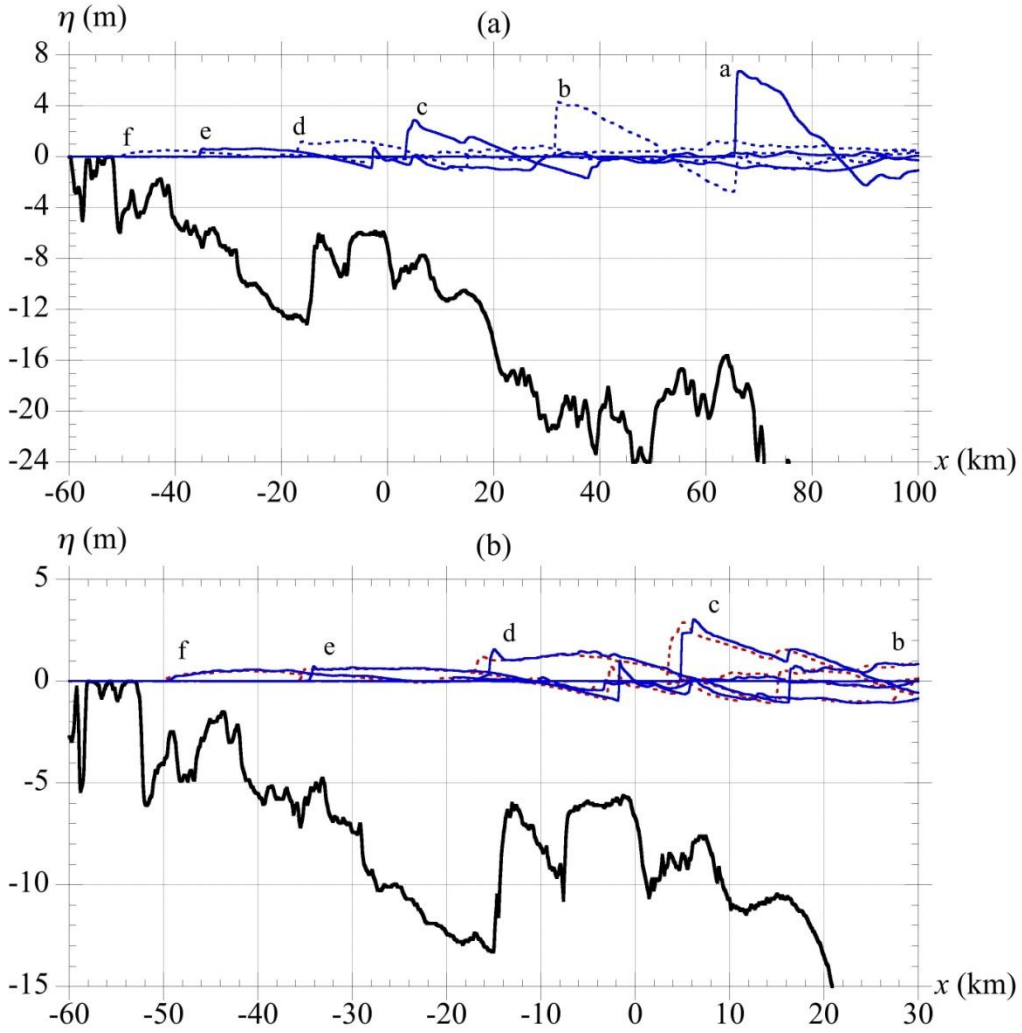

Figure 2.20 Instantaneous surface elevation in FNW simulations of the Currituck SMF tsunami (C_d = 0.0025), along the transect marked in Figure 2.19 (x = 0 at the mouth of the Chesapeake Bay): (a) in the 125 m resolution grid (—, - - -); and (b) in the 32 m (—) and 125 m (- - -) resolution grids (Figure 2.16). Surface profiles are shown at times: t = (a) 56.6; (b) 86.6; (c) 116.6; (d) 146.6; (e) 176.6; and (f) 200.6 min.

More specifically, Eggeling's (2012) analysis of sediment availability in the 4 study areas concluded that Area 1, in the Hudson Apron (Figure 2.1 and Figure 2.21a), is characterized by large soil deposits, because it has experienced high sedimentation

rates during the Pleistocene. Since most landslides along the U.S. Atlantic continental margin consist primarily of Quaternary sediment (a combination of Pleistocene and Holocene sediment), this site likely contains enough sediment for a Currituck volume SMF to occur. In Area 2, which is located southwest of Ryan Canyon (Figure 2.1 and Figure 2.21b), Eggeling (2012) reported that, on the basis of a cross-slope survey, there is sufficient sediment available to cause a 20 km wide SMF; hence this area likely also has both appropriate and thick enough sediment for a Currituck SMF proxy to occur. In Areas 3 and 4 (Figure 2.1 and Figure 2.21c,d), which are located in the Baltimore Canyon, results of deep drilling from the USGS indicate that there is a substantial thickness of Quaternary sediment (J. Chaytor, personal communication, 2013, USGS). However, in some locations, sediment thickness does not exceed ~100 m, as can be seen in cross-slope transects made through these areas, which show several hills 3 to 5 km wide, with a vertical distance between peaks and valleys of roughly 200 to 400 meters (Figure 2.23). Assessing whether the amount of sediment available is sufficient for a Currituck size SMF is difficult at these two locations, as the continuous action of down slope processes along the mid and north US Atlantic margins leads to variable along slope thicknesses on a ridge to ridge scale (J. Chaytor, personal communication, 2013, USGS). Despite these uncertainties, and consistent with the PMT approach adopted in this NTHMP work, we assumed that a failure of volume sufficient for a Currituck SMF proxy could extend slightly deeper than the available sediment accumulation in these study areas, thus representing multiple ridges failing at once.

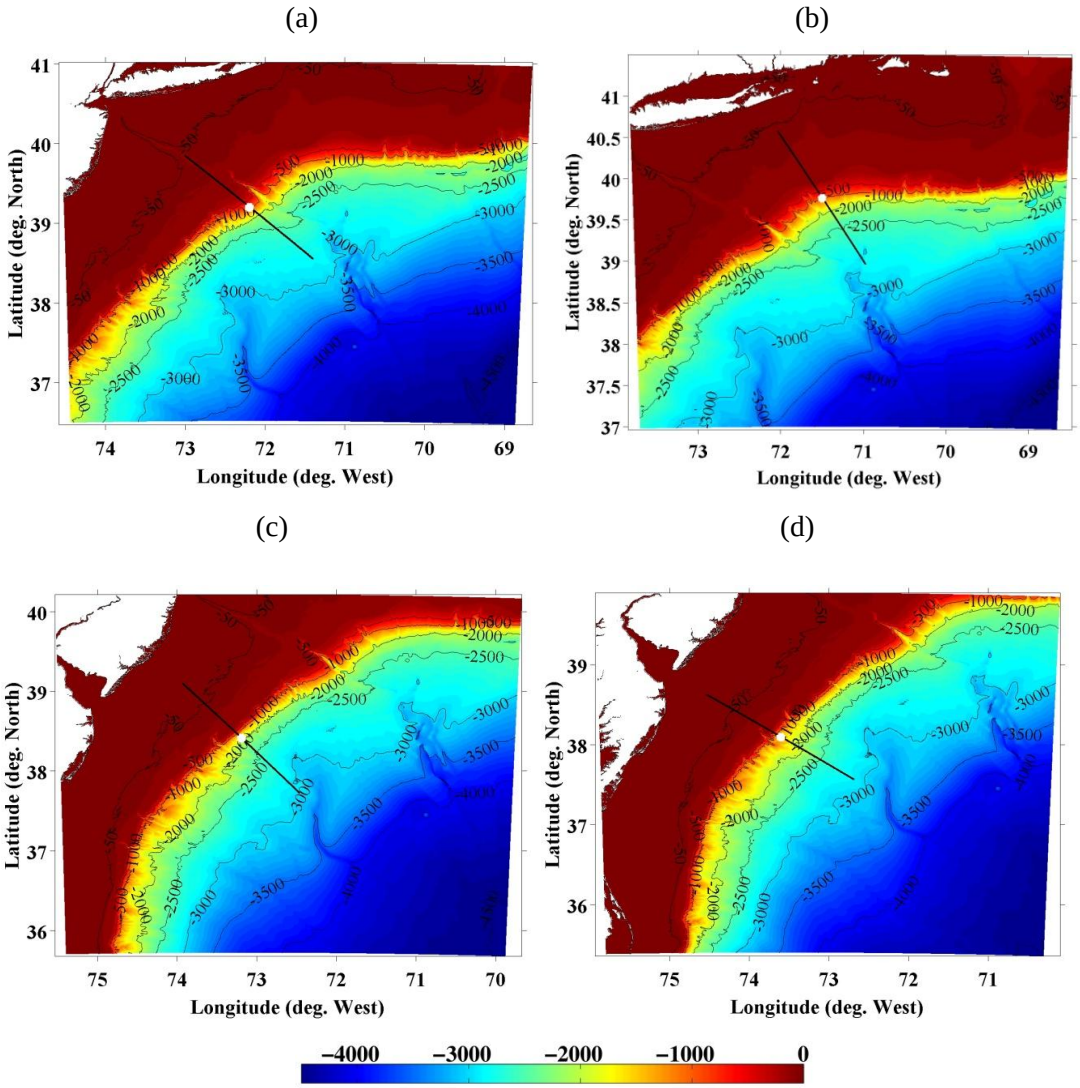

Figure 2.21 Bathymetry (color scales and contours in meter) in Study Areas (Figure 2.1): (a) 1; (b) 2; (c) 3; and (d) 4; (—) mark locations of transects in SMF direction of motion θ, through SMF centers, shown in Figure 2.22, and white dots mark the initial center of mass initial (x_0, y_0) of each SMF proxy (Table 2.1).

4.2 Simulation of tsunami sources for Currituck SMF proxies in study Areas 1-4

Figure 2.21a-d shows the bathymetry near and around study Areas 1-4, in which Currituck SMF proxies were sited to assess tsunami hazard along the upper USEC. [Note that several small spurious steps in the bathymetry were observed, which were removed using a filtering function prior to performing tsunami simulations.] The

white dots in the figures mark the four SMF proxy initial center of mass locations (x_0, y_0), and the black lines are transects through each center, in the selected azimuthal direction of SMF motion θ; for each site, both of these were inferred from seafloor morphology. Specific parameters for each SMF, which all correspond to Currituck proxies of same length, width and thickness, as well as information on numerical grids used in NHW simulations are listed in Table 2.1.

More specifically, in light of the historical Currituck event detailed before, the location (x_0, y_0) of each SMF proxy was selected in their respective area as a function of local seafloor morphology to replicate the headwall of Currituck Slide 2 (Locat et al., 2009), where ~150 to 200 m of sediment were removed by the landslide at the 500 m post-excavation depth location. Based on these, the assumed direction of motion θ and Quasi-Gaussian shape of each SMF (Figure 2.3 and Eqs. (1-2)), their initial bathymetry was constructed for each site. The resulting main SMF cross-sections along each transect marked in Figure 2.21a-d are shown in Figure 2.22a-d; in the latter figures, we see that despite having the same overall dimensions, each SMF, once place in its site-specific location, has quite a different cross-section.

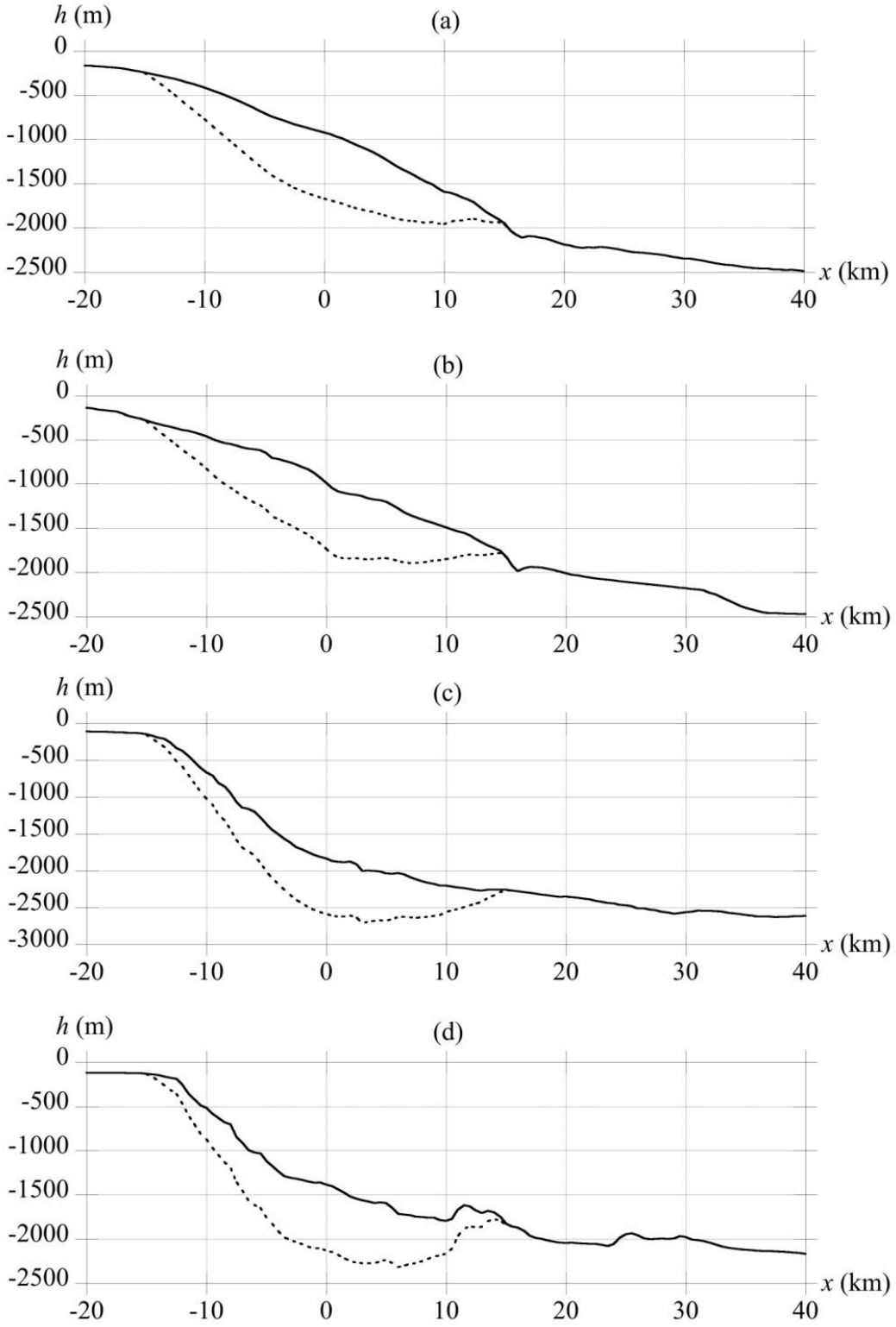

Figure 2.22 Transects through SMF proxy centers (x0, y0) in azimuthal direction θ (Table 2.1) in Study Areas (Figure 2.1, Figure 2.21): (a) 1; (b) 2; (c) 3; and (d) 4; (—) current bathymetry; (- - -) cross-section of a Currituck SMF proxy (at time *t = 0* in simulations).

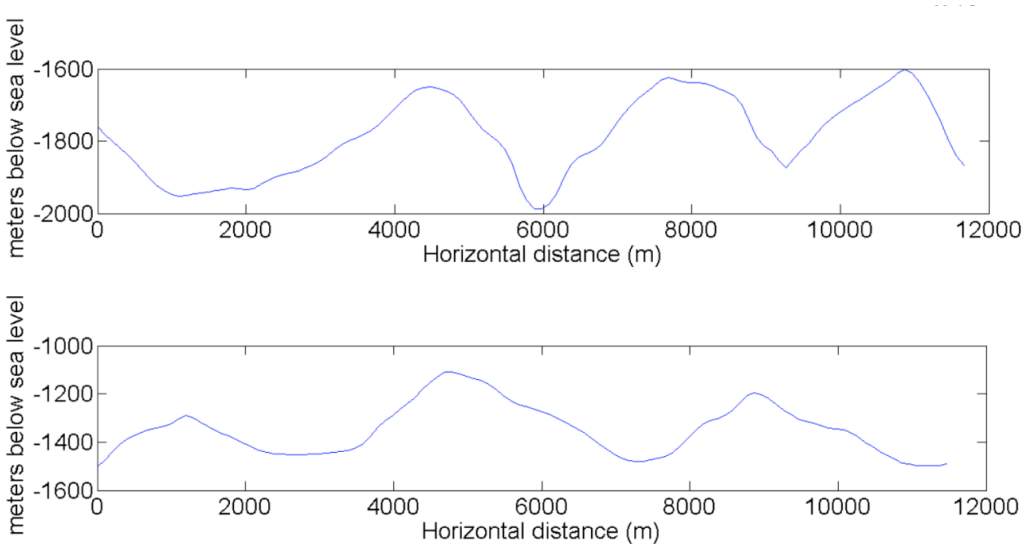

Figure 2.23 Cross-slope bathymetric transects in Areas 3 (top) and 4 (bottom) (Figure 2.1, Figure 2.21c,d), from Eggeling (2012).

Table 2-1 Parameters (see Eqs. (1-7) for parameter definitions) of the actual Currituck SMF and of SMF proxies used in selected study Areas 1-4 (Figure 2.1 and Figure 2.21), and horizontal footprint of grids used in NHW simulations if SMF sources.

SMF and grid	Currituck SMF	Study Area 1	Study Area 2	Study Area 3	Study Area 4
Grid lg. N (km)	400	500	500	500	500
Grid lg. E (km)	450	500	450	500	500
Grid SW corner	34.6N, 76.8W	36.5N, 74.6W	36.9N, 73.9W	35.7N, 75.5W	35.4N, 75.9W
SMF *T* (m)	750	750	750	750	750
SMF *b* (km)	30	30	30	30	30
SMF *w* (km)	20	20	20	20	20
Avg. slope (deg)	4	4	4	4	4
SMF center of mass (x_0, y_0)	36.39N, 74.61W	39.19N, 72.19W	39.76N, 71.49W	38.41N, 73.19W	38.09N, 73.60W
θ (deg. North)	90	136	153	140	126
s_f (km)	15.8	15.8	15.8	15.8	15.8
t_f (s)	710	710	710	710	710

Owing to the similarity of the bathymetric gradient in all selected areas (see depth contours in, e.g., Figure 2.1), an identical average slope of α= 4 deg. was used as the representative continental shelf slope for each site, to be used in Eq. (4). For

each SMF, the kinematics *s(t)* is computed by Eqs. (3-7), using parameters listed in Table 2.1. Since all the parameters governing each SMF proxy's motion are identical, runout and total time of motion are also identical for the 4 SMFs, i.e., s_f = 15.8 km and t_f = 710 s (Table 2.1). Based on these values, NHW (3 σ-layers; C_d = 0) was run to compute each SMF tsunami source, for 13.3 min (800 s) in 4 separate 500 m resolution grids whose footprints are marked in Figure 2.24 (Table 2.1), yielding the simulated surface elevations shown in Figure 2.24a-d. The figure shows that the initial features of each tsunami source are qualitatively identical, although, as expected, there are differences in surface elevation and dominant direction of wave propagation, due to site-specific effects of bathymetry on wave generation and propagation.

NHW results are then used to initialize many additional simulations of tsunami propagation with FNW (C_d = 0.0025), in a series of finer nested coastal grids, in order to compute tsunami inundation maps along the USEC. These FNW simulations all start in the 500 m Cartesian grid shown in Figure 2.25 (upper left panel), where each SMF tsunami source is specified one at a time, but then the next level of nesting, in 122 m resolution grids, is different for each sector of the upper USEC, each corresponding to a high resolution NOAA-NGDC DEM (see red boxes Figure 2.25, upper left panel). Full simulations have been completed to date for 6 such sectors/DEMs, of which due to lack of space we only provide detailed results in the next section, as an illustration, for the very exposed Ocean City, MD area. The final high-resolution inundation maps for the entire upper USEC will be posted on NOAA-NTHMP's website at the completion of this project.

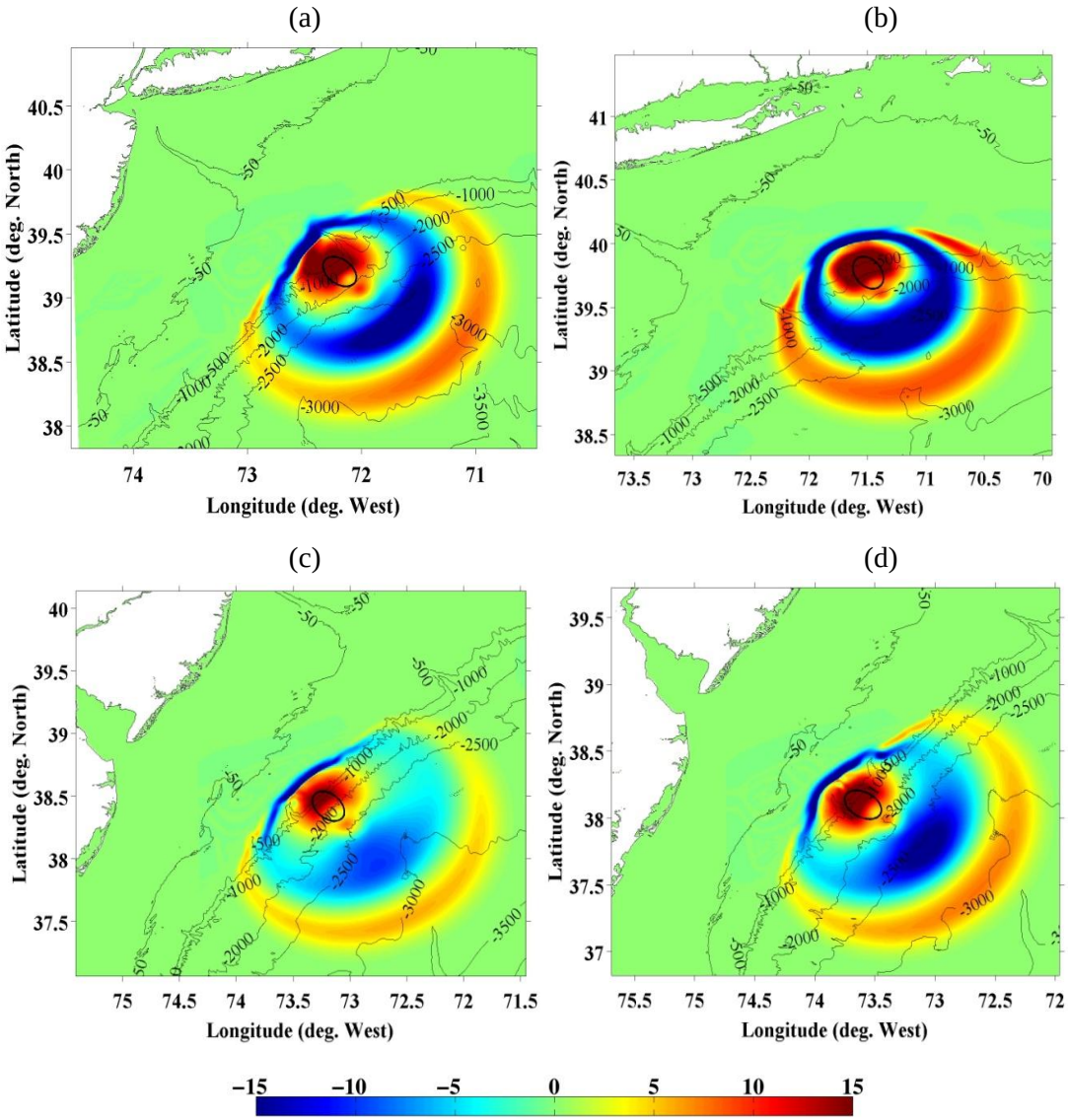

Figure 2.24 Surface elevation (color scale in meter) of tsunami sources, for 4 SMF proxies whose initial footprint is marked by a black ellipse, simulated with NHW (500 m resolution grids with 3 σ-layers, C_d = 0) in 4 selected areas (Figure 2.1 and Figure 2.21): (a) 1; (b) 2; (c) 3; and (d) 4. Results are shown at 13.3 min after SMF triggering (after the SMFs have stopped moving). SMF sources in areas 1-4 are parameterized as Currituck proxies (Figure 2.22 and parameters in Table 2.1). Bathymetric contours are marked in meter.

4.3 Detailed modeling of SMF tsunami inundation mapping in Ocean City, MD area

As discussed in the introduction, as part of the NTHMP inundation mapping activity along the USEC, both far-field and near-field SMF tsunami sources are considered, but only the work dealing with SMF tsunami hazard is reported here.

Thus, in the following, we detail simulations performed with FNW for the Ocean City, MD sector/DEM, to develop high-resolution inundation maps resulting from the impact of the 4 SMF tsunami sources computed above (Figure 2.24). To do so, we first define a series of nested Cartesian grids, from an initial 500 m grid in which SMF sources are specified down to many high resolution 10 m grids, in which inundation depth and other products are computed (Figure 2.25); to ensure good accuracy and stability of these one-way coupled simulations, the ratio of grid mesh size between two successive nesting levels is limited to around 4. To define bathymetry/ topography in each nested grid, for each particular resolution, we use commensurately accurate data interpolated from: (i) ETOPO-1 1 arc-min and NOAA-CRM 3 arc-sec data in deeper water and over the shelf; and (ii) nearshore, from NOAA-NGDC Ocean City 1/3 arc-sec DEM (Grothe et al., 2010). As shown in Figure 2.25, this DEM covers a major area of the Delmarva Peninsula, from the southern part of Delaware Bay down to Metompkin Bay in Virginia. The DEM datum for these simulations is set to mean high water (MHW).

The nested FNW Cartesian grids are all shown in Figure 2.25, i.e.: (i) a 1500 x1500 mesh, 500 m resolution grid, in which the 4 SMF proxy sources of Figure 2.24 (marked by green dots in the upper left panel) are specified as initial conditions (one at

a time); (ii) the “Ocean City DEM” grid, a 627x1072 mesh, 122 m resolution nested grid (red box in right panel; (iii) Grids OC-1 to OC-4, 750x1000 mesh, 31 m resolution grids (right panel); and (iv) a few finer 1080x1620 mesh, 10 m resolution grids defined in areas of greatest interest or impact. Only the 500 m grid has sponge layers, and the 122 and 31 m grids are used in one-way coupling simulations

Simulations of the 4 SMF proxies in the 500 m grid (not detailed here) indicate that the SMF sited in Area 4, which is the closest to Ocean City, causes maximum impact in the 122 m grid. Hence, only this SMF was used in subsequent inundation mapping for this sector/DEM; note that other SMFs will be dominant in different DEM sectors (not detailed here). Simulations of tsunami propagation are pursued by one way coupling in the 122 m grid (also not detailed here), using time series of surface elevation and depth-averaged current computed in the 500 m grid, as forcing along its ocean exposed boundary (Figure 2.24 and Figure 2.25), and then in the four 31 m resolution nested grids OC-1 to OC-4, for which inundation results are shown in Figure 2.26; in the latter figures, we see that significant areas along the shore would be impacted by over 2 m deep inundation.

One final level of nested simulations is performed in the 10 m grids (Figure 2.25), for some of the most impacted or critical areas. In these highly resolved simulations, besides inundation depth and penetration, we computed other metrics that can be helpful in quantifying tsunami impact, depending on the type of land use or coastal structures that are considered. Figure 2.27 thus shows a map of the tsunami-induced maximum momentum flux (N.m) in the highly developed area of Bethany Beach, DE (Figure 2.25). This metric can be directly related to the magnitude of

impact forces on structures and hence correlates well with the damage level caused by the tsunami to light buildings. Park et al. (2013) have shown that the magnitude and spatial variability of this metric is strongly affected by details of the interaction of overland flow with the ambient physical environment. This level of details is not well reproduced in the standard finest 1/3 arc sec (10 m) NOAA or FEMA DEMs, indicating a continuing need for developing more accurate DEMs and land use information. With those, one could perform even higher-resolution tsunami hazard mapping that could be used for developing zoning regulations at the local level (Yeh et al., 2005).

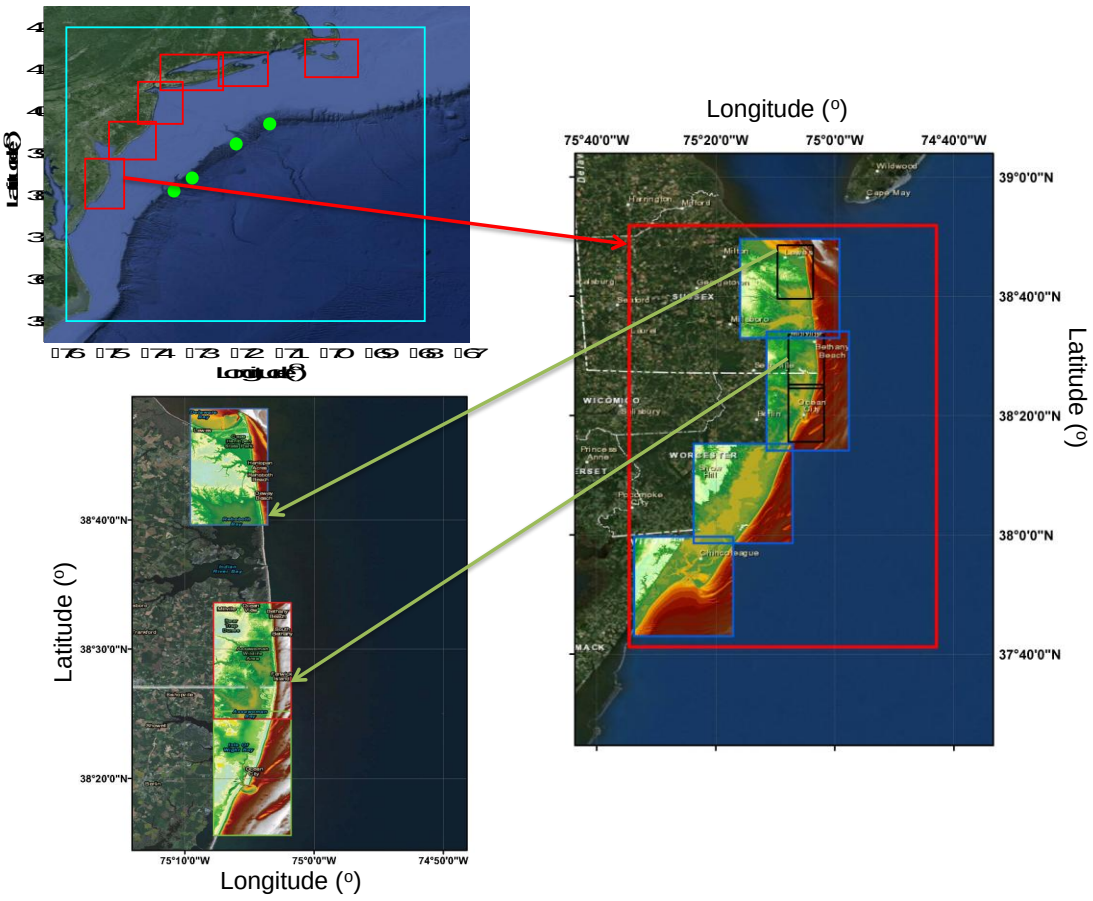

Figure 2.25 FNW nested grids used for detailed inundation mapping along the upper USEC, with details of the Ocean City, MD area. Upper left panel: (blue box) 500 m resolution grid initialized by the 4 SMF proxy sources of Figure 2.24 (marked by green dots); (red boxes) boundary of 122 m resolution grids for each

sector/DEM used so far along USEC, with the lowest being the Ocean City DEM. *Right panel*: (red box) Enlarged area of 122 m Ocean City grid; (blue boxes) 30 m resolution grids OC-1 to OC-4; and (black boxes) finer 10 m resolution grids defined in areas of greatest interest or impact. *Lower left panel*: enlarged areas of two 10 m grids (lower: Bethany Beach area; upper: Lewes area).

Similarly, Figure 2.28 shows a map of maximum tsunami-induced velocity (m/s), an important factor for navigational hazards during a tsunami, in the heavily traveled Indian River Inlet, DE, computed in the Rehoboth Beach 10 m resolution grid (Figure 2.25). Two maps of maximum velocity are presented, one for initially dry land (a) and one for initially wet inland areas (b) (river, pond), which the tsunami inundates. Finally, as a last important metric to quantify coastal tsunami impact, Figure 29 shows a map of tsunami-induced maximum vorticity (1/s), computed around the heavily traveled Ocean City Inlet, in the 10 m resolution Ocean City model grid. We see that, as a result of the tsunami, large eddies are spawned from the jetties, both offshore and onshore of the inlet. Such rotational flow structures are a hazard for navigation and can persist for a long time, even when the main tsunami inundation has receded.

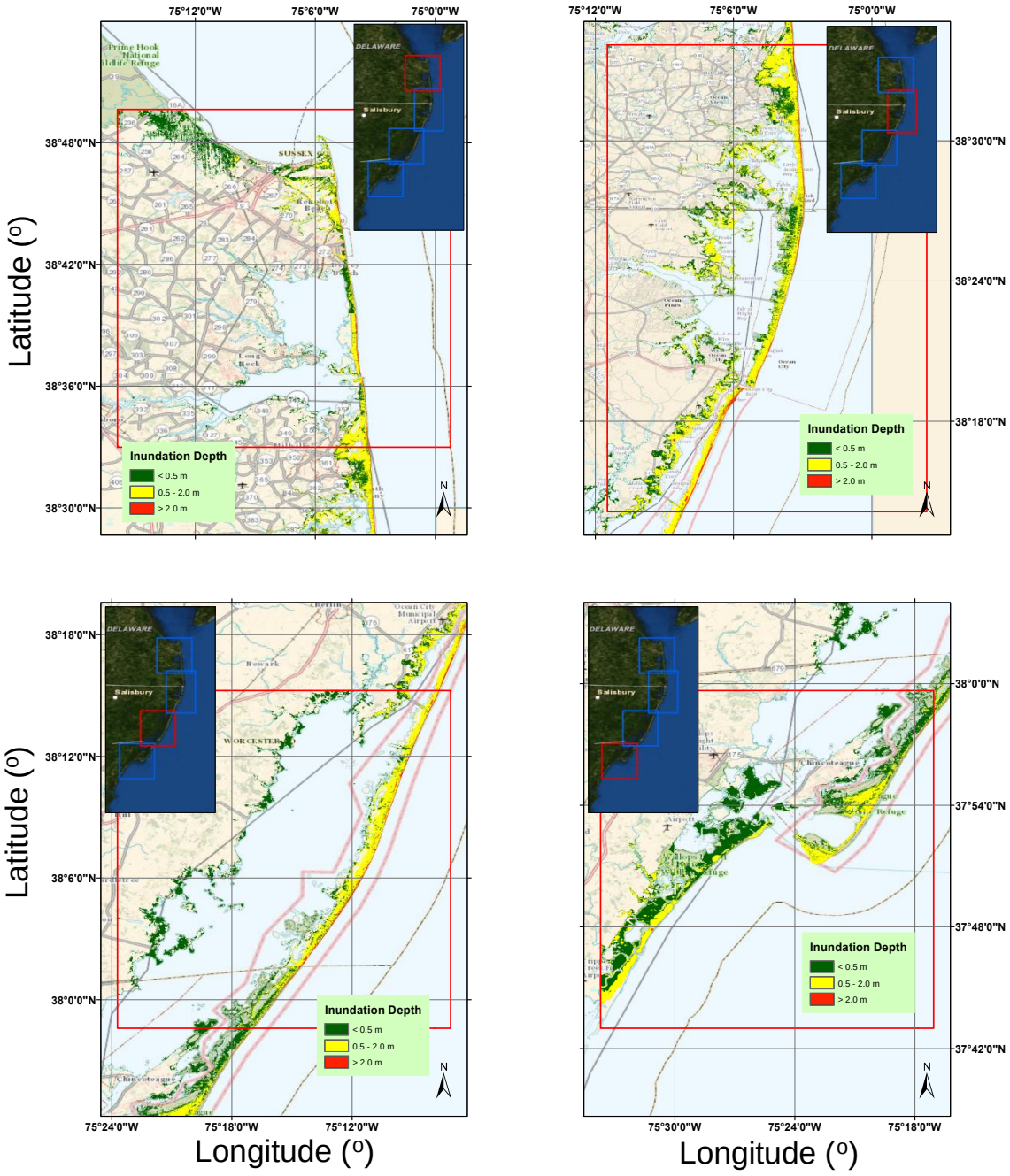

Figure 2.26 Maps of tsunami inundation depth computed with FNW in 31 m resolution Grids OC-1 to OC-4 (see Figure 2.25 and insets for actual locations); one-way coupled simulations are forced on their boundary by time series of surface elevation and currents computed in the 122 m Ocean City grid, for the area 4 SMF proxy (Figure 2.24)

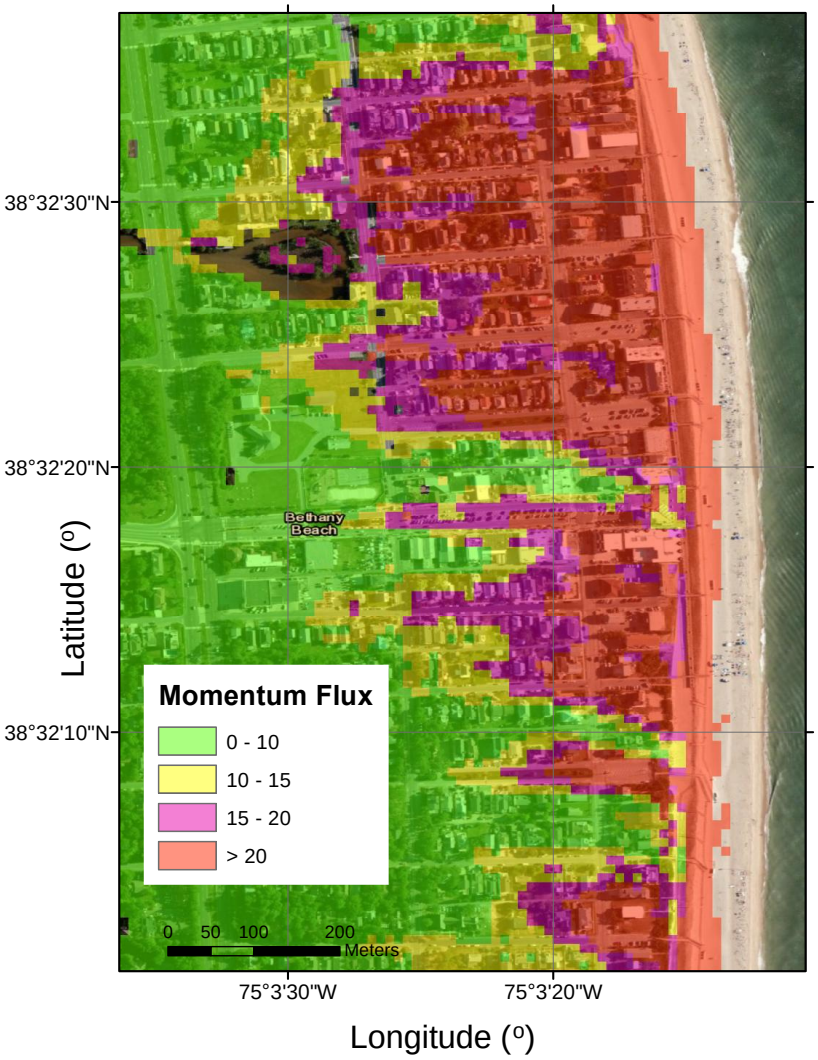

Figure 2.27 Map of tsunami-induced maximum momentum flux (N.m) computed with FNW in 10 m resolution Bethany Beach grid, using results of simulations in 31 m resolution OC-2 grid for the area 4 SMF proxy as forcing along the boundary (Figure 2.24, Figure 2.25).

5 Conclusions

In this paper, we presented both the modeling methodology and results of numerical simulations carried out under the umbrella of the US NTHMP, to develop comprehensive tsunami hazard maps for the upper USEC. While many types of tsunami sources were considered, particularly in the far-field (e.g., Grilli et al., 2010;

Abadie et al., 2012; Harris et al., 2012), here we only reported on coastal tsunami hazard associated with near-field tsunamigenic SMF sources.

In such work, the first important aspect was to properly site and parameterize the potentially tsunamigenic sources, here SMFs, that define the Probable Maximum Tsunamis (PMTs) for the considered areas. Then, for each of the selected sources, simulations of tsunami generation and propagation were performed in a series of nested grids with gradually finer resolution, centered on various areas of interest. Based on these, maps of maximum tsunami inundation and other metrics of tsunami hazard (e.g., flow velocity/vorticity, momentum flux) were constructed.

Tsunami simulations were performed using a combination of two state-of-the-art numerical models, which were validated as part of a NTHMP workshop. SMF tsunami generation was simulated using the 3D non-hydrostatic model NHWAVE (NHW; Ma et al., 2012) and subsequent propagation using the fully nonlinear and dispersive 2D Boussinesq model FUNWAVE-TVD in its Cartesian implementation (FNW; Shi et al., 2012). Both models can accurately simulate the more dispersive wavetrains generated by SMFs. After each SMF had stopped moving, simulations in the coarsest FNW grid (500 m resolution grid) were initialized using the surface elevation and horizontal velocity at the required depth computed with NHW. Then, simulations were pursued with FNW in a series of nested grids, based on a one-way coupling methodology. In the latter, simulations in a finer nested grid level are forced by time series of surface elevation and current, computed along its boundary in the coarser grid level (where the entire simulation has also been performed); this way,

both incident and reflected waves are included in the time series, which automatically satisfy an open boundary condition.

In the absence of sediment data and information on failure mechanisms, consistent with the PMT approach, SMFs were modeled as rigid slumps, which maximizes tsunami generation, all other parameters being equal (Grilli and Watts, 2005); hence, this approach is conservative. As this might be too pessimistic for some situations, in future work, based on field data, we are planning to investigate effects of SMF deformation on tsunami generation, e.g., using the recently extended NHW model (Ma et al., 2013); this could result in smaller tsunami inundation in some areas.

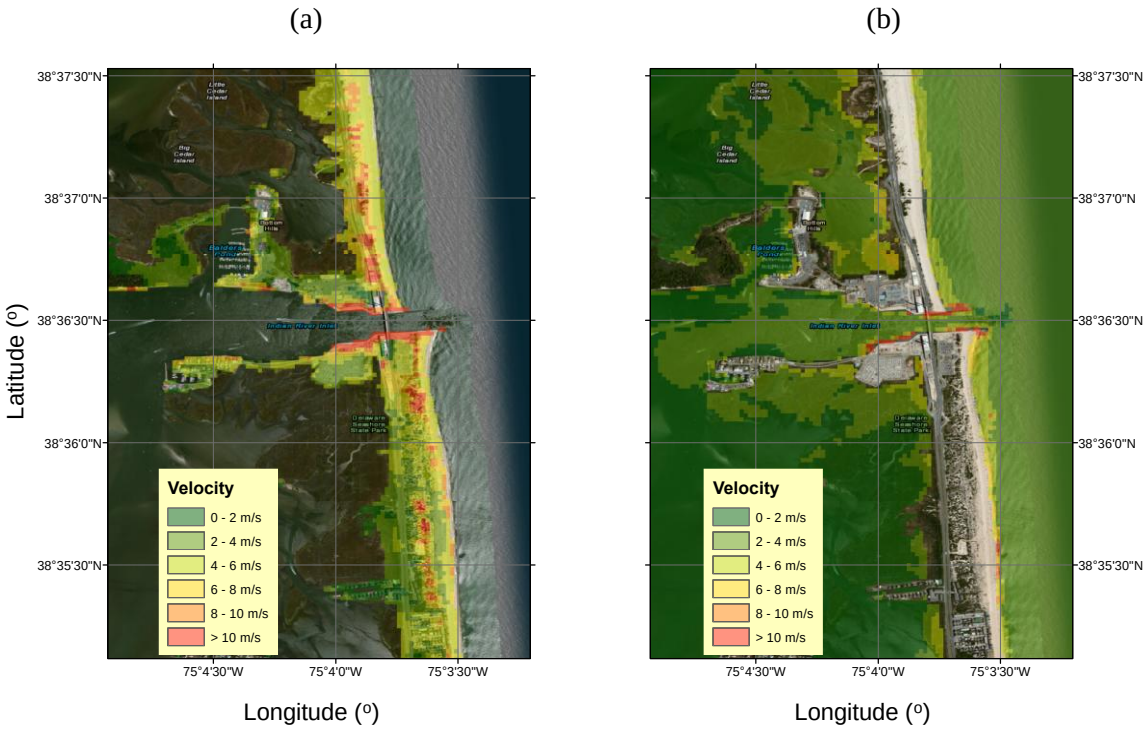

Figure 2.28 Maps of tsunami-induced maximum velocity (m/s) computed with FNW around Indian River Inlet, DE, in 10 m resolution Rehoboth Beach, DE grid, using results of simulations in 31 m resolution OC-1 grid for area 4 SMF proxy as forcing along the boundary (Figure 2.24,Figure 2.25): (a) results for initially dry inundated area; (b) results for initially wet inundated area.

In a preliminary phase to this work, overall SMF tsunami hazard was estimated along the USEC based on Monte Carlo Simulations (MCS; Grilli et al., 2009) of slope stability and tsunami generation and impact. These indicated an increased level of SMF tsunami hazard north of Virginia, potentially surpassing the inundation generated by a typical 100 year hurricane storm surge in the region; to the south, SMF tsunami hazard significantly decreased. Subsequent geotechnical and geological analyses (Krause, 2011; Eggeling, 2012) delimited 4 high-risk areas along the upper USEC, which based on field data (i.e., sediment nature and volume/availability) have the potential for large tsunamigenic SMFs.

Pending the acquisition of more detailed geological and geophysical field data, and consistent with the conservative SMF proxy methodology agreed upon by NTHMP investigators, we defined the SMF PMT in the 4 identified high-risk areas (Figure 2.1) as having the same characteristics as the Currituck slide (i.e., a so-called "Currituck proxy"), which is the largest historical event identified in the region. In future work, once site specific field data is available, some of the selected SMF proxies could be revised and a new generation of inundation maps developed based on these.

After an introduction to the problem and a presentation of the tsunami modeling methodology, the second part of the paper was devoted to parameterizing and modeling the historical Currituck SMF event, including: (i) a new reconstruction of the slide geometry and kinematics; (ii) the simulation of the resulting tsunami source generation; and (iii) the propagation of the tsunami source over the shelf to the coastline; and to assess the accuracy and convergence of various numerical results. For

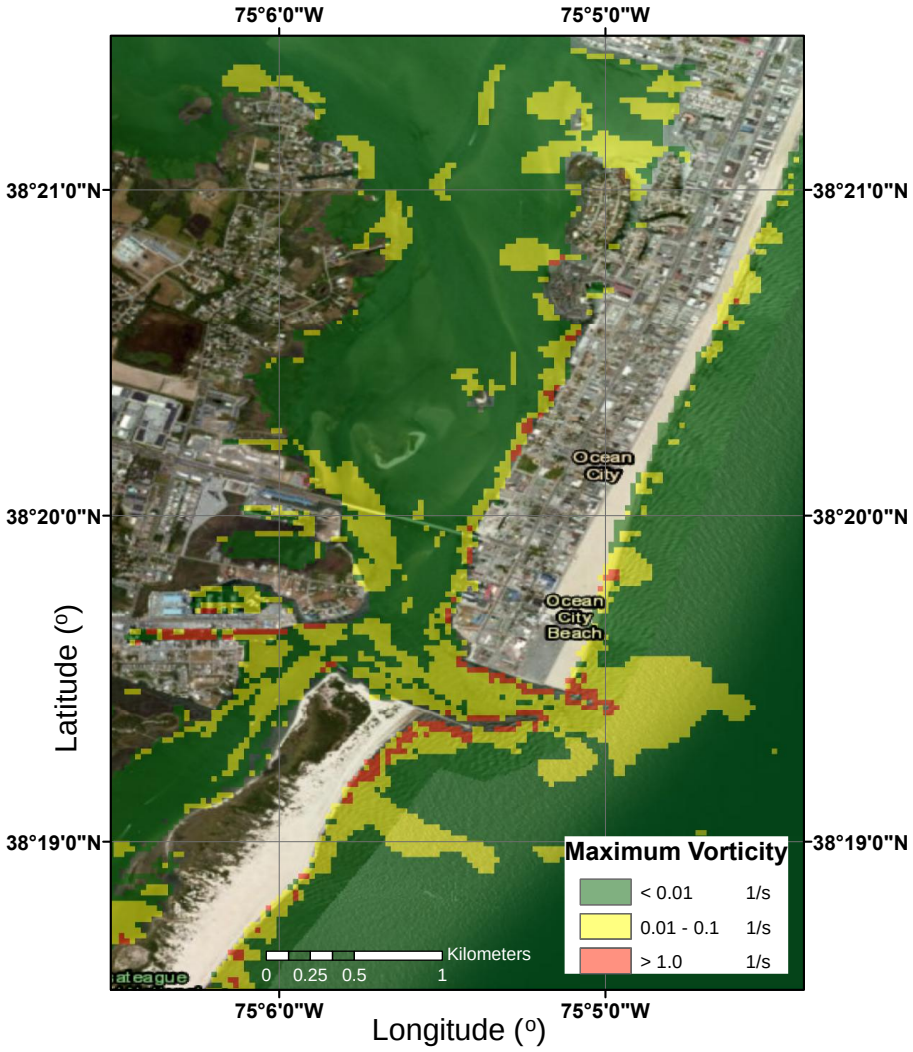

Figure 2.29 Map of tsunami-induced maximum vorticity (1/s) computed with FNW around Ocean City, MD inlet, in 10 m resolution Ocean City grid, using results of simulations in 31 m resolution OC-2 grid for area 4 SMF proxy as forcing along the boundary (Figure 2.24, Figure 2.25).

the latter, a sensitivity analysis to model and grid parameters was performed that confirmed the convergence and accuracy of the coupled modeling approach NHW/FNW and tsunami simulation results. Then, to further validate the proposed grid nesting and one-way coupling methodologies in this context, we modeled the impact of the historical Currituck tsunami event along the nearest coastline where its energy was focused. We thus showed that, assuming today's sea level, the brunt of tsunami

impact and inundation would have occurred off and south of Virginia Beach, VA, with the tsunami overtopping a large section of the barrier beaches. These results are in qualitative agreement with earlier modeling of the Currituck tsunami (Geist et al., 2009). Additionally, the tsunami would have propagated and refracted into the Chesapeake Bay, causing up to 3 m inundation in Norfolk, VA, inside the Bay.

In a third part, we finally modeled tsunami generation, propagation and coastal impact from SMF Currituck proxy sources sited in each of the 4 high-risk areas. Each tsunami source appeared to share many characteristics with the Currituck event, although details differed due to site-specific effects on wave generation and propagation. A full illustration of the SMF tsunami hazard assessment performed in the context of NTHMP along the USEC was finally presented for the Ocean City, MD area, which is highly vulnerable to tsunami inundation, particularly in the summer when its population increases many folds, due to evacuation problems. It was found that due to its southern location, Ocean City was only significantly affected by the Area 4 SMF proxy; this is expected due to the more directional nature of SMF tsunamis, as compared to co-seismic sources (Tappin et al., 2008). Although no details are provided in this paper, simulations for other areas further north, would show that these are primarily affected by other SMF proxies.

Complete high-resolution maps (up to 10 m) of maximum inundation, currents, vorticity and momentum flux, caused by the tsunami generated from the Area 4 SMF proxy, were thus presented for the most impacted areas around Ocean City. A comparison of these results with similar maps corresponding to the far-field tsunamis, not detailed here, indicates that SMF tsunamis represent one of the largest coastal

hazards for many coastal communities along the USEC. Similar to hurricane flood maps, tsunami hazard maps such as developed here, would allow both better defining zoning plans, relative to coastal developments, and mitigating the effects of future tsunamis by way of protective measures and educational programs. At the completion of the NTHMP project, all the final high-resolution maps of inundation and other products, computed for both SMF and other types of tsunami sources (PMTs), will be posted on the NTHMP website and available for download.

SMF tsunamis would offer little warning time along the USEC because they: (i) could be triggered by moderate seismic activity that would only be felt locally; and (ii) would occur close to shore thus having fairly short propagation times. Besides, standard deep water tsunami gages (e.g., NOAA's DART buoys) would be ineffective in sensing SMF tsunamis propagating towards the nearest shorelines. Hence, early warning systems appropriate to sensing near-field tsunamis should be developed, e.g., based on high frequency radar remote sensing. In this respect, SMF tsunami simulations such as presented here could help in assessing the salient tsunami flow properties to be sensed by such systems, for potentially high-impacted locations.

Acknowledgements: This work has been supported by the National Tsunami Hazard Mitigation Program (NTHMP), NOAA, through grant NA10NWS4670010 to the University of Delaware (with subaward to the University of Rhode Island). Additional support at the University of Rhode Island came from grant EAR-09-11499 from the US National Science Foundation, Geophysics Program. Development of the numerical models used in this study was supported by the Office of Naval Research,

Littoral Geosciences and Optics program. S. Banihashemi was supported by the Dept. of Civil and Environmental Engineering, Univ. of Delaware.

References

Abadie S, Morichon D, Grilli ST, Glockner S (2010) Numerical simulation of waves generated by landslides using a multiple-fluid Navier-Stokes model. Coast Engng 57:779-794

Abadie S, Harris JC, Grilli ST, Fabre R (2012) Numerical modeling of tsunami waves generated by the flank collapse of the Cumbre Vieja Volcano (La Palma, Canary Islands): tsunami source and near field effects. J Geophys Res 117:C05030

Amante C, BW Eakins (2009) ETOPO-1 1 arc-minute global relief model: Procedures, data sources and analysis. NOAA Tech. Mem. NESDIS NGDC-24, 19pp.

Barkan R, ten Brick US, Lin J (2009) Far field tsunami simulations of the 1755 Lisbon earthquake: impli-cation for tsunami hazard to the US East Coast and the Caribbean. Mar Geol 264:109-122

Bunn AR, McGregor BA (1980) Morphology of the North Carolina continental slope, Western North Atlantic, shaped by deltaic sedimentation and slumping. Mar Geol 37:253–266

Chaytor J, ten Brink US, Solow J, Andrews BD (2009) Size distribution of submarine landslides along the U.S. Atlantic Margin. Mar Geol 264:16–27

Eggeling T (2012) Analysis of Earthquake Triggered Submarine Landslides at Four Locations Along the U.S. East Coast. Masters Thesis. University of Rhode Island

Enet F, Grilli ST (2007) Experimental study of tsunami generation by three-dimensional Rigid Underwater Landslides. J Waterw Port Coast Oc Engng 133(6):442-454

Fine IV, Rabinovich AB, Bornhold BD, Thomson R, Kulikov EA (2005) The Grand Banks landslide-generated tsunami of November 18, 1929: preliminary analysis and numerical modeling. Mar Geol 215:45–57

Geist E, Lynett P, Chaytor J (2009) Hydrodynamic modeling of tsunamis from the Currituck landslide. Mar Geol 264:41-52

Grilli ST, Ioualalen M, Asavanant J, Shi F, Kirby JT, Watts P (2007) Source constraints and model simulation of the December 26, 2004 Indian Ocean tsunami. J Waterw Port Coast Oc Engng 133:414-428

Grilli ST, Dias F, Guyenne P, Fochesato C, Enet F (2010a) Progress In fully nonlinear potential flow modeling of 3D extreme ocean waves. Chapt 3 in Advances in Numerical Simulation of Nonlinear Water Waves (ISBN: 978-981-283-649-6, edited by Q.W. Ma) (Vol. 11 in Series in Advances in Coastal and Ocean Engineering). World Scientific Publishing Co. Pte. Ltd., pps. 75- 128

Grilli ST, Dubosq S, Pophet N, Pérignon Y, Kirby JT, Shi F (2010b) Numerical simulation and first-order hazard analysis of large co-seismic tsunamis generated in the Puerto Rico trench: near-field impact on the north shore of Puerto Rico and far-

field impact on the US East Coast. Nat Haz Earth Syst Sci 10:2109-2125. doi:10.5194/nhess-2109-2010

Grilli ST, Harris J, Shi F, Kirby JT, Tajalli Bakhsh TS, Estibals E, Tehranirad B (2013a) Numerical modeling of coastal tsunami dissipation and impact. Proc 33rd Intl Coast Engng Conf (P. Lynett and J. Mc Kee Smith, eds.) (ICCE12, Santander, Spain, July, 2012), 12 pps. World Sci Pub Co Pte Ltd

Grilli ST, Harris JC, Tajalli Bakhsh TS, Masterlark TL, Kyriakopoulos C, Kirby JT, Shi F (2013b) Numerical simulation of the 2011 Tohoku tsunami based on a new transient FEM co-seismic source: Comparison to far- and near-field observations Pure Appl Geophys 170:1333-1359. doi:10.1007/ s00024-012-0528-y

Grilli ST, Harris J, Tajalli Bakhsh TS (2011) Literature Review of Tsunami Sources Affecting Tsunami Hazard Along the US East Coast. NTHMP Progress report, Res Rept CACR-11-08, Center for Applied Coastal Research, University of Delaware, Newark. http://chinacat.coastal.udel.edu/papers/ grilli-etal-cacr-11-08.pdf

Grilli ST, Taylor O-DS, Baxter CDP, Maretzki S (2009) Probabilistic approach for determining submarine landslide tsunami hazard along the upper East Coast of the United States. Mar Geol 264(1-2):74-97

Grilli ST, Vogelmann S, Watts P (2002) Development of a 3D Numerical Wave Tank for modeling tsunami generation by underwater landslides. Engng Analys Boundary Elements 26(4):301-313

Grilli ST, Watts P (1999) Modeling of waves generated by a moving submerged body. Applications to underwater landslides. Engng Analys Boundary Elements 23:645-656

Grilli ST, Watts P (2005) Tsunami generation by submarine mass failure, I: Modeling, experimental validation, and sensitivity analyses. J Waterw Port Coast Ocean Engng 131(6):283-297

Grothe PR, Taylor LA, Eakins BW, Warnken RR, Carignan KS, Lim E, Caldwell RJ, Friday DZ (2010) Digital elevation model of Ocean City, Maryland: Procedures, data sources and analysis. NOAA Technical Memorandum NESDIS NGDC-37

Harris JC, Grilli ST, Abadie S, Tajalli Bakhsh TS (2012) Near- and far-field tsunami hazard from the potential flank collapse of the Cumbre Vieja Volcano. Proc 22nd Offsh Polar Engng Conf (ISOPE12, Rodos, Greece, June 17-22, 2012), Intl Soc Offsh Polar Engng, 242-249

Ioualalen M, Asavanant JA, Kaewbanjak N, Grilli ST, Kirby JT, Watts P (2007) Modeling of the 26th December 2004 Indian Ocean tsunami: Case study of impact in Thailand. *J Geophys Res* 112: C07024. doi:10.1029/2006JC003850

Kirby, J.T., Shi, F., Tehranirad, B., Harris, J.C. and Grilli, S.T. (2013) Dispersive tsunami waves in the ocean: Model equations and sensitivity to dispersion and Coriolis effects. Ocean Modeling 62:39-55. doi:10.1016/j.ocemod.2012.11.009

Krauss T (2011) Probabilistic Tsunami Hazard Assessment for the United States East Coast. Masters Thesis. University of Rhode Island, http://chinacat.coastal.udel.edu/nthmp/krause-ms-uri11.pdf

Locat J, Lee H, ten Brink US, Twichell D, Geist E, Sansoucy M (2009) Geomorphology, stability and mobility of the Currituck slide. Mar Geol 264:28-40

Lynett P, Liu PL-F (2002) A numerical study of submarine landslide generated waves and runup. Proc R Soc London A458:2885-2910

Lynett P, Liu PL-F (2005) A numerical study of the run-up generated by three-dimensional landslides. J Geophys Res 110:C03006. doi:10.1029/2004JC002443

Ma G, Shi F, Kirby JT (2012) Shock-capturing non-hydrostatic model for fully dispersive surface wave processes. Ocean Mod 43-44:22-35

Ma G, Kirby JT, Shi F (2013) Numerical simulation of tsunami waves generated by deformable submarine landslides. Ocean Mod 69:146-165

Park H, Cox DT, Lynett PJ, Wiebe DM, Shin S (2013) Tsunami inundation modeling in constructed environments: A physical and numerical comparison of free-surface elevation, velocity, and momentum flux. Coastal Eng 79:9-21

Pipe DJW, Cochonat P, Morrison ML (1999) The sequence of events around the epicentre of the 1929 Grand Banks earthquake: initiation of the debris flows and turbidity current inferred from side scan sonar. Sedimentology 46:79–97

Prior DP, Doyle EH, Neurauter T (1986) The Currituck Slide, Mid Atlantic continental slope-revisited. Mar Geol 73:25–45

Schnyder JSD, Kirby JT, Shi F, Tehranirad B, Eberli GP, Mulder T, Ducassou E (2013) Potential for tsunami generation along the western Great Bahama Bank by submarine slope failures. Abstract NH41A-1689, *AGU Fall Meeting*, San Francisco, December

Shi F, Kirby JT, Harris JC, Geiman JD, Grilli ST (2012) A high-order adaptive time-stepping TVD solver for Boussinesq modeling of breaking waves and coastal inundation. Ocean Mod., 43-44:36-51

Tappin DR, Watts P Grilli ST (2008) The Papua New Guinea tsunami of 1998: anatomy of a catastrophic event. Nat Haz Earth Syst Sci 8:243-266

Twichell DC, Chaytor JB, ten Brink US, Buczkowski B (2009) Morphology of late quaternary submarine landslides along the U.S. Atlantic Continental Margin. Mar Geol 264:4-15

ten Brink US, Twichell D, Geist E, Chaytor J, Locat J, Lee H, Buczkowski B, Barkan R, Solow A, Andrews B, Parsons T, Lynett P, Lin J, Sansoucy M (2008) Evaluation of Tsunami Sources with the Potential to Impact the U.S. Atlantic and Gulf Coasts. Report to the Nuclear Regulatory Commission. USGS

ten Brink US, Lee HJ, Geist EL, Twichell D (2009a) Assessment of tsunami hazard to the U.S. East Coast using relationships between submarine landslides and earthquakes. Mar Geol 264:65-73

ten Brink US, Barkan R, Andrews BD, Chaytor JD (2009b) Size distributions and failure initiation of submarine and subaerial landslides. Earth Planetary Sci Lett 287:31-42

Tehranirad B, Shi F, Kirby JT, Harris JC, Grilli ST (2011) Tsunami benchmark results for fully nonlinear Boussinesq wave model FUNWAVE-TVD, Version 1.0. Research Report No. CACR-11-02, Center for Applied Coastal Research Univ of Delaware, Newark

Tehranirad B, Kirby JT, Ma G, Shi F (2012) Tsunami benchmark results for non-hydrostatic wave model NHWAVE (Version 1.0). Research Report No. CACR-12-03.Center for Applied Coastal Research Univ of Delaware, Newark

Watts P, Grilli ST, Kirby JT, Fryer GJ, Tappin DR (2003) Landslide tsunami case studies using a Boussinesq model and a fully nonlinear tsunami generation model. Nat Haz Earth Syst Sci 3:391-402

Watts P, Grilli ST, Tappin DR, Fryer G (2005) Tsunami generation by submarine mass failure, II: Predictive equations and case studies. J Waterw Port Coast Oc Engng 131(6):298-310

Yeh H, Robertson I, Preuss J (2005) Development of design guidelines for structures that serve as tsunami vertical evacuation sites. Open File Rept. 2005-4, Washington Division of Geology and earth Resources

MANUSCRIPT 3

To be submitted.

Dynamic tidal effects on tsunami coastal hazard in large estuaries: Case of the Chesapeake Bay/James River, USA

Tayebeh S. Tajalli Bakhsh[1] , Stephan T. Grilli[1,+], Annette Grilli[1]

[1] Dept. of Ocean Engineering, University of Rhode Island, Narragansett, RI 02882

\+ Corresponding author

Abstract

In this work, we model coastal tsunami hazard in large river estuaries with significant tidal forcing, by simulating dynamic interactions between tide and tsunami, following a new methodology,, rather than using a static reference level in the tsunami propagation and inundation model equal to a high tide level (usually the 10% exceedance tide), as is typically done. Results show that nonlinear interactions between tide and tsunamis affect the tsunami wavetrain phase and elevation as it propagates up the river estuary, as compared to a simple long wave superposition. As this works takes place as part of a tsunami inundation mapping activity along the US East Coast, performed under the auspice of the National Tsunami Hazard Mitigation (NTHMP) program, as a case study, we have applied our novel modeling methodology to the Chesapeake Bay mouth and the James River estuary, VA.

In our modeling methodology, we first separately simulate the dominant unscaled M2 tide and the two most significant incident tsunamis in the Atlantic Ocean Basin, on the continental shelf off of the Chesapeake Bay; this is done using the nonlinear and dispersive long wave model FUNWAVE-TVD, in coarse to medium nested grids. Then, the tide is calibrated in a finer grid encompassing the Bay and the river, in order to reproduce observations for the average tide and the selected maximum tide level at a tide gage located at the mouth of the river. The combined tide-tsunami simulations are then performed, for a series of phases of the tides, by linearly superposing time series of surface elevation and horizontal currents of calibrated tide and tsunami wavetrains, along the offshore boundary of the Chesapeake Bay grid, which is located on the shelf, in deep enough water for the linear

approximation to apply. The dynamic tide-tsunami simulations are performed with FUNWAVE-TVD, using the time series as boundary conditions; note these include both incident and reflected waves and thus satisfy an open boundary condition along the grid boundary.

The dynamic tide-tsunami simulations are repeated for 4 different phases of the tide, for incident tsunamis caused by an extreme Cumbre Vieja flank Collapse in the Canary Islands (volume of 450 km^3), and the historical Currituck slide on the continental shelf break; 4 levels of nesting are used, from 1 arc-min in the deep ocean down to a 39 m Cartesian grid in the James river. Results show that the worst-case scenario, leading to maximum inundation and currents in the James River, is caused by the Cumbre Vieja tsunami, when combined with the extreme tide at one-eight of a period (about 1h34 min) ahead of the maximum tide, along the grid offshore boundary. The Currituck slide tsunami causes nearly the same inundation for the same phase of the tide, although the wavetrains and current patterns in the river are very different. Depending on the arrival time of tsunami waves with respect to the tide phase, the major flooding risk in the river might result from different crests in the tsunami incident wavetrain and the arrival time of maximum flooding at a given location may vary. In all tide phase cases, nonlinear interactions between tide and tsunami currents change the velocity of propagation of the various waves of the incident wavetrain, mostly in the shallower water area of the river where bottom friction dominates. Finally, for all cases simulated, results show that the standard approach in tsunami hazard assessment, of simulating each tsunami over the maximum static extreme tide level produces conservative results in terms of maximum

predicted inundation in the James River, but not by a large margin. In the present case, maximum tidal current are moderate, less than 0.6 m/s in the river; clearly, in an estuary with stronger tidal currents, this conclusion could be reversed.

Keywords: Tide, tsunami, tide and tsunami interaction, James River, Nonlinear effect, Dispersion, Numerical modeling of long wave propagation **.**

1. Introduction

Tides and tsunamis are both long waves, whose individual propagation is governed by long wave theories, such as linear Stokes theory in deep water and Saint Venant or Boussinesq equations in shallow water, depending on the relative magnitude of nonlinearity and dispersive effects (e.g., Dean and Dalrymple, 1990). In deep water, tsunamis are not affected by tides, because both the tidal range is small with respect to depth and tide-induced currents are weak. Hence, tsunami phase speed and shoaling are not significantly affected by the small change in water depth caused by tides and the current associated with the tsunami is usually stronger than tidal current. The same applies to shallow coastal waters with simple bathymetry and fairly straight coastlines. In this situation, which is prevalent for most of the ocean-exposed US east coast, from Florida to Massachusetts, while tide-induced currents may be larger and tidal range become more significant with respect to local depth, tsunami coastal hazard in terms of maximum inundation and runup can still be accurately assessed by modeling tsunami propagation using a static reference level corresponding to a large tide (typically the 10% exceedence tide). In this case, both tsunami phase speed and elevation are properly affected by the increased depth, yielding larger inundation further onshore. However, in coastal regions where tidal range is very large and/or the bathymetry is complex, and tide-induced flows are strong, tsunami-tide interactions may need to be more carefully and accurately evaluated, in order to achieve a conservative coastal hazard assessment. This requires, in particular, considering whether nonlinear interactions between tidal and tsunami flow velocities and elevations may lead to more hazardous conditions. Along the US East Coast,

significant tide-tsunami interactions could occur in a few large and complex estuaries, that are also be highly populated areas having numerous critical infrastructures (such as major harbors and powerplants), with prominent examples being New York, NY in the Hudson River estuary and Norfolk, VA near the mouth of the James River estuary in the Chesapeake Bay.

Since 2010, under the auspices of the US National Tsunami Hazard Mitigation Program (NTHMP; http://nthmp.tsunami.gov/index.html), together with colleagues from the University of Delaware, the authors have been involved with modeling tsunami coastal hazard along the US East coast, including at these strongly tide-affected estuaries, under the effects of all the Probable Maximum Tsunamis (PMTs) that could occur in the Atlantic Ocean basin. These PMTs included (Figure 3.1; see also ten Brink et al., 2008, 2014): (i) near-field submarine mass failures (SMFs) on or near the continental shelf break, represented in the Chesapeake Bay area by the historical Currituck (CRT) underwater landslide (Grilli et al. 2009; Grilli et al., 2013b; Grilli et al., 2014); (ii) an extreme hypothetical M9 seismic event occurring in the Puerto Rico Trench (Grilli et al., 2010; Grilli and Grilli, 2013a); (iii) a repeat of the historical 1755 M8.9 earthquake occurring in the Azores convergence zone (Madera Tore Rise; Barkan et al., 2009; Grilli and Grilli, 2013c); and (iv) a large scale flank collapse of the Cumbre Vieja Volcano (CVV) in the Canary Islands (Abadie et al., 2012; Grilli and Grilli, 2013b; Harris et al., 2014). To carry out this tsunami inundation mapping work, a large number of tsunami simulations were performed using the fully nonlinear and dispersive model FUNWAVE-TVD (Shi et al., 2012; Kirby et al., 2013), in a series of coarse to finer nested grids. According to the

standard methodology, in the simulations, the reference level in the coastal grids was statically set to a high tide value (such as Mean Highest High Water Level; MHHWL). Hence, potential dynamic interactions between tide- and tsunami-induced flows were neglected.

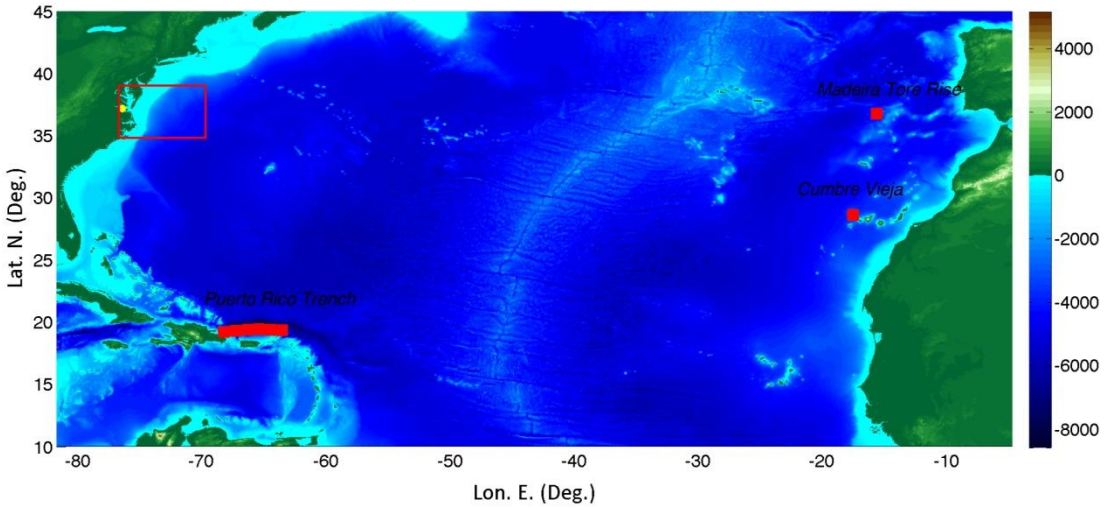

Figure 3.1 Area of the 1 arc-min Atlantic Ocean basin grid (Table 3-1), with marked location of the three PMT far-field sources. The red box shows the footprint of 20 arc-sec (606 m) regional grid off of the Chesapeake Bay and the yellow dots marks the location of the James River. Color scale is bathymetry (< 0) and topography (> 0) in meter, from ETOPO-1 data.

To date, interactions between tide and tsunami waves have only rarely been studied. Kowalik et al. (2006) first hypothesized that significant effects due to tsunami–tide interactions should be observed in the tidal and tsunami currents. Kowalik and Proshutinsky (2010) modeled tide-tsunami interactions in a simple channel and then in Cook Inlet (Alaska), which has one of the largest tidal ranges in North America. They found that results significantly differed from a simple linear superposition of separate simulations of tide and tsunami, and that maximum elevations depended on the tide amplitude and phase; with tsunami being intensified

or damped, depending on mean basin depth, which is regulated by tides. They concluded that, in their simulations, the main effects of the tide were to change water depth, thus affecting tsunami phase speed, propagation and amplification, and dissipation by bottom friction. These, however, were site specific conclusions and it is thus not possible to a priori predict the effects of tsunami–tide interactions without simulating tsunamis together with tidal forcing. Zhang et al. (2011) performed high resolution simulations of the impact of the 1964 Prince William Sound tsunami on the US Pacific Northwest coast, with and without dynamic tide effects. They evaluated the tidal influence on wave elevation, velocity and inundation. Their results showed that the tide, as could be expected, had minimal effects near the open coast, but significantly affected both wave runup and inundation near and in estuaries and rivers. On this basis, they concluded that dynamic tsunami–tide interactions should be considered in tsunami studies done near and in estuaries, as these could account for 50% of the observed runup and up to 100% of the inundation in some cases. Tolkova (2012) and Yeh et al. (2012) modeled tsunami-tide interactions in the Columbia River (Oregon), to better understand the observed 100 km upstream propagation of the Tohoku 2011 tsunami in the river. Tolkova found that tsunami waves propagated further on a rising tide in the lower portion of the river; however, upstream the tsunami propagated further at the maximum high tide. The simulations performed also showed potential amplification of tsunami waves directly after high tide. Tolkova concluded that the interaction of the two long waves is completely dependent on the specific environment in which the interaction occurs, which justifies performing site-specific studies.

In this work, we first develop a methodology to simulate the combined effects of tidal phase and current magnitude on the evolution of tsunami waves, using FUNWAVE-TVD. With this method, we then model tsunami hazard in the James River estuary, in order to both gain insight into the nature of the combination and assess whether the resulting scenarios can potentially lead to more hazardous conditions than would be expected from a standard linear superposition of tide and tsunamis elevations. In the fairly shallow James River, tsunami phase speed and elevation are very dependent on local depth and direction of pre-existing current flows, which are both controlled by tide magnitude and phase. Additionally, large and sudden water level increases, such as those caused by an incoming tsunami elevation at the river mouth, may cause the appearance of a strongly dispersive and nonlinear undular bore, made of shorter oscillatory waves (e.g., Wei et al., 1995). The James River area was selected as a test bed for this work, because of the significant tide-induced flows, the complex topography and bathymetry both in the river and in the Chesapeake Bay (Figsures 3.2 and 3.3), and the many critical infrastructures that can be found in low lying areas of the river banks, including the largest Naval Base in the world, in Norfolk (VA) and the Surry nuclear power plant, halfway upstream the river (37°9′56″N, 76°41′52″W).

More specifically, we will evaluate tide-tsunami interaction effects by first simulating the largest tides that can occur in the Chesapeake Bay and James River complex. Then, joint tide-tsunami simulations will be performed by superimposing incoming tsunami wave elevations and velocities with tidal forcing, along the offshore boundary of a computational grid selected where depth is large enough to justify their

linear superposition. Tidal forcing will be limited to the strongest semi-diurnal component, corresponding to the 10% exceedance tide on an average year, and will be obtained from a tide simulation model. Regarding PMTs, the NTHMP work referred to above indicates that, in the case study area, among the 4 near- and far-field PMTs, the two that by far are causing the largest waves at the mouth of the Chesapeake Bay are the CRT and CVV tsunamis. These two sources will thus be used as incident tsunamis to perform the tide-tsunami interaction study. Finally, effects of tide phase on the two incident tsunamis will be modeled by considering 4 different phases of the extreme M2 tide.

2. Modeling methodology

2.1 Tsunami propagation

Tsunami propagation is simulated using the fully nonlinear and dispersive Boussinesq model FUNWAVE (Wei et al., 1995; Grilli et al., 2007, 2010; Ioualalen et al., 2007), in its latest Cartesian (Shi et al., 2012a) and spherical (Kirby et al., 2013) implementations. FUNWAVE-TVD is fully parallelized for an efficient solution on shared memory clusters and has a more efficient Total Variation Diminishing (TVD) algorithm to follow breaking wave fronts in shallow water. The model has a quadratic bottom friction term controlled by a Manning friction coefficient C_d and, unlike the original FUNWAVE, it models dissipation in breaking waves by turning off dispersive terms in areas where breaking is detected based on a breaking index criterion. While FUNWAVE-TVD's Cartesian implementation is fully nonlinear, its spherical

implementation is only mildly nonlinear; hence, it is only applicable in areas where tsunami elevation over local depth is perhaps not more than 10 percent. Therefore, in tsunami simulations, spherical grids will be fairly coarse and used to model large ocean areas in relatively deeper waters, whereas Cartesian grids will have a higher resolution and be used to model coastal tsunami impact. This approach was successfully used to model the Tohoku 2011 tsunami (Grilli et al., 2013a; Kirby et al., 2013). Both implementations of FUNWAVE-TVD have been fully validated against standard benchmarks, as part of the NTHMP work (Tehranirad et al., 2011; Shi et al., 2012b).

Simulations with FUNWAVE-TVD, whether spherical or Cartesian, are performed in several levels of nested grids using a one-way coupling methodology. This works by computing time series of free surface elevations and currents in a coarser grid level, for a large number of numerical gages (stations) defined along the boundary of the finer grid level. Computations in the finer nested grid level are then performed using these time series as boundary conditions. With this approach, reflected waves propagating from inside the area covered by each finer grid are included in the time series computed in the coarser grids along the finer grid boundaries, thus satisfying an open boundary condition. To reduce reflection in the first coarsest grid level (here the 1 arc-min Atlantic Ocean basin grid used to compute the transoceanic propagation of the CVV source; Figure 3.1), 200 km thick sponge (absorbing) layers are specified along all the open boundaries.

Figures 3.1 to 3.3 show the footprints, locations, and bathymetry/topography of the FUNWAVE-TVD grids used in this work, i.e., a: (i) 1 arc-min (1800 m) resolution

ocean basin spherical grid (Table 3-1); (ii) 20 arc-sec (606 m) resolution spherical regional grid (Table 3-2); and (iii) 154 m and 39 m Cartesian coastal grids (Tables 3-3 and 3-4). Tables 3-4 give details of the location and discretization of each grid. In each of those, bathymetry and topography are interpolated from the most accurate source available, i.e., 1 arc-min ETOPO-1 data in deeper water, 3 arc-sec (90 m) NOAA Coastal Relief model data (NOAA-NGDC, 2013), and 1/3 arc-sec (10 m) NTHMP or FEMA Region 3 Digital Elevation Models (DEMs; e.g., Taylor et al., 2008). Figures 3.2 and 3.3 show that the higher-resolution Cartesian grids used to better resolve the propagation of tsunami wave trains in the Chesapeake Bay and the James River, also accurately represent the complex geography and bathymetry of the region, including the multiple deep and sometimes narrow channels.

Regarding reference levels, NOAA-NGDC's recommendation in deep water areas where ETOPO-1 bathymetry is used, is that tidal range should be neglected as it is within the error margin of the data. For computing tsunami inundation in coastal grids, however, using more accurate bathymetric data sources (such as the DEMs), the reference level should be adjusted to account for the high tides. In this work, however, rather than statically changing the reference level of tsunami simulations, dynamic tide-tsunami interactions will be simulated as detailed below.

Table 3-1 Parameters of the Atlantic Ocean basin model grid used for the CVV (450 km^3) far-field source definition and initial propagation modeling using FUNWAVE-TVD (Figure 3.1).

Grid/Source	Min. Lon. E. (Deg.)	Max. Lon. E. (Deg.)	Min. Lat. N. (Deg.)	Max. Lat. N.(Deg.)	Resolution	Spherical /Cartesian
CVV $\frac{450}{km^3}$	-82	-5	10	45	1 arc-min	Spherical

Table 3-2 Parameters of the 20 arc-sec regional grid used in FUNWAVE-TVD simulations (Figure 3.2).

20 arc-sec/ "606 m" grid	Min	Max	Number of Cells	Cartesian/ spherical	Spatial Discretization (Deg.)	Center of Mercator Projection
Lat. (y)	34.8000	39.0167	760	Spherical	0.0056	34.8000
Lon. (x)	-77.0000	-69.9833	1264	Spherical	0.0056	-77

2.2 Tsunami generation

As indicated above, based on earlier work, the two largest PMT sources selected for assessing tsunami coastal hazard in the Chesapeake Bay area are, in the far-field, an extreme 450 km^3 flank collapse of the Cumbre Vieja Volcano (CVV) in the Canary Islands (Abadie et al., 2012; Grilli and Grilli, 2013b; Harris et al., 2014), and in the near-field a Submarine Mass Failure (SMF) identical to the Currituck slide (CRT), which is the largest historical SMF observed on the US Atlantic Ocean margin (Grilli et al., 2013b, 2014; ten Brink et al., 2008, 2014). Tsunami generation and resulting propagation from both of these sources have been studied in earlier work; hence, only a summary is given below and results are given in a following section.

CVV Flank collapse PMT: Earlier inundation mapping work performed for NTHMP indicated that the tsunami generated by a complete flank collapse of the Cumbre Vieja Volcano (CVV) on La Palma, in the Canary Islands, represents the largest far-field tsunami source that can potentially affect the US east coast (Abadie et al., 2012; Grilli and Grilli, 2013b; Harris et al., 2014). Although the return period for this event is unknown and likely very long, it would generate such high waves that, even after transoceanic propagation, they would still pose a significant hazard to many

(a)

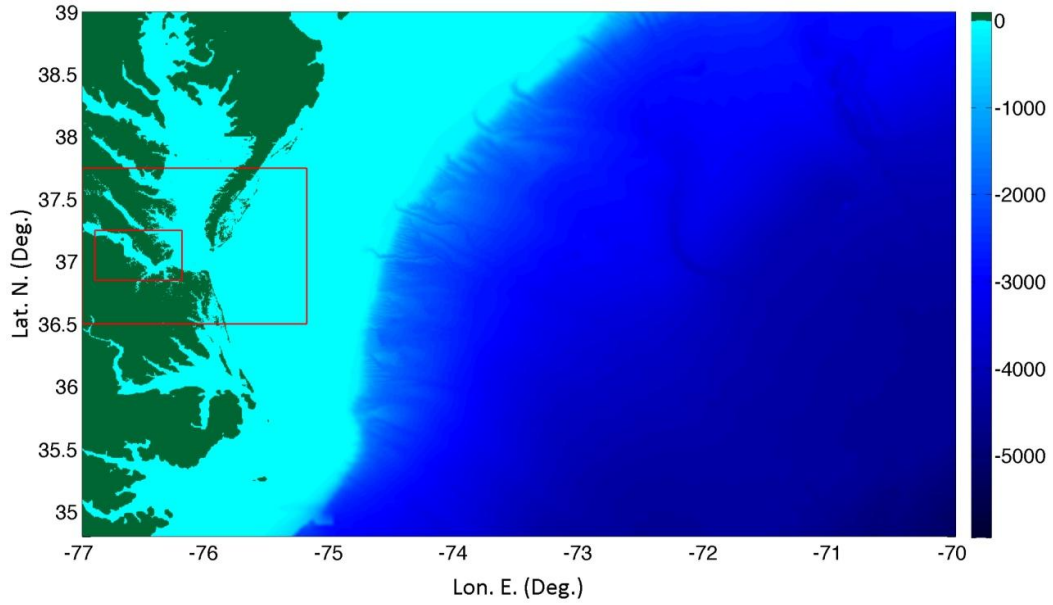

(b)

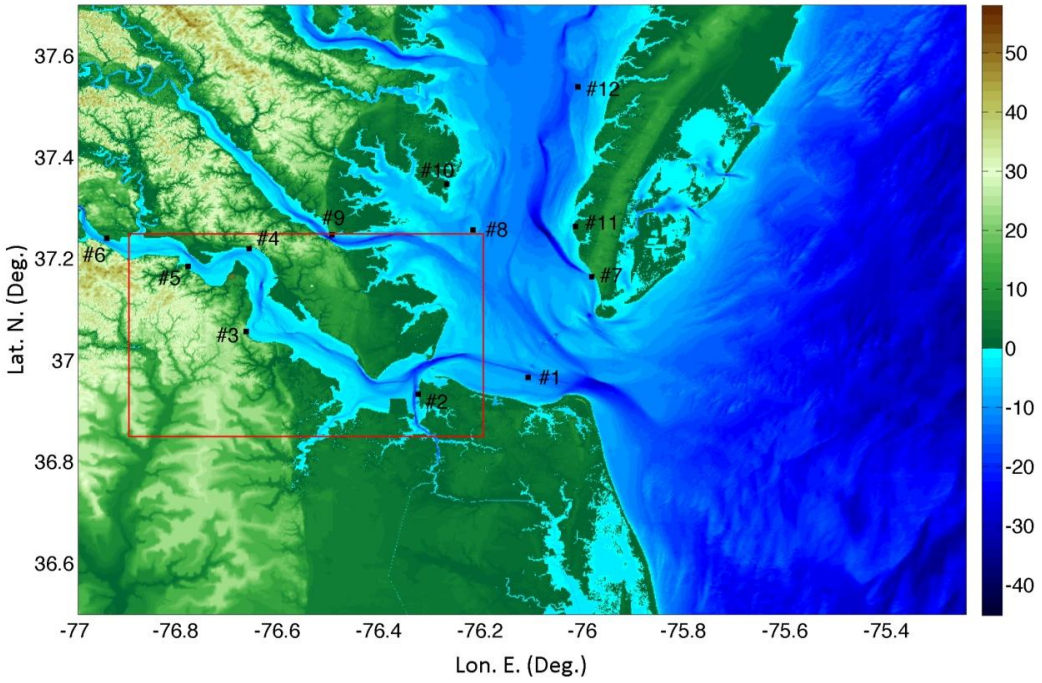

Figure 3.2 Case study area and grids used in FUNWAVE-TVD simulations: (a) Chesapeake Bay and shelf in 20 arc-sec (606 m) spherical grid (Table 3-2). Bathymetry/topography (in meter) is from ETOPO-1. Red boxes mark the areas of the 154 m and 39 m nested grids; (b) Mouth of the Chesapeake Bay and James River Area in 154 m Cartesian grid (Table 3-3). Bathymetry/topography (in meter) is from 90 m CRM and 10 m NTHMP and FEMA DEMs (referred to MHW level). The red box marks the area of the 39 m nested Cartesian grid (Figure 3.3) and black squares mark locations of NOAA tide gages #1-#12 (Table 3-5).

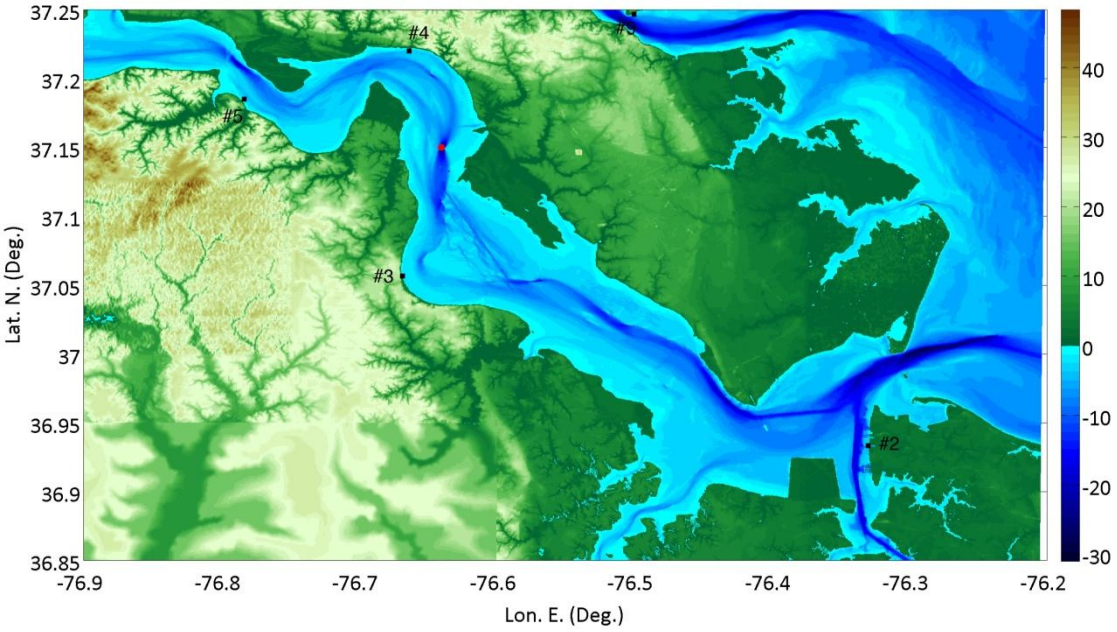

Figure 3.3 James River in area of the 39 m Cartesian grid used in FUNWAVE-TVD simulations (Table 3-4). Bathymetry/topography (in meter) is from 10 m NTHMP and FEMA DEMs (referred to MHW level). The black boxes mark locations of NOAA tide gages (Table 3-5), and the red circle is the "river station".

Table 3-3 Parameters of the 154 m coastal grid used in FUNWAVE-TVD simulations (Figures. 3.2, 3.3).

"154 m" grid	Min	Max	Number of Cells	Cartesian/ spherical	Spatial Discretization (m)	Center of Mercator Projection
Latitude	36.5	37.7478	909	Cartesian	154.1227	36.5
Longitude	-77.0	-75.2016	1029	Cartesian	154.1227	-77.0

Table 3-4 Parameters of the 39 m coastal used in FUNWAVE-TVD simulations (Figure 3.3).

"39 m" grid	Min	Max	Number of Cells	Cartesian/ spherical	Spatial Discretization (m)	Center of Mercator Projection
Latitude	36.8500	37.2495	1157	Cartesian	38.5307	36.8500
Longitude	-76.9000	-76.2014	1609	Cartesian	38.5307	-76.9000

coastal areas. The pioneering, but somewhat controversial, work of Ward and Day (2001) considered a CVV slide volume of 500 km^3, which they estimated would generate a tsunami causing 10 to 25 meter runup along the US East coast. More recent work, based on more accurate modeling, predicted significantly smaller runup,

although still very large in many areas (Abadie et al., 2012; Harris et al., 2014). More specifically, Abadie et al. (2012) used the 3D multi-fluid Navier-Stokes model THETIS to compute several scenarios of CVV western flank collapse, with the most extreme having a 450 km^3 volume. In these simulations, in addition to water and air, the subaerial slide material was modeled as a Newtonian fluid having the density of basalt (2500 kg/m3). THETIS was used to compute both slide motion and tsunami generation, as well as near-field tsunami impact in and near La Palma. FUNWAVE-TVD was then used to simulate tsunami impact on the other Canary Islands, by initializing simulations with THETIS' solution. The surface elevation and current computed by Abadie et al., 20 minute into this event, have been used to define the extreme CVV source for assessing tsunami hazard along the US East Coast in NTHMP work (Grilli and Grilli, 2013b; Harris et al., 2014). This was done by using this source as initial condition in a 1 arc-min FUNWAVE-TVD ocean basin scale grid, and performing further simulations in finer regional and coastal nested grids.

In this work, the propagation of the CVV tsunami will first be recomputed in a similar 1 arc-min ocean basin grid (Figure 3.1; Table 3-1) to compute time series of surface elevation and current along the boundary of the 20 arc-min regional grid off of the Chesapeake Bay (Figure 3.1).

CRT submarine mass failure PMT: Grilli et al. (2014) used the 3D non-hydrostatic sigma-layer model NHWAVE (Ma et al., 2012) to compute tsunami generation from the CRT-SMF motion. This model was validated for SMF tsunami simulations as part of NTHMP work (Tehranirad et al., 2012). To maximize tsunami generation, they used the total volume (165 km^3) of the reconstituted (unfailed)

historical slide and assumed a failure as a rigid slump (Grilli and Watts, 2005; Enet and Grilli 2007). Once the SMF had stopped moving, 13.3 minutes into the event, the surface elevation and horizontal current were used as initial conditions in FUNWAVE-TVD to continue simulating tsunami propagation and coastal impact, in a series of nested grids.

In this work, the CRT tsunami propagation and coastal impact will be similarly computed by initializing FUNWAVE-TVD's computations in the 20 arc-sec grid (Figure 3.2), using NHWAVE's solution at 13.3 min into the CRT event.

2.3 Tide-tsunami interactions

According to the methodology established by the US Nuclear Regulatory Commission (NUREG/CR-6966), tsunami runup and inundation should be evaluated coincidentally with a so-called "antecedent water level" (AWL) equal to the 10 percent exceedance high tide, defined as the tide that is equaled or exceeded by 10 percent of the maximum monthly tides over a continuous 21 year period (ANSI/ANS-2.8-1992). Additionally, the AWL includes a water level increase due to sea level rise. The main innovation in this work, however, will be to assess coastal tsunami hazard by considering dynamic interactions between tide and tsunami flows, rather than using an AWL as a high water reference static level in tsunami simulations. However, to be on the conservative side, in preliminary tide-only simulations, tidal forcing will be calibrated for the maximum dynamic tide elevation to still achieve AWL conditions at a selected reference point.

Since tsunami hazard is being assessed in the James River, the AWL is calculated using tide data obtained at NOAA's Sewells Point, VA, gage (NOAA Station 8638610; marked #2 in Figures. 3.2, 3.3; Lat. 36° 56.8', Lon. 76° 19.8'), which is near the river mouth. This yields, AWL = 1.244 m NAVD88, including 0.299 m for sea level rise (SLR) and 0.945 m for the 10% exceedance tide maximum elevation. At Sewells Point, NOAA's data also indicates that Mean High Water (MHW; the usual reference for bathymetric DEMs) is 0.287 m NAVD88, implying that the AWL = 0.957 m MHW. Also, Mean Sea Level (MSL) is 0.079 m below NAVD88. Additionally, the dominant tidal constituent at Sewells Point is clearly the M2 (semi-diurnal) tide, since it is nearly five times greater than the next two constituents (N2 and S2). Therefore, the M2 tide constituents will be considered as representative of the general tidal conditions in the Chesapeake Bay and the James River.

As indicated before, in deep enough water with respect to surface elevation, both tide and tsunami waves behave as nearly linear long waves. Accordingly, when these conditions are met, linear wave theory's superposition principle (Dean and Dalrymple, 1990) applies and their surface elevation and current can be added. Here, the 154 m grid (Figure 3.2) was designed such that its (eastern) offshore boundary is mostly located in a 20-30 m depth, where the linear approximation is deemed to apply. In view of this, the methodology used for simulating tide-tsunami interactions with FUNWAVE-TVD in the James River will be to: (i) obtain the unscaled tide components along the boundary of the 154 m grid from a regional tide model; (ii) perform tide only simulations in the 154 m grid using (i) as boundary condition, for a reference level equal to MHW + SLR = 0.586 NAVD88 (this choice will be discussed

later); (iii) in a few iterative simulations, calibrate the boundary forcing to obtain the expected AWL at Sewells Point, as well as realistic elevations at the other stations in the James River (#3-#5; Figure 3.2); (iv) perform tsunami simulations for each of the 2 selected PMTs (CRT and CVV), to obtain incident tsunami time series of elevation and current along the boundary of the 154 m grid; (v) perform joint tide-tsunami simulations in the 154 m grid, forced by the superimposition of tidal forcing (for a few selected phases) and each incident tsunami wave train along its boundary, and initialized with results of the calibrated tide only simulation; compute time series of the joint tide-tsunami solution along the boundary of the 39 m grid (Figure 3.2); and (vi) perform joint tide-tsunami simulations in the 39 m grid forced by time series along its boundary, and initialized with results of the calibrated tide only simulation.

In this work, the M2 tidal constituents were obtained from OSU's Regional Tidal Solution for the East Coast of America (Egbert et al, 1994, 2002), as unscaled surface elevation and horizontal velocity data, interpolated at the coordinates of all the boundary points of the 154 m grid. Due to the slow quasi-sinusoidal variation of the M2 tide over its 12.42 hour period (44,712 s), a large time step of 1,863 s (31 min) was used to create M2 tide time series; these, however, will be re-interpolated for the actual time steps used by FUNWAVE-TVD. Because of the periodicity, any time step can be used as the first step, allowing the incident tsunamis to be synchronized with various phases of the tides.

The joint tide-tsunami simulations will start with the arrival of the first crest (usually the highest one) in each tsunami wavetrain at the (eastern) offshore boundary of the 154 m grid (Figure 3.2). When this happens, a given phase of the tide will be

assumed to occur on the boundary, leading to a specific time lag in the tide boundary time series, before linearly superimposing them with the tsunami time series; both surface elevation and current computed at this time in the tide-only simulations will be used as initial condition in the 154 m domain.

Because both tide and tsunami are long waves, to the first order, they propagate at the same velocity in the Bay and the James River, so the selected combination of tide and tsunami elevations at the boundary should be preserved up the James River. Nonlinear effects, however, will make the tide and tsunami flows interact and modify their respective propagation; modeling these effects to see whether this potentially lead to more hazardous conditions (i.e., inundation and currents) is the object of this work. To do so, the tide-tsunami superposition will consider 4 different phases of the tide, at the middle of the eastern boundary of the 154 m grid (there will be small spatial variations of the tide along the boundary): (1) maximum tide; (2) T/8 after maximum tide; (3) T/4 after maximum tide (i.e., downward zero crossing tide), and (4) T/8 ahead of maximum tide. The case of a rising tide was a priori eliminated here because it was thought that, in a friction dominated environment such as the James River estuary, the superposition of co-flowing tide and tsunami currents would increase bottom friction dissipation and hence reduce the combined elevation. By contrast, a tsunami moving into an ebbing tide would have a relatively smaller current, causing less bottom friction dissipation and creating a blockage situation that could increase surface elevation.

Because tsunami and tide elevations in the James River are strongly affected by bottom friction, one needs using a realistic friction coefficient value. Data,

however, is lacking in this respect and we will thus use the typical value for coarse sand, which is prevalent in the region, C_d = 0.0025. This is the same value as used in the NTHMP work to model tsunami inundation on typical beaches (such as for nearby Virginia beach). Because tide data is available in the Bay and the James River for 12 NOAA stations, in the calibration of the tide-only simulations, we will verify that given this friction coefficient, simulations of average tides are in good agreement with field data.

3. Modeling of incident tsunami sources

3.1 Modeling of near-field CRT-SMF source

Tsunami generation from the near-field Currituck SMF (CRT; Figure 3.4) is simulated with the 3D model NHWAVE, using space and time varying bottom boundary conditions, calculated from the SMF geometry and kinematics. The latter are expressed using Grilli and Watts' (2005) and Enet and Grilli's (2007) approach, assuming a rigid slump motion, based on the CRT-SMF parameters: length b = 30 km, width w = 20 km, thickness T = 0.75 km, slope angle 4 deg., direction of failure due east, and center of the SMF located at 74.61W and 36.39N. This yields a SMF runout of s_f = 15.8 km and a failure time of motion of t_f = 710 s (11.8 min.); details can be found in Grilli et al. (2014). Using this kinematics NHWAVE simulations are performed in a 3D grid made of a 500 meter resolution horizontal Cartesian grid (Figure 3.4) and 3 sigma layers in the vertical direction. This yields the surface elevation shown in Figure 3.3b at t = 13.3 min., after the SMF has stopped moving,

which is identical to that found in earlier NTHMP work (Grilli et al. 2013b, 2014); at this time, surface elevation ranges between -20 and +20 m. The CRT tsunami simulations are pursued in FUNWAVE-TVD by re-interpolating the SMF source at 13.3 min. onto the 20 arc-sec grid. Note that sensitivity analyses performed.

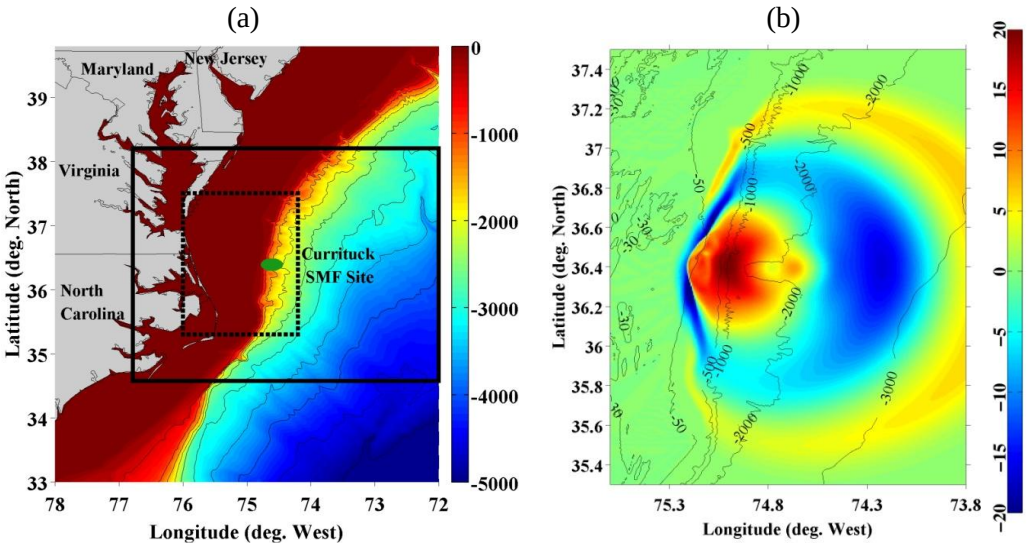

Figure 3.4 (a) Area of the historical Currituck SMF (green ellipse is the footprint of the unfailed SMF centered at 74.61W and 36.39N), with depth in meter in the color scale. The solid black box marks the boundary of a 500 m resolution grid used in NHWAVE simulations (3 sigma-layers) to compute the SMF tsunami source up to 13.3 min. after triggering; and (b) surface elevation (color scale is in meter) computed at 13.3 min. with NHWAVE, shown in the dashed box of plot (a). Bathymetric contours are marked in meter. [From Grilli et al. (2013b, 2014).]

Figure 3.5a shows the surface elevation at 13.3 min. re-interpolated in the 20 arc-sec grid, and Figures 3.5b and 3.5c show surface elevations computed with FUNWAVE-TVD at 34 min and 1h10 min., respectively, after SMF triggering. At the latter time, large elevation and depression waves, nearly +5 m and -4 m, respectively, are seen to propagate towards the mouth of Chesapeake Bay and even larger waves are heading for the coast of Virginia Beach, VA and south of it. [Note, in Figure 3.5c, south and north of the grid, there are slight artifacts caused by the sponge layers; these

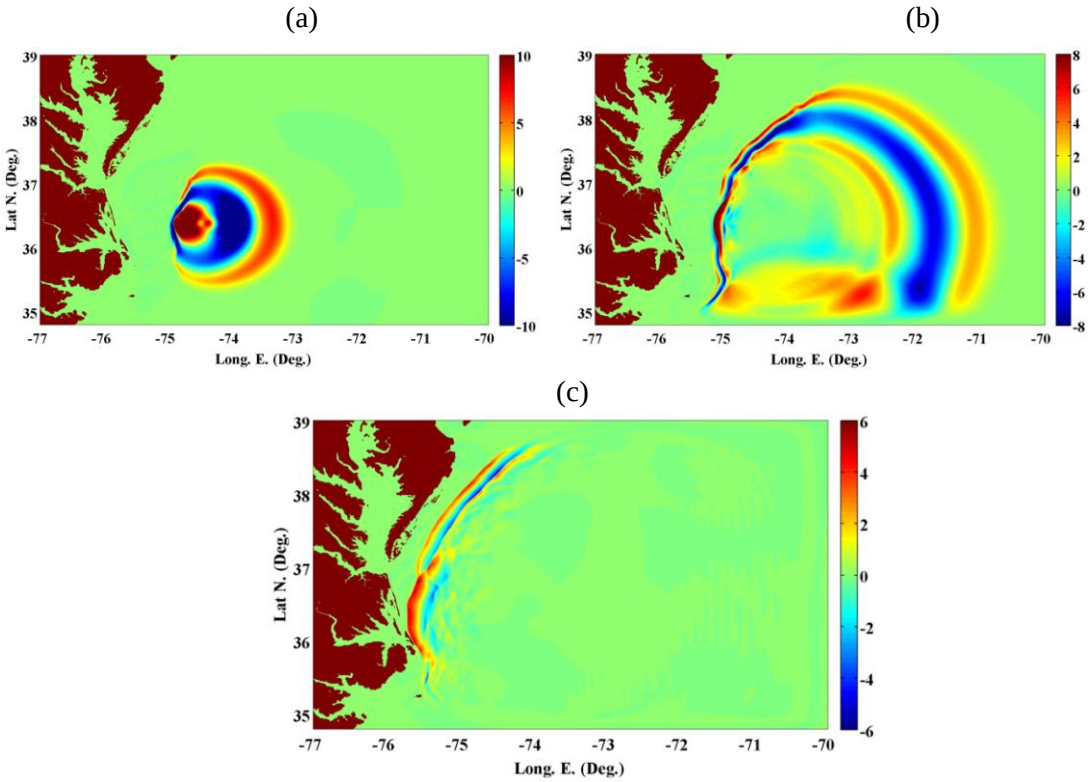

Figure 3.5 FUNWAVE-TVD simulations of the CRT-SMF tsunami in the 20 arc-sec grid (Figure 3.2; Table 3-2). Surface elevation computed at *t* = (a) 13.3 min.; (b) 34 min.; and (c) 1h10 min., after SMF triggering. Color scale is in meter.

do not affect results in the area of interest near the Chesapeake Bay mouth.] The large size of waves heading for the coast is confirmed in Figure 3.6, which shows the envelope of maximum surface elevations computed between 30 min. and 6h15 min. (where the initial time is selected to eliminate the large waves near the source that would make the figure less readable). The incident wave train of the CRT-SMF tsunami is shown in Figure 3.7. At the southeast corner of the 154 m grid (-77.2E, 36.5N), a very large elevation wave of about 9 m is seen to be heading for the coast south of Virginia. This is a location directly west of the Currituck failure, which is east-west oriented and has a center at 36.39N (Figure 3.4a), where the largest waves are expected to be found. Further north, east of the Chesapeake Bay mouth (-75.2E,

37.15N), the incident wave train has two leading waves, reaching up to +4 m, with a minimum of -4 m. Using such tsunami time series as boundary conditions, computations will be pursued by one-way coupling in 2 more levels of nested Cartesian grids (154 and 39 m; Figures 3.2 and 3.3), in combination with tidal forcing. This is detailed later.

3.2 Modeling of far-field CVV source

In accordance with earlier NTHMP studies (Grilli and Grilli, 2013b; Harris et al., 2104), FUNWAVE-TVD is used to compute the transoceanic propagation of Abadie et al.'s 450 km^3 CVV collapse scenario, in the 1 arc-min ocean basin grid (Figure 3.1; Table 3-1). The model is initialized from the surface elevation and horizontal velocity computed with THETIS at 20 min. into the event (Figure 3.8).

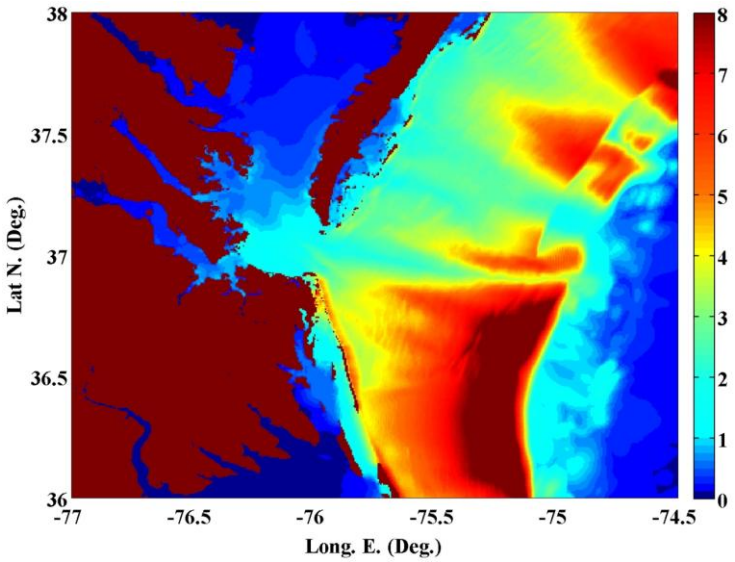

Figure 3.6 Maximum envelope of surface elevation (color scale in meter) in FUNWAVE-TVD simulations of the CRT-SMF tsunami, in a zoom-in of the 20 arc-sec grid (Figure 3.2; Table 3-2), from 30 min. up to 6h15 min. of propagation.

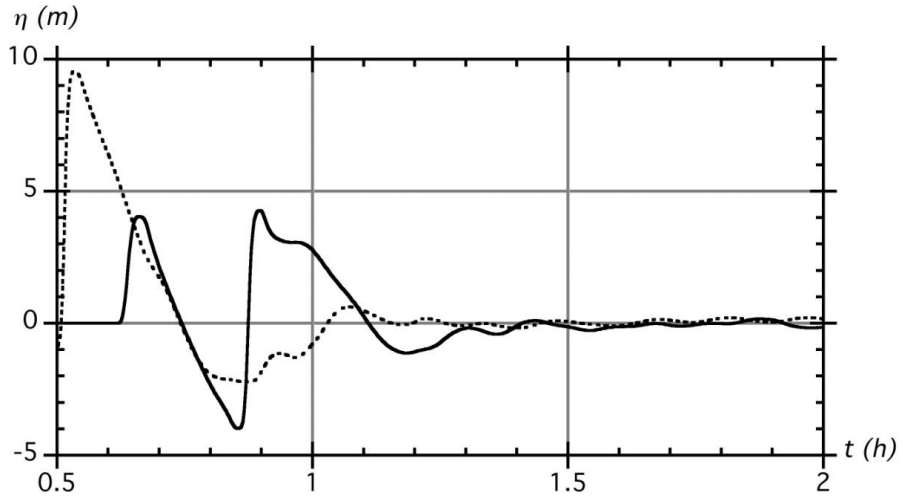

Figure 3.7 FUNWAVE-TVD simulations of the CRT-SMF in 20 arc-sec FUNWAVE grid (Figure 3.2, Table 3-2). Time series of surface elevation computed at the 154 m grid (Table 3-3): (dash line) southeast corner (36.5N; -75.2E); (solid line) middle of eastern boundary, in front of the Chesapeake Bay mouth (37.15N; -75.2E).

Computations are pursued by one-way coupling in the 20 arc-sec resolution grid (Figures 3.1 and 3.2). Figure 3.9 shows the instantaneous surface elevation computed in this grid at 8h20 min and 9h20 min after the start of the event, and Figure 3.10 shows the envelope of maximum surface elevation computed up to 9h20 min. We see that large elevations of up to 9 m occur off the shelf, east of the Chesapeake Bay mouth; but owing to dissipation over the wide shelf, elevations are reduced to 6 m closer to the Bay mouth, consistent with earlier work (Grilli and Grilli, 2013b; Harris et al., 2014). These large waves are confirmed by the time series of surface elevation shown in Figure 3.11, at the southeast corner of the 154 m grid; we also see the highly dispersive nature of the incident wave train. Using such time series as boundary conditions, computations are then pursued by one-way coupling in 2 more levels of nested Cartesian grids (154 and 39 m; Figures 3.2 and 3.3), in combination with tidal forcing. This is detailed later.

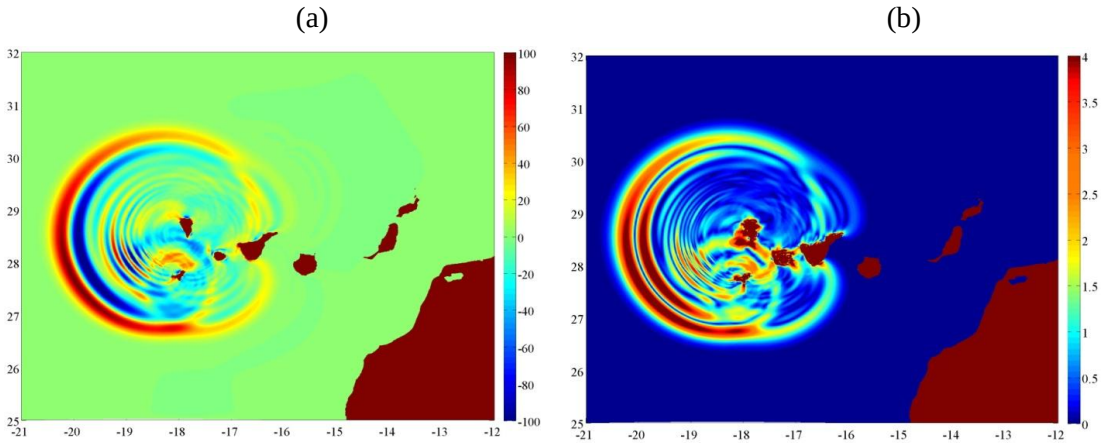

Figure 3.8 (a) Initial surface elevation (color scale in meter), and (b) module of the horizontal velocity (color scale in meter/second), at 20 minutes after the start of the event, for Abadie et al.'s (2012) 450 km^3 CVV subaerial landslide source.

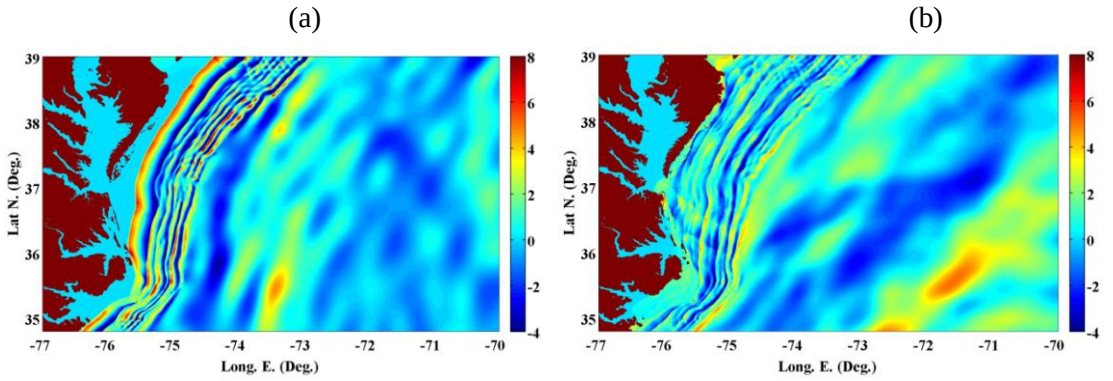

Figure 3.9 Surface elevation (color scale in meter) computed at *t* = (a) 8h20 min.; and (b) 9h20 min., in FUNWAVE-TVD simulation of the 450 km^3 CVV flank collapse in 20 arc-sec grid (Figures 3.1, 3.2; Table 3-2).

4. Modeling and calibrating the extreme tide

We simulate the M2 tide with FUNWAVE-TVD in the 154 m resolution grid (Figure 3.2; Table 3-3) and calibrate it to achieve the AWL at the Sewells Point tide gage, at the mouth of the James River (station #2 in Figure 3.2). The unscaled M2 tide was obtained from the "OTIS Regional Tidal Solution: East Coast of America" (OSU Tidal Prediction Software, version 2beta (OTPS2), at 2 arc-min resolution), as time series of one tidal period (12.42 h or 44,712 s) of surface elevation and horizontal

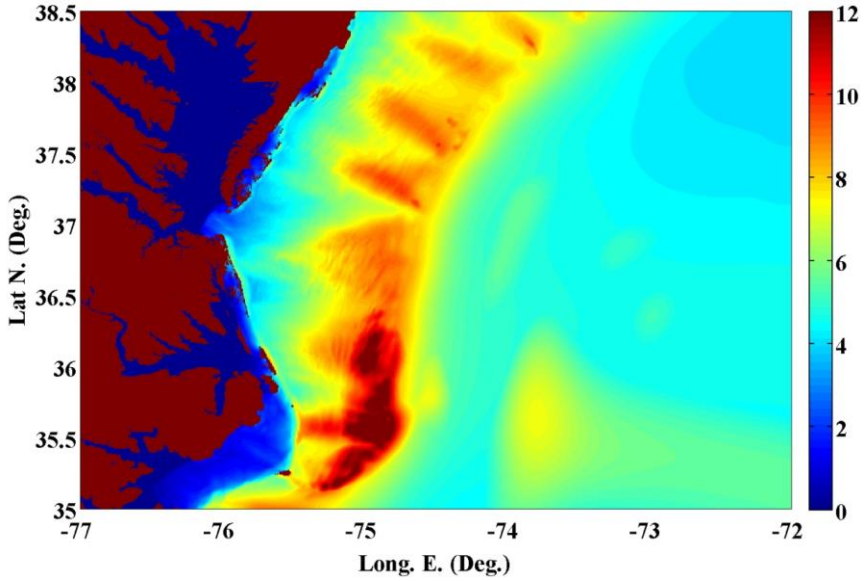

Figure 3.10 Envelope of maximum surface elevation (color scale in meter) computed up to 9h20 min., in FUNWAVE-TVD simulation of the 450 km^3 CVV flank collapse in zoom-in of 20 arc-sec grid (Figures 3.1, 3.2; Table 3-2).

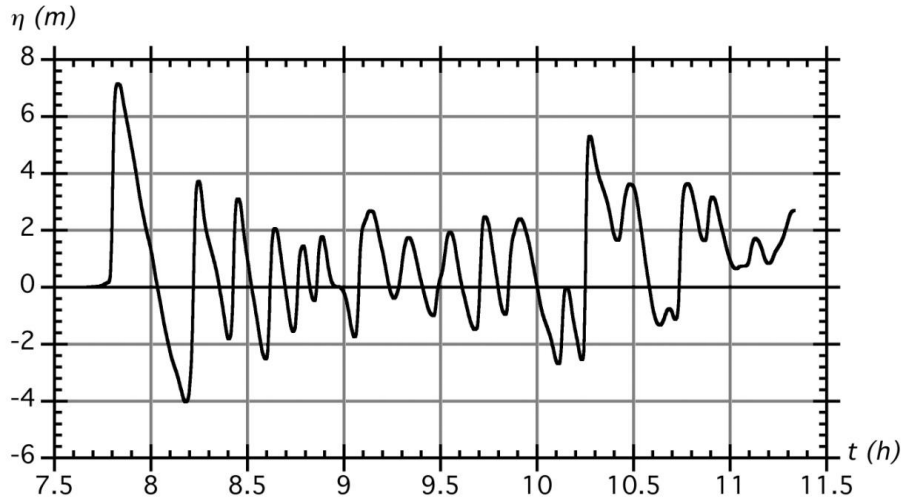

Figure 3.11 Time series of surface elevation computed in FUNWAVE-TVD simulation of the 450 km^3 CVV flank collapse in the 20 arc-sec grid (Figures 3.1 and 3.2; Table 3-2), at the 154 m grid south-east corner (Table 3-3).

current, directly interpolated at the locations of the 154 m grid boundary nodes, to be used as boundary conditions. In FUNWAVE-TVD, time step is a function of grid size

and wave celerity c to achieve a mesh Courant number of about 0.5; thus, in the 154 m grid, where maximum depth is about h_{max} = 45 m (Figure 3.2) and $c_{max} = (g\ h_{max})1/2$ = 21.2 *m/s*, time step is ~ 3.6 *s*. The tide time series were interpolated to provide forcing values at each of these time steps.

The unscaled M2 tide is the mean tide, so this data is used as boundary forcing in a first simulation to verify the agreement of numerical results with mean tidal ranges measured at 12 NOAA tidal stations in the Chesapeake Bay and the James River (Figure 3.2; Table 3-5; http://tidesandcurrents.noaa.gov/stations.html?type=Water+Levels). Then, based on results obtained at Sewells Point (station #2) in this simulation, the tidal forcing along the grid boundary is scaled up by a constant to achieve the expected AWL at Sewells Points. A second simulation is then performed using the scaled up tidal forcing, where it is verified that the AWL is indeed achieved at Sewells Point and corresponding maximum elevations in the James River are adequate for hazard assessment.

Because computations of tides with FUNWAVE-TVD are cold starts, to achieve a quasi-periodicity in the simulations, two full tidal periods will be simulated, plus a quarter period during which tidal forcing (both surface elevation and current) is gradually ramped-up along the 154 m grid offshore boundary (east, north and south) and northern boundary within the Bay (Figure 3.2). Specifically, the tide time series were first shifted in time for the forcing to start with a rising tide (from zero level) near the middle and off of the Chesapeake Bay mouth, along the 154 m eastern boundary. However, because of small spatial phase shifts in the tide along the grid boundary, to have all the station time series starting from a zero surface elevation (and

current) at the beginning of the simulation (thus ensuring model stability), a ramp-up was applied for the first quarter period of the M2 tide, or 3h6', in the form of a "*tanh*" multiplier function varying between 0 and 1 over this interval. Hence, the total tide simulations lasted for 2.25 periods or 100,602 s (~28h).

4.1 Reference level in simulations

Before performing the tide simulations with FUNWAVE-TVD, one needs to establish which reference level should be used. The 154 m grid bathymetry shown in Figure 3.2 is referenced to MHW, which at Sewell Point is 0.287 m NAVD88, implying that the AWL, which is 1.244 m NAVD88, is 0.957 m above MHW; this values includes 0.299 m of sea level rise (SLR) and thus the 10% exceedence tide elevation should be an additional 0.658 m at Sewells Point.

While the logical choice for a reference level might a priori be Mean Sea Level (MSL), which at Sewells Point is -0.079 NAVD88, plus SLR in the present case, there are many uncertainties in surface elevation damping in the model, during tide propagation up the James River (e.g., in relation to bottom friction and grid resolution) as well as other uncertainties in the actual mean sea level associated with the occurrence of an extreme tide elevation (such as the 10% exceedence tide). Therefore, owing to the small difference between MSL and MHW (0.366 m) at Sewells Point, and in view of these uncertainties, for simulating inundation in the James River as a result of the combination of extreme tides and tsunamis, it was deemed more conservative calibrating the dynamic tidal forcing to achieve the AWL at Sewells

Point, using MHW plus SLR as the reference level (i.e., +0.586 m NAVD88); this means adding SLR to the current bathymetry. A comparison of numerical results to actual measurements at NOAA tide gages for the mean tide, as well as other targeted simulations using MSL plus SLR reference level, were conducted that confirmed the relevance of this choice (see details below).

4.2 Mean M2 tide simulation

We first simulate the mean M2 tide in the 154 m grid, with the depth referenced to MHW+SLR, using the mean (unscaled) M2 tide data as boundary condition. Figure 12a thus shows the envelope of maximum surface elevations computed for 2.25 periods of tidal forcing and corresponding time series of surface elevation are plotted in Figure 3.13a, for NOAA stations #1-6 in the James River. Table 3-5 compares maximum minus minimum computed surface elevations and their phases at the 12 NOAA stations (Figure 3.2) to measured tidal ranges and phases provided by NOAA. Overall, errors on tidal range are reasonably small, with the RMS of the relative error for the 12 gauges being 8%. Errors on phases of maximum tides are similarly reasonably small. More specifically, however, while the maximum level is overpredicted in the simulation at stations #1 and #2, near the mouth of the Bay and at Sewells Pt., respectively, when going up the James River, the maximum tide elevation is gradually underpredicted at stations #3 to #6. This over- then under-prediction justifies using a slightly higher reference level in these simulations (i.e., MHW+SLR instead of MSL+SLR), to achieve a maximum level in the James River

closer to the expected value of the AWL, when the scaled M2 tide forcing will be used. This will be seen next.

4.3 Extreme M2 tide simulation

Simulations are run in the 154 m grid using a scale up tidal forcing on its boundary, to achieve AWL at Seawells Point, which requires a maximum tide elevation of 0.66 m when using MHW+SLR as a reference level. In Table 3-5, we see that the tide elevation is 0.41 m at this location, when forcing the simulation with the mean tide. Hence, based on these results the calibration factor to scale up the tidal forcing should be about 0.66/0.41 = 1.61. Because of nonlinear effects in tide propagation (including bottom friction which is enhanced for larger tides), however, a couple of iterations of simulations were necessary to eventually find the calibration of 1.9 that allows achieving the AWL at Sewells Point. The envelope of maximum surface elevation obtained for this scaling is plotted in Figure 3.12b and corresponding time series of surface elevation are plotted in Figure 3.13b, for NOAA stations #1-6 in the James River. In the latter, the time series of surface elevation at Sewells Point (gages #2), confirms that the maximum tide level reaches 0.66 m above MHW+SLR. Further upstream the James River, at station #4, the maximum tide elevation reaches 0.58 m, which is 0.08 m below the maximum elevation at Sewells Point. This is entirely consistent with the NOAA's data for mean tide levels listed in Table 3-5, where the maximum elevation in station #4 is 0.04 m less than that in station #2, yielding 0.076 m after scaling up by a factor 1.9. These results confirm the relevance

of using MHW+SLR as a reference level in simulations aimed at calibrating the extreme tide.

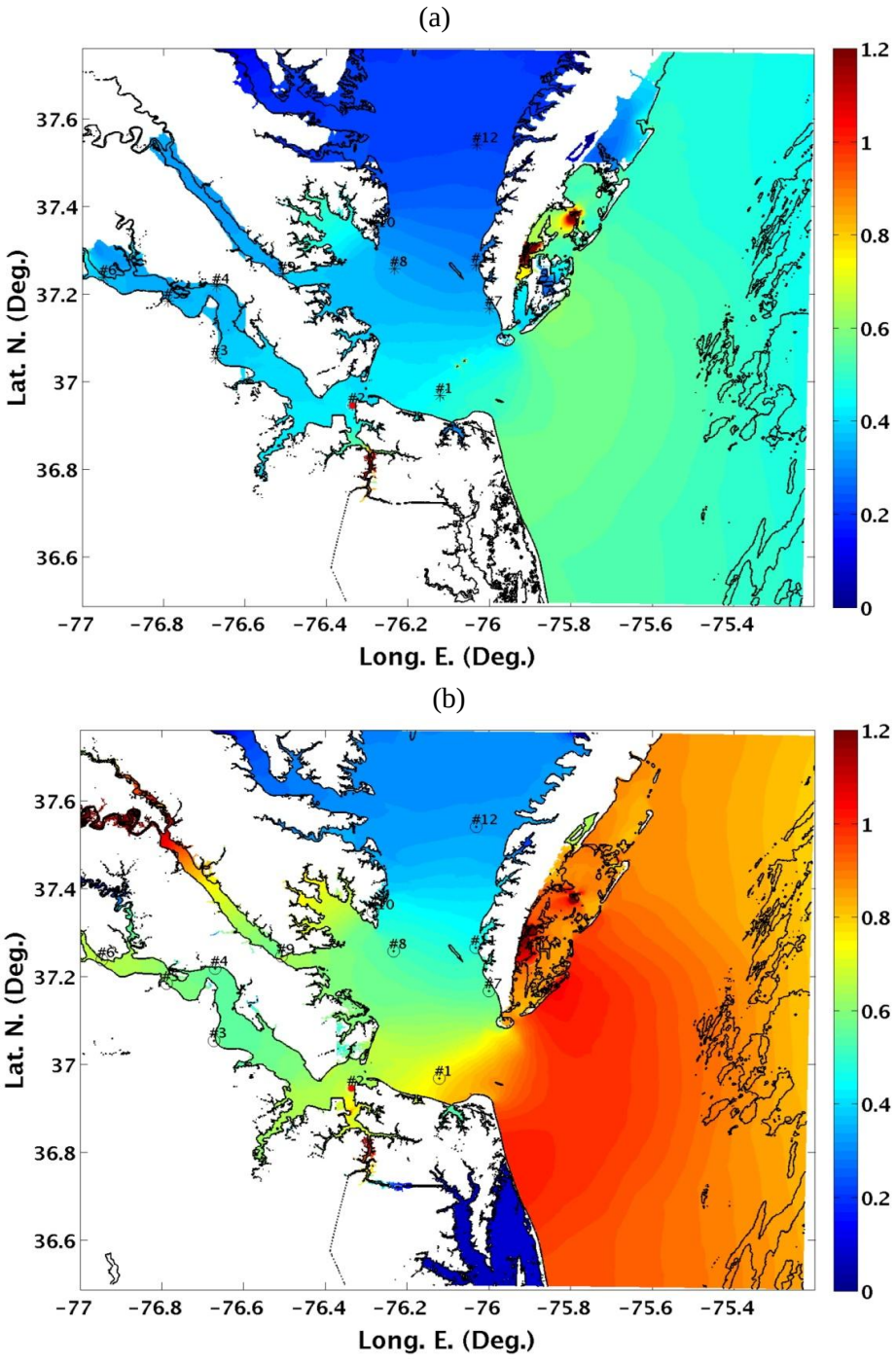

Figure 3.12 Envelope of maximum surface elevation (color scale in meter) computed with FUNWAVE-TVD in the 154 m grid (Figure 3.2; Table 3-3), using MHW+SLR as a reference level, for the M2 tide: (a) mean (unscaled) tidal forcing; and (b) scaled tidal forcing (by a 1.9 factor) to achieve AWL (1.244 m NAVD88) at Sewells Point (gage #2), i.e., 10% exceedance tide. Results are for 2.25 tidal periods of simulation (including a quarter period ramp-up). Numbered circles mark locations of 12 NOAA tide gages (Table 3-5).

Table 3-5 Results of FUNWAVE-TVD computations for the mean (unscaled) M2 tide, in 154 m grid (Figure 3.12a), compared to data at 12 NOAA stations in Chesapeake Bay (Figures 3.2 and 3.3; see http://tidesandcurrents.noaa.gov/stations.html?type=Water+Levels). RMS of relative error on computed range is 8% (based on computed minus reference values).

No.	NOAA Station	Comp. max elevat. (m)	Comp. min elevat. (m)	Comp. range (m)	NOAA range (m)	Relative Error on range (%)	Comp. period (h)	Comp. Phase (from #2) (deg.)	NOAA Phase (from #2) (deg.)
#1	Chesapeake Bay Bridge, VA	0.44	-0.40	0.84	0.76	+9.5	12.50	239.96	220.60
#2	Sewells Point, VA	0.41	-0.37	0.78	0.73	+6.4	12.50	261.70	261.70
#3	Burwell Bay, James River, VA	0.39	-0.24	0.63	0.71	-12.7	12.58	305.18	299.30
#4	Kingsmill, VA	0.37	-0.14	0.51	0.66	-22.7	12.50	343.83	318.00
#5	Scotland, VA	0.35	-0.12	0.47	0.57	-17.8	12.58	360.73	339.20
#6	Tettington, James River, VA	0.37	-0.08	0.45	0.52	-14.4	12.42	46.63	10.60
#7	Kiptopeke, VA	0.37	-0.38	0.75	0.78	-2.9	12.58	244.79	247.50
#8	New Point, VA	0.34	-0.30	0.64	0.62	+3.6	12.50	259.28	256.00
#9	Gloucester Point, VA	0.36	-0.31	0.67	0.72	-7.0	12.67	256.87	268.60
#10	New Point, VA	0.30	-0.20	0.50	0.49	+2.0	12.42	264.12	262.70
#11	Cape Charles Hbr, VA	0.28	-0.30	0.58	0.68	-14.7	12.42	259.28	259.40
#12	Rappahannock Light, VA	0.22	-0.20	0.42	0.48	-11.5	12.50	295.52	301.90

Figure 3.14 shows plots of instantaneous tide-induced currents (both magnitude and direction) for the calibrated M2 tide simulation, for 5 stages separated by 3h6 min (186 min.), thus nearly covering one tidal period. Figure 3.15 shows the corresponding time series of current magnitude at tide stations #1-6. Fig 3.14a shows the simulation after 755 s which, based on the time series shown in Figures 3.13b and 3.15, corresponds to a stage where the surface elevation at station #4, upstream the James River, is decreasing and is about 0.16 m below the reference level, and the ebb

currents are large (flowing out of the James River), at about 0.5 m/s (1 knot) near station #5 (less at the tide gage station #4, about 0.3 m/s, because it is near the shore). This stage repeats itself in Figure 3.14e. Another stage of the simulation with both large currents and elevation near station #4 is shown in Figure 3.14c, after 1135 s, for which Figures 3.13b and 3.15 indicate that the surface elevation at station #4 is about 0.53 m and the flooding currents (flowing into the James River) are again large, about 0.5 m/s (about 0.35 m/s at station #4). At other locations in the James River, currents reach up to 0.9 m/s depending on the stage of the tide (locally more).

In the combined tide-tsunami simulations presented next, we will show which stage of the tide (i.e., combination of tidal elevation and current when the main tsunami waves propagate up the river) leads to the worst-case scenario in terms of inundation in the James River.

(a)

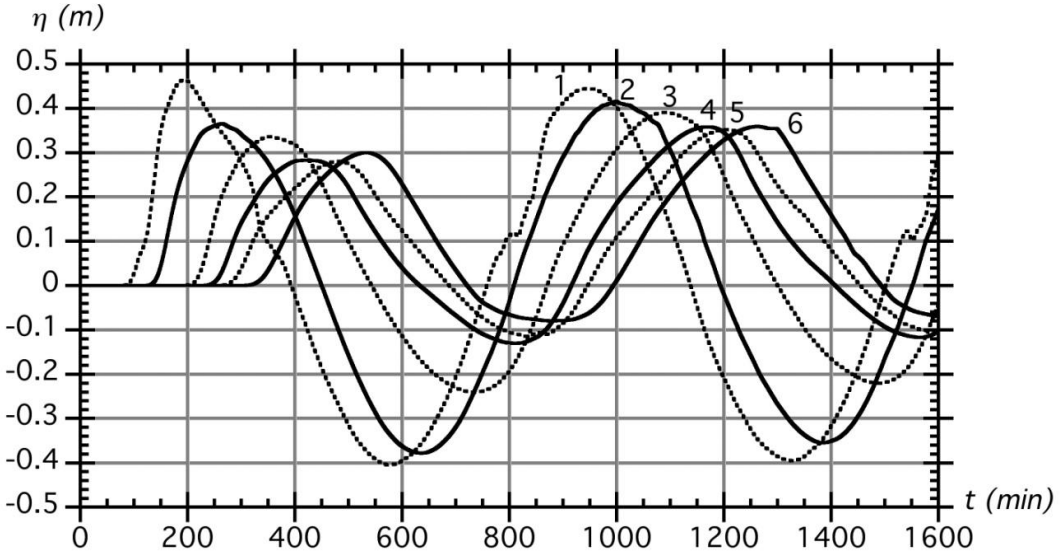

(b)

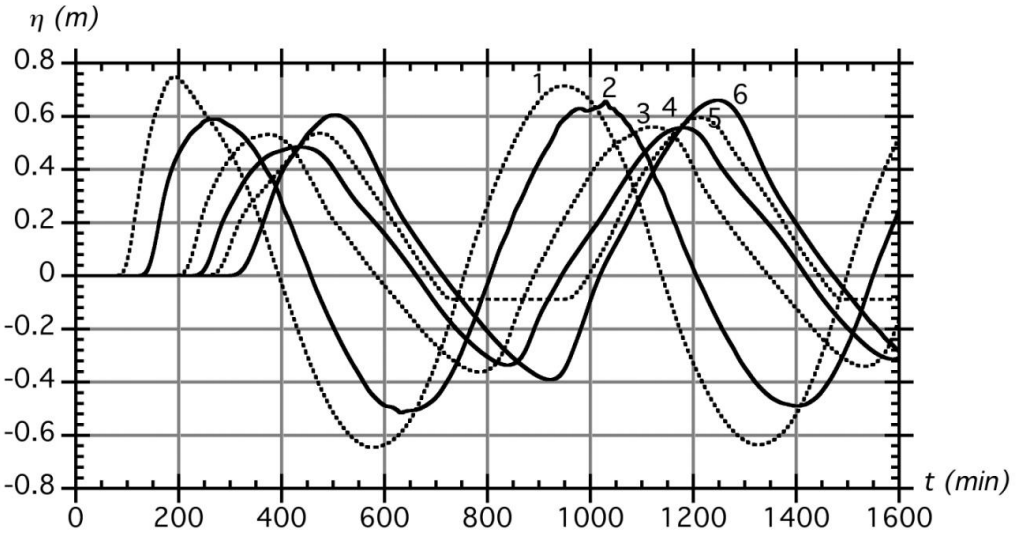

Figure 3.13 Time series of surface elevation computed at NOAA stations #1-6 in the James River (Table 3-5), with FUNWAVE-TVD in the 154 m grid (Figure 3.2; Table 3-3), using MHW+SLR as a reference level, for the M2 tide: (a) mean (unscaled) tidal forcing (case of Figure 3.12a); and (b) scaled tidal forcing (by a 1.9 factor; case of Figure 3.12b) to achieve AWL (1.244 m NAVD88; 0.957 MHW) at Sewells Point (gage #2), i.e., 10% exceedance tide. Results are for 2.25 tidal periods of simulation (including a quarter period ramp-up).

(a)

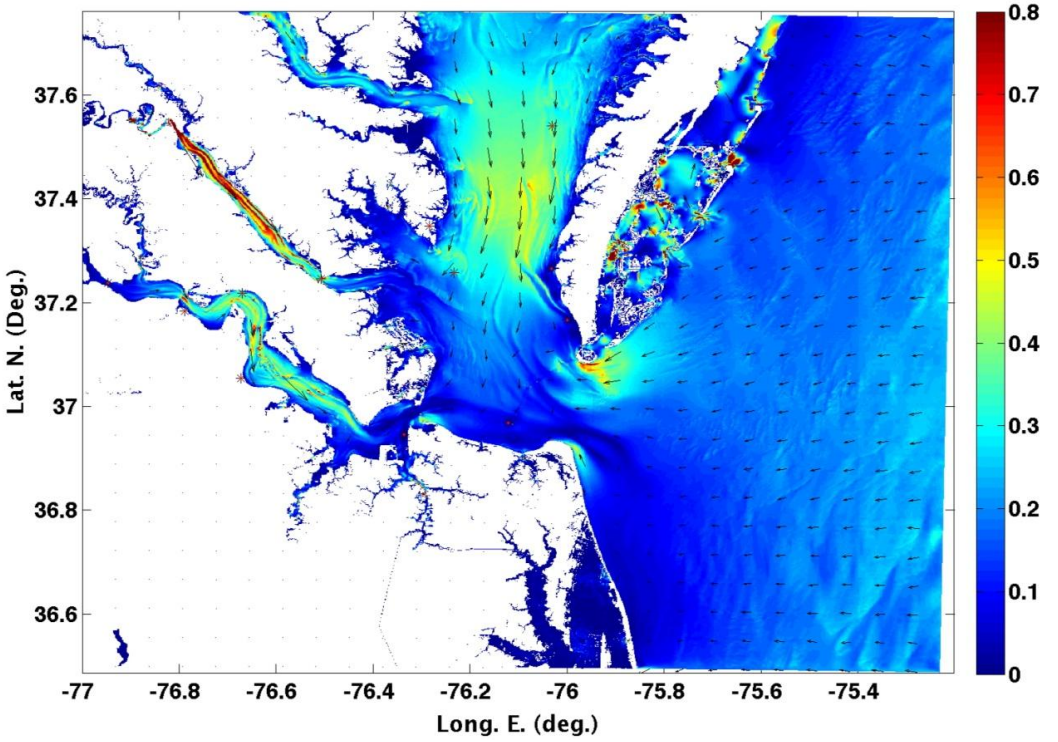
Lat. N. (Deg.)
37.6
37.4
37.2
37
36.8
36.6
-77
-76.8
-76.6
-76.4
-76.2
-76
-75.8
-75.6
-75.4
Long. E. (deg.)
0.8
0.7
0.6
0.5
0.4
0.3
0.2
0.1
0

(b)

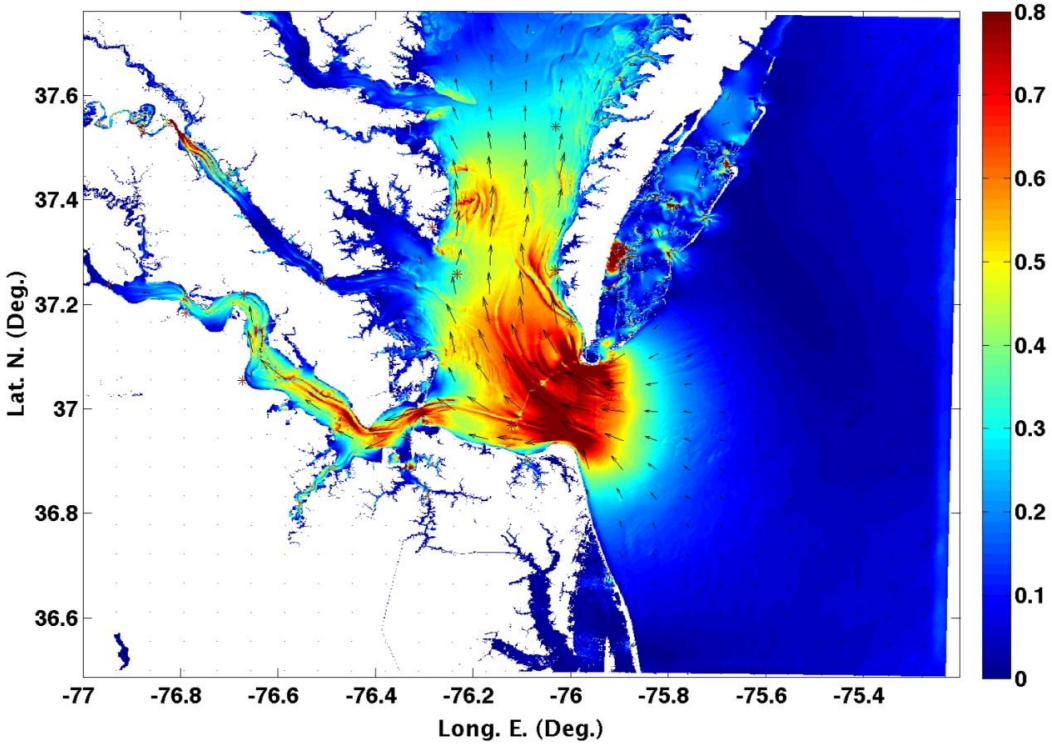
Lat. N. (Deg.)
37.6
37.4
37.2
37
36.8
36.6
-77
-76.8
-76.6
-76.4
-76.2
-76
-75.8
-75.6
-75.4
Long. E. (Deg.)
0.8
0.7
0.6
0.5
0.4
0.3
0.2
0.1
0

(c)

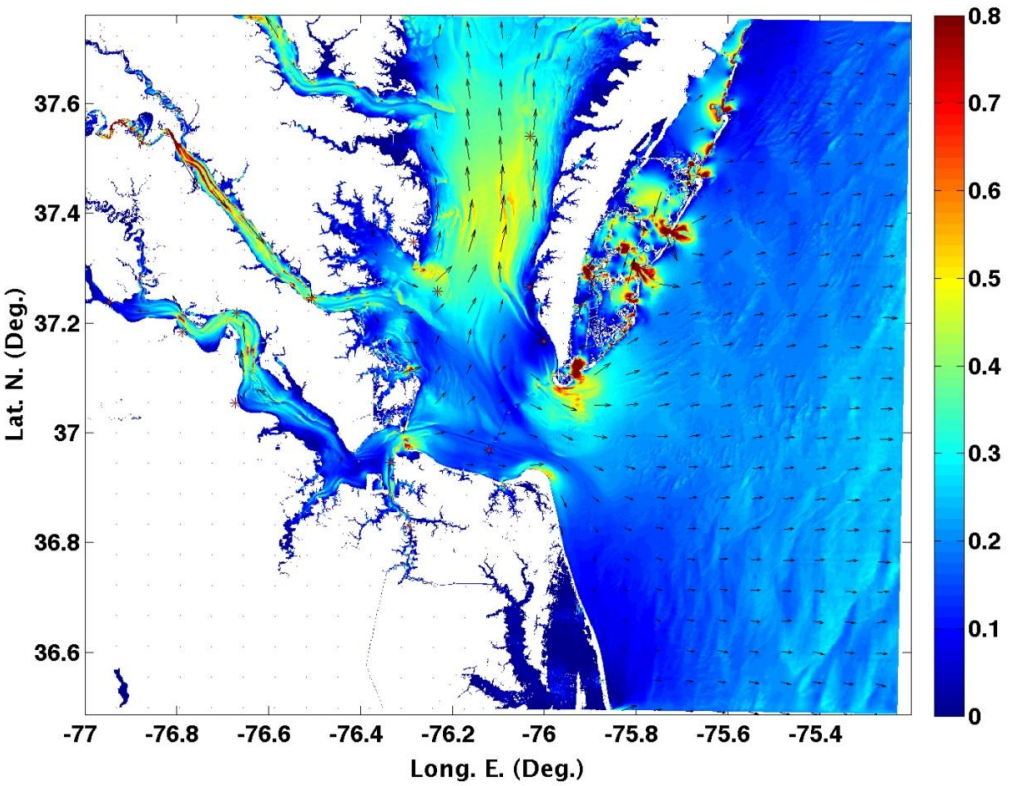
Lat. N. (Deg.)
37.6
37.4
37.2
37
36.8
36.6
-77
-76.8
-76.6
-76.4
-76.2
-76
-75.8
-75.6
-75.4
Long. E. (Deg.)
0.8
0.7
0.6
0.5
0.4
0.3
0.2
0.1
0

(d)

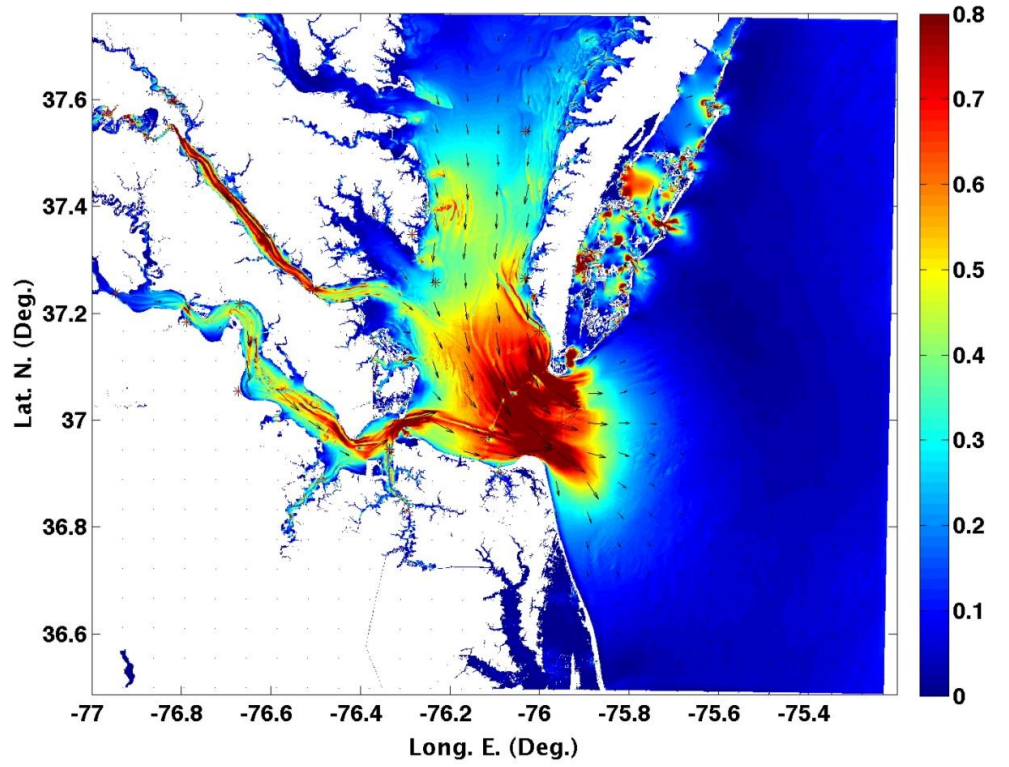
Lat. N. (Deg.)
37.6
37.4
37.2
37
36.8
36.6
-77
-76.8
-76.6
-76.4
-76.2
-76
-75.8
-75.6
-75.4
Long. E. (Deg.)
0.8
0.7
0.6
0.5
0.4
0.3
0.2
0.1
0

(e)

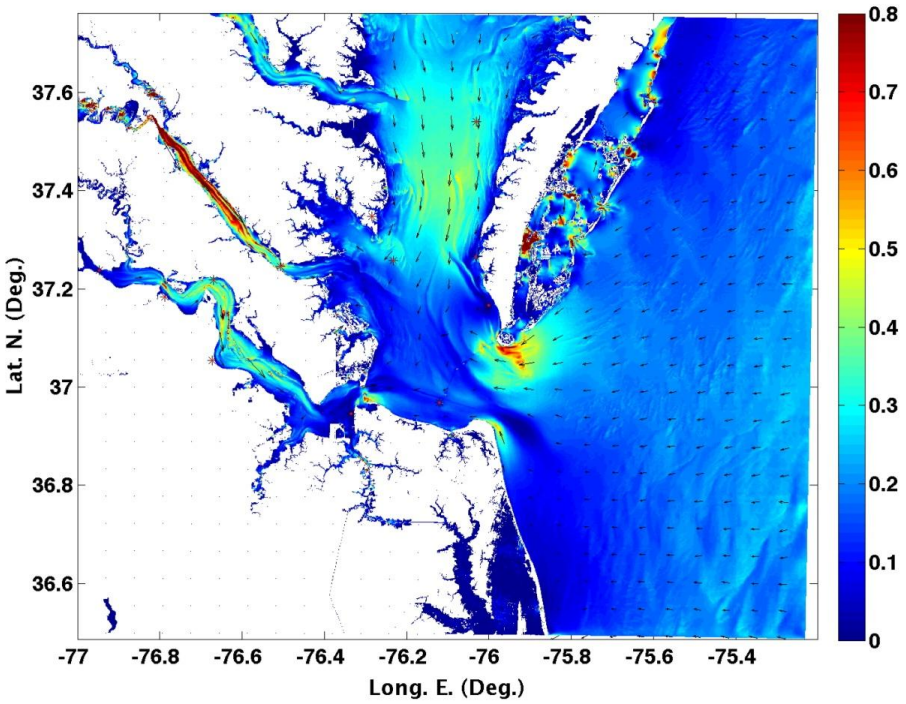

Figure 3.14 Instantaneous current magnitude (color scale in m/s) and direction (arrows) computed with FUNWAVE-TVD in the 154 m grid (Figure 3.2; Table 3-3), using MHW+SLR as a reference level, for the scaled M2 tide (by a 1.9 factor; case of Figure 3.12b). Results are at t = (a) 755; (b) 945; (c) 1135; (d) 1325; and (e) 1515 min. into the simulation (186 min. intervals, about a quarter period). Red stars mark locations of NOAA tide gage stations (see Table 3-5).

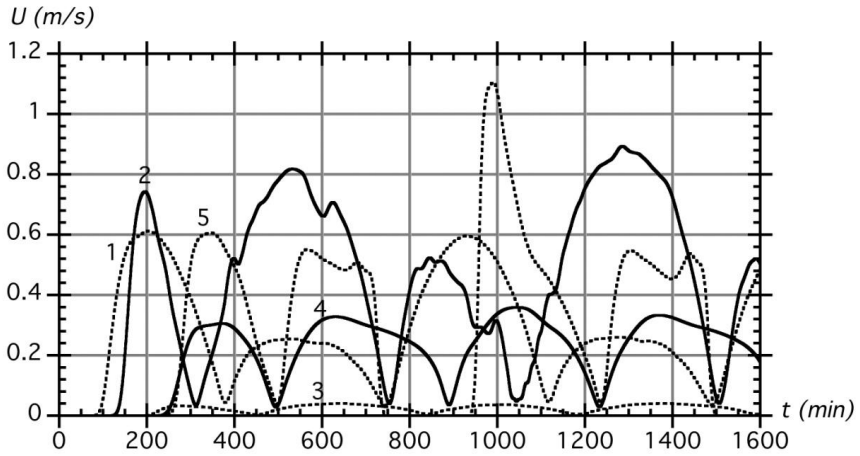

Figure 3.15 Time series of current magnitude at NOAA stations #1-5 in the James River (Table 3-5), computed with FUNWAVE-TVD in the 154 m grid (Figure 3.2; Table 3-3), using MHW+SLR as a reference level, for the scaled M2 tide (by a 1.9 factor; case of Figure 3.12b).

5. Modeling tide-tsunami interactions

We perform joint simulations with FUNWAVE-TVD of tide and tsunami interactions by superimposing time series of incident CRT and CVV wave trains and the calibrated (scaled up) M2 tide that creates AWL conditions for the MHW+SLR reference level, along the boundary of the 154 m grid. Simulations will be performed in this grid and continued by one-way coupling in the finer nested 39 m grid (Figure 3.3), in order to more accurately resolve tsunami inundation in the James River and study tide-tsunami interactions.

Because both tide and tsunami are long waves, they are expected to propagate at the same phase speed in the shallow waters of the Chesapeake Bay and the shelf off of it. Hence, to the first-order (i.e., neglecting nonlinear effects) if one superimposes a phase of the tide with the maximum elevation in the tsunami train (here the first crest) along the offshore boundary of the 154 m grid, then one should expect those "phases" to propagate together, including up the James River. Nonlinearity, however, will affect this superposition and both create time lags between tide and tsunami maxima and spreading out of the tsunami wave train, particularly when the current (of either the tide, the tsunami or both) is large.

The first tidal phase (referred to as TT1) we consider is when both tide and maximum tsunami waves are synchronized on the offshore boundary, thus causing maximum elevation in the James River by way of superposition. The second situation (referred to as TT2) is selected when the tide level is starting to decrease from its maximum, by specifying the maximum tsunami at about one-eighth tidal period after

the maximum tide. The third phase (referred to as TT3) is selected when the ebb current is quite large in the river (e.g., Figure 3.14d), thus flowing against the incoming tsunami and possibly causing it to shoal up; this is achieved by specifying the maximum tsunami when the tide is crossing the zero level going down, at one-fourth tidal period after the maximum tide. Finally, a last phase (referred to as TT4) is selected at one-eight tidal period ahead of the maximum tide, thus superposing the maximum tsunami with a rising tide.

Full details of results will be provided for the TT1 case, for both the CVV and CRT tsunamis. Then, we will show comparisons of selected results obtained for the four phases of the tide, in order to assess which tide-tsunami interaction processes lead to increased inundation in the river.

5.1 Joint simulations of maximum tide and tsunami (TT1)

Far-field subaerial landslide (CVV). Figure 3.16a shows the superposition of the incident CVV tsunami wave train with the calibrated M2 tide elevation at the SE corner of the 154 m grid, for the TT1 phase situation; as expected, the maximum tsunami and tide elevations have been synchronized. On the same figure, we see the computed time series at the Sewells Pt. reference station (NOAA tide gauge #2; Table 3-5). We see that there is a strong reduction of the CVV tsunami elevation across the wide shelf and in the shallow entrance of the Chesapeake Bay, due to both directional spreading and dissipation of the larger incident waves by bottom friction and breaking. From a maximum elevation of 8 m on the offshore boundary of the 154 m grid, the

tsunami elevation at Sewells Pt. is reduced to 1.7 m. Many of the smaller oscillations in the incident wavetrain also have disappeared.

Computations are pursued by one-way coupling in the 39 m grid. Figure 3.16b first shows that there is a good agreement of the tsunami surface elevation computed at Sewells Pt. in both grids, with expectedly more higher frequency oscillations occurring in the 39 m grid, owing to the better resolution.

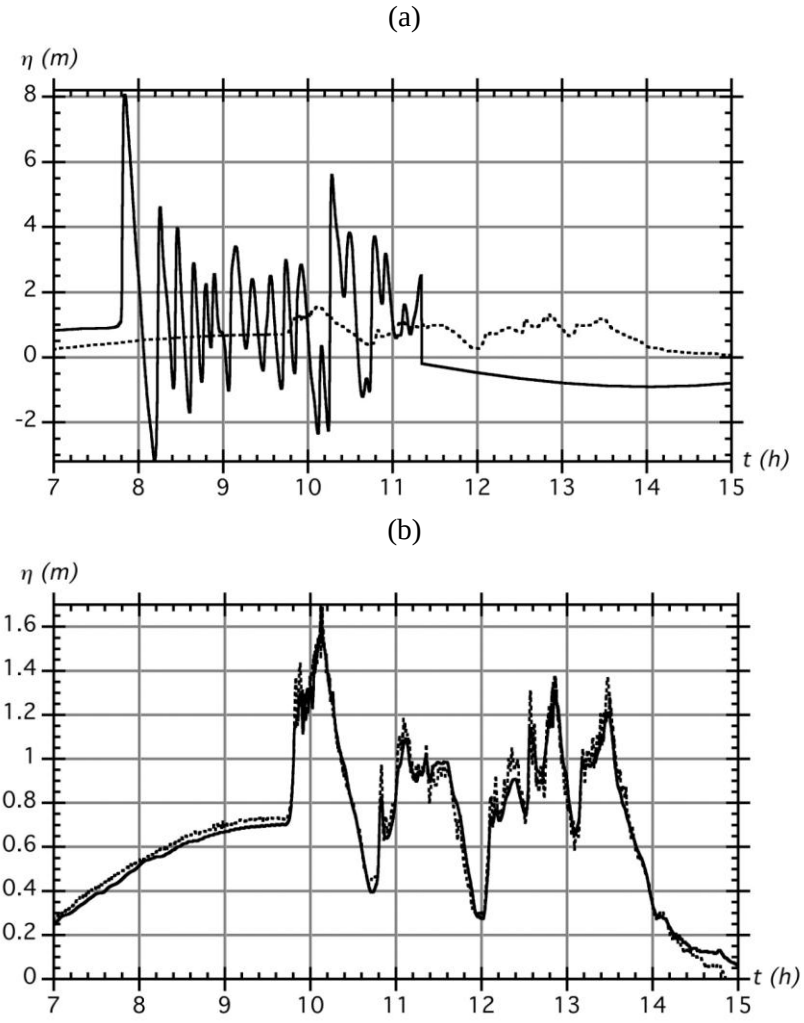

Figure 3.16 Simulation with FUNWAVE-TVD (MHW+SLR reference level) of the calibrated M2 tide plus CVV tsunami (TT1 phase situation). Time series of surface elevation at: (a) SE corner (solid) and NOAA station #2 Sewells Pt (dashed), in 154 m grid (Figure 3.2); (b) at NOAA station #2 Sewells Pt, in 154 m grid (solid) and in 39 m grid (Figure 3.3) (dashed). Time is from the start of the CVV event.

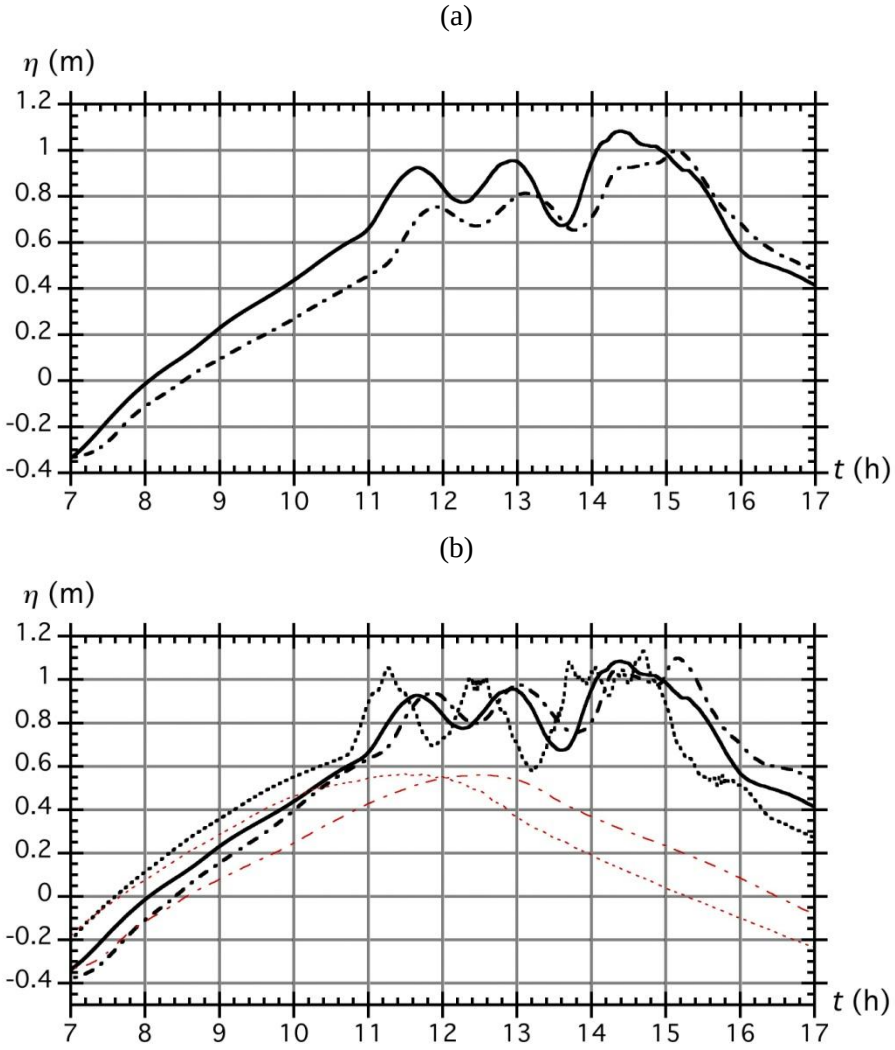

Figure 3.17 Simulation with FUNWAVE-TVD (MHW+SLR reference level) of the calibrated M2 tide plus CVV tsunami (TT1 phase situation). Time series of surface elevation at: (a) "river station" (Figure 3.3), in 154 m (chained) and 39 m grids (solid); (b) Station #3 (thick dashed), Station #4 (thick chained) and the "river station" (thick solid) in 39 m grid. Thin red lines in (b) show the tide only results at Stations #3 and #4. Time is from the start of the CVV event.

Figure 3.17a then compares the surface elevations computed at the so-called "river station" (Figure 3.3), located upstream and in the middle of the James River (-76.64 E, 37.15 N), in the 154 m and 39 m grids. The agreement is good, but elevations in the finer grid are up to 0.15 m higher than in the coarser grid, which justifies using the 39 m grid to compute tsunami inundation levels in the James River. Compared to

Figure 3.16 at Station #2, we also see that during its propagation up the James River, the tsunami wave train has lost all of its higher-frequency oscillations and is reduced to three main oscillations of about 1.5 hour period; also, unlike in Figure 3.16, the larger elevations occur later in the wave train. Figure 3.17b then shows results computed in the 39 m grid at NOAA Stations #3 and #4, with the "river station" used as a reference (Figure 3.3), compared to surface elevations obtained for the calibrated M2 tide only. As expected for TT1, the leading tsunami and tide elevations are almost synchronized. However, higher surface elevations are seen to occur for later times in the wave train, likely due to an enhancement of smaller incident tsunami waves by the ebbing tidal currents.

Finally, Figure 3.18 shows the envelope of maximum surface elevation computed for this case in both the 154 m and 39 m grids. While at and near the James River mouth, maximum tsunami inundation reaches 2-2.5 m, in the river, however, we see a significant decrease in maximum inundation, in the 1.1-1.5 m range. Nevertheless, Figure 3.18b shows that many low lying areas of the river banks would be flooded.

Near-field Submarine Mass Failure (CRT). Figure 3.19a shows computed time series at Sewells Point (NOAA station #2; Table 3-5) of the CRT tsunami elevation with the calibrated M2 tide, in both the 154 m and 39 m grids. As expected, the maximum tsunami and tide elevations have been synchronized. Comparing to the large incident tsunami elevation (without tide) at the offshore boundary of the 154 m

grid shown in Figure 3.7, similar to the CVV case, there has been a strong reduction of the tsunami

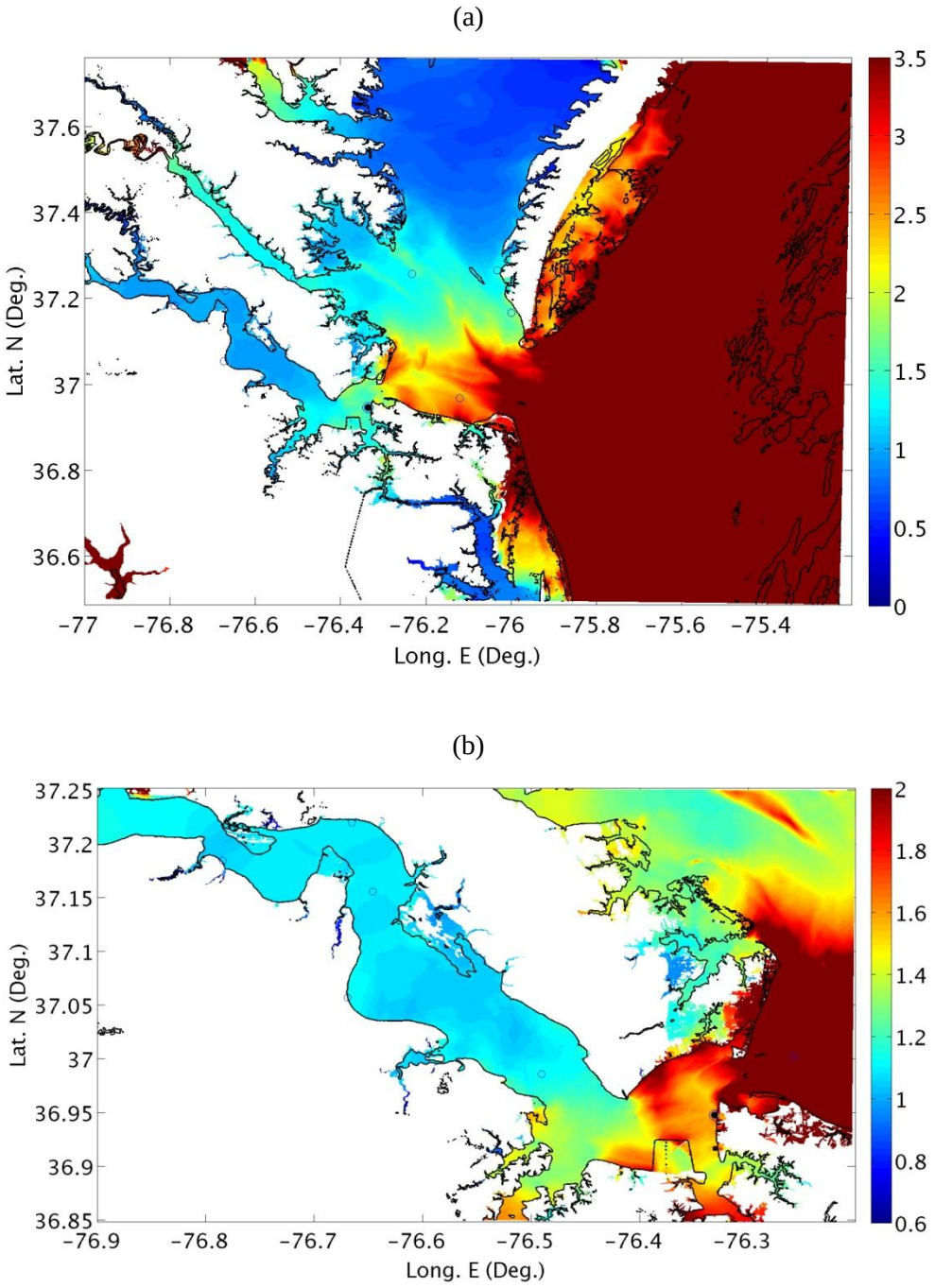

Figure 3.18 Simulation with FUNWAVE-TVD (MHW+SLR reference level) of the calibrated M2 tide plus CVV tsunami (TT1 phase situation). Envelope of maximum surface elevation in: (a) 154 m grid; (b) 39 m grid. Circles mark locations of the NOAA stations (Table 3-5) and the "river station"; solid circle symbol is Sewells Point (Station #2).

(a)

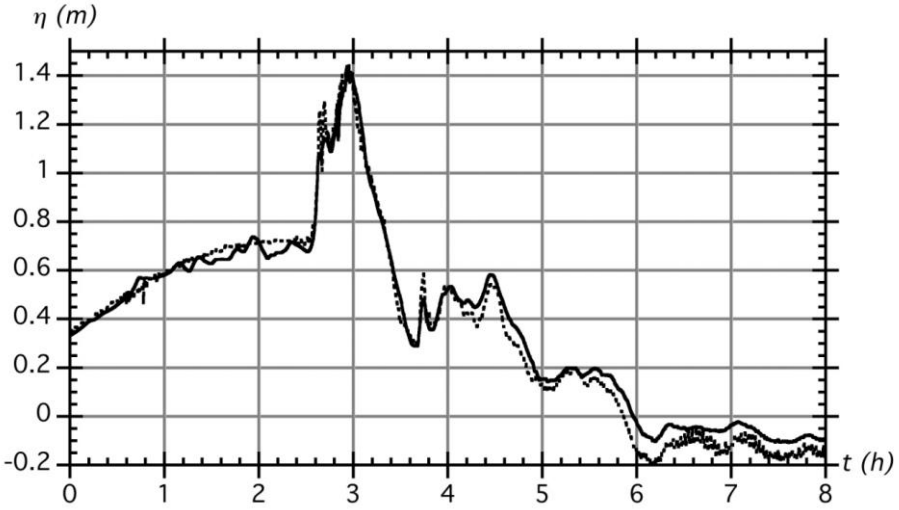

(b)

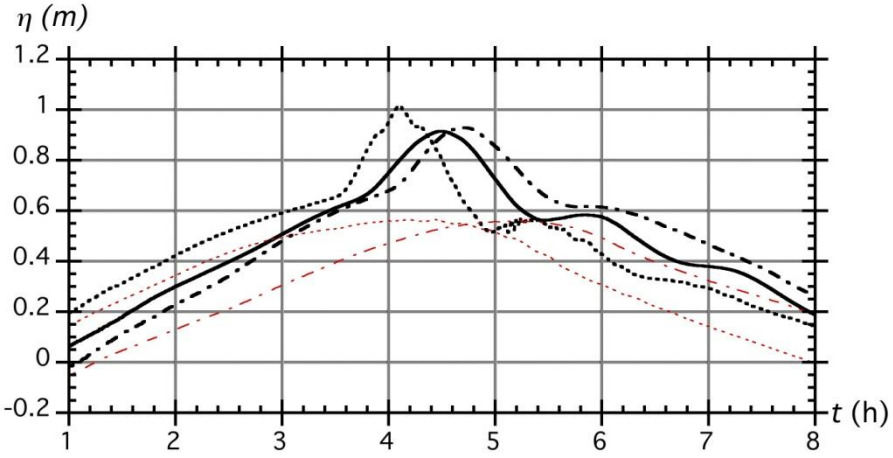

Figure 3.19 : Simulation with FUNWAVE-TVD (MHW+SLR reference level) of the calibrated M2 tide plus CRT tsunami (TT1 phase situation). Time series of surface elevation at: (a) Sewells Point (Figure 3.3), in 154 m (solid) and 39 m grids (dashed); (b) Station #3 (thick dashed), Station #4 (thick chained) and the "river station" (thick solid) in 39 m grid. Thin red lines in (b) show the tide only results at Stations #3 and #4. Time is from the start of the CRT event.

elevation across the wide shelf and the shallow entrance of the Bay, due to both directional spreading and dissipation of the large incident waves by bottom friction and breaking. From a maximum elevation of 4-9 m along the offshore boundary of the 154 m grid, the tsunami elevation at Sewells Point is reduced to 1.45 m.

(a)

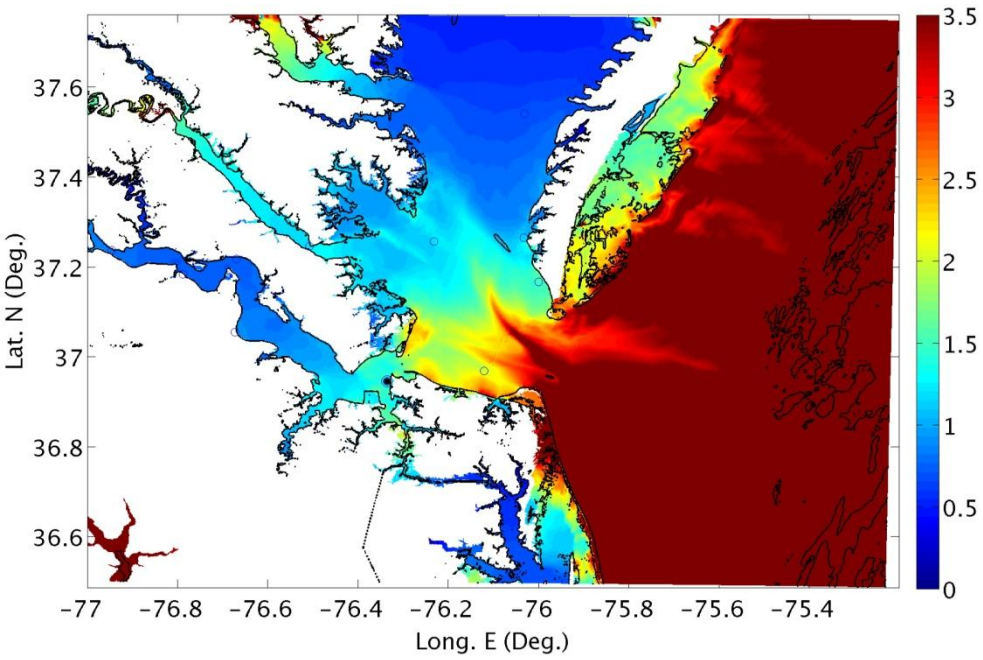

(b)

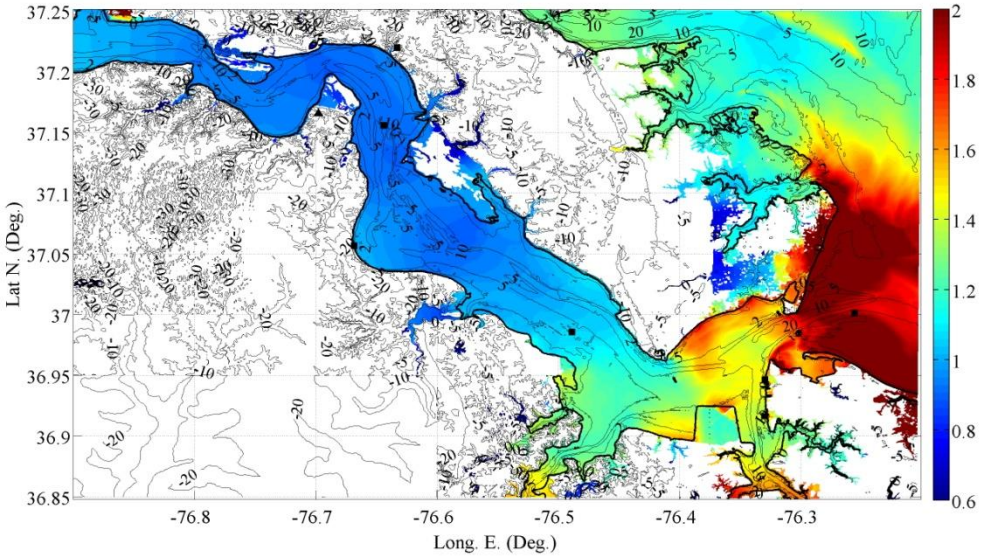

Figure 3.20 Simulation with FUNWAVE-TVD (MHW+SLR reference level) of the calibrated M2 tide plus CRT tsunami (TT1 phase situation). Envelope of maximum surface elevation in: (a) 154 m grid; (b) 39 m grid. Circles/black squares mark locations of the NOAA stations (Table 3-5) and the "river station"; solid circle symbol is Sewells Point (Station #2).

Similar to the CVV case, Figure 3.19b shows results computed in the 39 m grid at NOAA Stations #3 and #4, with the "river station" used as a reference (Figure 3.3), compared to surface elevations obtained for the calibrated M2 tide only. The

leading tsunami and tide elevations are again almost synchronized but this time the highest combined surface elevations occur for the leading crest in the wave train, with about 0.9-1 m above the MHW+SLR reference level. Compared to Figure 3.19a at Station #2, we again see that during its propagation up the James River, the tsunami wave train has lost all of its higher-frequency oscillations and as for CVV is reduced to three main oscillations of about 1.5 hour period.

Finally, Figure 20 shows the envelope of maximum surface elevation computed for this case in both the 154 m and 39 m grids. While at and near the James River mouth, maximum tsunami inundation reaches 1.5-2 m, in the river, however, we see a significant decrease in maximum inundation, in the 0.9-1.1 m range. Although less than for CVV, Figure 3.20b shows that some low lying areas of the river banks would be flooded for this case as well.

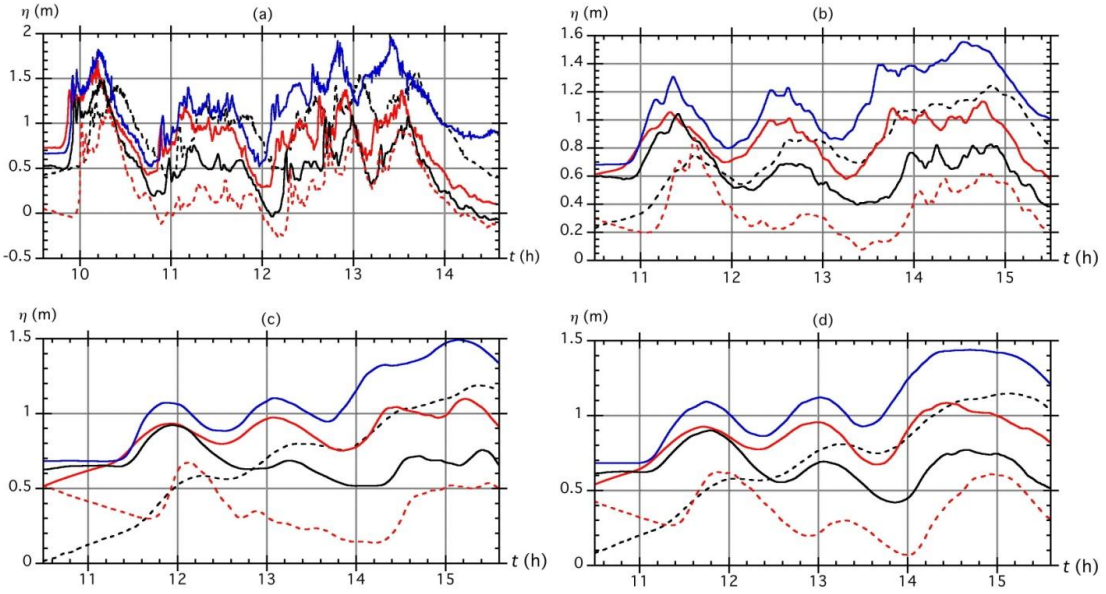

Figure 3.21 Simulation with FUNWAVE-TVD (MHW+ SLR reference level) of the CVV tsunami plus the calibrated M2 tide for phase: TT1 (solid red); TT2 (solid black); TT3 (dashed red); and TT4 (dashed black). Time series of surface elevation at station (Figure 3.3; Table 3-5): (a) #2 (Sewells Point); (b) #3 (c) #4 and (d) "river station". For comparison, we plotted with reference to MHW+SLR (solid blue) the CVV tsunami computed on a static reference level AWL (0.957 m MHW) (CVVSL). Time is shown from the start of the CVV event.

5.2 Joint simulations of tide and tsunami for other phases of the tide

Far-field subaerial landslide (CVV).

Figure 3.21 shows computed surface elevations in the 39 m grid, at 4 gauges (Figure 3.3; Table 3-5): #2 (Sewells Pt), #3, #4 and the "river station", for the superposition of the incident CVV tsunami with the calibrated M2 tide, for the 4 phases of the tide (with respect to the MHW + SLR reference level). Additionally, for comparison, we plotted results of computations of the CVV tsunami over a high reference static level equal to the maximum AWL (0.957 m MHW), with respect to the same reference level (MHW + SLR); this is referred to as CVVSL in the following.

In all cases, we see a gradual reduction of the maximum surface elevation when moving up the James River, from Sewells Pt. to station #4, due to bottom friction in the gradually shallower river and its banks. For the cases TT2 and TT3 the first two tsunami wave crests are seen to reach all the stations at almost the same time as for the CVVSL case. Likely due to the ebb current effects, for phases TT1 and TT4, however, we see that the arrival of the tsunami wave crests is gradually more delayed, when moving upstream. Regarding maximum water level, while the first crest for case TT1 reaches nearly the same level as the CVVSL case, later on and up the river, as the tide level both decreases due to bottom friction and to the tide time variation, the maximum water level for any phase case is never higher than that calculated for CVVSL; hence, this approach which is recommended by NRC for tsunami hazard assessment appears to be conservative in the present case, despite the presence of tidal currents. However, comparing among computations for the various tide phases, we see

that the case TT4, which starts at a lower level than all the other cases but TT3 at Sewells Pt, ends up causing higher surface elevations at all stations upstream the river, although it takes a few hours for this to occur. This is clearly a result of dynamic effects of tide and tsunamis current interactions (this will be further analyzed later). The next higher level is achieved for the case TT1 and then cases TT2 and TT3 are always lower than the other cases. Finally, depending on the case, when tide and tsunami interact, other waves in the wave train can end up being amplified, thus causing larger flooding; for instance, the third crest is that with the highest amplitude in the TT4 phase.

To better assess tide and tsunami interactions, Figures 3. 22 and 3.23 show the computed current magnitude (m/s) and direction at the Sewells station #2 and at station #4, upstream the James River (Figure 3.3; Table 3-5), for the CVV tsunami alone (CVVSL case), the calibrated M2 tide alone, and the TT1 and TT4 phase combinations, which were seen to cause the worst case scenarios as far as surface elevation. As expected from the water level results, current velocities for the combined tsunami-tide cases are always larger at Sewells Pt than those at station #4, with maximum values 0.55 m/s and 0.42 m/s for case TT4, respectively; when propagating upstream, the current speed decreases and higher frequency fluctuations are gradually damped out as a result of bottom friction, similar to what was observed for surface elevations. Although the maximum velocity is slightly larger at Sewells Pt for the tsunami alone case (0.6 m/s in its tail), than when combined with the tide for TT1 or TT4 phases, it is larger at station #4 when combined with the tide, for the two latter cases, than for the tsunami or tide alone cases; this results from destructive or

constructive interferences with the tide, respectively. Finally, it can be seen that because of interactions with tidal currents, the direction of currents in the TT1 and TT4 case is different from the CVVSL case at various times of propagation at both stations. This clearly illustrates the site and case specific nature of tsunami-tide interactions, and that these cannot be anticipated by simple linear superposition, as they are strong nonlinear effects when combining tsunami and tidal currents (such as related to bottom friction).

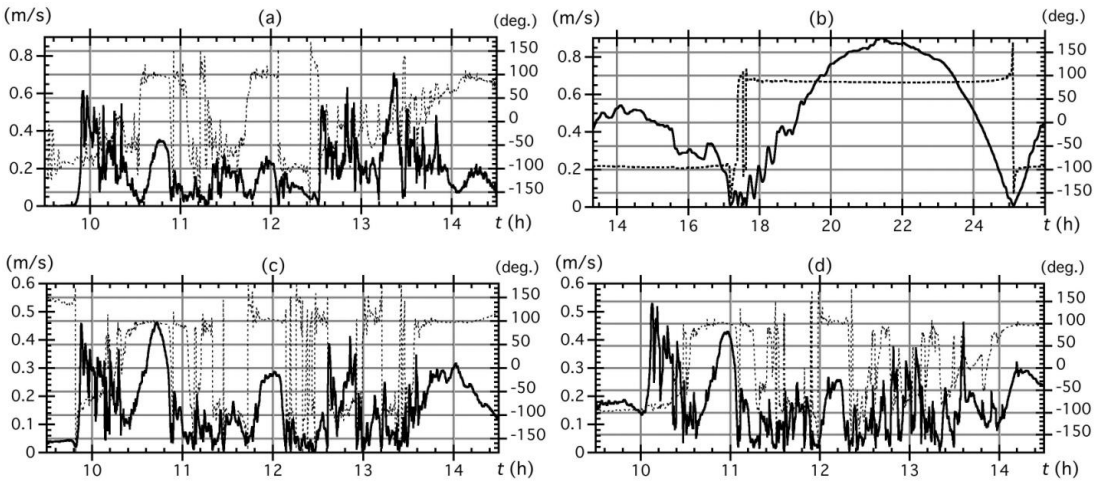

Figure 3.22 Simulation with FUNWAVE-TVD (MHW+ SLR reference level) of the CVV tsunami and calibrated M2 tide. Time series of current magnitude (solid) and direction (dashed; in degree with respect to east) at Sewells Pt station #2 (Figure 3.3; Table 3-5): (a) tsunami alone; (b) tide alone; tsunami plus tide for phase (c) TT1, and (d) TT4. Tsunami and TT1/TT4 simulations are in 39 m grid, and time shown is from the start of the CVV event. Tide alone simulations are in 154 m grid, and time shown is total time of tide simulation, starting at 13.33 h (800 s) when the second tidal cycle is zero-up-crossing at Sewells Pt. (curve 2 in Figure 3.13b).

To provide a comprehensive picture of maximum tsunami inundation, Figure 3.24 shows the envelope of maximum surface elevation computed for the CVV event in the 39 m grid, for the different phases TT1 to TT4. We see the strong reduction of surface elevation seen for all phases in Figure 3.21 when moving upstream the river.

From a maximum elevation of over 2 m at the mouth of the James River, the maximum elevation is reduced to about 1.0-1.1 m up the river.

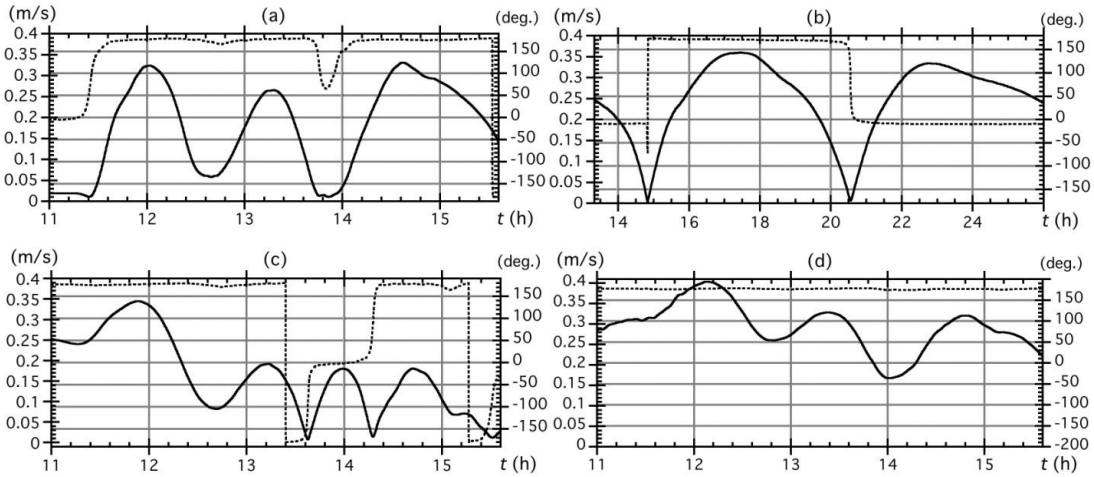

Figure 3.23 Same case as in Figure 3.22 for results at Station #4 in the James River (Figure 3.3; Table 3-5).

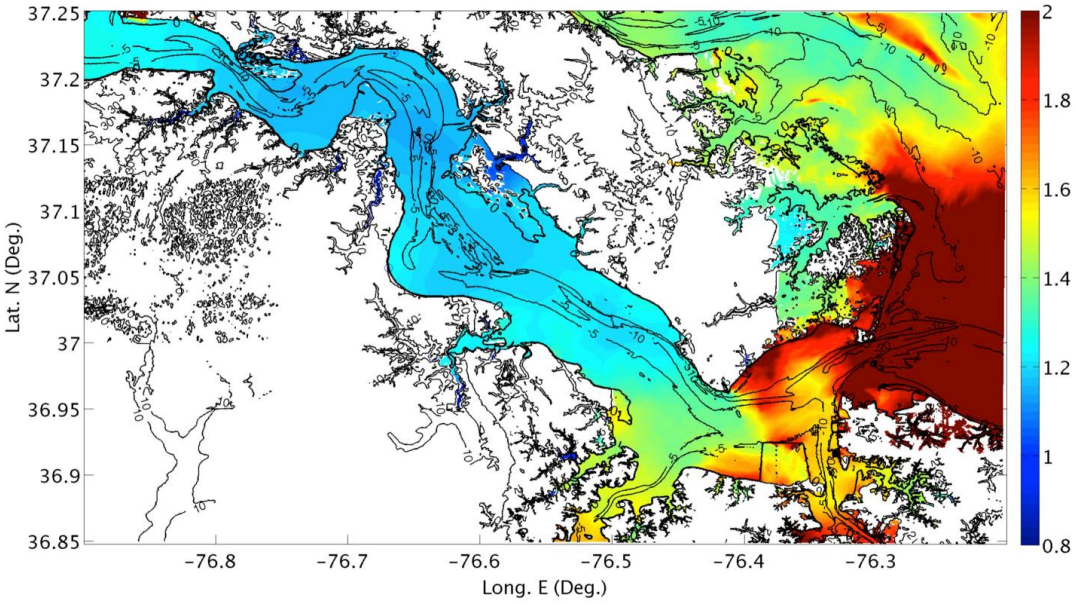

Figure 3.24 Simulation with FUNWAVE-TVD (MHW+SLR reference level) of the calibrated M2 tide plus CVV tsunami. Envelope of maximum surface elevation (colorbar in meter) computed in 39 m grid for all tide phases (TT1, TT2, TT3 and TT4).

Near-field Submarine Mass Failure (CRT).

The same comparison as for CVV, among simulation results obtained for various tide phases, is repeated for the CRT tsunami. In Figure 3.25 we see this comparison for surface elevations; although the incident tsunami wave train is quite different from that of CVV, we observe the same overall behavior, with a gradual decrease in maximum surface elevation when moving upstream the James River, and the case TT4 being again the worst-case scenario in terms of maximum inundation level. In fact, at Sewells Pt, although initially cases TT1 and CRTSL cause a higher surface elevation, later on case TT4 causes a larger inundation than the TT1 case, and for quite a long time. However, as far as maximum level reached at any gauge, CRTSL still is higher than results from the dynamic tide-tsunami simulations and, hence, the static approach, although quite artificial for a tide-driven flow in an estuary, can still be deemed to be conservative in the present case. Among the various tide phases, unlike for CVV, here, TT1 provides the worst case scenario in terms of maximum level reached at any gage. As the tsunami wave train of CRT has just one main peak, the interaction of this maximum tsunami when synchronized with the maximum tide (i.e., case TT1) generates the maximum flooding effect, and the ebb and flood currents have a smaller impact in amplifying the tail of the tsunami wave train. Also, when moving upstream, and even more so than for CVV, we see a gradual smoothing out of tsunami waves, with first the damping out of higher frequency oscillations and then a gradual flattening of even the longer waves in the incident tsunami wave train. As this process is much stronger for the tide phases, particularly for TT2 and TT3, than for the static CRTSL case, this is clearly another effect of

tsunami tide current interactions (this aspect again is analyzed in more details later). Finally, there is a stronger time lag of the arrival of the tsunami wave crests at the various gauges, when combined with the tide, with respect to the static CRTSL case than for the CVV tsunami.

Similar to the CVV case, Figures 3.26 and 3.27 show the computed current magnitude (m/s) and direction at the Sewells station #2 and at station #4 (Figure 3.3; Table 3-5), respectively, for the CRT tsunami alone (CRTSL case), the calibrated M2 tide alone, and the TT1 and TT4 phase combinations, which were seen to again cause the worst case scenarios as far as surface elevation. As expected from the water level results, current velocities for the combined tsunami-tide cases are always larger at Sewells Pt than those at station #4, with maximum values 0.48 m/s and 0.37 m/s for case TT4, respectively; similar to CVV, when propagating upstream, the current speed decreases and higher frequency fluctuations are gradually damped out as a result of bottom friction, similar to what was observed for surface elevations.

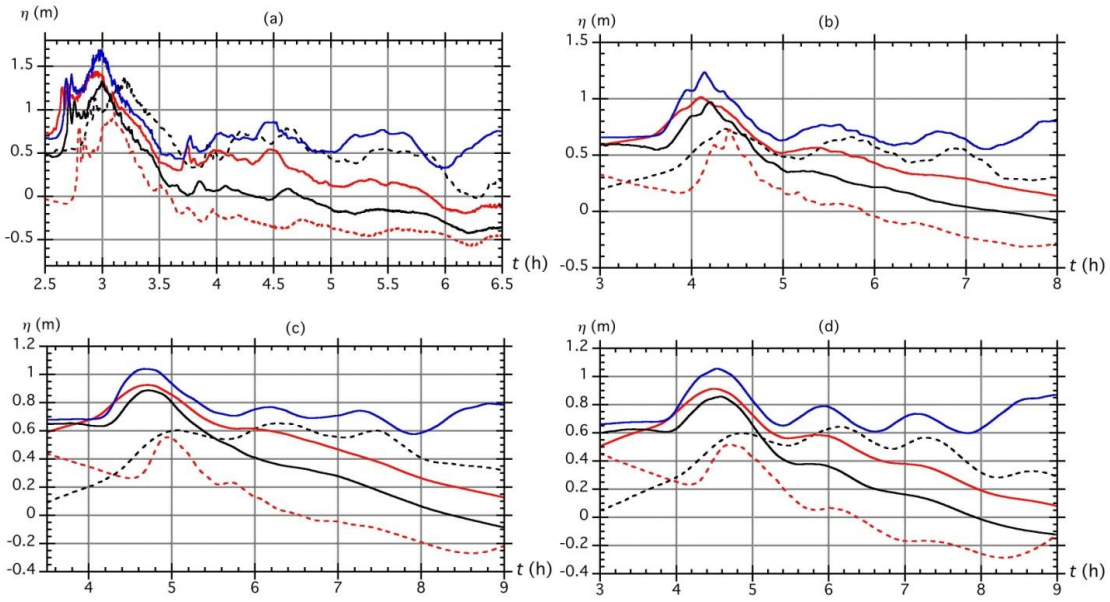

Figure 3.25 Simulation with FUNWAVE-TVD (MHW+ SLR reference level) of the CRT tsunami plus the calibrated M2 tide for phase: TT1 (solid red); TT2 (solid black); TT3 (dashed red); and TT4 (dashed black). Time series of surface elevation at station (Figure 3.3; Table 3-5): (a) #2 (Sewells Point); (b) #3 (c) #4 and (d) "river station". For comparison, we plotted with reference to MHW+SLR (solid blue) the CVV tsunami computed on a static reference level AWL (0.957 m MHW) (CRTSL). Time is shown from the start of the CRT event.

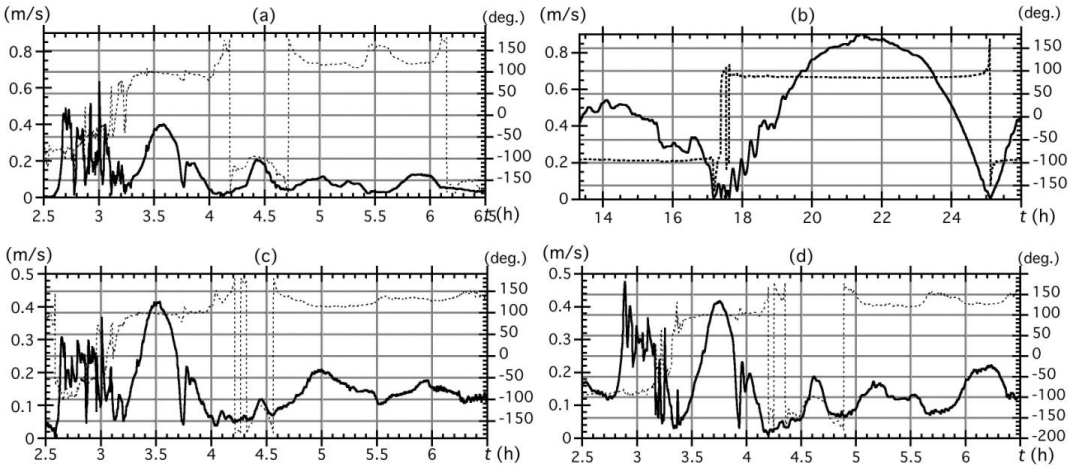

Figure 3.26 Simulation with FUNWAVE-TVD (MHW+ SLR reference level) of the CRT tsunami and calibrated M2 tide. Time series of current magnitude (solid) and direction (dashed; in degree with respect to east) at Sewells Pt station #2 (Figure 3.2; Table 3-5): (a) tsunami alone; (b) tide alone; tsunami plus tide for phase (c) TT1, and (d) TT4. Tsunami and TT1/TT4 simulations are in 38 m grid, and time shown is from the start of the CRT event. Tide alone simulations are in 154 m grid, and time shown is total time of tide simulation, starting at 13.33 h (800 s) when the second tidal cycle is zero-up-crossing at Sewells Pt. (curve 2 in Figure 3.13b).

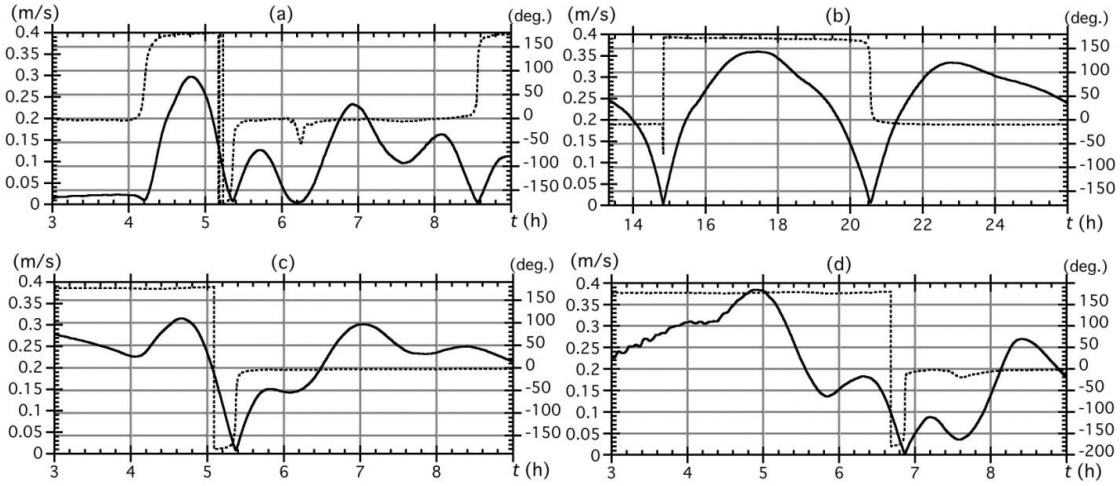

Figure 3.27 Same case as in Figure 3.26 for results at Station #4 in the James River (Figure 3.2; Table 3-5).

Although the maximum velocity is slightly larger at Sewells Pt for the tsunami alone case (0.65 m/s), than when combined with the tide for TT1 or TT4 phases, it is larger at station #4 when combined with the tide, for the two latter cases, than for the tsunami or tide alone cases. Finally, it can be seen that because of interactions with tidal currents, the direction of currents in the TT1 and TT4 case is different from the CTRSL case at various times of propagation at both stations. This confirms the importance of doing case and site specific studies of tide and tsunami interactions in the presence of strong tidal currents.

To provide a comprehensive picture of maximum tsunami inundation, Figure 3.28 shows the envelope of maximum surface elevation computed for the CRT event computed in the 39 m grid for the different phases TT1 to TT4. We again see the strong reduction of surface elevation seen for all phases in Figure 3.25 when moving upstream the river. From a maximum elevation of over 2 m at the mouth of the James River, the maximum elevation reduces to about 0.9-1.0 m up the river.

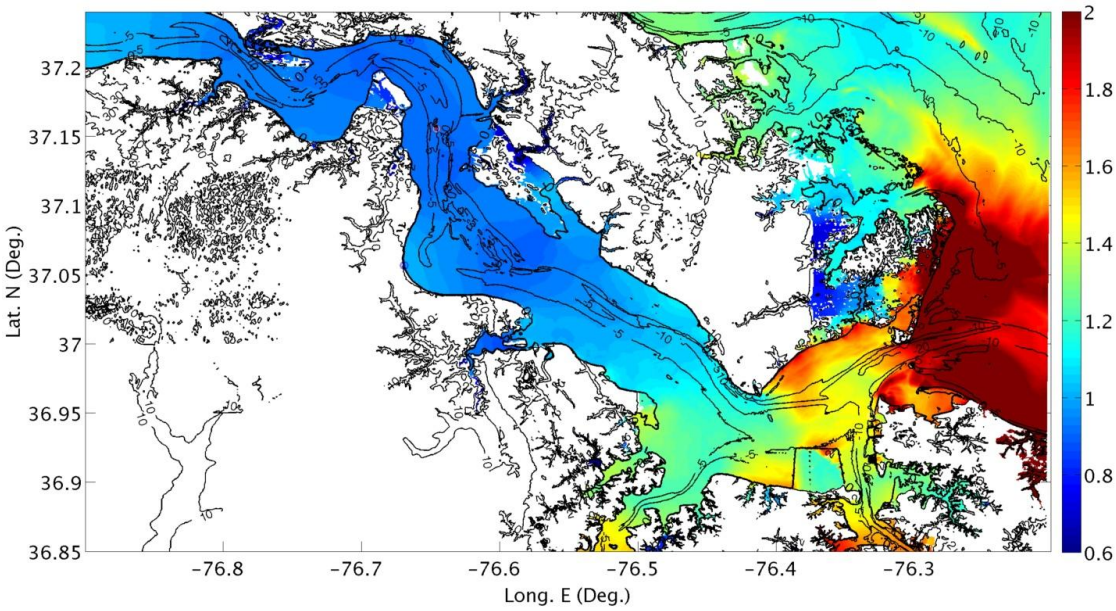

Figure 3.28 Simulation with FUNWAVE-TVD (MHW+SLR reference level) of the calibrated M2 tide plus CRT tsunami. Envelope of maximum surface elevation (colorbar in meter) computed in 39 m grid for all tide phases (TT1, TT2, TT3 and TT4).

6. Conclusions

We conducted numerical simulations in a series of nested grids (up to 4 levels of nesting) that combined incident tsunami wavetrains off the mouth of the Chesapeake Bay (2 extreme tsunami sources: one near-field Currituck SMF and one far-field CVV sources), plus the forcing from the M2 extreme tide for four phases of the tide.

The M2 tide was first calibrated from the mean values that were obtained from an independent model, by running simulations for the tide alone, to achieve the expected maximum antecedent water level (AWL) at the reference station of Sewells Pt (+0.957 m, MHW), near the mouth of the James River. In view of the observed reduction of modeled tide elevations, when going up the river to the locations of other

tidal gages, these simulations revealed that, to match the expected reduction in tide elevation from Sewells Pt to upstream the James River, the relevant reference level in the model ought to be MHW, to which a sea level rise (SLR) value was added, yielding the actual mean water level in the tide plus tsunami simulations as MHW+SLR.

Simulations were then conducted for the 2 tsunamis, either alone over the static AWL, or combined with various phases of the tide. We first combined tide and tsunamis for the two maximum elevations to be synchronized at the mouth of the Chesapeake Bay. We then used a reduced tide elevation but maximum ebb current in the river (in order to cause tsunami shoaling) when the tide lags by one eight of its period (T/8) after the maximum tide (TT2) and when tide lags by T/4 after the maximum, downward zero crossing (TT3). As a last tide phase we used T/8 ahead of the maximum tide (TT4). To assess the effects of a these dynamic tide-tsunami simulations, we compared results of surface elevation and currents computed for various tide phases in the James River, to those obtained for both tsunamis when considering a static reference level equal to the maximum AWL at Sewells Pt, as recommended by the Nuclear Regulatory Commission (NRC) for performing tsunami hazard assessment at open ocean sites.

Based on these simulations, it appears that among the two tsunami sources and 4 tested phases of the tide, the worst-case scenario, leading to maximum inundation and currents in the James River, is the tsunami resulting from an extreme flank failure (450 km^3) of the Cumbre Vieja Volcano for the tide case TT4; for CVV, the tide phase case TT1, which synchronizes maximum tsunami with the maximum tide also causes

nearly the same flooding at the mouth of the bay and in the James River. Other cases TT2 and TT3 cause less inundation and currents in the James River. For the latter CVV case (TT4), the inundation upstream the river near station #4 reaches 1.2 m above MHW+SLR reference level, or +1.686 NAVD88, which is +0.44 m above the Sewells Pt AWL. The tsunami resulting from such an event would take approximately 8 hours to travel across the Atlantic Ocean to the continental shelf break and approximately another 6.5 additional hours to travel from the shelf break to station #4, upstream the river.

Results for the CRT tsunami, although predicting a smaller impact, show that the maximum inundation at station #4 would be within 0.1 m of that of CVV and currents only 5 cm/s slower, when synchronized with the maximum tide elevation (TT1 case, unlike the maximum level for CVV, which occurs for the TT4 case). Hence, CRT results for cases TT1 and/or TT4 are also nearly worst-case scenarios for the James River; while CRT is not the absolute Probable Maximum Tsunami (PMT) expected for the upper US East coast (Grilli et al., 2014), it is still the near-field PMT for the Chesapeake Bay and James River areas. Because it is in the near-field, this SMF tsunami would offer less time for warning (only a couple of hours to the mouth of the Bay and 4.5 hours to the upper part of the river) than the distant CVV source and, hence, may pose a greater hazard. As a mitigating factor, however, this SMF, if it occurred as a repeat of the historical Currituck slide, would likely be triggered by a large regional earthquake that would be very quickly felt in the area of the James River.

In both the CVV and CRT cases, the standard simulation in tsunami hazard assessment recommended by NRC, of each tsunami over the maximum static AWL still produces conservative results in terms of maximum predicted inundation, at both station #2 and #4, but not by a large margin as compared to tsunami-tide interaction cases TT1 to TT4. Also, for cases TT1 and TT4, the duration of maximum inundation is longer and levels reached for subsequent waves in the tsunami wave-train higher than those obtained in the tsunami alone simulations (CVVSL, CRTSL). Clearly, such conclusions are case and site specific and, for river estuaries with stronger tidal currents than the order one-knot that occur in the James River, these conclusions could be reversed.

Various detailed results presented for both surface elevation and current time series in the river show that there are significant interactions of the tide induced current with the leading tsunami wave, but also in some cases with the second and third waves in the tsunami train, while these are propagating up the James River. Therefore, depending on the arrival time of tsunami waves with respect to the tide phase, the major flooding risk might result from different crests in the tsunami incident wave train and the arrival time of maximum flooding at a given gage may vary. This indicates that for tsunami event lasting hours, one should not downgrade the level of warning too soon since higher flooding and currents may occurs hours after the leading wave has arrived. Also, for tsunamis occurring at different phases of the tide, nonlinear interactions change the velocity of propagation of the various waves of the incident wave-train in the shallower water area of the river. This can be seen in the time lag between the maximum elevation at Sewells Pt. and station # 4, which is not

constant in different scenarios. Finally, the wave period at each station changes based on the phase of the tide, which is another sign of nonlinear interactions.

Acknowledgment: RPS-ASC Inc. (Wakefield, RI) is acknowledged for providing us with the unscaled M2 tide forcing computed along the boundary of our 154 m grid result, and also for computing the antecedent water level at Sewells Pt., VA.

References

Abadie S., Harris J.C., Grilli S.T. and R. Fabre 2012. Numerical modeling of tsunami waves generated by the flank collapse of the Cumbre Vieja Volcano (La Palma, Canary Islands): tsunami source and near field effects. J. Geophys. Res., 117, C05030, doi:10.1029/2011JC007646.

Dean R.G. and R.A. Dalrymple 1990. Water wave mechanics for engineers and scientists. World Scientific Pub. (2nd edition), Singapore.

Egbert G.D., Bennett A.F., and M.G.G. Foreman 1994. TOPEX/POSEIDON tides estimated using a global inverse model. J. Geophys. Res., 99(C12), 24821–24852.

Egbert G.D. and S.Y. Erofeeva 2002. Efficient Inverse Modeling of Barotropic Ocean Tides. J. Atmos. Oceanic Technol., 19, 183–204

Enet F. and S.T. Grilli 2007. Experimental Study of Tsunami Generation by Three-dimensional Rigid Underwater Landslides. Journal of Waterway Port Coastal and Ocean Engineering, 133(6), 442-454.

Grilli A.R. and S.T. Grilli 2013a. Modeling of tsunami generation, propagation and regional impact along the upper US east coast from the Puerto Rico trench. Research Report no. CACR-13-02. NTHMP Award, #NA10NWS4670010, National Weather Service Program Office, 18 pps.

Grilli A.R. and S.T. Grilli 2013b. Far-Field tsunami impact on the U.S. East Coast from an extreme flank collapse of the Cumbre Vieja Volcano (Canary Island). Research Report no. CACR-13-03. NTHMP Award, #NA10NWS4670010, National Weather Service Program Office, 13 pps.

Grilli A.R. and S.T. Grilli 2013c. Modeling of tsunami generation, propagation and regional impact along the U.S. East Coast from the Azores Convergence Zone. Research Report no. CACR-13-04. NTHMP Award, #NA10NWS4670010, National Weather Service Program Office, 20 pps.

Grilli S.T. and P. Watts 2005. Tsunami generation by submarine mass failure Part I : Modeling, experimental validation, and sensitivity analysis. J. Waterway Port Coastal and Ocean Engng., 131(6), 283-297.

Grilli S.T., Ioualalen, M., Asavanant, J., Shi, F., Kirby, J. and P. Watts, 2007. Source Constraints and Model Simulation of the December 26, 2004 Indian Ocean Tsunami. Journal of Waterway Port Coastal and Ocean Engineering, 133(6), 414-428.

Grilli S.T., Taylor, O.-D. S., Baxter, D.P. and S. Maretzki 2009. Probabilistic approach for determining submarine landslide tsunami hazard along the upper East

Coast of the United States. Marine Geology, 264(1-2), 74-97, doi:10.1016/j.margeo.2009.02.010.

Grilli S.T., Dubosq S., Pophet N., Pérignon Y., Kirby J.T. and F. Shi 2010. Numerical simulation and first-order hazard analysis of large co-seismic tsunamis generated in the Puerto Rico trench: near-field impact on the North shore of Puerto Rico and far-field impact on the US East Coast. Natural Hazards and Earth System Sciences, 10, 2109-2125, doi:10.5194/nhess-2109-2010.

Grilli S.T., Harris J.C., Tajalibakhsh T., Masterlark T.L., Kyriakopoulos C., Kirby J.T. and F. Shi, 2013a. Numerical simulation of the 2011 Tohoku tsunami based on a new transient FEM co-seismic source: Comparison to far- and near-field observations Pure and Applied Geophysics, 170, 1333-1359, doi:10.1007/s00024-012-0528-y (published online 7/24/12).

Grilli S.T., O'Reilly C. and T. Tajalli-Bakhsh 2013b. Modeling of SMF tsunami generation and regional impact alng the upper U.S. East Coast. Research Report no. CACR-13-05. NTHMP Award, #NA10NWS4670010, National Weather Service Program Office, 46 pps..

Grilli S.T., O'Reilly C., Harris J.C., Tajalli-Bakhsh T., Tehranirad B., Banihashemi S., Kirby J.T., Baxter C.D.P., Eggeling T., Ma G. and F. Shi 2014. Modeling of SMF tsunami hazard along the upper US East Coast: Detailed impact around Ocean City, MD. Natural Hazards, 42pps. (submitted).

Grilli, S.T. and P. Watts 2005. Tsunami generation by submarine mass failure Part I : Modeling, experimental validation, and sensitivity analysis. J. Waterway Port Coastal and Ocean Engng., 131(6), 283-297.

Harris J.C., Tehranirad B., Grilli A.R., Grilli S.T., Abadie S., Kirby J.T. and F. Shi 2014. Far-field tsunami hazard in the north Atlantic basin from large scale flank collapses of the Cumbre Vieja volcano, La Palma. Pure and Applied Geophysics, 34pps. (submitted).

Ioualalen M., Asavanant J., Kaewbanjak N., Grilli S.T., Kirby J.T. and P. Watts 2007. Modeling the 26th December 2004 Indian Ocean tsunami: Case study of impact in Thailand. J. Geophys. Res., 112, C07024, doi:10.1029/2006JC003850.

Kirby J.T., Shi F., Tehranirad B., Harris J.C. and S.T. Grilli 2013. Dispersive tsunami waves in the ocean: Model equations and sensitivity to dispersion and Coriolis effects. Ocean Modeling, 62, 39-55, doi:10.1016/j.ocemod.2012.11.009.

Kowalik Z., Proshutinsky T., and Proshutinsky A. 2006. Tide–tsunami interactions. Science of Tsunami Hazards. 24(4), 242- 256 .

Kowalik Z. and A. Proshutinsky 2010. Tsunami–tide interactions: A Cook Inlet case study. Continental Shelf Res.,30(6), 633–642.

Ma G., Shi F. and J.T. Kirby 2012. Shock-capturing non-hydrostatic model for fully dispersive surface wave processes. Ocean Modelling, 43-44, 22-35.

NOAA-NGDC (2013). National Geophysical Data Center, U.S. Coastal Relief Model, Retrieved December 2013, http://www.ngdc.noaa.gov/mgg/coastal/crm.html.

Shi F., Kirby J.T., Harris J.C., Geiman J.D. and S.T. Grilli 2012a. A High-Order Adaptive Time-Stepping TVD Solver for Boussinesq Modeling of Breaking Waves and Coastal Inundation. Ocean Modeling, 43-44, 36-51, doi:10.1016/j.ocemod.2011.12.004.

Shi, F., Kirby, J. T. and Tehranirad, B. 2012b. Tsunami benchmark results for spherical coordinate version of FUNWAVE-TVD (Version 1.1). Research Report No. CACR-12-02, Center for Applied Coastal Research, Univ. of Delaware, Newark.

Taylor L.A., Eakins B.W., Carignan K.S., Warnken R.R., Sazonova T., Schoolcraft D.C. and G.F. Sharman 2008. Digital Elevation Model of Virginia Beach, Virginia: Procedures, Data Sources and Analysis, NOAA Technical Memorandum NESDIS NGDC-7, National Geophysical Data Center, Boulder, CO, 34 pp. http://ngdc.noaa.gov/dem/squareCellGrid/download/423.

Tehranirad B., Shi F., Kirby J.T., Harris J.C. and S.T. Grilli 2011. Tsunami benchmark results for fully nonlinear Boussinesq wave model FUNWAVE-TVD (Version) 1.0. Research Report No. CACR-11-02, Center for Applied Coastal Research, Univ. of Delaware, Newark.

Tehranirad B., Kirby J.T., Ma, G. and F. ShI 2012. Tsunami benchmark results for non-hydrostatic wave model NHWAVE (Version 1.0). Research Report No. CACR-12-03, Center for Applied Coastal Research, Univ. of Delaware, Newark.

ten Brink U.S., Twitchell D., Geist E., Chaytor J., Locat J., Lee H., Buczkowski B., Barkan R., Solow A., Andrews B., Parsons T., Lynett P., Lin J., and M. Sansoucy

2008. Evaluation of tsunami sources with the potential to impact the U.S. Atlantic and Gulf Coasts. Report to the Nuclear Regulatory Commission. USGS. 322 pp.

ten Brink U.S., Chaytor J.D., Geist E.L., Brothers D.S. and B.D. Andrews 2014. Assessment of tsunami hazard to the U.S. Atlantic margin. Marine Geology, 353, 31-54.

Tolkova, E. 2012. Tide-tsunami interaction in Columbia River, as implied by historical data and numerical simulations. Pure and Applied Geophysics, 170(6-8), 1115-1126.

Yeh H., Tolkova E., Jay D., Talke S. and H. Fritz 2012. Tsunami Hydrodynamics in the Columbia River. J. Disaster Res., 7(5), 604-608.

Ward S.N. and S. Day 2001. Cumbre Vieja Volcano – potential collapse and tsunami at La Palma, Canary Islands. Geophys. Res. Lett., 21, 397-400.

Wei J., Kirby J.T, Grilli S.T. and R. Subramanya 1995. A Fully Nonlinear Boussinesq Model for Surface Waves. Part1. Highly Nonlinear Unsteady Waves. J. Fluid Mech., 294, 71-92.

Zhang Y., Witter R.C. and G.R. Priest 2011. Tsunami–tide interaction in 1964 Prince William Sound tsunami. Ocean Modelling, 40, 246–259.

MANUSCRIPT 4

To be submitted.

Novel Parameterization and Modeling of the 1998 Papua New Guinea SMF Tsunami

Tayebeh S. Tajalli Bakhsh[1], Stephan T. Grilli[1+], David Tappin[2].

[1]Dept. of Ocean Engineering, University of Rhode Island, Narragansett, RI 02882.

[2]British Geological Survey, Kingsley Dunham Centre, Keyworth, Nottingham, NG12 5GG, UK.

+ Corresponding author

Summer, 2014

Abstract

In the past few years, significant progress were made in the modeling of tsunami generation by Submarine Mass Failures (SMFs), using non-hydrostatic three-dimensional models such as NHWAVE (Ma et al., 2012), and of their propagation and coastal transformations, as two-dimensional nonlinear and dispersive wave trains, using long-wave Boussinesq models such as FUNWAVE-TVD (Shi et al., 2012). By applying these new modeling tools together with the most recent bathymetric and geophysical data, in this chapter, we revisit the simulation of perhaps the most significant and damaging SMF tsunami case study in modern history: the 1998 Papua New Guinea (PNG) tsunami, that caused over 2000 fatalities and devastated the Sissano Lagoon and nearby villages with over 10 m runup. Based on these new simulations, which are both more physically meaningful and resolved (in a series of nested model grids), and within the geological uncertainty of the event, we propose a new parameterization of the PNG slump. Results of simulations of tsunami coastal impact, in terms of inundation and runup, are compared with available tsunami field data and a reasonable agreement is found between these. The new improved understanding and modeling of this important historical case study can provide a unique field benchmark for validating operational models of SMF tsunamis.

Keywords:1998 Papua New Guinea tsunami, submarine mass failure, slump, numerical modeling of long wave propagation.

1. Introduction

On July 17th, 1998, at 08:49 GMT, a moderate earthquake of magnitude Mw 7.1 struck the northern coast of Papua New Guinea (PNG), triggering a devastating tsunami that caused up to 16 m runup on the Sissano sand spit, and killed over 2,000 people (Figure 4.1; Davies, 1998; Kawata et al., 1999; Tappin et al., 2008). A tsunami with very large incident waves, causing onshore flow depths of 10-15 m, was not expected to be triggered by an earthquake of this magnitude, and the nearshore location of the earthquake epicenter (green star in the Figure 4.1) would have resulted in an almost immediate wave impact on the nearby coast. Tappin et al. (2008) simulated the PNG co-seismic tsunami and concluded it would have only caused a 1 m high wave, arriving on the coast less than 10 minute after the earthquake; such a small wave may not even have been noticed by the large crowd that was celebrating a national holidays on the beach.

Much larger and devastating waves, however, arrived on the Sissano spit with a time delay of 10-25 min (Davies et al., 2003). Based on field surveys performed in 1998, to explain this second and larger tsunami wave train, it was suggested that there might have been some secondary process generating the waves, rather than a direct coseismic seafloor motion, which was found moderate for an earthquake of this magnitude (Davies, 1998). Based on follow up onshore and offshore field surveys, done as part of international cruises, extensive numerical modeling, and the discovery of submarine landslide deposits offshore of Sissano, the hypothesis that the most likely source for this devastating tsunami was a nearly rigid rotational Submarine Mass Failure (SMF), or “slump”, became gradually and increasingly widely accepted

(Newman and Okal, 1998; Titov and Gonzalez, 1998; Geist, 1998; Tappin et al., 1999a,b, 2001, 2002, 2008; Grilli et al., 1999; Synolakis et al., 2002; Tappin, 2004 and Watts et al., 2005).

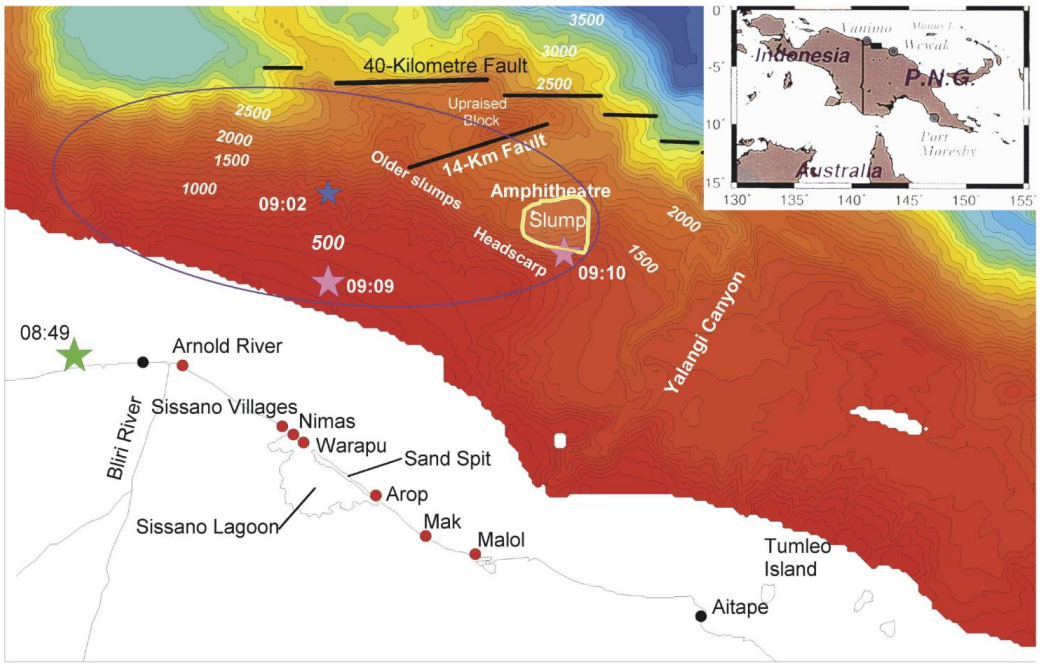

Figure 4.1 Location map of the northern PNG coast struck by the tsunami of July 1998 (from Tappin et al., 2008), with bathymetry from the 1999 Kairei survey. The Green star indicates the Mw 7.1 earthquake epicenter; the pink stars indicate the aftershocks of 09:09:30 and 09:10:00; the blue star (with error ellipse in blue from Synolakis et al., 2002) indicates the T-phase slump signal of 09:02; red dots indicate the main villages destroyed. The slump area identified in geological surveys, and main seabed features are also indicated. Water depth is in meters.

Based on Newman and Okal (1998), the earthquake was not a "slow" source, with "slowness" being defined as the ratio between high-frequency energy and low-frequency seismic moment, with the average value being 4.98. For PNG, the earthquake yielded a 5.50 slowness, suggesting that there could have been a secondary source, such as a SMF, generating the tsunami. Titov and Gonzalez (1998) used the nonlinear shallow water wave (NSW) model MOST to simulate the PNG tsunami and

compare runups caused by an idealized landslide and the earthquake with the observed impact on the Sissano spit. None of their sources could match the observed runup.

However, multibeam bathymetric surveys, together with comprehensive geophysical and sedimentological studies, revealed the presence of a large slump in a 1500 m depth, 25 km offshore of Sissano (Figure 4.1). If this slump had been triggered by the earthquake and generated a tsunami, this could explain both the delay between the earthquake and tsunami arrival, as well as the very large waves in the second wave train (Tappin et al. 1999, 2001).

Heinrich et al. (2001) developed a numerical model to study the generation of a tsunami by an underwater landslide in PNG. They treated the SMF as a homogeneous gravity flow of a heavy fluid and used shallow water approximation to simulate the generated water waves; they assumed a 4 km^3 SMF in a 550 m depth, moving over a 5 km runout, and tested different friction coefficients. Their results reproduced the trend in inundation depth along the coast fairly well, considering the uncertainties in SMF volume and position. Although the modeled SMF was not unique, these results confirmed that the main tsunami could have been due to a deep and large SMF. Synolakis et al. (2002) discussed the abnormal hydroacoustic records made at the Wake Island monitoring station (Okal, 1999), of an aftershock that occurred about 13 minutes after the main shock; they interpreted it as a slump, which generated the large observed tsunami.

Sweet and Silver (2003) collected high-resolution seismic profiles in the source region of the presumed SMF that caused the PNG tsunami and used bathymetry

collected by the JAMSTEC/SOPAC groups. They estimated the slump volume to be 3.8-4.6 km^3 within the identified Amphitheater (Figure 4.1), including a central mass over 700 m thick, which had rotated southward about 14 degrees, causing a vertical drop of the SMF center of mass of 380 m, and a horizontal displacement of 840 m.

Imamura and Hashi (2003) developed several scenarios of tsunamigenic SMF sources, with varying sizes, between 4–8 km^3, and a triggering time about 10 minutes after the main shock, to simulate the PNG tsunami propagation and runup; they used the deep water bathymetry measured by JAMSTEC and other bathymetric data for a depths less than 60 m. They sited the SMF based on a wave ray analysis, which suggested a small source, 1000 m deep, located about 25 km offshore of the lagoon to fit the arrival time reported by eyewitnesses. Their computed runup heights on the Sissano spit were lower than measurements. They indicated that, although the SMF volumes they used should be large enough to be seen in bottom surveys made by JAMSTEC, no significant traces were seen, except for some cracks and headwall collapse, as reported by Sweet and Silver (2003).

Lynett et al. (2003) gave a detailed review of the field surveys and numerical modeling done for the PNG tsunami to date, and showed some possible misinterpretations in the recorded data. They performed simulations with a Boussinesq and a nonlinear shallow water wave (NLSW) model. They indicated that both models predicted similar maximum inundation on the Sissano spit. They did not simulate the actual movement of the slump but just specified an initial free surface elevation, with zero velocity above the slump, as a sinusoidal wave. They compared three different initial conditions and showed that, regarding tsunami coastal impact, the initially

displaced water volume is more important than both its initial shape or the initial orientation of tsunami waves. They defined a series of numerical gages placed along the spit where they compared simulations of the maximum water elevation to the field measured flow depths.

Satake and Tanioka (2003) modeled the PNG tsunamis generated both in the near- and far-field, by the earthquake and a small 0.6 km^3 slump source and compared results with the recorded waves in Japan and the measured runup/inundaiton on the coast around the Sissano Lagoon. For the submarine slump source, they used a static surface elevation estimated using Grilli and Watts' (1999) empirical formula. As there was no information on timing of the slump, they modeled three different slumps. Waves generated by the slump alone could not reproduce the far-field tsunami waveforms whose amplitudes were proportional to the displaced water volume at the source. They showed that the near field tsunami elevations were controlled by the potential energy of water displaced by the slump, which was $2*10^{12}$ J in their case. Simulations for all three slump sources yielded almost similar tsunami elevations along the coast, which showed the same trend as the observed runup. They concluded that any tsunami source around the amphitheater could generate a tsunami directed towards the Sissano Lagoon.

Based on work initiated immediately after the event (Tappin et al., 1999), Watts et al. (2003) simulated the PNG event by modeling both the tsunami caused by the Mw 7 earthquake and that caused by a SMF, using the fully nonlinear and dispersive Boussinesq long wave model FUNWAVE (Wei et al., 1995). As inferred from marine geology and direct water wave observations, a 6 km^3 SMF was

parameterized as a rigid slump, located at 142.25 Lon and 2.85 S Lat, along the edge of the Amphitheater (Figure 4.1), in a depth d = 1500 m, with length b = 4.5 km, maximum thickness T = 760 m, and width w = 5 km. The slump rotated parallel to an average 12 deg. slope and reached a maximum velocity of 11.6 m/s for a characteristic time of motion t_0 = 32 s and characteristic distance of motion s_0 = 375 m (see Grilli and Watts, 2005 for definitions); as we shall see, this leads to a short runout of s_f =750 m over a time t_f = 101 s. Based on the methodology reported in Grilli and Watts (1999, 2005) and Watts et al. (2005), in the simulations, the surface elevation caused by the slump motion was specified as initial condition in FUNWAVE at $t = t_0$, without initial velocity. They did not compare simulated runups to observations, but discussed instead the important effects of dispersion on both the surface elevation and number of leading waves generated in the tsunami, by running FUNWAVE with and without dispersive terms.

In a further iteration to Watts et al.'s (2003) study, using more accurate field data, Tappin et al (2008) modeled a few slump failures found in and around the Amphitheatre with the most prominent one having a width w = 4.2 km, length b = 4.5 km, and maximum thickness T = 750 m, in a depth d = 1500 m, for a total volume of about 6.4 km^3. They concluded that this slump was triggered by the earthquake after a 12 min delay and showed that tsunami simulation results could explain field observations quite well, despite the semi-empirical method used to initialize the slump source.

Before the occurrence of this devastating tsunami, SMFs were not routinely considered as being able to cause significant tsunamis hazard, so they were not well

studied or modeled. The exact parameterization of the PNG slump source still remains somewhat controversial, although Tappin et al (2008) proposed a slump source whose location, depth, size and sediment parameters were based on the best available geological observations at the time, and simulated the PNG event using the best available modeling tools to date as well. Doing so, they were able to reproduce fairly well the observed runup and inundation on the Sissano spit, as well as other eyewitness observations. However, as indicated, their modeling approach used a semi-empirical SMF tsunami source, i.e., not an actual three-dimensional (3D) modeling of SMF tsunami generation, although this source was derived from curve fits of results of many idealized slump simulations performed with two-dimensional and 3D Fully Nonlinear Potential Flow (FNPF) models (Grilli et al., 1999, 2002, 2005, and Watts et al., 2003, 2005). In these simulations, the FNPF models were forced by the motion of rigid, Gaussian-shaped, SMFs of different size, depth and density, over a series of plane slopes, derived from a balance of inertia, gravity, buoyancy and friction (both basal and drag) forces. Based on SMF geometrical and material parameters, the semi-empirical equations provided the initial tsunami surface elevation at the characteristic time t_0, for which most of the transfer of energy from SMF to water wave motion was assumed to have occurred. Clearly, because an actual 3D model was not applied to simulate the SMF tsunami generation, with the slump moving over the actual PNG bathymetry, rather than a plane slope, the tsunami source was too simplistic, and possibly inaccurate. Additionally, the initial water velocity was neglected.

It is our purpose here to revisit the PNG slump simulations, using our more recent and comprehensive modeling tools (i.e., NHWAVE and FUNWAVE-TVD), together with more accurate nearshore bathymetric data and evaluate the relevance of the earlier parameterization proposed for the slump, such as by Tappin (et al. (2008), by comparing results with observations made on the Sissano spit.

More specifically, in this work, we perform new simulations using both the earlier and some slightly revised slump parameters, based on recent marine geology field data, a state-of-the-art 3D model of SMF tsunami generation (NHWAVE; Ma et al., 2012), improved nearshore bathymetry, and the latest version of the long-wave propagation of the fully nonlinear long-wave Boussinesq propagation model referred to as FUNWAVE-TVD (Shi et al., 2012). NHWAVE (Ma et al., 2012) is a 3D non-hydrostatic wave model, with horizontal Cartesian grids and a boundary-fitted σ-coordinate in the vertical direction. It was validated by Ma et al. (2012) for SMF tsunami generation against the 3D laboratory experiments of Enet and Grilli (1997). NHWAVE has recently been used for SMF tsunami hazard assessment along the US East coast (Grilli et al., 2014). FUNWAVE-TVD is the latest implementation of FUNWAVE, which was initially developed and validated for coastal wave dynamics problems (Wei et al. 1995; Chen et al. 2000, 2003; Kennedy et al. 2000); later however, FUNWAVE was used to perform many successful tsunami case studies (e.g., Watts et al., 2003). FUNWAVE_TVD has both Cartesian and spherical implementations (although here only the Cartesian formulation is used), and uses a Total Variation Diminishing (TVD) shock-capturing algorithm to more accurately simulate wave breaking and inundation. The code is fully parallelized using the

Message Passing Interface (MPI) protocol. Because of their more complex equations, BMs are typically more computationally demanding than NSW models (Grilli et al., 2013). FUNWAVE-TVD has been validated for tsunami propagation and coastal impact, against a large set of analytical, laboratory, and field benchmarks, as part of the development of tsunami hazard maps for the US East Coast (Tehranirad et al., 2011) and was applied to the modeling of the Tohoku 2011 earthquake (Grilli et al., 2013). Specifically, we will simulate SMF tsunami generation and propagation in a series of Cartesian nested model grids of increasingly fine resolution towards the Sissano lagoon; model results will be compared with available tsunami field data. In addition to a new understanding of the important PNG case study, it is hoped that this more detailed modeling work of this historical event will provide a unique field benchmark for validating models of SMF tsunami generation and propagation.

In the following, we summarize the available field data, both bathymetry and topography, and those from tsunami field surveys. We discuss the SMF slump source parameters, starting from those used in the hot start simulations of Tappin et al. (2008) as an initial guess for the location and size of the slump. NHWAVE is used to simulate SMF tsunami generation, based on the inferred simplified kinematics (one-degree of freedom) of the SMF center of mass. Then, FUNWAVE-TVD is used in a series of nested grids (two levels of Cartesian grid nesting: 200 , 50 and 12 m) to simulate wave propagation to shore and coastal impact in terms of inundation and runup. Results are compared with measured runup and inundation data along the coast and the Sissano spit. Discrepancies are discussed and used as a measure of accuracy to iteratively

modify the parameters of the proposed slump, within the allowable geological uncertainty, in order to achieve a good agreement with field data.

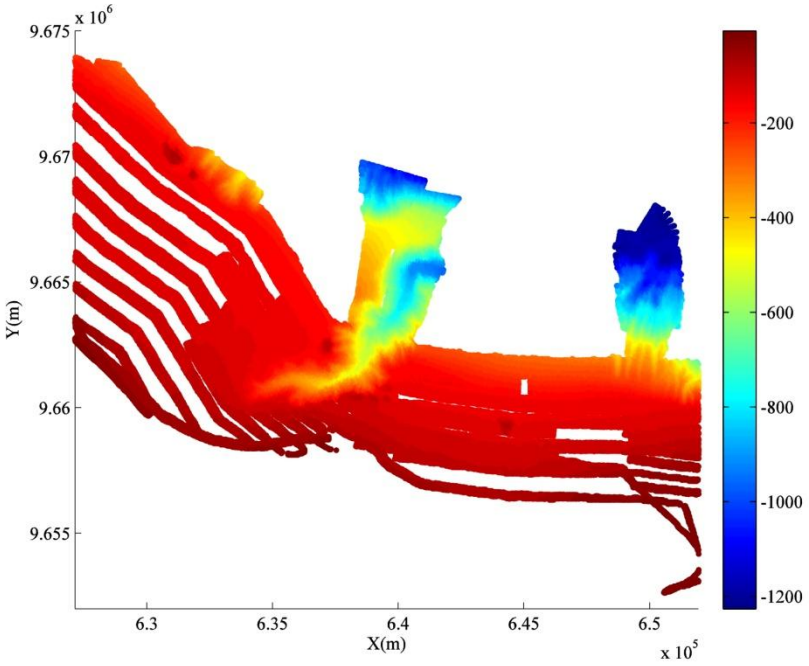

Figure 4.2 Bathymetric data (color scale in meter) obtained from the MBES surveys of Krüger and Kumar (2008), in the area of the Sissano spit in PNG (X and Y are local UTM coordinates (UTM Zone 54 South (Sissano, Vanimo) from WGS84).

2. Available Field Data

2.1 Bathymetry

Improved bathymetry for the area, as compared to earlier studied (e.g., Tappin et al., 2008), was obtained from high-resolution bathymetric surveys carried out in 2006 (Krüger and Kumar, 2008). These provided over 733 linear kilometers of multibeam echosounder (MBES) data. The survey achieved variable coverage from

approximately 50 m in the inshore area to an average offshore distance of 4 km, reaching a maximum water depth of about 2000 m. The projection used in mapping the data was based on UTM Zone 54 South (Sissano, Vanimo) from WGS84 (Figure 4.2). This high resolution data was combined with ETOPO-1 (1 arc-min bathymetry and topography) data, to cover the required modeling area. This is detailed later.

2.2 Eyewitness interviews and field mapping information

The first scientific investigation of the PNG tsunami was carried out by an international team in August 1998, during a one week period. Results of this investigation were reported by Kawata et al. (1999a,b), Tappin et al. (1999, 2001), and Synolakis et al. (2002). The worst damage was in the region around Sissano Lagoon, where precise measurements of the maximum runup and inundation penetration were difficult, because of the unique features of the long and narrow sand spit located between the lagoon and the sea, with an elevation of less than 3 m and a 150 m width in some parts. This caused tsunami waves to overtop the spit and flow over the spit into the lagoon. So the data are neither runup nor inundation penetration, but the maximum water elevation, or flow depth reached on the spit based on some markers such as trees (Lynett et al. 2003). Davis et al. (2003) reported interviews with eyewitness survivors and disaster managers, and mapped the damage and inundation. This included information on the height, shape and timing of the incoming waves; maximum wave heights and greatest damage were recorded along a 14 km section of coast centered on the Sissano Lagoon and spit (Figs. 4.1 and 4.4), where wave fronts were reported to have moved from east to west along the coast. All existing structures on the spit were destroyed, and 20-40 percent of the population was killed (over 2000

fatalities). Partial destruction extended 23 km to the southeast and 8 km to the northwest, and tsunami effects were felt as far as 250 km to the west-northwest. A 50-70 cm subsidence of the coastal sand barrier was observed.

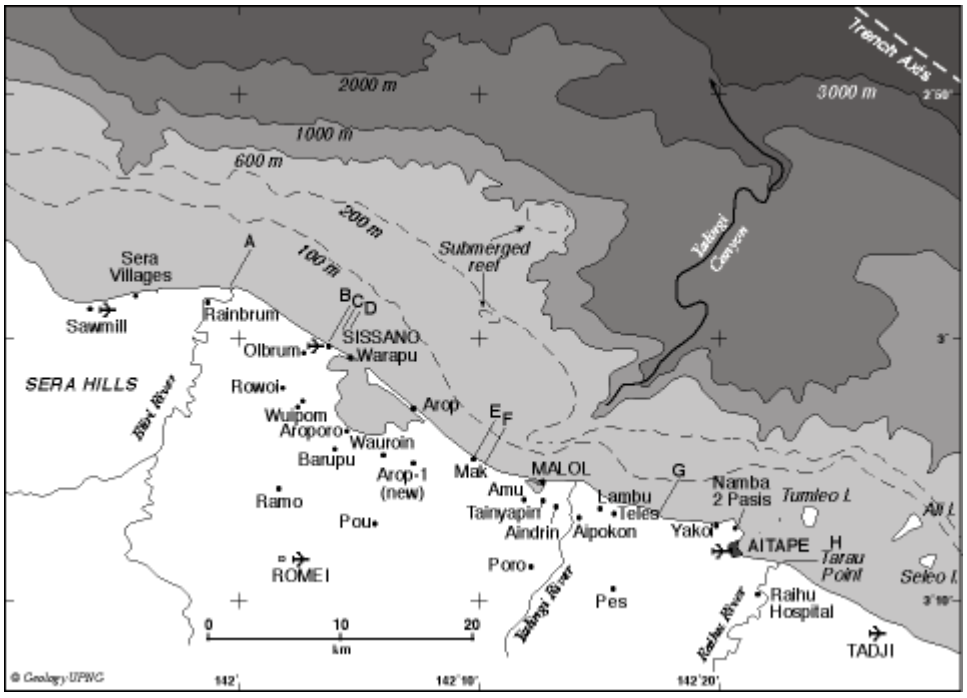

Figure 4.3 Map of the Aitape coast. Bathymetry is from multibeam survey (Matsumoto et al., 2003: solid lines) and from spot depths on a navigation chart supplementary to chart Aus 389: dashed lines. The main focus of the wave (wave heights ≥ 10 m) was on the 14 km sector of coast from Mak to Warapu, which includes the Sissano spit, where all buildings were destroyed as far as 500 m inland. From the mouth of the Bliri River to Sissano (AB), and from Mak toTarau Point (FH), surface elevations were less than 4 m above sea level (Davis et al., 2003).

The preceding authors reported that the tsunami was seen by observers as an initial lowering of the sea level, followed by three large waves, which caused significant damage along 45 km of coastline (from A to H in Figure 4.3). The largest waves and damage, however, were fairly narrowly focused on a 14 km section (from D to E in Figure 4.3), where surface elevations were 10-15 m above sea level on shore, with extensive damage for up to 500 m inland. The first wave was described as coming onshore as a breaking wave or bore, about 1 m high. Tappin et al. (2008)

mentioned that, based on its small elevation and timing, this wave could be attributed to have been generated by the direct coseismic displacement caused by the earthquake. Davis et al. (2003) reported that from the mouth of the Bliri River to Sissano (AB), and from Mak to Tarau Point (FH), surface elevations were less than 4 m above sea level.

Kawata et al. (1999a,b) reported wave elevations of up to 10 m along a 25 km stretch of coastline, with a maximum value of 15 m and overland flow velocities of 15-20 m/s in the area of maximum devastation (from D to E on Figure 4.3), based on survivors' reports at Arop and Warapu. Davis et al. (2003) mentioned that it was the second wave that reached the maximum heights and concluded, contrary to what has been generally accepted from the International Team Survey results, that it was unlikely that waves were approaching the beach with a 10-15 m height, and they estimated that incoming wave height were only about 4 m based on eyewitness reports at Arop and Warapu. According to these reports, the first large wave started breaking, at 200-300 m (10-11m depth) from shore at Arop, and reached the shore as a broken wave (breaking bore). Davis et al. imagined that the second wave was "deflected upwards" (shoaled-up) when it reached the shore, which was already flooded by the first wave, causing a reduced bottom friction.

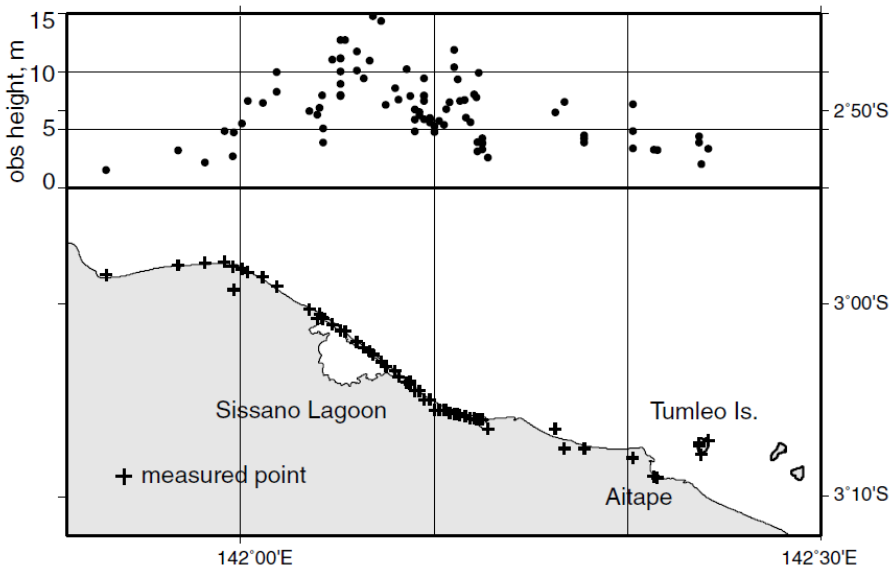

Figure 4.4 Tsunami elevations (flow depth above sea level) measured along the northern coast of PNG by the International Tsunami Survey Team. The map shows the location of measurement points (plus signs), and the measured water heights are shown in the upper diagram based on the longitude (from Kawata et al., 1999b).

2.3 Field data on submarine mass failure (SMF)

From1999 to 2001, several research cruises surveyed the area offshore of the Sissano Lagoon. The first one, in January 1999, done by the R/V Kairei of Japan Marine Science and Technology Center (JAMSTEC), performed bathymetry and side-scan sonar surveys with sub-bottom profiling and core sampling at four sites (Tappin et al., 1999). The bathymetric mapping showed some submarine features, including arcuate amphitheater and fault. The amphitheater is located at approximately 2.83 S, 142.26 E, about 30 km northeast of Sissano Lagoon (Figure 4.1), with the scarp of the amphitheater being approximately 10 km wide and 1 km high. There is an upraised block, 600 m high, to the north of the amphitheater, and the arcuate amphitheater indicated that a large-scale SMF was involved in the formation process, but it was not a recent event based on the detailed features observed, that showed erosion had

continued for some time, and the slope was covered with sediments (Tappin et al., 1999). The major fault linearments are 40 km long in the E-W direction on the northern slope of the upraised block and about 15 km long in the ENE-WSW direction, just south of the block. Also there is a convex-shaped slope, as a submerged delta, just off the Sissano Lagoon, which can act like a refractor and thus likely concentrated tsunami energy.

Two other cruises in 1999, by JAMSTEC's R/V Natsushima, provided visual observations of the ocean bottom by the Remotely Operated Vehicle (ROV) Dolphin and another with the manned submersible Shinkai 2000. Along the fault linearments, a a few features showed recent movement, which indicated that strong shaking occurred at the amphitheater. Tappin et al. (2001) interpreted the above bottom features as a submarine slump; however, Satake and Tanioka, (2003) believed these features alone did not prove the occurrence of a submarine slump during the PNG event, as similar features were also reported by Takuechi et al., (1998) for other tsunami sources where submarine slumps were not interpreted.

A seismic reflection survey cruise in 1999 was performed as well by the R/V Maurice Ewing (Sweet and Silver. 2003). One of the profiles showed a depression 100 m deep and 760 m long, which was interpreted as a rotational slump. The cross-sectional area of the displaced mass was 2.3 km^2, with a total estimated volume of 3.8–4.6 km^3. Based on these interpretations, Sweet and Silver (2003) reconstituted the slump and found that its center of mass had dropped by 380 m vertically, moved by 840 m horizontally, and slipped by 980 m along the slide plane.

Then, another cruise was performed in February 2001 by JAMSTEC's R/V Natsushima in the amphitheater, which confirmed the slump feature found earlier by the R/V Maurice Ewing, but also found several other slump features in the area. Slumps are typical features on the continental slope of this active margin and the timing of the slumps cannot be estimated from the seismic survey data (Satake and Tanioka, 2003). Matsumoto et al (2003) also reported the result of these cruises and documented underwater topographic features, which played a probable role in the generation of the PNG tsunami.

3. Modeling methodology

3.1 Slump geometry and kinematics for tsunami generation

As detailed above, there is a consensus in earlier work on the PNG case study that the maximum waves approaching the Sissano Lagoon and the large onshore runup were caused by a tsunami triggered by a delayed SMF, rather than by the coseismic tsunami. Hence, regarding tsunami sources, we do not consider here the coseismic tsunami source, which may have generated a first wave of only 1 m height or so (Tappin et al. 2008), but instead focus on tsunami waves generated by a large slump (rotational SMF) that the earthquake is believed to have triggered 25-30 km offshore of the Sissano Spit, with a 12 min delay (Tappin et al. 2008). Specifically, we parameterize and model the motion of the rigid underwater slump identified in field surveys (e.g., Figure 4.1), based on which the SMF tsunami source will be simulated in 3D using NHWAVE.

Among a few slump candidates (Tappin et al., 2001; Watts et al., 2003; Lynett et al. 2003; Watts et al., 2005), Tappin et al. (2008) identified from marine geology

surveys, their likeliest candidate slump for SMF tsunami generation, with an initial center of mass located (approximately in the middle of the slump) at 2.8791 S lat. and 142.2582 E long., at a d = 1.42 km depth where the local average slope is a steep β = 12 deg. (Table 4.1). The slump width was w = 4.2 km, its length was b = 4.5 km and maximum thickness T = 0.76 km; this led to an estimated volume of V_s = 6.4 km^3. The slump main direction of motion was θ = 349 deg. from North clockwise or α = 101 deg. from east anticlockwise (See the details in appendix).

Based on both eyewitness reports and tsunami simulations, Tappin et al. (2008) estimated that slump motion started 720 seconds (12 min) after the main earthquake shock, i.e., at 09.02 (GMT) to within approximately 45 s. They used a modified version of Watts, et al.'s (2005) equations and parameters (detailed in appendix). Using the slump geometry characteristics the radius of curvature of slump motion is R = 3711 m. Using this value, we calculate the characteristic time t_0 =32.2 s, where $\gamma = \frac{\rho_b}{\rho_w} = 2.146$ is the estimated slump sediment specific density, assuming a bulk density ρ_s = 2200 kg/m^3 and water density $\rho_w = 1025$ kg/m^3; the slump added mass coefficient is estimated at C_m=1.0 (Grilli and Watts, 1999), and g = 9.81 m/s^2 is the acceleration of gravity.

For PNG, the slump runout was estimated at s_f = 980 m, which we have used, although Watts et al. (2005) initially used 766 m; hence, s_0 = 490 m. With these values the slump initial acceleration is found as, $a_0 = \frac{s_0}{t_0^2}$ = 0.47 m/s^2 and the slump maximum velocity as, u_{max}=s_o / t_o = 15.2 (m/s) at the middle of its motion. These parameters, together with the law of motion in Eq. (A.3) will be used to specify the

bottom boundary condition in NHWAVE simulations, assuming a quasi-Gaussian shape for the slump, moving over the actual bottom bathymetry.

Before performing the simulations with NHWAVE, we verify consistency of the above parameters with those of the semi-empirical slump source used by Tappin et al. (2008) in their simulations. They calculated a basal shear strength of $S_u \approx 0.8$ MPa, with a corresponding Coulomb friction coefficient of $C_n \approx 0.11$. Based on Grilli and Watts (2005) we have,

$$s_0 = RC_n cos\beta \quad (1)$$

Tappin et al. reported using $R = 3.71$ km, but if they did, they would have had, $C_n = 0.135$. Hence, based on their reported data for C_n and with $s_0 = 490$ m, in our NHWAVE simulations, to be consistent with Tappin et al., we should use $R = 4.55$ km and by Eq. (A.1) (see appendix for the equations), $b = 5.04$ km and Eq. (A.2), $t_0 \approx$ 35s. Finally, because we increased the SMF length b, if we keep the same horizontal aspect ratio $b/w = 4.5/4.2 = 1.07$ as in Tappin et al. (2008), we would also increase the width to $w = 5.04/1.07 = 4.71$ km.

In NHWAVE simulations, following Enet and Grilli (2007), we represent the SMF geometry as a 3D quasi-Gaussian mound having an horizontal elliptical footprint (b,w), and an elevation ζ perpendicular to the average local slope, with a peak defined by a parameter ε as detailed in appendix. To calculate the ε value that is consistent with Tappin et al.'s data, knowing their value for basal shear strength S_u and volume, using Grilli and Watts' (2005) equations and Enet and Grilli's (2007) geometry, we

first express the shear force balance parallel to the average slope, that assumes failure at $t = 0$ (i.e., a factor of safety of 1),

$$C_n V_b(\rho_b - \rho_w) g \cos\beta = \frac{\pi}{4} bw\, S_u \quad (2)$$

which using Eq. (A.6) leads to,

$$C_n = S_u \frac{\pi(1-\varepsilon)}{4(f^2-\varepsilon)(\rho_b-\rho_w)Tg\cos\beta} \quad (3)$$

Using, as Tappin et al., a slump volume V_b = 6.4 km^3 with the above dimensions b = 5.04 km, w = 4.71 km, and T = 0.76 km, does not yield a possible value of ε. Instead, assuming $\varepsilon = 0.8$ (i.e., C = 0.693 *;* f = 0.928), which is a little more bunched up than in Enet and Grilli's experiments, and keeping a maximum thickness T = 0.76 km we find that to satisfy the volume, the elliptical footprint surface area must be increased by 15%, or each of the horizontal dimensions by 7%, yielding b = 5.40 km and w = 5.04 km. Alternately, if we keep the (b,w) values, we would need to increase the thickness by 15%, i.e., T = 0.874 km, which is still a realistic thickness for a slump where thickness is typically 10-20% of downslope length b, i.e., here a maximum of 1.14 km. If we change the thickness this way, assuming $C_n = 0.11$, the shear equilibrium Eq. (3) yields S_u = 0.43 MPa, which is too small. Satisfying $S_u = 0.8$ MPa would require further increasing slump thickness by 86% to T = 1.64 km, which is beyond the realistic range.

Therefore, to satisfy the various constraints above, we need to both increase the slump thickness and the Coulomb friction coefficient value. The following parameter values satisfy approximately the various constrains, given s_0 = 490 m and V_b = 6.4 km^3: $\varepsilon = 0.44$ (i.e., C = 1.46*;* f = 1.001), b = 5.047 km, w = 4.717 km, T = 1.06 km (=0.21b); $C_n = 0.2$; S_u = 0.77 MPa , R = 2.505 km, Cm = 1.8, t_0 = 30 s.

Hence, this slump will also have a faster kinematics, with an initial acceleration a_0 = 0.54 m/s^2 and maximum velocity u_{max} = 16.3 m/s and, despite a flatter shape (due to the reduced ε), it should be slightly more tsunamigenic.

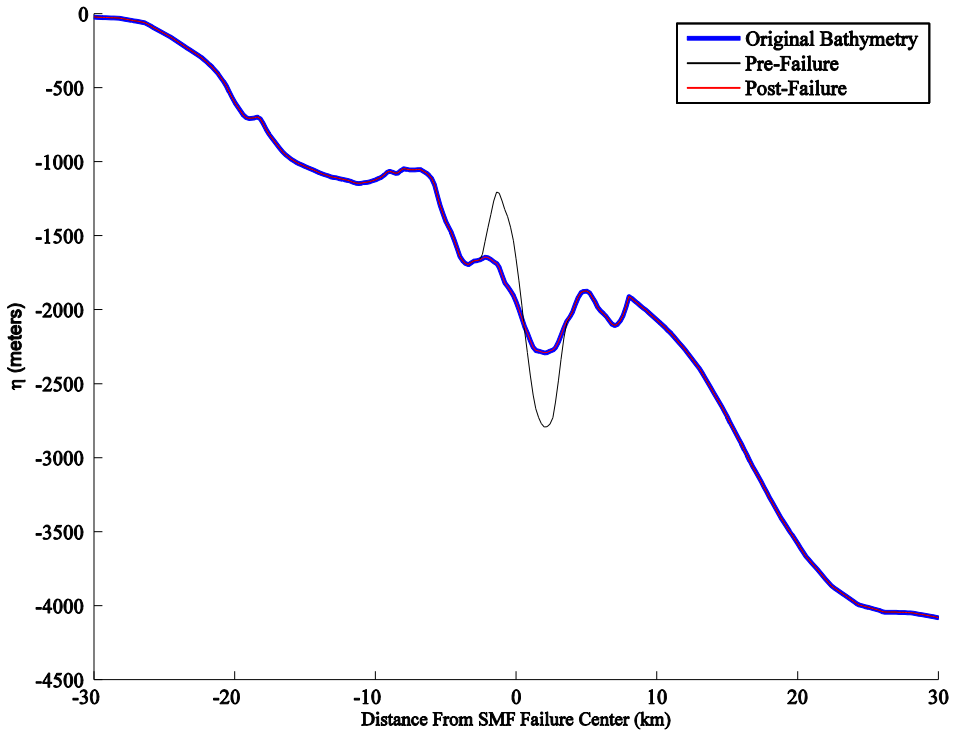

Figure 4.5 Transect of bathymetry (white line in Figure 4.8) difference between the bathymetry in the model at $t \approx 100$ s and 0 s. The Gaussian hump removed from the current bathymetry (blue line), and added back to the initial location of the slump to have pre-failure bathymetry (black line). As it shows after slump failure, the Gaussian slump would rotate and fill in the removed area.

The pre-failed bathymetry of the Currituck SMF is reconstructed, to the first-order, by adding the sediment volume V_b to the post-failed area, which is the existing bathymetry of the domain. Adding the SMF geometry as a hump to the current bathymetry would not accurately fit to the final bathymetry. Therefore, part of the sediment at the final location of the slump is removed as a Gaussian hump (pre-failed bathymetry), and then the slump is added to the pre-failed bathymetry at the initial location of the slump. During the modeling of SMF failure, upon moving over the runout, the SMF volume will

fill in the removed area and we will recover the existing bathymetry of the domain at the post-failure stage.

In the bottom boundary condition used in NHWAVE, using the above parameters (see Tables 4.1 and 4.2), we specify the slump geometry described by Eqs. (A.4-5) and the kinematics described by Eq. (A.3). The first and second derivatives of the latter equation give the velocity and acceleration of the slump center of mass, respectively, the former being used to specify the bottom velocity in NHWAVE. One can find details of equations of motion in Grilli and Watts (2005) and Enet and Grilli (2007).

The slump comes to rest after about t_f = 94 s, at which time its center of mass has advanced about s_f = 980 m down the slope. This information, which approximately matches that used in Tappin et al. (1998), is used here as our initial guess for SMF kinematics in the present simulations with NHWAVE. The approximate location of the slump can be seen in Figure 4.6 and the initial surface elevation used as a hot start initialization at $t = t_0$ of in Tappin et al.'s (1998) simulations with FUNWAVE (Wei et al., 1995) is shown for comparison in Figure 4.7. This surface elevation is based on the semi-empirical formulas of Watts (2002a,b), also detailed in Grilli and Watts (2005) and Watts et al. (2005). We see that initial surface elevations of the SMF tsunami at $t = t_0$ = 30 s, are predicted to vary, at least, between -15 and + 15 m on this figure. However, as we shall see in the following, the actually maximum elevations and trough are much larger.

Table 4-1 Updated parameters for the PNG slump, based on Tappin et al. (2008)

Mean initial depth d (km)	1.42	Initial maximum width w (km)	4.72
Mean local slope angle β (deg.)	12^o	Initial downslope length b (km)	5.05
Initial maximum thickness T (km)	1.06	Bulk density ρ_s (kg/m^3)	2,200
Basal shear strength S_u (MPa)	0.77	Coulomb friction coefficient C_n	0.2
Distance of slump motion/runout s_f (km)	0.98	Slump azimuth of motion, from North clockwise θ (deg)	349

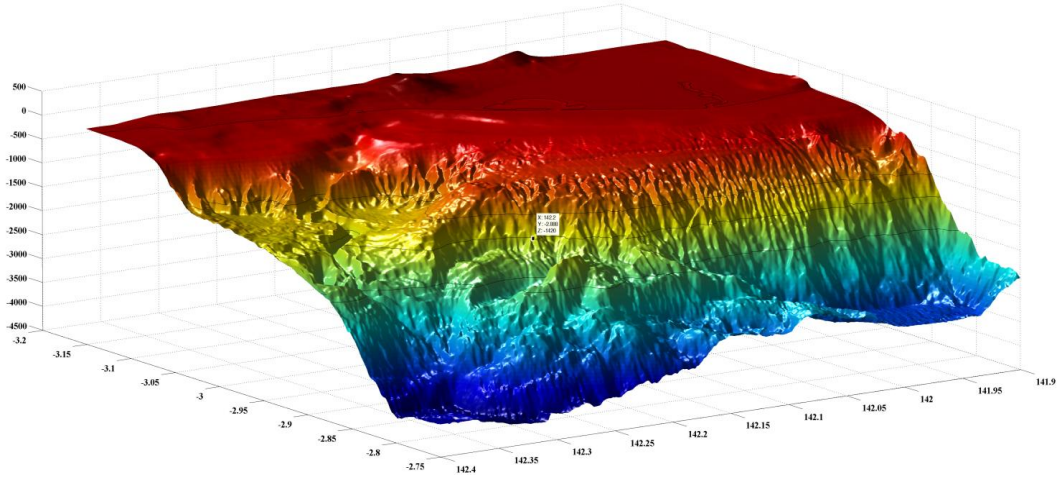

Figure 4.6 Approximate location of the PNG slump, and bathymetry, based on Tappin et al. (2008).

Table 4-2 Characteristicsas parameters for the knematics of the PNG slump to be used in NHWAVE simulations (based on Tappin et al., 2008)

characteristic distance s_0	490	initial acceleration (m/s^2)	0.54
characteristic time t_0 (s)	30	maximum velocity	16.3

3.2 Simulation of SMF Tsunami Generation with NHWAVE

The 3D non-hydrostatic σ-layer model NHWAVE (Ma et al., 2012) is used to compute tsunami generation, in a 200 m resolution horizontal grid (Table 4-3), based

on specified underwater slump geometry and motion, as detailed above. In doing so, boundary conditions are computed for pursuing simulations further nearshore, in a finer 50 m resolution nested grid towards the Sissano spit, and further down in 12m resolution grid (Table 4-3; Figure 4-8), using the long Wave model FUNWAVE-TVD (Shi et al., 2012). New bathymetry and topography were constructed for the area by interpolating the new sources of MBES data with the ETOPO-1 data. This led to the map of Figure 4-8, which shows the areas covered by the 200 m, 50 m and 12 m model grids.

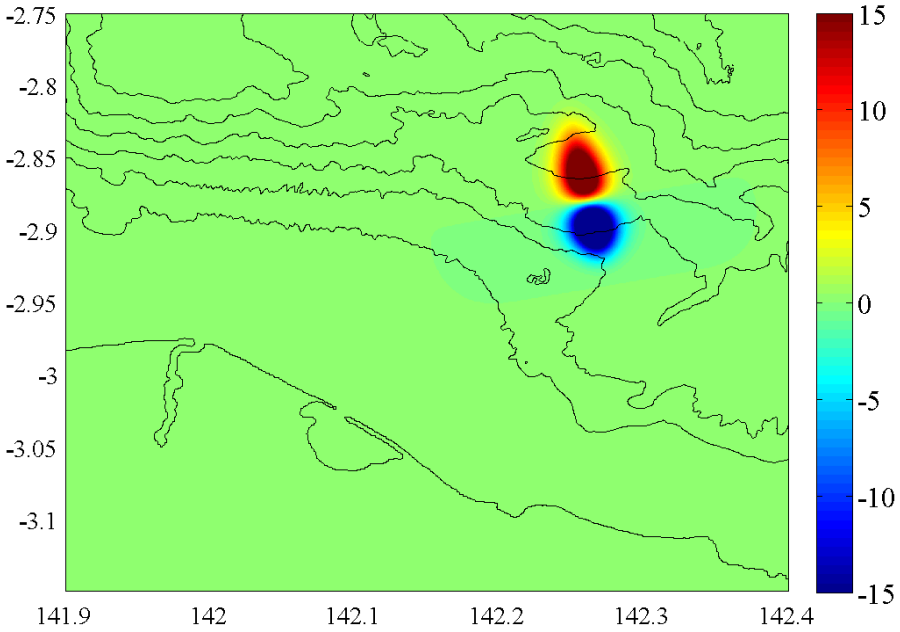

Figure 4.7 Initial surface elevation used as a hot start at $t = t_0$, in Tappin et al.'s (2008).

Table 4-3 Computational domains used by numerical models

Grid	X Grid Cells	Y Grid Cells	Longitude (Deg.) E	Latitude (Deg.) S	Cartesian X (km) (UTM)	Cartesian Y (km) (UTM)	Resolution
NHWAVE	525	580	141.7195, 142.6632	3.2748, 2.2265	580 - 684.8	9638 - 9753.8	200 m
FUNWAVE -TVD	933	665	141.988, 142.4076	3.2131, 2.9123	609.8 - 656.4	9644.8 - 9678	50 m
FUNWAVE -TVD	1449	1077	142.0047, 142.1677	3.109, 2.987	611.65-629.75	9656.3-9669.75	12 m

NHWAVE solves the inviscid Euler equations, with fully nonlinear free surface boundary conditions, and has been validated for both coseismic and rigid SMF tsunami generation and propagation, according to NOAA-NTHMP guidelines (Tehranirad et al., 2012). FUNWAVE-TVD is a fully nonlinear and dispersive Boussinesq long wave propagation model, which was similarly benchmarked as part of NTHMP (Tehranirad et al., 2011).

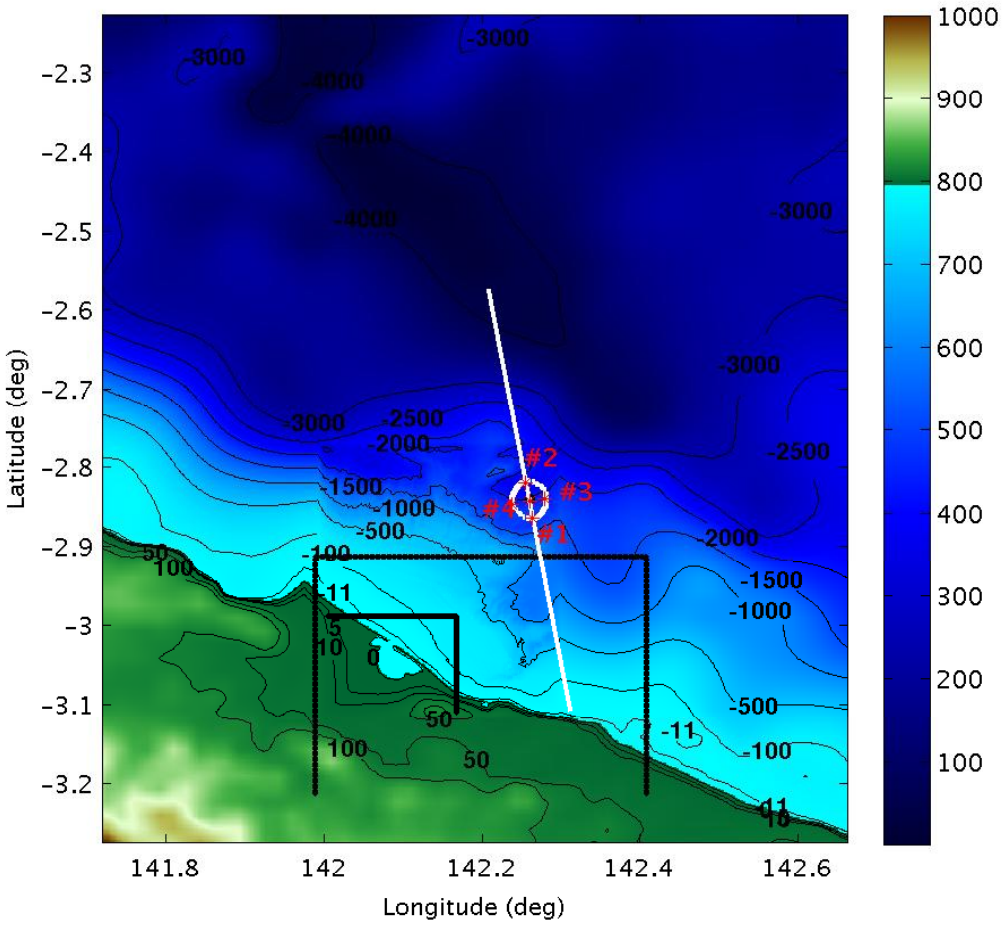

Figure 4.8 Footprint of the NHWAVE 200 m resolution grid, with boundaries of FUNWAVE-TVD 50 m and 12m grids (black nested solid lines). Interpolated bathymetry and topography from ETOPO-1 and MBES data (color scale and contours in meter). Slump (white ellipse) moves down the local 12 deg. average slope, in direction 349 deg. clockwise from North (white line; this transect in the direction of movement is used in next figures). The red star marks the center of the slump and the red labels are 4 station located around it.

Owing to the proximity to shore of the PNG slump, we use a fairly resolved initial horizontal Cartesian grid in NHWAVE, with a 200 by 200 m mesh size (Table 4-3; Figure 4.8). To eliminate reflection of outgoing waves into the domain, 40 km wide sponge layers were used along the offshore boundaries (West, East and North). We specify the bottom boundary condition in NHWAVE (both geometry and kinematics), based on the slump parameters (Tables 4-1 and 4-2) and equations detailed above. Figure 4.9 illustrates the specified failed slump geometry on the seafloor, as simulated in NHWAVE, by showing the difference between the bathymetry at $t = 0$ and 100 s, which is slightly after the slump has stopped moving, at $t_f \approx 94$ s. As can be seen on the figure, the slump has been moving nearly orthogonally to the -1500 and 2000 m depth contour level, in a direction 349 degree from North (clockwise).

For simulating long wave generation, NHWAVE typically only requires 3 σ-layers in the vertical direction (e.g., Grilli et al., 2014), owing to the fairly uniform horizontal velocity over depth. However, here, the slump fails in fairly large depth compared to its downslope length (d/b = 3.56), which means that intermediate to deep water waves will be generated, which will be strongly dispersive (e.g., Grilli and Watts, 2005). Accurately modeling such dispersive (i.e., non-hydrostatic) waves requires using a larger number of σ-layers in NHWAVE in the vertical direction. To verify this, we run simulations with 3 to 11 σ-layers and compared results obtained at t = 100 s. Figure 4.9, shows the comparison of transect line (white line Figure 4.8) simulated water surface elevations at t = 100 s,; By increasing the number of layers from 7 to 11, we observed only a very small difference in results, indicating that an

accurate solution of the non-hydrostatic equations of motion was achieved using 9 layers. Thus, 9 σ-layers will be used in our simulations.

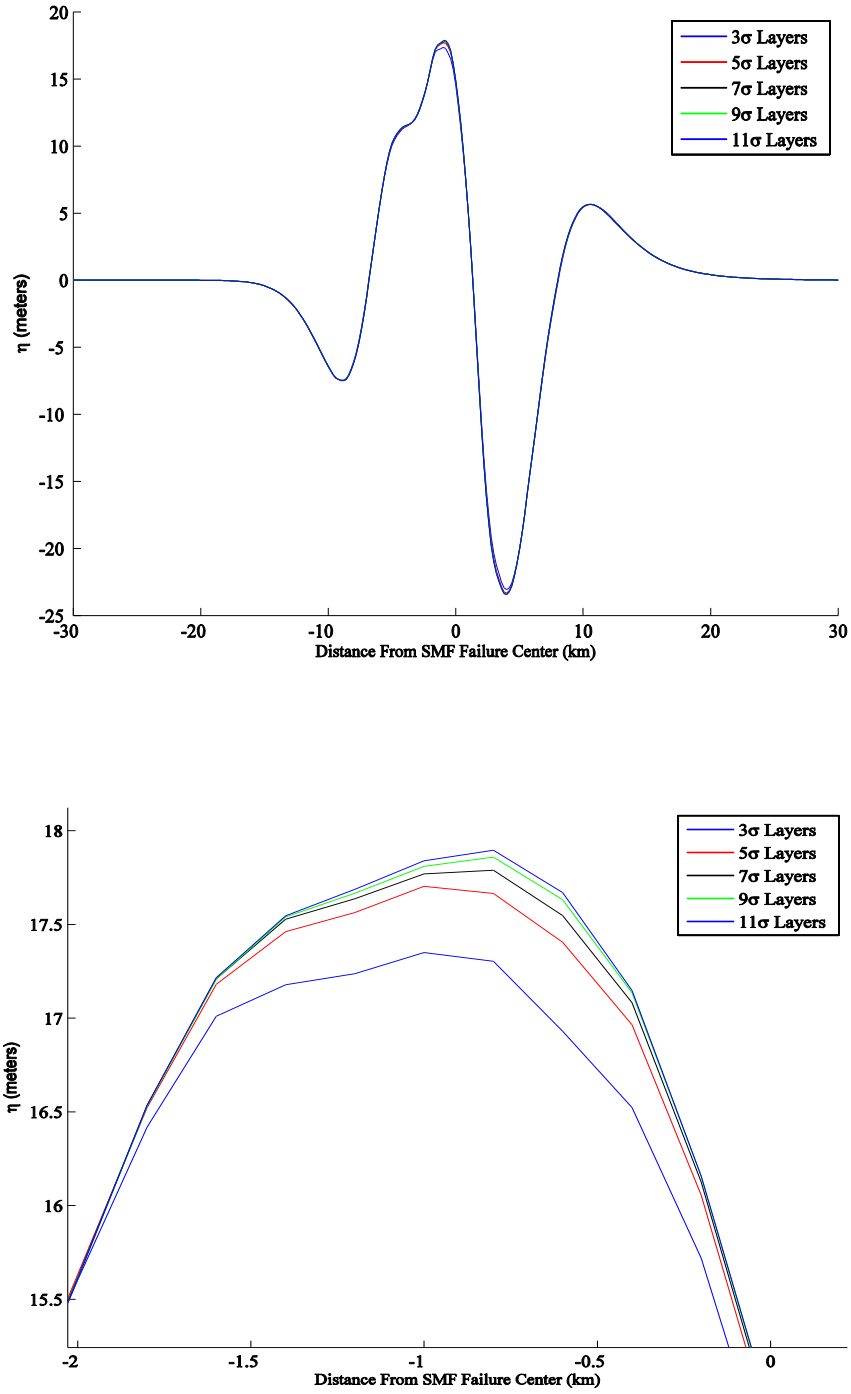

Figure 4.9 Differences in simulated surface elevation at *t* = 100 s, using NHWAVE with different σ- layers, for the updated PNG slump parameters based on Tappin et al. (2008) (Tables 4-1, 4-2); the lower panel is zoomed in of the wave crest in the upper panel.

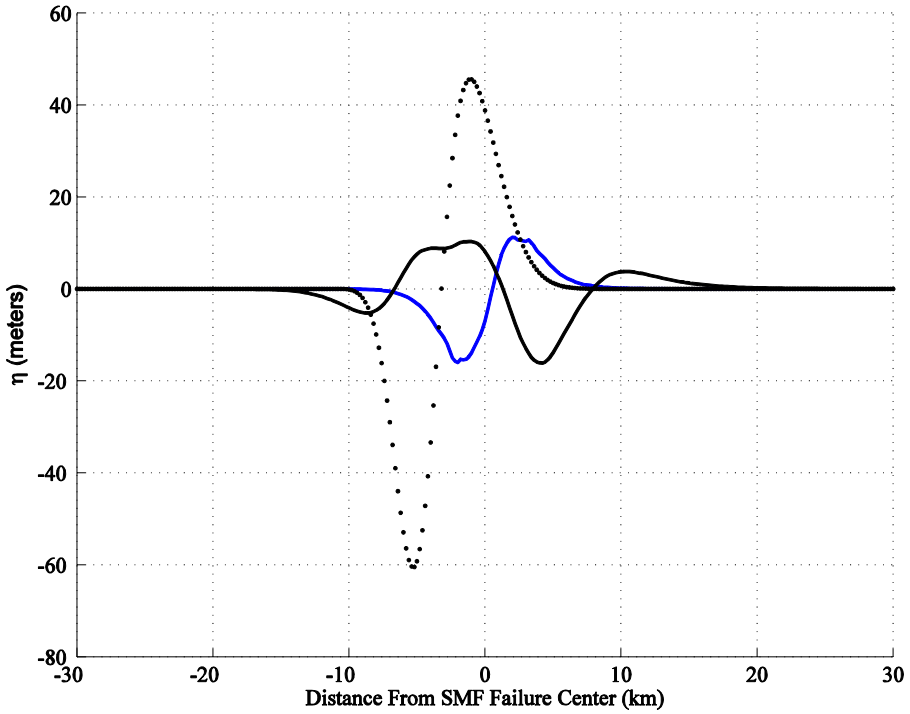

Figure 4.10 Tansect of surface elevation computed by NHWAVE at t_0 (blue) and t_f (solid black), and using TOPICS (Figure4.7) at t_0 (dotted black)

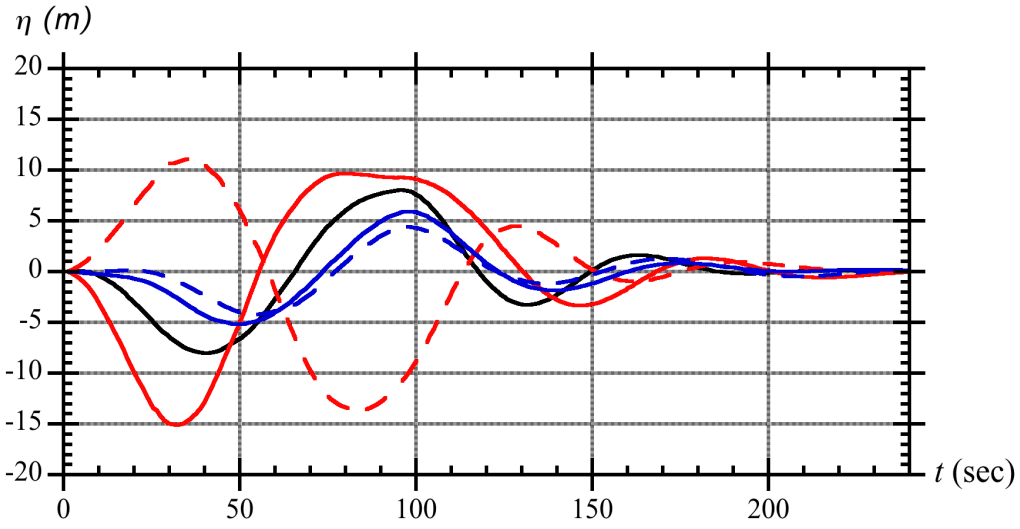

Figure 4.11 Time series of surface elevation at the stations around the slump (Figure4-8): center of the slump (black); stations: #1 (solid red), #2 (dashed red), #3 solid blue, #4 dashed blue.

NHWAVE simulations show that, qualitatively similar to Figure 4.7, the initiation of slide motion creates two negative and positive Gaussian-like humps, with

the trough located in shallower depth and the elevation wave in deeper water. Figure 4.10 shows the comparison of initial condition generated by TOPICS based on semi-empirical equations at t_0 and the same slump motion simulated by NHWAVE. It can be seen that TOPICS is predicting the amplitude about 4-5 times that of the NHWWAVE's. As mentioned earlier, NHWAVE is using the slump movement specified over the actual bathymetry; additionally, the equations used by TOPICS to calculate η_0 are based on idealized laboratory experiments on a plane slope (see Appendix). Figure 4.11 shows the time series of surface elevation computed at the 4 stations around the initial location of the slump, at locations shown on Figure 4.8. Figure 4.12a then shows that, later in time, after the slump has stopped moving, at t = 100 s, the initial trough has "rebounded" into a crescent-shape negative wave (maximum -8 m) followed by a larger (maximum +14 m), both propagating onshore, while the initial elevation wave in the Gaussian dipole propagates offshore as a crescent-shape wave (maximum + 5 m).

Figure 4.12b finally shows, at t = 200 s, that as waves propagate both onshore and offshore, away from the initial SMF location, they behave as cylindrical wave trains, i.e., spreading out and decreasing in elevation, with however, a larger elevation (both positive and negative) within a small angular spread around the initial azimuthal direction of slump motion. This results from the fact that there is preferential energy transfer form slump to wave motion near this direction, yielding more directional wave trains. In this figure, we also see that, as a result of frequency dispersion, additional waves are being continuously created and the back of each onshore and offshore propagating wavetrain.

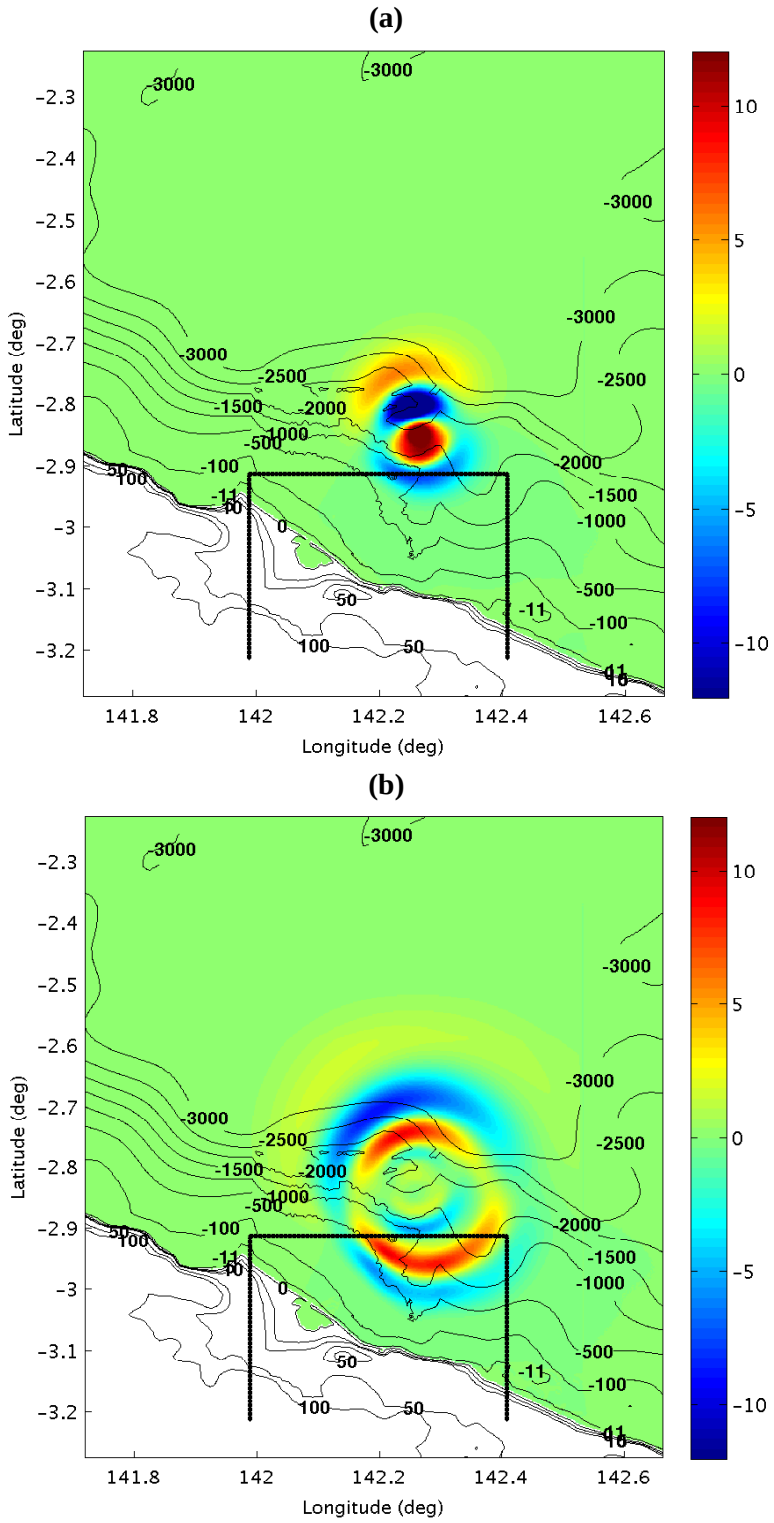

Figure 4.12 Simulation using NHWAVE (9 σ-layers) of tsunami surface elevations (color scale in meter) generated by the PNG slump, at t = (a) 100 and (b) 200 s, based on updated parameters from Tappin et al.'s (2008) (Tables 4-1, 4-2). The black solid lines show the location of the boundary of FUNWAVE-TVD's 50 m resolution grid. Bathymetric and topographic contours are in meter.

Finally, to the south of Figure 4.12b, we clearly see the beginning of wave refraction, with a bending of the crescent-shape wave rays towards the Sissano spit, as wave crests and troughs become increasingly more parallel to the local bathymetric contours.

3.3 Tsunami propagation

Nearshore tsunami propagation and coastal impact (runup) are simulated using the fully nonlinear and dispersive Boussinesq model FUNWAVE-TVD in its latest Cartesian implementation (Shi et al., 2012). FUNWAVE-TVD is fully parallelized for an efficient solution on shared memory clusters and has a more efficient Total Variation Diminishing (TVD) algorithm to follow breaking wave fronts in shallow water. The model has a quadratic bottom friction term controlled by a friction coefficient C_d and simulates dissipation in breaking waves by turning off dispersive terms in areas where breaking is detected, based on a breaking index criterion; this turns the model into solving NSW equations, which have been showed to accurately simulate the physical dissipation in breaking wave bores. As indicated before, FUNWAVE-TVD has been fully validated for tsunami propagation and runup against standard benchmarks, as part of the National Tsunami Hazard Mitigating Program work (Tehranirad et al., 2011).

Simulations to the shoreline of tsunami propagation and runup are performed by one-way coupling in FUNWAVE-TVD's 50 m resolution nested Cartesian grid, based on time series of surface elevation and horizontal velocity (at the required 0.53 times the local depth for FUNWAVE-TVD) computed with NHWAVE, in the 200 m resolution grid, along the boundary of the 50 m resolution grid (Figure 4.12). Using

these as boundary conditions, computations in FUNWAVE TVD are restarted from time $t = 0$. Specifically, along the offshore boundary of the 50 m grid, time series are computed for 565 grid points in the 200 m grid (233 grid points on the northern boundary, and 166 grid points on both eastern and western boundaries). Because simulations are run for a long time in NHWAVE, the time series include both incident and reflected waves and thus satisfy the open boundary condition.

Figure 4.13 shows surface elevations computed with FUNWAVE-TVD in the 50 m resolution grid based on boundary conditions obtained from NHWAVE's simulations in the 200 m grid. At $t = 300$ s, a leading depression wave (maximum -7 m) is followed by a larger elevation wave (maximum over +10 m), then followed by two smaller negative and positive waves. As they approach the shore in shallower water, all these waves significantly shoal up and reduce in wavelength. The larger elevation wave is seen to impact almost the entire coastline, east of the Sissano spit (with over 10 m inundation depth) and half the spit, at $t = 600$ s (10 min., i.e., about 22 min after the earthquake occurred). Figure 4-14 shows the maximum envelope of surface elevations computed at any time during these computations. Maximum runup is seen to reach over 14 m on the coast, east of the Sissano spit, which is within the order of magnitude of the maximum measured runup of 16 m in the Sissano area.

Many measurements of flow depths and runup were made shortly after the PNG event along the shore of the Sissano spit, and east of it. These were reported as runup by Tappin et al. (2008), but are clearly a combination of both flow depth on the spit (West of Lon. 142.13 deg.), near its shoreline (e.g., measured by way of water marks on and debris caught in the trees), and actual runup to the east of the spit (East

of Lon. 142.13 deg.) where the shore is sloping and actual runup can occur. There is therefore no easy way to compare model results to these field measurements.

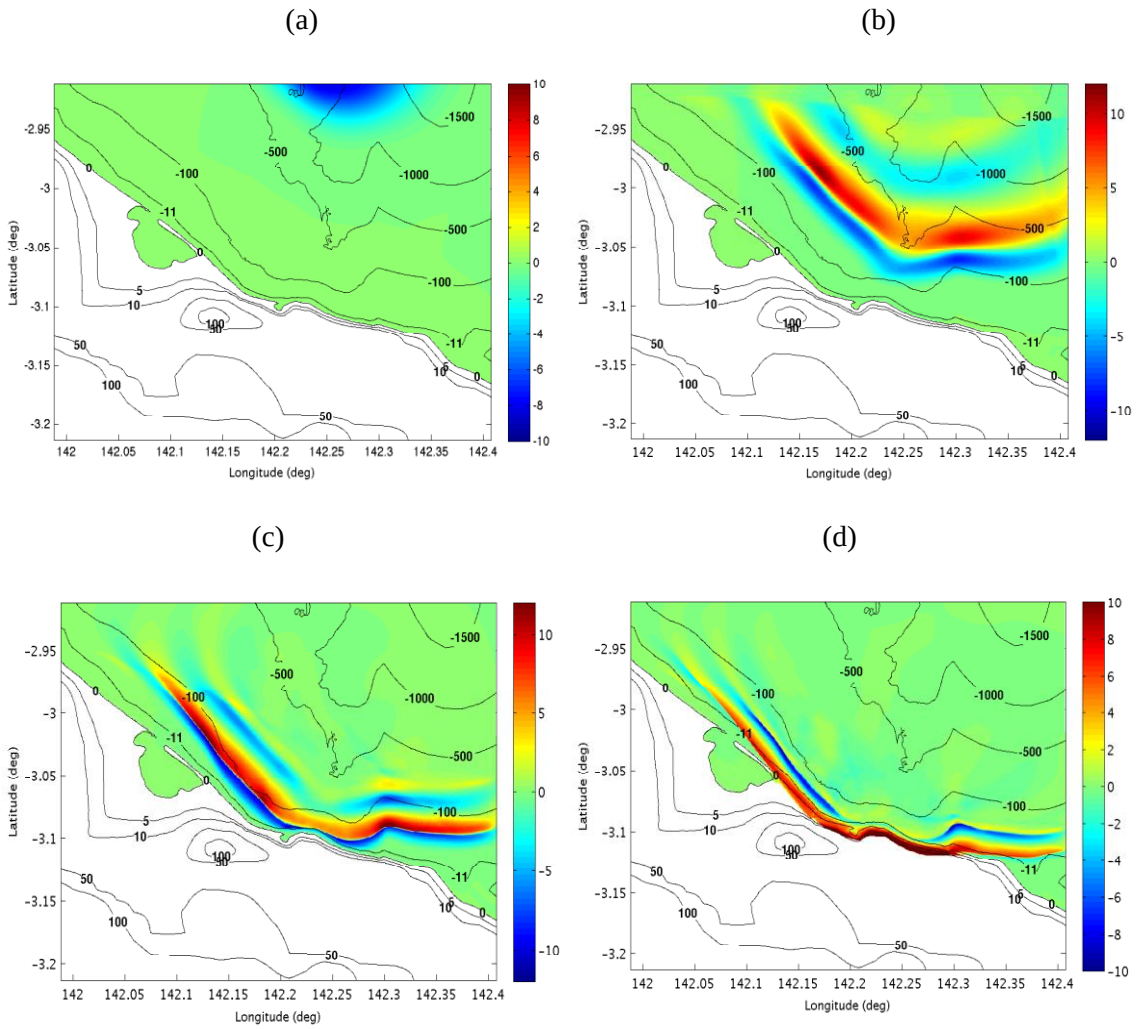

Figure 4.13 Surface elevation (color scale in meter) computed with FUNWAVE-TVD in the 50 m grid domain, based on boundary conditions provided by NHWAVE for the simulations of the PNG slump (Tables 4.1, 4.2), at *t* = a) 90, b) 300, c) 450, and d) 600 s.

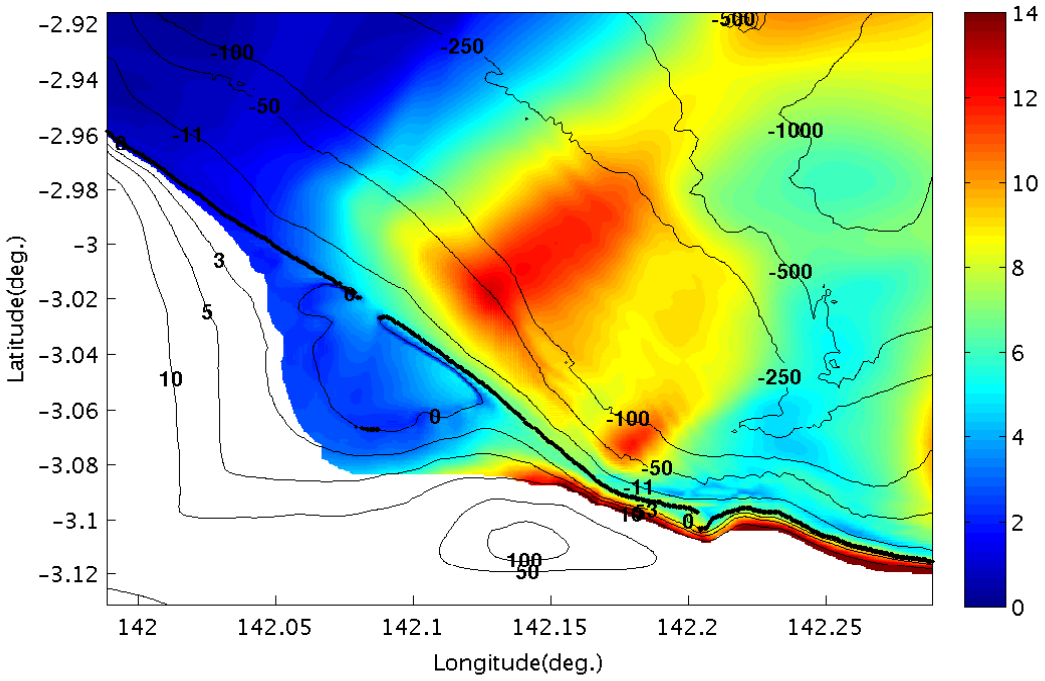

Figure 4.14 Maximum surface elevation computed with FUNWAVE-TVD (50 m grid resolution) for the tsunami generated by the PNG slump (parameters given in Tables 4-1 and 4-2). The red circles mark locations where inundation depth is measured in 50 m resolution grid, and red circles show where it is measured in the 12 m resolution domain.

Thus, in Figure 4.15, we first compared the computed inundation (flow) depth at the measurement locations at both 50 m and 12 m grid (see Figure 4.14) and compared it to field data. The figure shows that the simulated flow depth along the shore is less than the measured data, particularly along the Sissano Lagoon, between Lon. 142.07-142.13 deg. East of this area, the discrepancy between simulations and observations is reduced and, considering Figure 4.14, which shows maximum runup, the agreement would likely be much better between computed runup and observations in this part of the shoreline. Figure 4.15 also shows that offshore of the spit, maximum surface elevations were much larger and hence, perhaps bottom friction dissipation is too large in the model and causes too much of a decrease in wave elevation before the tsunami floods the spit. Tappin et al. (2008) reported as maximum runup along the

shoreline the maximum surface elevation reached along some transects across the shoreline and hence this confusion between runup and flow depth tended to improve the agreement between their model results and observations. Also, the older version of FUNWAVE they used modeled the moving shoreline using a "slot method" that has been since then proven inaccurate and replaced by a more accurate algorithm in FUNWAVE-TVD (see Shi et al, 2012 for detail). Finally, Figure 4.15 shows that increasing the resolution of bathymetry and using finer grid, does not dramatically change the measured flow depth close to Sissano Lagoon, likely because the bathymetry is too coarse anyway.

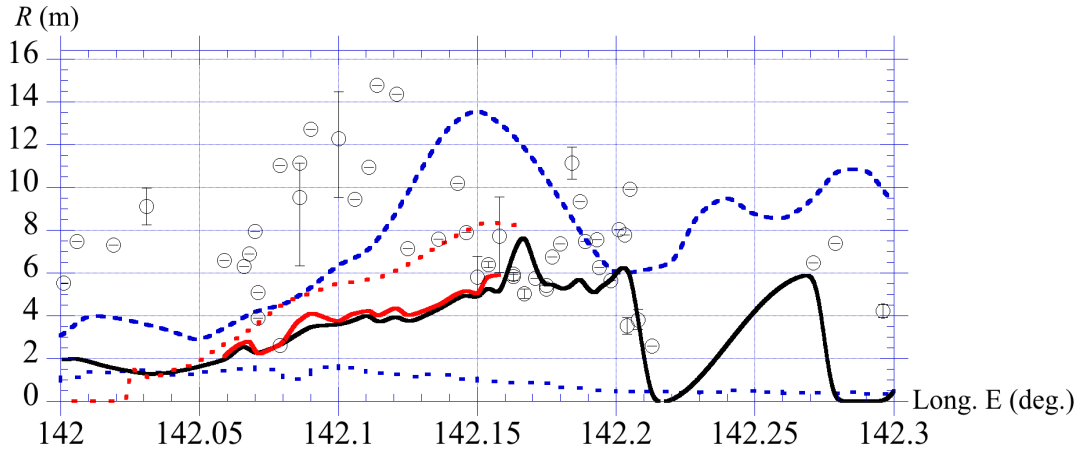

Figure 4.15 Maximum flow depth computed with FUNWAVE-TVD in the 50 m grid (black line) and 12 m grid (red line), at the actual locationd of field survey measurement (Figure 4.13), compared to field measurements of "flow depth" (black circles), caused by the PNG slump failure (Tables 4-1 and 4-2). The error bars are due to different measurements reported at the same location. The lower and upper dashed blue lines are the simulated runup by earthquake and SMF sources, respectively, presented by Tappin et al. (2008). The dashed red line shows maximum runup in 12 m grid; it has a better agreement with measurements.

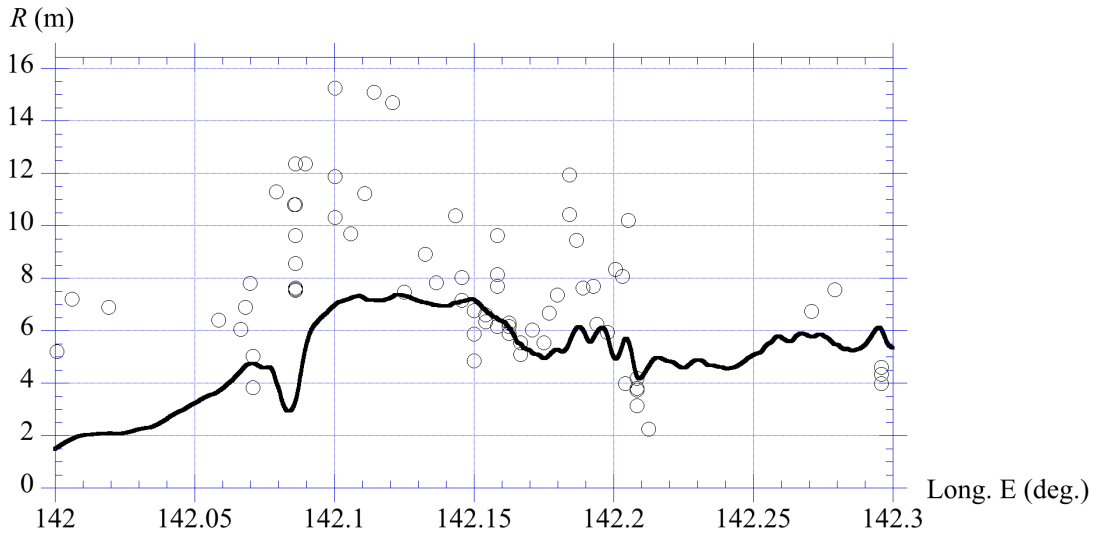

Figure 4.16 Maximum flow depth (inundation; thick black line) computed with FUNWAVE-TVD in 50 m grid along the initial shoreline (Figure 4.13), compared to field measurements of "runup" (black circles), caused by the PNG slump failure (Tables 4-1 and 4-2), but here moving in azimuth 40 deg. from North.

To further reduce discrepancies between observations and our simulations, one would need to consider the various ranges of uncertainty in the slump parameters used in the simulations. Hence, some of the slump parameters could legitimately be adjusted within the allowable geological uncertainty for the simulation results to better match observations. One value that could be modified here, which affects where the largest tsunami impact will occur, is the orientation (or azimuth) of the slump motion. While Tappin et al. (2008) mentioned a downslope motion in azimuth 349 deg. (clockwise from north). Carefully checking the bathymetry in the area (e.g., Figure 4.8), one could conclude that the slump moved in a direction more down the local slope, in the direction of a submerged coral reef (Figure 4.3), i.e., to the northeast with an azimuth of 40 deg. (clockwise from North). Assuming this direction of motion and keeping all the other parameters identical, we obtain the flow depths shown in Figure 4.16, which have a somewhat better agreement with measurements along the shoreline

between Lon. 142.13-142.21 deg., but not again on the Sissano spit itself. Clearly, more work needs to be done here to further parameterize the slump, in order to achieve a better agreement with observations. This will be the object of future work, where a new interpretation of geologic surveys will be made in order to better estimate the slump geometry.

4 Conclusions

In this paper, we reviewed the historical case of the 1998 Papua New Guinea tsunami that is believed to have been caused by a deep slump failure induced by the earthquake, after a 12 min. delay. We proposed a new improved modeling of tsunami generation by the SMF motion, using the 3D non-hydrostatic model NHWAVE. This led us to revise the slump parameters used for this event in earlier studies (such as Tappin et al., 2008). The new modeling methodology was implemented and numerical simulations carried out to achieve a better understanding of this important historical event.

The slump source was first re-parameterized based on available data and the existing literature, in view of the geometric model of SMFs proposed by Enet and Grilli (2007) and the rigid slump kinematics equations of Grilli and Watts (2005) and Watts et al. (2005), as also detailed in Grilli et al. (2014). Then, tsunami generation and propagation were simulated using two state-of-the-art, fully validated, numerical models. As indicated, NHWAVE was used to simulate wave generation in 3D based on slump geometry and motion, specified as bottom boundary conditions, and FUNWAVE-TVD, a fully nonlinear and dispersive long wave model was used for simulating the 2D (horizontal) tsunami propagation in a finer resolution nested

Cartesian nested grid domain. When the slump stopped, time series of NHWAVE results were used in a one-way coupling algorithm, as boundary conditions along the offshore boundary of FUNWAVE-TVD's grid, and wave propagation to the shoreline and runup were further simulated. Maximum flow depth was computed along the initial shoreline and compared with available field measurements (which combined some runup and flow depth measurements). A reasonably good agreement between simulations and observations was found, using the original (updated) slump parameters of Tappin et al. (2008). Some of the discrepancies could be explained by differences between flow depth at the shoreline and maximum runup for the eastern part of the coastline. Discrepancies on the Sissano spit, however, were quite large (a 40-50% under-prediction in some cases).

The lack of high-resolution bathymetric data for this area could explain in part the under-prediction of runup around the Sissano spit and Lagoon. Even without a finer bathymetry, simulations on a finer nested grids of 12 m around the lagoon did not increase the calculated maximum flow depth/runup along the shoreline significantly, in order to have a better agreement with measured values.

Finally, uncertainties in the slump parameters themselves mean that one could vary some of the parameters within their acceptable range of variation, by reanalyzing geologic surveys, and perform a sensitivity of simulation results to those. In this work, we showed that the azimuthal direction of slump motion played an important role on where maximum inundation is focused on the shoreline. Likewise, having a better estimation for the range of acceptable slump thickness and length (hence volume), could lead to modified results; for instance, increasing the slump size/volume, will

increase initial acceleration and hence initial wave generation and eventually inundation and runup on the shore. This sensitivity analysis will be left out for future work.

Appendix

SMF kinematics

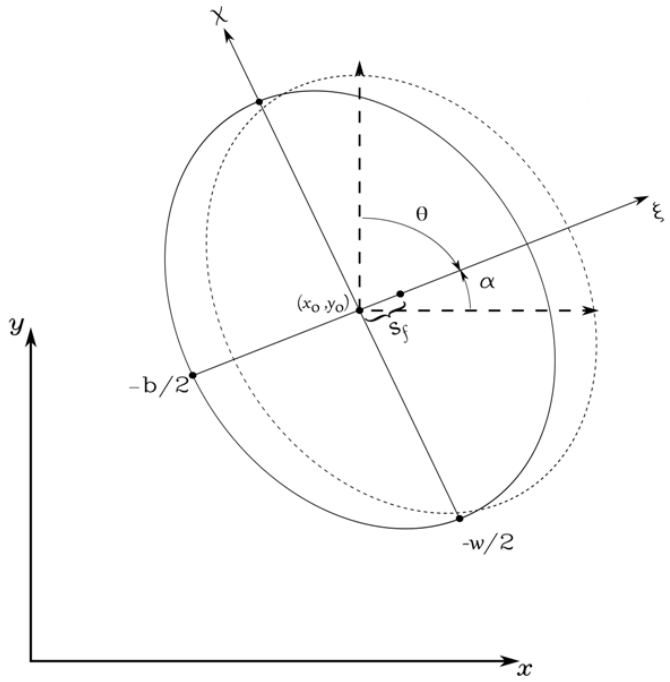

Figure 4.17Appendix Geometry of a slump initially centered at (x_0, y_0), with elliptical footprint (*b*,w), moving in direction ξ, with an azimuth angle θ from North clockwise or α from East counterclockwise, and center of mass motion *s(t)* measured parallel to the mean local slope of angle β.

The radius of curvature of slump motion on a circular arc, along a chord parallel to the mean local slope, based on geometry is,

$$R = \frac{b^2}{8T} + \frac{T}{2} \qquad \text{(A.1)}$$

the slump characteristic time of motion t_0 (Grilli and Watts, 2005):

$$t_0 = \sqrt{\frac{R(\gamma + C_m)}{g(\gamma - 1)}} \tag{A.2}$$

The simplified slump kinematics proposed by Grilli and Watts (1999, 2005) for the slump center of mass motion *s(t)* parallel to the mean local slope reads,

$$s(t) = s_0\left(1 - \cos\left(\frac{t}{t_0}\right)\right) \tag{A.3}$$

assuming, the slumps starts at rest at $t = 0$ and covers a runout distance $s_f = 2s_0$ over time $t_f = \pi\, t_0$, with s_0 the slump characteristic distance of motion.

Following Enet and Grilli (2007), the SMF geometry is presented as a 3D quasi-Gaussian mound having an horizontal elliptical footprint (*b*,*w*), and an elevation ζ perpendicular to the average local slope:

$$\zeta(\xi, \chi) = \frac{T}{1-\varepsilon} \max\left[0, \operatorname{sech}(k_b \xi)\, \operatorname{sech}(k_w, \eta) - \varepsilon\right] \tag{A.4}$$

where ε is a spreading parameter (within]0,1[) that controls how "peaky" or bunched up the SMF is. ξ and η are two orthogonal directions, down slope and normal to that, respectively, and,

$$k_b = \frac{2}{b}\mathrm{C}\,, k_w = \frac{2}{w}\mathrm{C} \quad \text{with} \quad C = \operatorname{acosh}\frac{1}{\varepsilon} \tag{A.5}$$

The SMF volume corresponding to Eqs. (4-5) is calculated as,

$$V_b = bwT\left(\frac{f^2 - \varepsilon}{1-\varepsilon}\right) \quad \text{with } f = \frac{2}{C}\operatorname{atan}\sqrt{\frac{1-\varepsilon}{1+\varepsilon}} \tag{A.6}$$

Equation solved by TOPICS (GEOWAVE)

d : initial depth of the middle of slump (m)

θ: mean slope along failure plane (rad)

b: initial slump length during failure (m)

T: maximum initial slump thickness (m)

w: maximum initial slump width (m)

cut: maximum tsunami cutoff width (m)= 2 w

S: distance traveled by center of mass (m)

ρ_b: the slump bulk density (kg/m^3)

$\gamma = \frac{\rho_b}{\rho_o}$

$R = \frac{b^2}{8T} + \frac{T}{2}$

$d\varphi = S / R$

$S_0 = S / 2$

$t_o = \sqrt{R(\gamma + 1)/(g(\gamma + 1))}$

$a_0 = \frac{S_0}{t_0^2}$

$u_t = \frac{S_0}{t_0}$

$\text{lambda} = 2t_0\sqrt{gd}$

Hammack number : hao = lambda / (2b)

Submergence number $S_g = S_0 \sin(\theta) / d$

maximum Froude number $Fr = \frac{u_t}{\sqrt{gd}}$

characteristic wave amplitude

$$\eta = .723 S_0 (1.4662(\gamma - 1) - .3454(\gamma - 1)^2) (\sin(\theta))^{.22} \left(\frac{T}{b}\right) \left(\frac{b}{d}\right)^{1.25} d\varphi^{.39} \frac{b}{R}^{.63} .1309$$

Trough position $x_{min} = .565 \left(\frac{d + \frac{T}{\cos(\theta)}}{\tan(\theta)} + .4597 S_0 \cos(\theta) \right) - \frac{d + \frac{T}{\cos(\theta)}}{\tan(\theta)}$

Quadratic number: $Qn = \frac{\eta}{S_0 (\sin(\theta))^{1.5}}$

Trough to peak distance = 0.5 lambda

Equations of slump motion solved by NHWAVE

Input parameters:

T: height of slump

b: length

w: width

e: parameter e in Enet and Grilli

α: slide angle (rad) from east clockwise

x_0: initial center x_0 of slump (m)

y_0: initial center y_0 of slump (m)

Slope_slide: bathymetry slope at slump (rad)

ut : terminal velocity of slump (calculated using Enet and Grilli)

S_f: Total movement distance :$2S_0$ (Grilli and Watts (2005))

t_f: Total time of movement πt_0 （Grilli and Watts (2005))

Calculations

$k_b = \frac{2\text{acosh}\left(\frac{1}{e}\right)}{b}$

$k_w = \frac{2\text{acosh}\left(\frac{1}{e}\right)}{w}$

a_0 = acceleration_lab（Grilli and Watts (2005))

$t_0 = \frac{u_t}{a_0}$

$S_0 = \frac{u_t^2}{a_0}$

$L_0 = -T\tan(\alpha_0) + S_t$

$$x_1 = \left(L_0 - \frac{b_l}{2}\right)\cos(\alpha)$$

$$x_2 = \left(L_0 + \frac{b_l}{2}\right)\cos(\alpha)$$

$S(t) = \frac{S_f}{2}(1 - \cos(\frac{t*3.14}{t_f}))\cos(slope\_slide)$ Slump movement

$$x_{0s} = \mathrm{x}_0 + \mathrm{S}*\cos(\alpha)$$

$$y_{0s} = \mathrm{y}_0 + \mathrm{S}*\sin(\alpha)$$

$$x_t = (x - x_{0s})\cos(\alpha) + (y - y_{0s})\sin(\alpha)$$

$$y_t = -(x - x_{0s})\sin(\alpha) + (y - y_{0s})\cos(\alpha)$$

$h_t = \frac{T}{(1-e)}(\frac{1}{\frac{\cosh(k_b x_t)}{\cosh(k_w x y_t)}} - e)$ Slump hump geometry

References

Chen, Q., J.T. Kirby, R.A. Dalrymle, A.B. Kennedy, and A. Chawla. Boussinesq modeling of wave transformation, breaking and runup. II: Two horizontal dimensions. *J Waterway, Port, Coastal and Ocean Engrng.*, **126**, 48–56, 2000.

Chen, Q., J.T. Kirby, R.A. Dalrymle, F. Shi, and SHIF, B. Thorntone. Boussinesq modeling of longshore currents. *J. Geophys. Res.*, **108**(C11), 3362, 2003.

Davies H.L. Tsunami PNG 1998 - Extracts from Earth Talk. *Waigani: University of Papua New Guinea*, 1998.

Davies, H. L., J. M. Davies, R. C. B. Perembo, and W. Y. Lus. The Aitape 1998 Tsunami: Reconstructing the Event from Interviews and Field Mapping. *Pure appl. geophys.*, **160**, 1895–1922, 2003.

Day, J., P. Watts, Grilli S. T., and J.T. Kirby. Mechanical models of the 1975 Kalapana, Hawaii earthquake and tsunami. *Marine Geology*, **215**(1-2):59–92, 2005.

Enet F. and S. T. Grilli. Experimental study of tsunami generation by three-dimensional rigid underwater landslides. *J. Wtrwy, Port, Coast, and Oc. Engrg.*, **133**(6), 442–454, 2007.

Geist E.L. Origin of the 17 July, 1998 Papua New Guinea tsunami: Earthquake or landslide? , *Seis. Res. Lett.*, **71**, 344–351, 2000.

Grilli S.T. and P. Watts. Modeling of waves generated by a moving submerged body. applications to under water landslides. *Engng. Analysis with Boundary Elements*, **23**, 645–656, 1999.

Grilli, S.T., P. Watts, S. Guignard, and C.E. Synolakis. Wave amplitude and runup predictions for tsunamis generated by underwater landslides. *EOS Transactions*, **46**, F549, AGU 1999.

Grilli, S.T., S. Vogelmann, and P. Watts. Development of a 3d numerical wave tank for modeling tsunami generation by underwater landslide. *Engng. Analysis Boundary Elemt.*, **26**(4), 301–313, 2002.

Grilli S. T. and P. Watts. Tsunami generation by submarine mass failure part i: Modeling, experimental validation, and sensitivity analyses. *J. Wtrwy, Port, Coast, and Oc. Engrg.*, **131**(6), 283–297, 2005.

Grilli, S., J. C. Harris, T. S. Tajalli Bakhsh., T. Masterlark, C.Kyriakopoulos, J. T. Kirby, and F. Shi. Numerical Simulation of the 2011 Tohoku Tsunami Based on a New Transient

FEM Co-seismic Source: Comparison to Far- and Near-Field Observations. *Pure and Applied Geophys.*, **170**, (6-8) 1333-1359, 2013.

Grilli S.T., O'Reilly C., Harris J.C., Tajalli-Bakhsh T., Tehranirad B., Banihashemi S., Kirby J.T., Baxter C.D.P., Eggeling T., Ma G. and F. Shi. Modeling of SMF tsunami hazard along the upper US East Coast: Detailed impact around Ocean City, MD. *Natural Hazards*, 42pps. (resubmitted), 2014.

Heinrich, P., A. Piatanesi, E. A. Okal, and H. Hebert. Near-field modeling of the July 17, 1998 tsunami in Papua New Guinea. *Geophys. Res. Lett*. **27**, 3037-3040, 2000.

Heinrich, P., A. Piatanesi, and H. Hebert. Numerical modelling of tsunami generation and propagation from submarine slumps: the 1998 Papua New Guinea event. *Geophys.J. Int*., **145**, 97-111, 2001.

Imamura, F. and K. Hashi: Re-examination of the source mechanism of the 1998 Papua New Guinea earthquake and tsunami, *Pure Appl. Geophys.*, **160**, 2071–2086, 2003.

Kawata, Y., Y. Tsuji, H. Matsutomi, F. Imamura, M. Matsuyama and T. Tahakashi. Field Survey of the 1998 Tsunami in the Northwestern Area of Papua New Guinea, *Report to Ministry of Education, Science, Sports and Culture*, Japan, 1999a.

Kawata, Y., B. C. Benson, J.C. Borrero, J. L. Borrero, H. L. Davies, W.P. Delange, F. Imamura, H. Letz, J. Nott, and C.E. Synolakis. Tsunami in Papua New Guinea was as Intense as First Thought, EOS Transactions of the Am. Geophys. Union **80**, 101, 104–105,1999b.

Krüger J. and S. Kumar. Papua New Guinea technical report, High-Resolution Bathymetric Survey Fieldwork undertaken from 28 May to 15 June 2006; *EU-SOPAC Project Report* **115**, September, 2008.

Lynett, P. J., J. C. Borrero, P. L.F. Liu and C. E. Synolakis. Field survey and numerical simulations: A review of the 1998 Papua New Guinea tsunami. *Pure appl. geophys.* **160**, 2119–2146, 2003.

Ma, G., F. Shi, and J.T. Kirby , Shock-capturing non-hydrostatic model for fully dispersive surface wave processes. *Ocean Modelling*, **43-44**, 22-35, 2012.

Matsumoto, T., D.R. Tappin and SOS Onboard Scientific Party. Possible coseismic large-scale landslide off the northern coast of Papua New Guinea in July 1998: Geophysical and geological results from SOS cruises, *Pure Appl. Geophys*. **160**, 1923–1943, 2003.

Newman A. V. and E. A. Okal. Moderately slow character of the july 17, 1998 Sandaun earthquake as studied by teleseismic energy estimates. *Eos Transactions, American Geophysical Union*, **79**, F564, Fall Meeting 1998.

Okal E. A.. The probable source of the 1998 Papua New Guinea tsunami as expressed in oceanic t waves. *Eos, Trans. Amer. Geophys. Un.*, **80**(46), F750, 1999.

Shi, F., J.T. Kirby, J.C. Harris, and J.D. Geiman and S.T. Grilli. A high-order adaptive time-stepping TVD solver for Boussinesq modeling of breaking waves and coastal inundation. *Ocean Modeling*, **43-44**, 36-51, 2012.

Satake, K. and Y. Tanioka. The July 1998 Papua New Guinea earthquake: mechanism and quantification of unusual tsunami generation, *Pure Appl. Geophys*., **160**, 2087–2118, 2003,

Sweet, S. and E. A. Silver, Tectonics and slumping in the source region of the 1998 Papua New Guinea tsunami from seismic reflection images. *Pure Appl. Geophys.*, **160**, 1945–1968 , 2003.

Synolakis, C. E. , J. P. Bardet, J. C. Borrero, E. A.and Silver E. A.and Sweet S. Davies, H. L.and Okal, and D. R. Tappin. The slump origin of the 1998 Papua New Guinea tsunami. *Proc. Royal. Soc. London*, **458**(2020), 763–790, 2002.

Takuechi A. and shipboard scientific party of R/V Yokosuka : Bottom response to atsunami earthquake: Submersible observations in the epicenter area of the 1993 earthquake off southwestern Hokkaido, Sea of Japan, *J. Geophys. Res*. **103**(24),109–24,125, 1998,

Tappin D. R.. Submarine slump generated tsunamis. *Mar. Geol. Special Issue*, **203**(3-4), 199–380, 2004.

Tappin, D. R., T. Matsumoto, P. Watts, K. Satake, G. M. McMurtry, M. Matsuyama, Y. Lafoy, Y. Tsuji, T. Kanamatsu,W. Lus, Y. Iwabuchi, H. Yeh, Y. Matsumotu, M. Nakamura, M. Mahoi, P. Hill, K. Crook, L. Anton, and J. P. Walsh. Energy concentration and recurrence of the 1998 Papua New Guinea tsunami: sediment slump likely caused 1998 Papua New Guinea tsunami. *EOS, Transactions of the American Geophysical Union*, **80**, F572, 1999a.

Tappin, D.R., P. Watts, J. Borrero, J.P. Bardet, S.T. Grilli, and C.E. Synolakis. Submarine slump generation of the 1998 papua new guinea tsunami : the evidence so far. *EOS Transactions AGU*, **46**, F750, 1999b.

Tappin, D. R. , P.Watts, G. M. McMurtry, Y. Lafoy, and T. Matsumoto. The sissano, papua new guinea tsunami of july 1998 offshore evidence on the source mechanism. *Mar. Geol*, **175**, 1–23, 2001.

Tappin, D. R., P. Watts, G. M. McMurtry, Y. Lafoy, and T. Matsumoto. Prediction of slump generated tsunamis:The july 17th 1998 papua new guinea event. *Sci. Tsunami Hazards*, **20**(4), 222–238, 2002.

Tappin, D. R., P. Watts, and S. Grilli. The papua new guinea tsunami of 17 july 1998: anatomy of a catastrophic event. *Nat. Hazards Earth Syst. Sci.*, **8**, 243–266, 2008.

Tehranirad, B., F. Shi, J.T. Kirby, J.C. Harris, and S. Grilli. Tsunami benchmark results for fully nonlinear Boussinesq wave model FUNWAVE-TVD (Version) 1.0. Research Report No. CACR-11-02, Center for Applied Coastal Research, Univ. of Delaware, Newark, 2011.

Tehranirad, B., J.T. Kirby, G. Ma, and F. Shi. Tsunami benchmark results for non-hydrostatic wave model NHWAVE (Version 1.0). Research Report No. CACR-12-03, Center for Applied Coastal Research, Univ. of Delaware, Newark, 2012.

Titov V. and F. Gonzalez. Numerical study of the source of the july 1998 png earthquake (abs.). *Eos Transactions.Am. Geophys.Union*, **79**, F564), Fall Meeting Supplement 1998.

Watts, P. Geowave V1.0, courtesy of Applied Fluids, 2002a.

Watts, P. TOPICS V1.2, (a component of Geowave), courtesy of Applied Fluids, 2002b.

Watts, P., S. T. Grilli, J. T. Kirby, G. J. Fryer, and D. R.Tappin. Landslide tsunami case studies using a Boussinesq model and a fully nonlinear tsunami generation model. *Nat. Hazards Earth Syst. Sci.*, **3**, 391–402, 2003.

Watts, P., S. T. Grilli, D. R. Tappin, and G. J. Fryer. Tsunami generation by submarine mass failure part ii: Predictive equations and case studies. *J. Wtrwy, Port, Coast, and Oc. Engrg.*, **131**(6), 298–310, 2005. 16.

Wei, J., J.T. Kirby, S.T. Grilli, and R. Subramanya. A Fully Nonlinear Boussinesq Model for Surface Waves. Part1. Highly Nonlinear Unsteady Waves. *J. Fluid Mech*., **294**, 71-92, 1995.